MICROSTRUCTURE-SENSITIVE WEIGHTED PROBABILITY APPROACH FOR MODELING SURFACE TO BULK TRANSITION OF HIGH CYCLE FATIGUE FAILURES DOMINATED BY PRIMARY INCLUSIONS

A Dissertation
Presented to
The Academic Faculty

by

Nima Salajegheh

In Partial Fulfillment
of the Requirements for the Degree
Doctor of Philosophy in the
School of Mechanical Engineering

Georgia Institute of Technology
August 2011

MICROSTRUCTURE-SENSITIVE WEIGHTED PROBABILITY APPROACH FOR MODELING SURFACE TO BULK TRANSITION OF HIGH CYCLE FATIGUE FAILURES DOMINATED BY PRIMARY INCLUSIONS

Approved by:

Prof. David L. McDowell, Advisor
School of Mechanical Engineering
Georgia Institute of Technology

Prof. Richard W. Neu
School of Mechanical Engineering
Georgia Institute of Technology

Prof. Hamid Garmestani
School of Materials Science and Engineering
Georgia Institute of Technology

Prof. Naresh Thadhani
School of Materials Science and Engineering
Georgia Institute of Technology

Dr. James M. Larsen
Air Force Research Laboratory
Wright-Patterson Air Force Base, Ohio

Date Approved: 05/10/2011

To my wife Golnaz, parents Ali and Maliheh, and brothers Sina and Pooya

ACKNOWLEDGMENTS

First and foremost, I am grateful to my research advisor Prof. David McDowell for his guidance and steadfast support whilst allowing me the room to work in my own way. He sets an example of a world-class researcher for his energy and enthusiasm for research in his field. This dissertation would not have been possible without his advisement and encouragement.

I express my sincere appreciation to the members of my committee Dr. James Larsen, Prof. Richard Neu, Prof. Hamid Garmestani, and Prof. Naresh Thadhani for their helpful feedback and suggestions. I thank the staff members at the George W. Woodruff School of Mechanical Engineering who have assisted me enormously throughout my graduate studies at the Georgia Institute of Technology. Special thanks go to Dr. Jeffrey Donnell for his help in revising my thesis manuscript. I would like to acknowledge the financial support for my PhD studies provided by:

- The George W. Woodruff School of Mechanical Engineering fellowship.
- Carter N. Paden, Jr. Distinguished Chair in Metals Processing fellowship.
- The NSF Center for Computational Materials Design (CCMD).
- ONR D3D from QuesTek Innovations LLC.

I would like to thank my friends and fellow group members at Georgia Tech. I would also like to thank my former supervisor at Michigan State University Prof. Farhang Pourboghrat for his support of my decision to attend Georgia Tech for my PhD. Last but not the least; I owe my deepest gratitude to my family for their unconditional love. None of this work would have been possible without their support and encouragement.

TABLE OF CONTENTS

LIST OF TABLES

LIST OF FIGURES

SUMMARY

The mechanical alloying and casting processes used to make polycrystalline metallic materials often introduce undesirable non-metallic inclusions and pores. These are often the dominant sites of fatigue failure origination at the low stress amplitudes that correspond to the high cycle fatigue (HCF) and very high cycle fatigue (VHCF) regimes, in which the number of cycles to crack initiation is more than 10^6.

HCF and VHCF experiments on some advanced metallic alloys, such as powder metallurgy Ni-base superalloys, titanium alloys, and high-strength steels have shown that the critical inclusions and pores can appear on the surface as well as in the bulk of the specimen. Fatigue lives have been much higher for specimens that fail from a bulk site.

The relative number of bulk initiations increases as the stress amplitude decreases such that just below the traditional HCF limit, fatigue life data appears to be evenly scattered between two datasets corresponding to surface and bulk initiations. This is often referred to as surface to bulk transition in the VHCF regime. Below this transition stress, the likelihood of surface versus bulk initiation significantly impacts the low failure probability estimate of fatigue life. Under these circumstances, a large number of very costly experiments need to be conducted to obtain a statistically representative distribution of fatigue life and to predict the surface versus bulk initiation probability.

In this thesis, we pursue a simulation-based approach whereby microstructure-sensitive finite element simulations are performed within a statistical construct to examine the VHCF life variability and assess the surface initiation probability. The methodology introduced in this thesis lends itself as a cost-effective platform for

development of microstructure-property relations to support design of new or modified alloys, or to more efficiently predict the properties of existing alloys.

1 Introduction

1.1 Problem statement

The mechanical alloying and casting processes used to make polycrystalline metallic materials often introduce undesirable non-metallic inclusions and pores that are large relative to the mean grain size. These are often the dominant sites of fatigue failure origination at the low stress amplitudes that correspond to the high cycle fatigue (HCF) and very high cycle fatigue (VHCF) regimes, in which the number of cycles to crack initiation is more than 10^6. Inclusions and pores cause a host of issues that can be broadly grouped into two categories:

1. Issues related to the inclusion/pore density. These include matters such as large scatter in HCF and VHCF fatigue life data, specimen size dependence [1-3], and surface to bulk transition of HCF and VHCF crack origins. The experimental approaches to the study of these issues require large numbers of experiments to be conducted for large-scale components, and this is not yet practical due to time and cost limitations.
2. Issues related to the fatigue crack formation processes. These include matters such as the nature of fatigue crack initiation from inclusions and pores, and their effects on the next stages of fatigue crack growth in the matrix. The experimental approaches to the study of these issues are particularly challenging due to the complex and subtle nature of the underlying processes.

The problems in both categories pose questions that are probabilistic in nature; studies of such issues require the use of appropriate statistics to characterize the underlying variability.

HCF experiments on some advanced metallic alloys, such as Ni-base superalloys, titanium alloys, and high-strength steels show that fatigue life can be unexpectedly much higher for some specimens [4-18] where the failure origin is located in the bulk. The relative number of internal initiations increases as the stress amplitude decreases in the HCF regime such that just below the traditional HCF limit, fatigue life data appears to be evenly scattered between two datasets corresponding to surface and bulk initiations. The occurrence of two distinct failure distributions has been referred to as "Competing Failure Modes" [19, 20]. Under these circumstances, a large number of experiments need to be conducted to obtain a statistically representative distribution of fatigue life in the HCF and VHCF regimes.

Other sources of information about variability in fatigue life may help to reduce the number of costly fatigue experiments that must be conducted to obtain a specific confidence level. In this thesis, microstructure-sensitive finite element analysis (FEA) is pursued as an additional source of knowledge about variability in fatigue life. Parametric crystal plasticity FEA simulations are performed within a statistical construct to study surface to bulk transition of fatigue crack origins. It will also be shown that the likelihood of surface versus bulk initiation significantly impacts the low failure probability estimate of fatigue life when the bimodal fatigue behavior is present.

To provide an experimental context, the application material for the crystal plasticity simulations is a fine-grained subsolvus microstructure of a powder metallurgy (PM) processed Ni-base superalloy, IN100.

Computational approaches to characterizing fatigue life variability do not eliminate the need for experiments. Rather, they need to be calibrated according to experimental fatigue data, and they should be duly based on the underlying physical mechanisms that are inferred from experiments. When these conditions have been met, computational approaches can be intelligently implemented to guide experiments or to effectively explain experimental trends. Physically-based and properly formulated computational tools may provide the following advantages:

- A cost-effective platform for development of microstructure-property relations to support design of new or modified alloys, or to more efficiently predict the properties of existing alloys.
- The ability to study the effects of significant variation in microstructures. Such studies can be costly using experimental methods, if indeed feasible.
- The ability to isolate and study the effects of microstructural attributes of interest, via reproducible "virtual" experiments.
- The ability to predict response measures that can be intractable or costly to measure via experiments, such as fine scale behavior within the microstructure.
- The ability to estimate the life expectancy of existing parts by capturing the *relative* effect of the controlling mechanisms at the different length scales

associated with the regimes of crack incubation, microstructurally small crack (MSC) growth, physically short crack (PSC) growth, and long crack (LC) growth.

1.2 Dissertation structure

The remainder of this thesis is organized as follows. In the next section, we introduce two materials of interest, namely Ni-base superalloy and martensitic gear steel. In Chapter 2, the two main computational tools of this study, crystal plasticity model and the Fatigue Indicator Parameters (FIPs), are presented with the corresponding model constants and material parameters. A brief discussion of the Statistics of Extreme Value follows. This chapter concludes by presenting the finite element (FE) model and techniques we used to efficiently simulate the grains around inclusions and pores.

Chapter 3 begins by summarizing the experimental literature concerning the role and nature of critical inclusions and pores in Ni-base superalloys. Using the crystal plasticity model, we calculate and compare the driving force for fatigue crack initiation (formation and early growth) in the matrix, surrounding the intact, cracked, and partially debonded inclusions as well as pores.

Chapters 4 and 5 investigate two of the possible surface-to-bulk transition mechanisms in Ni-base superalloys, using the crystal plasticity model to construct statistics of relevant FIPs for multiple simulated grain orientation distributions. The dependence of these statistics on microstructure attributes, as well as applied uniaxial strain amplitude ($R_\varepsilon = -1$), is explored.

Chapter 4 explores the interplay of external loading and local microstructure changes that affect inclusion-related FIPs. In particular, the dependence of stress distribution at the inclusion-matrix interface on inclusion radius and applied uniaxial strain amplitude ($R_\varepsilon = -1$) is examined. In Chapter 5, we examine the local state and

degree of residual stress relaxation around partially debonded inclusions and pores for several applied uniaxial strain amplitudes ($R_\varepsilon = -1$) and initial residual stress values.

In Chapter 6, the HCF and VHCF fatigue life variability are discussed with emphasis on the implications of competition between surface and bulk inclusions on the design of systems with very low probability of fatigue failure. The shortcomings of the existing approaches to computing these probabilities are presented followed by a simulation-based model that overcomes these shortcomings. The underlying probabilistic approach is explained, building on the notion that at low cyclic stress amplitudes, the inclusion-controlled fatigue response of advanced alloys is a probabilistic realization of the competing mechanisms of surface- and internally-initiated failures.

Subsequently there is a discussion of possible mechanisms, as suggested by experimental findings, which can drive the surface to bulk transition of fatigue crack initiation sites in alloys with inclusions. These mechanisms provide the context for the FE simulations of Chapters 4 and 5.

In Chapter 7, we will examine a case study where we incorporate the findings of Chapters 4 and 5 into the weighted probabilistic model presented in Chapter 6 to simulate the surface initiation probability in a fine-grained subsolvus microstructure of PM Ni-base superalloy, IN100. We will explore the dependence of the simulated surface initiation probability on such microstructure attributes as inclusion density, inclusion radius distribution, inclusion-matrix interface strength as well as specimen size and applied strain amplitude ($R_\varepsilon = -1$).

In contrast to Ni-base superalloys, non-metallic inclusions often fracture into smaller pieces during deformation processing or during manufacturing in high strength

steels. These inclusions appear as inclusion stringers, acting as the dominant sources of fatigue failure origination [21]. It is instructive to study how inclusions interact within a cluster. In Chapter 8, the magnification/shielding effect of a neighbor inclusion on the inclusion's potency to form a HCF crack in the adjacent matrix is studied. The finite element (FE) simulations of this section utilize the J2 elasto-plastic material behavior and the application material is a low carbon martensitic gear steel, Ferrium® C61 [22].

This thesis concludes with a summary of findings and a discussion of recommendations for future improvements in Chapter 9.

1.3 Materials examined in the Finite Element Analysis

1.3.1 Ni-base superalloys

Ni-base superalloys are the most widely used of all the classes of superalloys [23-27]. Two of the most important Ni-base superalloy properties are superior yield strength and creep resistance at high temperatures. Other crucial material properties include good fatigue life, phase stability, as well as oxidation and corrosion resistance [25, 26]. With such unique properties, Ni-base superalloys find extensive applications in the hot sections of gas engine turbines as well as in rocket motors and nuclear reactors.

A schematic of the Rolls-Royce Trent 800 aircraft gas turbine engine is shown in Figure 1-1 (a), showing the pressure and temperature profiles in various sections of the engine [27, 28]. Turbine Inlet Temperature (TIT), which is a direct indicator of the efficiency of a gas turbine engine, depends on the temperature capability of first stage high pressure turbine blades, which are often made of single crystal Ni-base superalloys [24, 29]. These alloys allow the turbine to operate more efficiently by withstanding higher temperatures. Polycrystalline Ni-base superalloys are used mainly in gas turbine engines for parts operating in the intermediate temperature regime, especially for components such as disks, spacers, and seals, as shown in Figure 1-1 (c) [27].

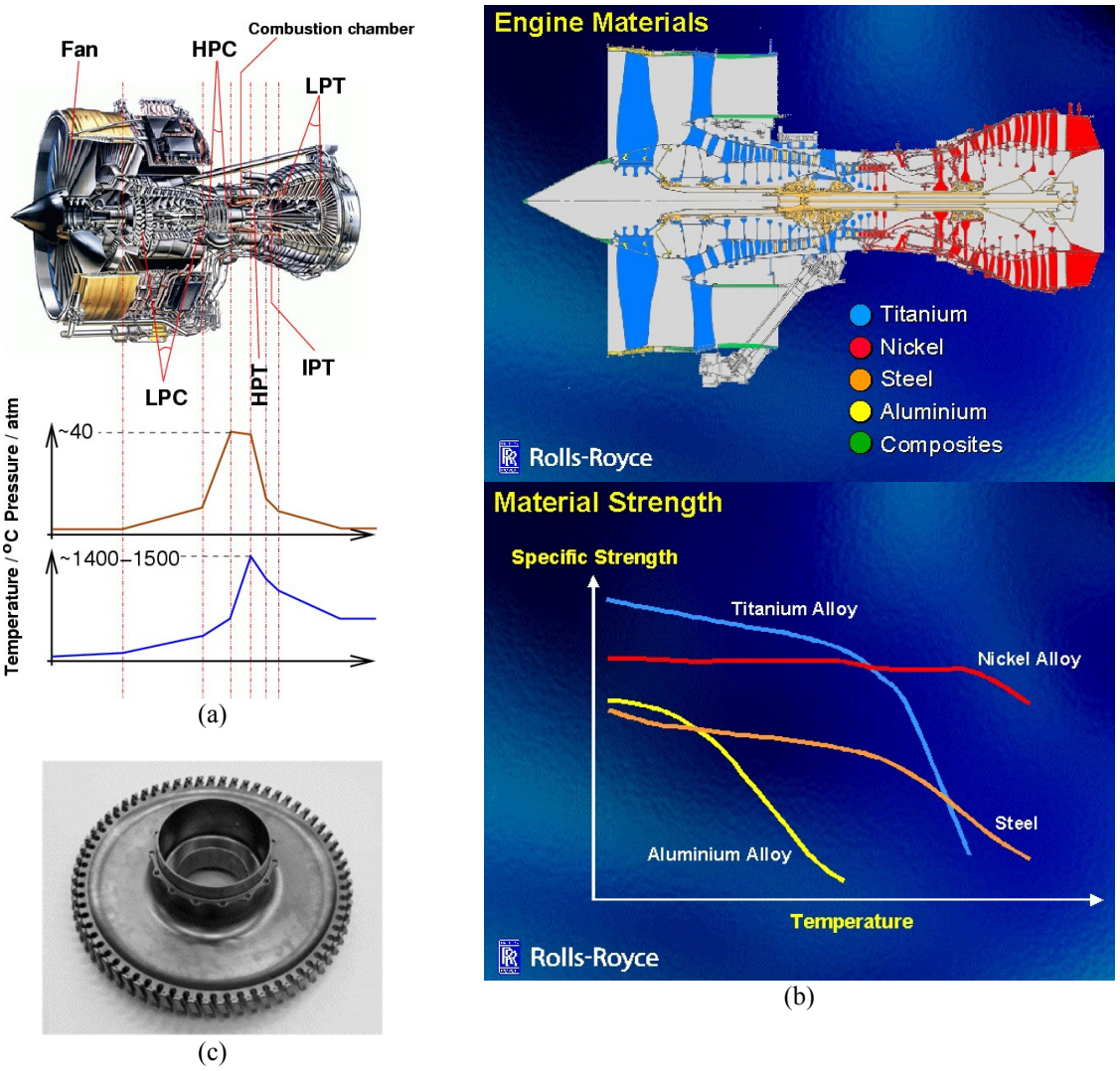

Figure 1-1: (a) pressure and temperature profiles in the Rolls-Royce Trent 800 jet engine, (b) common application alloys, and (c) A PM processed turbine disk [28].

The structure of most precipitation-strengthened Ni-base superalloys consists of the γ matrix, and of intermetallic γ′ precipitates of the [Ni3(Al,Ti)] type; these act as coherent barriers to dislocation motion. The γ phase is a solid solution with a face-centered crystal (FCC) lattice and randomly distributed different species of atoms. By contrast, the γ′ phase has an ordered crystalline lattice of type *LI2*. A two-phase

equilibrium microstructure is generated with a very unusual crystallographic relationship between the γ and γ' phases. Both phases are face-centered-cubic, have almost identical lattice parameters, and are coherent for the fine γ' phase [30].

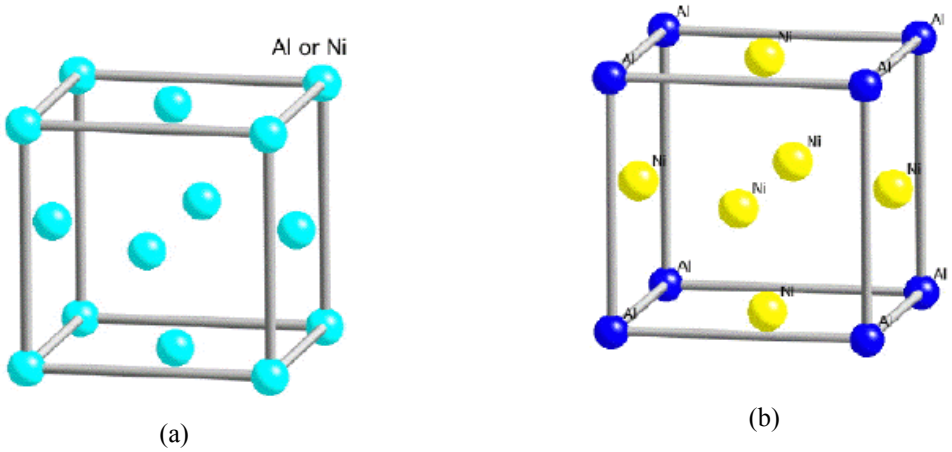

(a) (b)

Figure 1-2: Crystal structure of γ (a) and γ' (b) [31].

The lattice sites in the γ phase are occupied by similar atoms, i.e., either *Al* or *Ni*. In the pure Ni_3Al phase, atoms of aluminum are placed at the vertices of the cubic cell and form the sublattice *A*. Atoms of *Ni* are located at the centers of the faces and form the sublattice *B*, as shown in Figure 1-2 [31].

These sublattices of the γ' phase can accept as solute a considerable proportion of other alloying elements, which are dissolved in the γ phase as well. The γ' phase hardens the alloy through an unusual mechanism called the yield stress anomaly. Dislocations dissociate in the γ' phase, leading to the formation of an anti-phase boundary (APB). At elevated temperatures, the free energy associated with the APB is considerably reduced if it lies on a particular plane, which by coincidence is not a permitted slip plane. One set of

partial dislocations bounding the APB can cross-slip so that the APB lies on the low-energy plane; since this low-energy plane is not a permitted slip plane, the dissociated dislocation is now effectively locked [25]. By this mechanism, the yield strength of the γ′ phase actually increases with temperature up to about 1000 °C, giving superalloys their currently unrivalled high-temperature strength [32].

Alloying elements such as aluminum and titanium are used to promote the formation of the γ′ phase. Their close match in matrix-precipitate lattice parameters (~0-1%), combined with their chemical compatibility, allows the γ′ to precipitate homogeneously throughout the matrix and to have long-term stability. Extremely small γ′ precipitates always occur as spheres, because this shape best minimizes surface energy. As the γ′ density grows, the overall energy can be minimized by forming cubes, and thus the γ′morphology changes from spheres to cubes or plates depending on the value of the matrix-precipitate lattice mismatch [30].

The γ′ phase size can be controlled by certain precipitation-hardening heat treatments. Many superalloys have a two step heat treatment that creates a dispersion of cuboidal γ′ particles, known as the primary phase, with a fine dispersion between these known as secondary γ′ [27]; this is referred to as the subsolvus microstructure, as shown in Figure 1-3 for PM processed IN100 [13]. The material contains large γ′ precipitates that do not dissolve during the solutionizing step, as well as secondary and tertiary precipitates that form during cooling and subsequent aging. The subsolvus microstructure is noted for its high yield strength, fatigue resistance, and good fracture toughness, and is found mostly in disks of the lower temperature compressor sections. Temperature and cooling rate are varied to produce various microstructures.

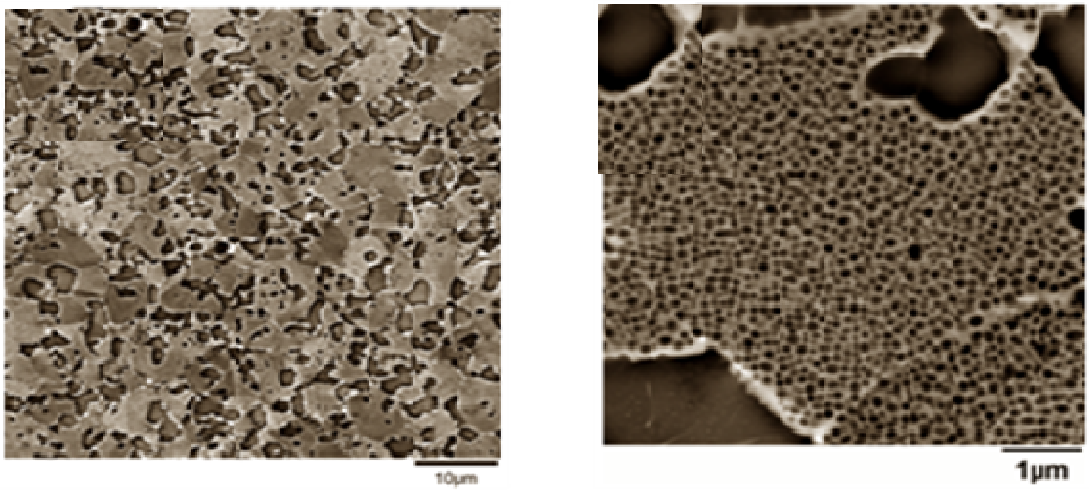

(a) (b)

Figure 1-3: The microstructure of subsolvus IN100, (a) the γ-primary-γ′morphology and (b) the secondary γ′ structure [13].

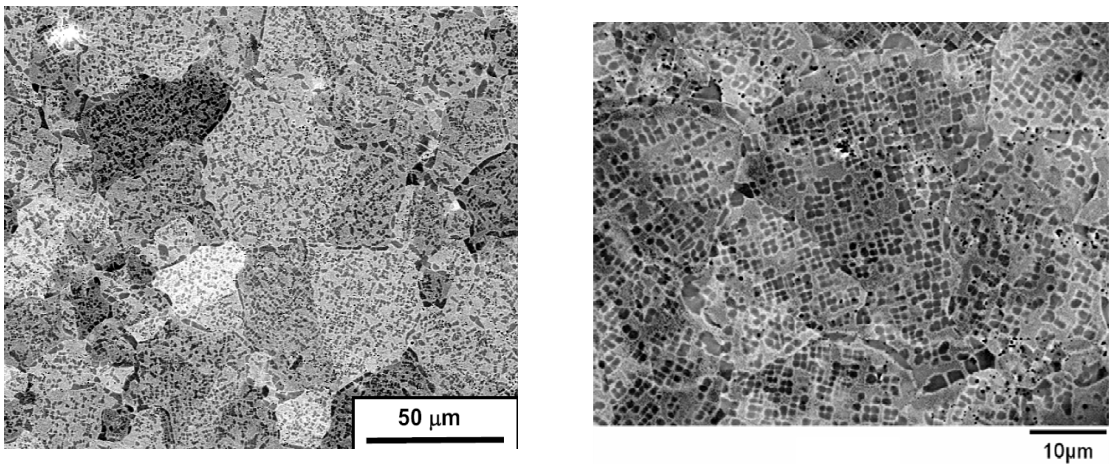

(a) (b)

Figure 1-4: The microstructure of supersolvus IN100, (a) the γ- secondary-γ′morphology and (b) the secondary γ′ structure [33].

The supersolvus microstructure is noted for its moderate strength and superior creep and fracture toughness; it is better suited for compressor and turbine disks than the subsolvus material. A supersolvus microstructure of a coarse grain PM processed IN100 with an average grain size of approximately 20 microns is shown in Figure 1-4 [33]. The reference material for the finite element simulation of chapter three is a fine-grained (having an average grain size of approximately 5 microns) subsolvus PM processed IN100.

It is often beneficial for a polycrystalline Ni-base superalloy to contain carbides to improve creep strength, as carbides are precipitated at grain boundaries and act to pin the boundaries and resist sliding [25, 27]. Oxidation or corrosion resistance is provided by adding elements such as aluminum and chromium that promote the formation of a protective surface oxide layer. A small amount of yttrium enhances an oxide layer's bond to the substrate [26].

Superalloy development has relied heavily on both chemical and process innovations and has been driven primarily by the aerospace and power industries. Directionally solidified and single crystal alloys are developed for turbine blade applications where grain boundaries are minimized or eliminated in order to obtain enhanced creep properties.

In contrast, disk material is designed for enhanced strength coupled with good fatigue properties in order to cope with the stress cycles in the flight cycle. Grain boundaries are beneficial and polycrystalline Ni-base superalloys are the materials of choice. But the benefits are obtained at the expense of creep life.

Highly alloyed Ni-base disks suffer from excessive ingot segregation, which makes grain size difficult to control. The development of powder metallurgy (PM) processing has alleviated this issue; in PM processing, a molten stream of metal is gas atomized in an inert argon atmosphere, and the resultant powder is consolidated by HIPing and/or superplastic forging to near-net shape [24].

Although PM results in remarkable chemical and microstructure homogeneity, as well as excellent strength and toughness properties, such products are prone to fatigue; failure often originates from ceramic inclusions, a by-product of the PM processing technique. Fatigue failure experiments highlight the increasing role of this failure mode at the lower stress amplitudes that correspond to HCF and VHCF regimes; such failures have raised a number of nontrivial issues in the design of PM Ni-base superalloy components for low probability of fatigue failure.

1.3.2 Ferrium® C61 martensitic gear steel

The application of steels in modern high-power-density gears demands an optimized combination of improved case hardness and superior core toughness. Good case hardness provides resistance against contact and bending fatigue, whereas core toughness is intended to alleviate the detrimental effects of internal flaws [34-41].

Ferrium® C61, accompanied by Ferrium C64 and C69, are three new alloys developed by QuesTek Innovations LLC (www.questek.com) using their Materials by Design® methodology for power transmission applications. All of these alloys utilize an engineered nanoscale M_2C carbide strengthening dispersion within a Ni-Co lath martensitic matrix [42].

At tempering temperatures of 450-600°C, these alloys exhibit a secondary hardening response in which fine M_2C carbide dispersions form as replacements for coarse cementite particles [43]. Thus these alloys are often referred to as secondary hardening steels [42]. Case carburizing produces a gradient in the volume fraction of the M_2C carbides and results in increased hardness and increased surface compressive residual stress. The efficiency of the M_2C strengthening response allows this class of steels to achieve very high surface hardness with very low carbon content. Thus, this class of steels has the ability to achieve very high surface hardness without the formation of detrimental primary carbides [44]. A typical hardness profile of carburized Ferrium® C61 is shown in Figure 1-5.

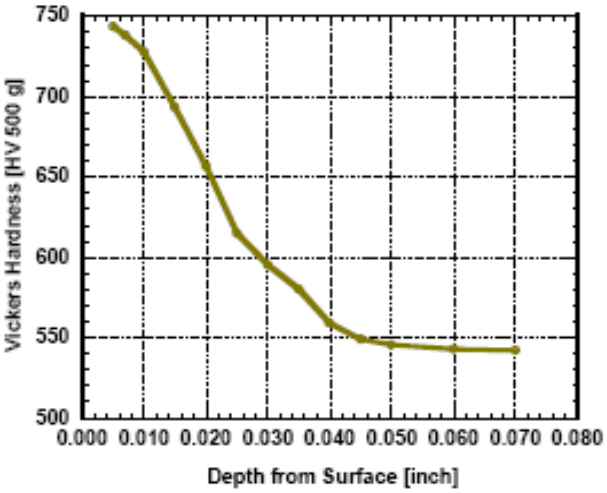

Figure 1-5: Typical hardness profile of carburized Ferrium® C61 [44].

Ferrium® C61 is targeted as a superior alternative to current gear materials in applications where component redesign is not feasible, but elevated core strength is required.

Figure 1-6: Typical high-power-density gear, made of carburized Ferrium® C61 [44].

Figure 1-6 shows a high-power-density gear, made of secondary hardening steels. Such gears often go through the following manufacturing stages:

1. The gear is commonly machined from a cast ingot that has been forged into stock. Additional gear manufacturing methods include direct casting and powder metallurgy techniques such as powder forging [21].
2. Carburization is performed to achieve hardening by diffusing carbon into the surface at solutionizing temperatures [34]. High-temperature vacuum carburizing is desirable for high power density gear applications, as it avoids the intergranular surface oxidation that is common to conventional gas carburizing and that commonly initiates bending fatigue failures [45].
3. Once carburized, the gears are quenched and often subjected to cryogenic treatments to ensure complete martensitic transformation. Tempering treatments are then performed to achieve secondary hardening through the precipitation of alloy carbides.
4. Various surface treatments can then be performed. Shot peening is commonly employed to impart compressive residual stress to the surfaces of the gear teeth and to the root notches.
5. Different means are employed to improve the surface finish of the gear to get rid of stress-increasing asperities; these means include honing, grinding and burnishing [46].

The application material for FE simulations in Chapter 8 is Ferrium® C61 with the composition listed in Table 1. The case and core hardness values are typically (60-62 HRC) and (47-50 HRC), respectively. A representative precipitation hardened case microstructure is shown in Figure 1-7. Heat treatment of this steel involves the following stages [22]:

1. Normalizing: The material is heated uniformly to 1875°F and air cooled.
2. Annealing: The material is heated uniformly to 1250°F, held for 2 to 8 hours and air cooled. Hardness should be less than 327 HBW.
3. Carburization and Hardening: The material is vacuum carburized at 1830°F, followed by quenching in a gas (1.5 Bar Nitrogen or higher) or oil medium.
4. Refrigeration: The material is refrigerated at -100°F or lower for 1 hour in order to obtain optimum case hardness. This should be performed with minimal delay after completion of the quench.
5. Tempering: The material is tempered at 900°F for 15 hours to achieve the desired case strength.

Table 1: Composition of C61 martensitic steel (wt %) [22].

C	Cr	Ni	Co	Mo	V	Fe
0.15	3.5	9.5	18	1.1	0.08	Bal

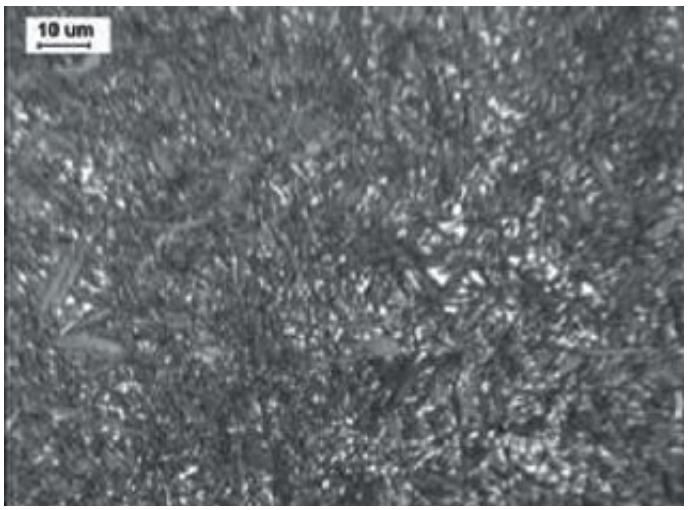

Figure 1-7: The Ferrium® C61 microstructure for treatment processed specimens [47].

2 Study tools

2.1 Material models

2.1.1 Homogeneous initially isotropic constitutive model for steel

Homogeneous continuum formulations of inelastic behavior are computationally inexpensive tools for qualitative study of such attributes as inclusion orientation and spacing when one wishes to smear other aspects of microstructure heterogeneity. Chapter 8 uses a homogenized elastoplastic material response having nonlinear kinematic hardening constitutive relations [48] to serve as the macroscopic material model; this model is included in the standard material model library of the commercial finite element software ABAQUS 6.7 [49]. It employs the simple Mises yield surface, i.e.,

$$F = f(\underset{\sim}{\sigma} - \underset{\sim}{\alpha}) - \sigma_{ys}^2 \tag{2.1}$$

with F = 0 during plastic flow, and

$$f\left(\underset{\sim}{\sigma} - \underset{\sim}{\alpha}\right) = \frac{3}{2}\left(\underset{\sim}{S} - \underset{\sim}{\alpha}'\right) : \left(\underset{\sim}{S} - \underset{\sim}{\alpha}'\right) = \frac{3}{2}\left(S_{ij} - \alpha'_{ij}\right)\left(S_{ij} - \alpha'_{ij}\right) \tag{2.2}$$

Here, $\underset{\sim}{S}$ is the deviatoric stress tensor, $\underset{\sim}{\sigma}$ is the stress tensor, $\underset{\sim}{\alpha}$ is the back stress tensor and $\underset{\sim}{\alpha}'$ is its deviatoric component. The uniaxial cyclic yield strength is defined by σ_{ys}. The associative plastic flow rule is given by

$$\dot{\underset{\sim}{\varepsilon}}_{pl} = \sqrt{\frac{3}{2}}\dot{\bar{\varepsilon}}_{pl}\frac{\partial F}{\partial \underset{\sim}{\sigma}}\left\|\frac{\partial F}{\partial \underset{\sim}{\sigma}}\right\|^{-1} = \sqrt{\frac{3}{2}}\dot{\bar{\varepsilon}}_{pl}\underset{\sim}{N} = \sqrt{\frac{3}{2}}\dot{\bar{\varepsilon}}_{pl}\frac{\underset{\sim}{S} - \underset{\sim}{\alpha}'}{\left\|\underset{\sim}{S} - \underset{\sim}{\alpha}'\right\|} \tag{2.3}$$

where $\dot{\underset{\sim}{\varepsilon}}_{pl}$ is the plastic strain rate tensor and $\dot{\bar{\varepsilon}}_{pl}$ is the equivalent plastic strain rate, defined by

$$\dot{\bar{\varepsilon}}_{pl} = \sqrt{\frac{2}{3}\dot{\underset{\sim}{\varepsilon}}_{pl} : \dot{\underset{\sim}{\varepsilon}}_{pl}} \tag{2.4}$$

The evolution equation for the back stress tensor $\underset{\sim}{\alpha}$ is expressed as

$$\dot{\underset{\sim}{\alpha}} = \frac{c}{\sigma_{ys}}\left(\underset{\sim}{\sigma} - \underset{\sim}{\alpha}\right)\dot{\bar{\varepsilon}}_{pl} - r\underset{\sim}{\alpha}\dot{\bar{\varepsilon}}_{pl} \tag{2.5}$$

where c and *r* are material parameters. Here, *c* is the initial kinematic hardening modulus and *r* determines the rate of dynamic recovery of the back stress with increasing plastic deformation. Isotropic hardening is neglected in view of the desire to simulate a cyclically stable response in parametric studies with pure kinematic hardening. The elastic response is given by

$$\underset{\sim}{\sigma} = \underset{\approx}{C} : \underset{\sim}{\varepsilon}_{el} \tag{2.6}$$

where $\underset{\sim}{\varepsilon}_{el}$ denotes the elastic strain tensor, and $\underset{\approx}{C}$ is the isotropic elastic stiffness tensor. Model parameters, presented in Table 2, are chosen to mimic the cyclic deformation behavior of the candidate low-carbon high-strength martensitic steel.

Table 2: Material parameters of Ferrium® C61 martensitic steel

E^m (GPa)	ν^m	σ_{ys}^m (MPa)	c^m (GPa)	r^m
193.6	0.28	1500	112.1	200

2.1.2 Crystal plasticity based model for polycrystalline Ni-base superalloys

Homogeneous continuum constitutive models for inelastic behavior are computationally inexpensive tools to support the qualitative study of attributes such as inclusion size, aspect ratio, and surface irregularities when one wishes to smear out or disregard explicit consideration of other aspects of microstructure heterogeneity. Such formulations are useful at higher stress amplitudes, i.e., the low-cycle fatigue regime.

Depending on the ratio of inclusion size to grain size and the heterogeneity level of cyclic plastic deformation, polycrystal plasticity is preferred relative to a homogeneous continuum constitutive formulation. Therefore, a continuum crystal plasticity model for IN100, based on the work of Shenoy *et al.* [50] and summarized by Przybyla and McDowell in complete form [51] is used for the bulk of the simulation work in this thesis.

This approach is more appropriate for capturing anisotropy and slip activity within individual grains on specific slip systems, and it accounts for the temperature-dependence of deformation mechanisms. Additional advantages of the crystal plasticity approach are:

- The physics of the crystallographic slip can be embedded more accurately in a crystal plasticity framework.
- Grains can be modeled explicitly using different crystallographic orientations and sizes as desired; this is especially important since grains play an important role in determining the crack initiation life in polycrystalline Ni-base superalloys [52].

- The crystal plasticity framework is appropriate for application in a hierarchical scheme for bridging length scales from precipitates in single crystals to polycrystalline aggregate to the homogenized stress-strain macroscopic response.

Since this thesis primarily emphasizes the role of non-metallic inclusions and pores that may be an order of magnitude larger than grains [53], it is not necessary to consider the constituent phases of a single grain, e.g., γ matrix and γ' precipitates. The crystal viscoplasticity constitutive model to be used in this work implicitly accounts for the precipitates in an average sense and assumes a homogeneous stress-strain response within a grain.

Deformation and stress heterogeneity within a grain due to its interaction with neighboring grains is not to be confused with this notion of grain-level homogeneous stress-strain response, as the former is seen in the finite element simulations if the simulated grain comprises more than one finite element integration point. In simulating the polycrystal, grain boundaries are treated only as idealized boundaries maintaining compatibility of deformation. This is a limitation of the present work.

2.1.2.1 Kinematics of crystal plasticity

The generalized plane strain finite elements, also referred to as 2.5D (See Section 2.4.1), implement the kinematics of a fully 3D continuum. The kinematics of crystal plasticity theory is based on the multiplicative decomposition of the total deformation gradient, $\mathbf{F}$, into a plastic part, $\mathbf{F}^p$, and a part that includes lattice deformation and rigid

body rotation, $\mathbf{F}^e$, based on the assumption of successive plastic and elastic deformation processes, as shown in Figure 2-1 [54, 55].

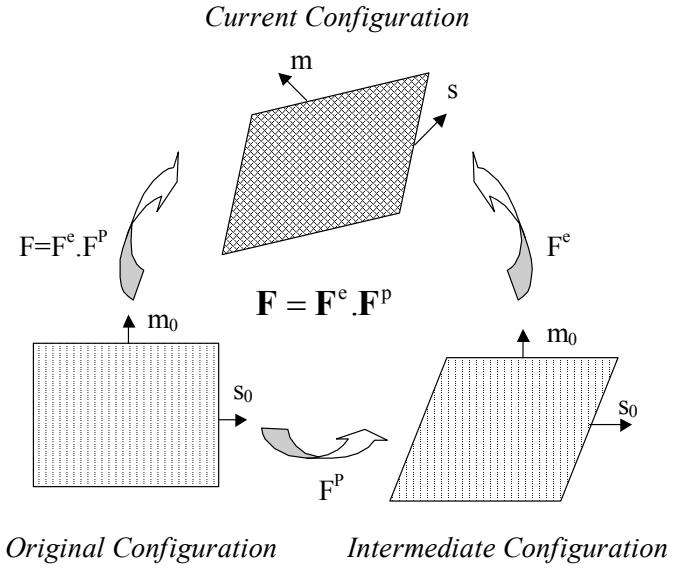

Figure 2-1: Successive elastic and plastic deformation.

Plastic deformation of the crystal [56-58] is due to dislocation glide on close-packed slip planes along close-packed directions; the isoclinic intermediate configuration in Figure 2-1 is selected, as that unique configuration that does not alter the orientation of the slip plane normal, $\mathbf{m}_o^\alpha$, and slip direction, $\mathbf{s}_o^\alpha$, unit vectors. In this case, the elastic deformation and rigid body rotation of the crystal lattice are embedded in $\mathbf{F}^e$, i.e.,

$$\mathbf{s}^\alpha = \mathbf{F}^e \cdot \mathbf{s}_o^\alpha \quad \text{and} \quad \mathbf{m}^\alpha = \mathbf{m}_o^\alpha \cdot \mathbf{F}^{e-1} \tag{2.7}$$

Here, α corresponds to a specific slip system, and zero subscripts denote the reference or original configuration in Figure 2-1. The net effect of dislocation glide on the α^{th} slip

system is modeled by the continuum shearing rate, $\dot{\gamma}^{\alpha}$. The plastic velocity gradient in the intermediate configuration is related to the rate of shearing by [56]

$$\mathbf{L}_{\mathrm{o}}^{\mathrm{P}} = \dot{\mathbf{F}}^{\mathrm{P}} \cdot (\mathbf{F}^{\mathrm{P}})^{-1} = \sum_{\alpha=1}^{\mathrm{N_{sys}}} \dot{\gamma}^{\alpha} (\mathbf{s}_{\mathrm{o}}^{\alpha} \otimes \mathbf{m}_{\mathrm{o}}^{\alpha}) \tag{2.8}$$

where the summation is taken over all the slip systems, N_{sys}, in the crystal, and the quantity $(\mathbf{s}_{\mathrm{o}}^{\alpha} \otimes \mathbf{m}_{\mathrm{o}}^{\alpha})$ is the Schmid tensor in the intermediate configuration. The resolved shear stress on the α^{th} slip system, τ^{α}, serves as the driving force for dislocation glide. The resolved shear stress on a slip system in the intermediate configuration is given by

$$\tau^{\alpha} = \boldsymbol{\sigma}^{PK2} : \left(\mathbf{s}_{o}^{\alpha} \otimes \mathbf{m}_{o}^{\alpha} \right) \tag{2.9}$$

where $\boldsymbol{\sigma}^{PK2}$ is the 2nd Piola-Kirchhoff stress tensor.

2.1.2.2 Constitutive behavior

The crystal plasticity model for IN100 is based on the work of Shenoy *et al.* [50] and presented in complete form by Przybyla and McDowell [51]. In this section, we present a summary of the model. The inelastic slip rate (flow rule) for the α^{th} slip system is a two-term potential given by [59, 60].

$$\dot{\gamma}^{\alpha} = \dot{\gamma}_{o} \left[exp\left(-\frac{Q_1}{kT} \right) \left\langle \frac{\left| \tau^{\alpha} - \chi^{\alpha} \right| - \kappa^{\alpha}}{D^{\alpha}} \right\rangle^{n_1} + exp\left(-\frac{Q_2}{kT} \right) \left\langle \frac{\left| \tau^{\alpha} - \chi^{\alpha} \right|}{D^{\alpha}} \right\rangle^{n_2} \right] sgn\left(\tau^{\alpha} - \chi^{\alpha} \right) \tag{2.10}$$

where T is the absolute temperature, k is the Boltzmann's constant, and Q_1 and Q_2 are activation energies; $\dot{\gamma}_o$ is a reference shearing rate and n_1 and n_2 are flow exponents; χ^α is the slip system back stress accounting for the Bauschinger effect in cyclic loading, κ^α is the threshold slip resistance, and D^α is the average drag resistance.

There are two types of dislocation slip systems that may be activated in a FCC ordered structure, 12 octahedral slip systems <110>{111} and 6 cube slip systems <110>{001}. The octahedral slip systems are active over the entire temperature range, while the cube slip systems are active only at higher temperature [61, 62]. The evolution equations for the threshold slip resistance and the back stress internal state variables depend on the microstructure. These equations are elaborated in [50], and references therein and are summarized in the following.

Three Internal State Variables (ISVs) are used: the threshold slip resistance, the dislocation density and the back stress variable. The threshold slip resistance, κ^α, is given by

$$\kappa_\lambda^\alpha = \kappa_{o,\lambda}^\alpha + \alpha_t \mu_{mix} b_{mix} \sqrt{\rho_\lambda^\alpha} \tag{2.11}$$

where λ stands for either the octahedral or cube slip systems, ρ^α is the dislocation density and μ_{mix} is the volume fraction averaged shear modulus given by

$$\mu_{mix} = \left(f_{p1} + f_{p2} + f_{p3} \right) \mu_{\gamma'} + f_m \, \mu_m \tag{2.12}$$

and

$$b_{mix} = \left(f_{p1} + f_{p2} + f_{p3} \right) b_{\gamma'} + f_m \, b_m \tag{2.13}$$

where $\mu_{\gamma'}$ and μ_m are the shear moduli for the precipitate and matrix phases, respectively, and f_m is the volume fraction of the matrix phase. Similar volume fraction averaging is employed for all the elastic properties (i.e. C_{11}, C_{12}, and C_{44}) as well. The slip resistance is expressed in terms of an initial reference critical resolved shear stress (CRSS) and the Taylor hardening term due to interactions of the statistically stored dislocations, ρ_λ^α.

A statistical coefficient, α, accounts for the deviation from the regular spatial arrangements of the dislocation population. The initial threshold slip resistance $\kappa_{o,\lambda}^\alpha$ is analogous to the yield strength and is influenced by microstructure attributes such as the grain size, precipitate size distribution, and associated volume fractions. The functional form for the microstructure dependence of the CRSS is based on Reppich and co-workers [63, 64]. The influence of the grain size, d_{gr}, is introduced through the Hall-Petch relations. The initial CRSS is given by

$$\begin{aligned}\kappa_{o,oct}^\alpha &= \left[\left(\tau_{o,oct}^\alpha\right)^{n_\kappa} + \psi_{oct}\left(f_{p1}, d_2, f_{p2}, d_3, f_{p3}\right)^{n_\kappa}\right]^{1/n_\kappa} + \left(f_{p1} + f_{p2}\right)\tau_{ns}^\alpha \\ \kappa_{o,cub}^\alpha &= \left[\left(\tau_{o,cub}^\alpha\right)^{n_\kappa} + \psi_{cub}\left(f_{p1}, d_2, f_{p2}, d_3, f_{p3}\right)^{n_\kappa}\right]^{1/n_\kappa}\end{aligned} \tag{2.14}$$

and

$$\psi_{oct} = \psi_{cub} = \left[c_{p1}\sqrt{\zeta\frac{f'_{p1}}{d_1}} + c_{p2}\sqrt{\zeta\frac{f'_{p2}}{d_2}} + c_{p3}\sqrt{\zeta\, f'_{p3}\, d_3} + \frac{c_{gr}}{\sqrt{d_{gr}}}\right], \qquad \zeta = \frac{\Gamma_{APB}}{\Gamma_{APB\_ref}} \tag{2.15}$$

where λ is the octahedral or cube slip system, and the precipitate volume fractions are normalized and given as

$$f'_{p1} = \frac{f_{p1}}{f_{p1} + f_m}, f'_{p2} = \frac{f_{p2}}{f_{p2} + f_m}, f'_{p3} = \frac{f_{p3}}{f_{p3} + f_m} \tag{2.16}$$

Here, Γ_{APB} is the anti-phase boundary energy, w is a constant that accounts for the elastic repulsion within the precipitates and λ_{p1} is the primary precipitate spacing. The parameters c_{p1}, c_{p2}, c_{p3}, and c_{gr} are determined by fitting the initial yield strength to the experimental data. The non-Schmid stress dependence of the octahedral slip systems is given by [59]

$$\tau_{ns}^{\alpha} = h_{pe}\tau_{pe}^{\alpha} + h_{cb}\left|\tau_{cb}^{\alpha}\right| + h_{se}\tau_{se}^{\alpha} \tag{2.17}$$

where τ_{pe}^{α}, τ_{cb}^{α}, and τ_{se}^{α} are the resolved shear stresses on the primary, cube, and secondary slip systems, respectively, and h_{pe}, h_{cb}, and h_{se} are constants that are experimentally determined. The evolution equation for the dislocation density is

$$\dot{\rho}_{\lambda}^{\alpha} = h_o\left\{Z_o + k_1\sqrt{\rho_{\lambda}^{\alpha}} - k_2\rho_{\lambda}^{\alpha}\right\}\left|\dot{\gamma}^{\alpha}\right| \tag{2.18}$$

where

$$Z_o = \frac{k_{\delta}}{b_{mix}\, d_{\delta eff}} \quad and \quad d_{\delta eff} \approx \left(\frac{2}{d_{2\delta}}\right)^{-1} \tag{2.19}$$

where k_1, k_2, and k_δ are constants and $d_{\delta eff}$ represents the secondary precipitate spacing. Hardening is controlled by a competition between dislocation storage and annihilation (dynamic recovery) mechanisms [65, 66]. A backstress term (χ^{α}) is included in the model to capture the Baushinger effect due to heterogeneous distribution of dislocations

at the γ' precipitate interfaces since the two-phase microstructure is not modeled explicitly. The backstress evolution is given as

$$\dot{\chi}_{\lambda}^{\alpha} = C_{\chi}\left\{\eta\mu_{s}b\sqrt{\rho_{\lambda}^{\alpha}}\ sgn\left(\tau^{\alpha}-\chi_{\lambda}^{\alpha}\right)-\chi_{\lambda}^{\alpha}\right\}\left|\dot{\gamma}^{\alpha}\right| \tag{2.20}$$

and

$$\eta = \frac{\eta_{o}z_{o}}{z_{o}+k_{1}\sqrt{\rho_{\lambda}^{\alpha}}} \tag{2.21}$$

where C_{χ} is a fitting parameter, the coefficient η establishes the ratio of back stress amplitude relative to the cyclic flow stress for various slip systems and η_{o} describes the contribution from the GNDs. Shenoy *et al.* [50] calibrated the model for several distinct IN100 microstructures, using experimental fatigue data under variable strain rates to obtain some of the constants. Their work suggested physically reasonable values for the remaining model constants. A constant subsolvus-processed IN100 microstructure is used throughout this study; it is prepared using powder metallurgy techniques. Common model constants and microstructure parameters specific to this study are listed in Table 3 and Table 4, respectively. Initial values of all slip system back stresses are set to zero. The constitutive equations formulated in the previous section are implemented as a User MATerial (UMAT) in ABAQUS [49].

Table 3: Common model parameters for all microstructures calibrated for T = 650ºC [50, 51, 67].

$\tau^{\alpha}_{o,oct}$ (MPa)	$\tau^{\alpha}_{o,cub}$ (MPa)	c_{p1}	c_{p2}	c_{p3}	c_{gr} (MPa $\sqrt{mm}$)	k_{δ}
85.1	170.2	1.351	1.351	$1.22x10^{5}$	9.432	$2.5x10^{-3}$

$b_{\gamma'}$ (nm)	b_{γ} (nm)	$\mu_{\gamma'}$ (MPa)	μ_{γ} (MPa)	k_1 (mm^{-1})	k_2	D^{α} (MPa)	h_o
0.25	0.41	81515	130150	$2.6x10^{5}$	8.2	150(oct) 180(cube)	4.8(oct) 2.4(cube)

h_{pe}	h_{cb}	h_{se}	η_o	$\Gamma_{APB}\left(=\Gamma_{APB\_ref}\right)$ (J/m^2)	$\dot{\gamma}_1$ (s^{-1})	$\dot{\gamma}_2$ (s^{-1})	n_1	n_2
0.8	0.0	-0.4	2.82	$164x10^{-3}$	8.7	$3.9x10^{-11}$	15	9

$C_{11\gamma'}$ (MPa)	$C_{12\gamma'}$ (MPa)	$C_{44\gamma'}$ (MPa)	$C_{11\gamma}$ (MPa)	$C_{12\gamma}$ (MPa)	$C_{44\gamma}$ (MPa)	n_{κ}	$\rho^{\alpha}_{\lambda}(0)$ (mm^{-2})
135000	59210	81515	158860	73910	130150	1	$1.0x10^{5}$

Also, $\dot{\gamma}_1 = \dot{\gamma}_o \exp\left(\frac{-Q_1}{RT}\right)$ and $\dot{\gamma}_2 = \dot{\gamma}_o \exp\left(\frac{-Q_2}{RT}\right)$, where T = 923 K (650ºC) and

$\dot{\gamma}_o$	R (J /(mol-K))	Q_1 (J/mol)	Q_2 (J/mol)
$6.1x10^{16}$ s^{-1}	8.314	280,000	480,452

Table 4: Model parameters for our specific subsolvus processed IN100 [50, 51, 67].

f_{p1}	d_2 (nm)	f_{p2}	d_3 (nm)	f_{p3}	d_{gr} (μm)	α_t (MPa)	C_χ (MPa)	$d_{2\delta}$ (nm)
0.053	320	.439	17	.078	6.6	.0385	2.713	8.2

2.2 Fatigue Indicator Parameters

Fatigue Indicator Parameters (FIPs) are employed in this study at the microstructure scale to reflect the driving force for fatigue crack formation and early growth. The term "Critical Plane" is applied to the crystallographic facets and microstructure scale planes along which Stage I fatigue cracks often form and grow. This happens in shear-dominated cases that are common for alloys exhibiting dominant single or double slip in LCF at moderate temperatures, and particularly for low stacking fault energy FCC materials or Ni-base superalloys, as in the present study. In this simulation-based approach, the "potency" of inclusions to form fatigue cracks in a given material is judged by the magnitude of the mechanism-specific relevant FIP parameter in the adjacent matrix.

Several "two-parameter" FIPs have been introduced, for example emerging from the work of Findley, Stulen, and Cummings in the 1950s [68-71]. These FIPs differ from one another based on whether they use stress, strain, or energy as field variables, but in general they all seek to relate a multiaxial state of stress or deformation to an equivalent scalar parameter [72, 73] that can correlate fatigue tests under various conditions. The choice of an appropriate parameter is largely influenced by the fatigue regime under study, the material behavior, the loading conditions, and their interplay.

In polycrystalline Ni-base superalloys, the HCF life is typically composed of the following stages when cracks form via slip band cracking:

1. Fatigue crack formation on crystallographic planes at the subgrain scale.
2. Microstructurally Small Crack (MSC) growth.

3. Physically Small Crack (PSC) and Long Crack (LC) growth until specimen failure.

The total fatigue life is modeled as the sum of the numbers of cycles spent in several consecutive stages, i.e.,

$$N_T = N_{inc} + N_{MSC} + N_{PSC} + N_{LC} \tag{2.22}$$

where N_{inc}, the crack incubation life, refers to the number of cycles required for a crack to nucleate and grow through the spatial domain of influence of the micronotch (e.g., debonded inclusion) to some particular scale on the order of grain size or a fraction of inclusion size. Hence, N_{inc} includes both fatigue crack nucleation and some degree of early crack growth.

This decomposition has greater utility in the present context than one that considers nucleation and growth because it associates specific material length scales with different regimes, whereas the spatial scale for nucleation per se is typically ill-defined. N_{MSC} is the number of cycles required for propagation of a MSC through perhaps 3-10 grains in which fatigue crack growth is stochastic in terms of interaction with the microstructure, and N_{PSC} is the number of cycles required for propagation of a PSC during the transition to long crack growth. The long crack propagates according to LEFM with an associated number of cycles N_{LC}.

Initiation life, $N_{initiation}$, is typically defined subjectively. It often refers to the number of cycles required to form a detectable crack, which of course depends on

detection limits, instrumentation and methods. Thus, one can usually rank order the nucleation, incubation, and initiation lives as

$$N_{nucleation} < N_{inc} < N_{initiation} \tag{2.23}$$

In the HCF and VHCF regimes, crack incubation and early stages of MSC growth consume most of the total fatigue life. These stages are known to be controlled by cyclic irreversible deformation at the scale of microstructure, associated with to-and-fro slip and the impingement of slip bands on the grain boundaries [74]. To address fatigue crack incubation in shear (Stage I), shear-based FIPs are candidates for the relative assessment of fatigue crack incubation potency. In this thesis, the following shear-based FIPs are utilized.

2.2.1 Maximum nonlocal cyclic plastic shear strain range

Maximum nonlocal cyclic plastic shear strain range, $\Delta\gamma^*_{p,\max}$, is a simple yet revealing FIP that forms the basis for calculation of other FIPs. To obtain $\Delta\gamma^*_{p,\max}$, we start by calculating the range of the plastic strain tensor, $\Delta\varepsilon^p_{ij}$, over a stabilized loading cycle at the finite element integration points, as $\Delta\varepsilon^p_{ij} = \varepsilon^p_{ij}\big|_{\mathrm{A}} - \varepsilon^p_{ij}\big|_{\mathrm{B}}$. The instances A and B are shown in Figure 2-2 for strain ratios of R_ε = -1 and 0 ($R_\varepsilon = \varepsilon^{\min}{}_{yy} / \varepsilon^{\max}{}_{yy}$). Figure 2-2 plots the applied nominal strain amplitude, normalized relative to the macroscopic yield strain, versus time for three loading cycles.

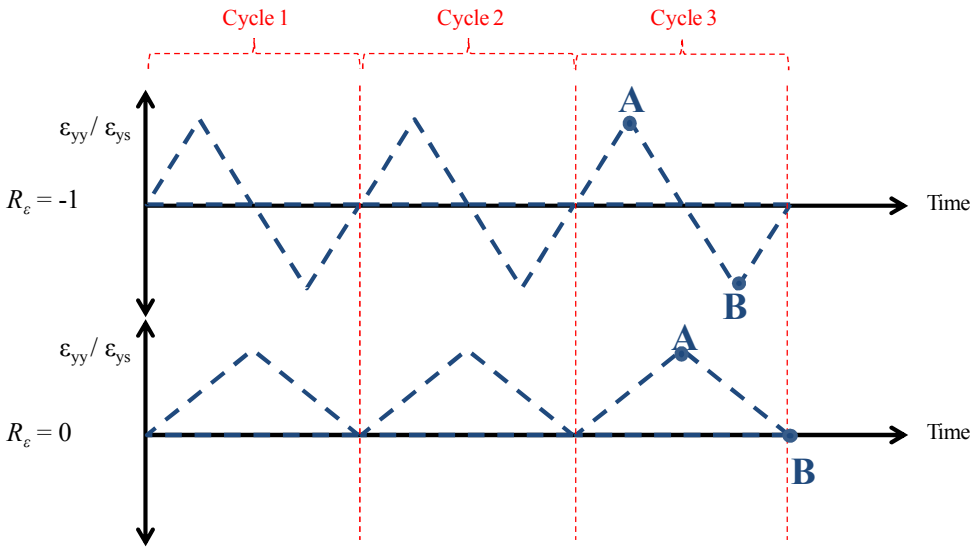

Figure 2-2: Instances A and B for strain ratios of R_ε = -1 and 0.

The range of plastic strain tensor is then averaged over some finite domain with length scale on the order of microstructure, representative of the scale at which crack incubation is defined.

$$\Delta\varepsilon_{ij}^{p*} = \frac{1}{V}\int \Delta\varepsilon_{ij}^{p} dV \tag{2.24}$$

The asterisk denotes a quantity that is averaged over some finite averaging region. In this study, the nonlocal averaging region is taken to be of a constant size in order to account for size effects, and is located at the slip-intensified region of the inclusion notch root, as shown in Figure 2-3. The averaging procedure also helps to ensure computationally consistent and objective results by regularizing to avoid mesh-size dependence. Further, it accounts for the fact that cracks physically form over a finite region, as noted in other studies [75-78].

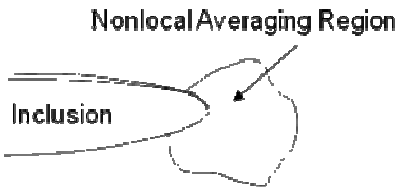

Figure 2-3: Averaging region.

In general, experimental studies necessary to justify a particular domain size for averaging are lacking, so it is important for a measure to be consistently applied in parametric studies that seek to compare microstructures. In the finite element simulations of the following chapters, the size of the averaging area is chosen to (a) have a reasonable physical association with damage process zone and (b) offers some degree of computational regularization. As such, it depends on the model and element size and is specified accordingly.

The nonlocal plastic shear strain range, $\Delta\gamma^*_{p,\theta}$, on a given plane-θ with unit normal vector $\boldsymbol{n}$ and along a given direction with unit vector $\boldsymbol{t}$, is calculated by projecting the nonlocal range of plastic strain tensor, $\Delta\varepsilon^{p*}_{ij}$, onto the plane as

$$\Delta\gamma^*_{p,\theta} = 2\boldsymbol{n}\bullet\Delta\boldsymbol{\varepsilon}^{p*}\bullet\boldsymbol{t} \tag{2.25}$$

The maximum of the nonlocal plastic shear strain range, $\Delta\gamma^*_{p,\theta}$ amongst all planes is taken to be the maximum nonlocal cyclic plastic shear strain range, $\Delta\gamma^*_{p,\max}$, i.e.,

$$\Delta\gamma^*_{p,\max} = \max_{\theta}(\Delta\gamma^*_{p,\theta}) \tag{2.26}$$

In this thesis, the $\Delta\gamma^*_{p,max}$ parameter is calculated as

$$\Delta\gamma^*_{p,\max} = \max_{\theta}(\Delta\gamma^*_{p,\theta}) = \Delta\varepsilon^*_{p,1} - \Delta\varepsilon^*_{p,3} \tag{2.27}$$

where $\Delta\varepsilon^*_{p,1} > \Delta\varepsilon^*_{p,2} > \Delta\varepsilon^*_{p,3}$ are the ordered eigenvalues of $\Delta\varepsilon^{p*}_{ij}$.

*2.2.2 The Fatemi-Socie (*FS*) parameter*

The Fatemi-Socie (*FS*) critical plane parameter [79, 80] is defined as

$$P_{FS} = \max_{\theta}\left[\frac{\Delta\gamma^*_{p,\theta}}{2}\left(1 + k_{FS}\frac{\sigma^*_{n,\theta}}{\sigma_{ys}}\right)\right] \tag{2.28}$$

where $\Delta\gamma^*_{p,\theta}$ is the nonlocal plastic shear strain range (c.f. 2.2.1), on a given plane-θ with unit normal vector $\boldsymbol{n}$ and $\sigma^*_{n,\theta}$ is the maximum tensile stress acting normal to the plane of $\Delta\gamma^*_{p,\theta}$ during a cycle. This particular definition pertains to proportional loading, as relevant to our purposes. Here $\sigma^*_{n,\theta}$ accounts for the influence of peak tensile normal stress on microstructurally small crack formation and early growth and is normalized by the cyclic yield strength, σ_{ys}.

The FS parameter was shown by McDowell and Berard [72] to have relation to small crack growth under combined stress states and by McDowell [81] to correlate trends of observed multiaxial fatigue data for fatigue crack initiation quite well. The FS parameter is relevant to this study as the focus is on cyclic plasticity in the microstructure that governs crack formation at the scale of grains and early stages of microstructurally

small crack growth which are mainly responsible for the variability in the fatigue life at low applied stress amplitudes.

Parameter k_{FS} weights the contribution of normal stress and can depend on the material as well as the multiaxial strain state [73]. A constant value of this parameter serves this study's objective of comparing microstructures for a given alloy system. Parameter k_{FS} is selected as $k_{FS} = 0.5$ in this study, consistent with the work of Findley [52] on a similar superalloy, René 88DT, albeit in the macroscopic scale.

2.2.3 Cumulative equivalent plastic strain

Another grain scale measure to assess the driving force for forming microstructure cracks in the HCF regime is the cumulative equivalent plastic strain [82], defined for one cycle as

$$P_P = \sqrt{\frac{2}{3}\Delta\varepsilon_{ij}^{*p}\Delta\varepsilon_{ij}^{*p}} \tag{2.29}$$

The cumulative equivalent plastic strain may be computed for one stable loading cycle (c.f. Eq. 29) or for an arbitrary time period (t_1 to t_2) as

$$P_P = P_P\big|_0 + \int_{t_1}^{t_2} \sqrt{\frac{2}{3}\varepsilon_{ij}^{*p}\varepsilon_{ij}^{*p}}\, dt \tag{2.30}$$

Averaging volumes of 1 and 2-3 grains are used to obtain the averaged plastic strain tensor, ε_{ij}^{*p} from the plastic strain tensor at finite element integration points, ε_{ij}^{p}.

2.2.4 Inclusion-matrix interface separation parameters

Chapter 4 focuses on the likelihood and location of inclusion-matrix interface separation at various applied uniaxial strain amplitudes. Accordingly, two FIPs will be used as qualitative measures of the driving force for the inclusion-matrix interface separation.

The inclusion-matrix interface traction is calculated for each grain adjacent to the inclusion as

$$T_{\text{int}} = \begin{cases} \max\left(n^{incl} \bullet \sigma^{*} \bullet n^{incl}\right) & \text{if positive} \\ 0 & \text{if negative} \end{cases} \tag{2.31}$$

Here, σ_{ij}^{*} is the Cauchy stress tensor averaged over the grain and n^{incl} is the unit vector normal to the grain interface with the inclusion. For inclusions with a circular 2D section, n^{incl} is unique for each grain. It is determined based on the location of the grain relative to the inclusion center. The compressive interface traction is excluded in the calculation of T_{int}. The $\max\left(n^{incl} \bullet \sigma^{*} \bullet n^{incl}\right)$ refers to the maximum value of $\left(n^{incl} \bullet \sigma^{*} \bullet n^{incl}\right)$ over a loading cycle.

Additionally, a particular FIP (called modified interface traction parameter or P_T) is useful for identifying potential interface debonding sites that may include soft grains adjacent to hard, non-metallic inclusions. These grains experience large plastic strains due to their orientation but do not transfer high magnitudes of interface traction [83]. As such, any measure of interface separation potency that is solely based on the interface loads (i.e. stress or traction) falls short of identifying these potential hot spots. This new

indicator parameter P_T includes the inclusion-matrix interface traction and impingement of slip bands on the interface and is defined as

$$P_T = \left(n^{incl} \bullet \Delta\varepsilon_{ij}^{p*} \bullet n^{incl} \right) \left[1 + k_T \frac{T_{\text{int}}}{\sigma_{ys}} \right] \tag{2.32}$$

Here, $\Delta\varepsilon_{ij}^{p*}$ is the range of plastic strain tensor averaged over the grain adjacent to the inclusion. Parameter k_T is a material constant that weights the contribution of tensile inclusion-matrix interface traction. Due to the lack of experimental data regarding the relative effects of interface traction versus plastic strain on the degree of interface separation, a constant value $k_T = 0.2$ is used in this study for comparison between microstructures for a given alloy system. Of course, this parameter can be calibrated to the experiments. Parameters T_{int} and P_T are calculated for each interface grain, as shown in Figure 2-4. It should be noted that similar impingement parameters have been introduced by Zhang [84] and McDowell [85] that help to characterize the effects of directional plastic strain accumulation at the continuum level. Table 5 summarizes the main FIPs that are used in this thesis.

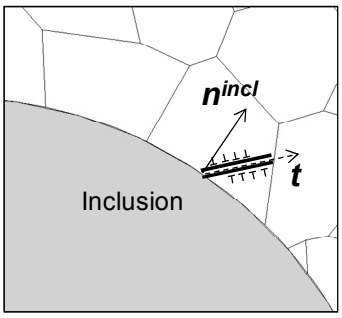

Figure 2-4: Schematic of calculation method for T_{int} and P_T.

Table 5: Summary of the FIPs used in this thesis.

Parameter Name	Definition	Candidate references	Used in Chapter(s)
Maximum nonlocal cyclic plastic shear strain range	$\Delta\gamma^*_{p,\max} = \max_\theta(\Delta\gamma^*_{p,\theta})$ $\Delta\gamma^*_{p,\theta} = 2\boldsymbol{n}\bullet\Delta\boldsymbol{\varepsilon}^{p^*}\bullet\boldsymbol{t}$		3, 6, 8
Fatemi-Socie (FS)	$P_{FS} = \max_\theta\left[\frac{\Delta\gamma^*_{p,\theta}}{2}\left(1+k_{FS}\frac{\sigma^*_{n,\theta}}{\sigma_{ys}}\right)\right]$	[52, 73, 79, 80]	3, 6, 8
Cumulative equivalent plastic strain	$P_P = \sqrt{\frac{2}{3}\Delta\varepsilon^{*p}_{ij}\Delta\varepsilon^{*p}_{ij}}$	[82]	3, 6, 8
Interface traction	$T_{\text{int}} = \begin{cases}\max\left(n^{incl}\bullet\sigma^*\bullet n^{incl}\right) & \text{if positive}\\ 0 & \text{if negative}\end{cases}$	[86-90]	4
Modified interface traction	$P_T = \left(n^{incl}\bullet\Delta\varepsilon^{p^*}_{ij}\bullet n^{incl}\right)\left[1+k_T\frac{T_{\text{int}}}{\sigma_{ys}}\right]$	[86-90]	4

This thesis focuses on a *comparative* study of microstructure attributes. The fatigue crack initiation (formation and early growth) potency is measured by the FIP magnitude. Comparison of absolute predicted fatigue life is not undertaken among various microstructure realizations, as that is a much more challenging and long term endeavor. However, one may relate FIPs to fatigue crack initiation life using modified Coffin-Manson laws if so desired, with the caveat that they represent only crack initiation life relations.

2.3 Statistics of extreme value (SEV)

Fatigue is probabilistic in nature. HCF and VHCF failures are rare event phenomena that depend on the extreme attributes of microstructure and applied loading. The inherent variability in fatigue failure processes requires that suitable statistics be used to characterize fatigue properties [91]. In particular, the theory of statistics of extreme value (SEV) [92] has been successfully used in the pioneering work of Murakami *et al.* [93-95] to estimate the largest inclusion size in clean steels. In Murakami's work, this value is linked to the range of stress intensity factor, ΔK , as

$$\Delta K = 0.65 \Delta S \sqrt{\pi \sqrt{area}} \tag{2.33}$$

where $\sqrt{area}$ is the square root of the projected area of estimated largest inclusion and ΔS is the applied stress range [96].

Extreme value distributions are used to model the smallest or largest values among a large set of independent, identically distributed random values representing measurements or observations. Three types of extreme value distributions exist within the extreme value theory, and these can be applied to different classes of underlying distributions [92]:

1. Gumbel (type I): For distributions whose tails decrease exponentially (i.e., normal distribution)
2. Fréchet (type II): For distributions whose tails decrease as a polynomial (i.e., the t distribution)
3. Weibull (type III): For distributions whose tails are finite (i.e., beta distribution)

These three distributions are combined into a single form, referred to as the generalized extreme value distribution (GEV), allowing a continuous range of possible shapes such that the data can decide which distribution type is more appropriate. The generalized extreme value distribution has cumulative distribution function:

$$c(x;\mu,\sigma,\xi)=\exp\left\{-\left[1+\xi\left(\frac{x-\mu}{\sigma}\right)\right]\right\}^{\frac{-1}{\xi}} \qquad \text{for } \left(1+\xi\left(\frac{x-\mu}{\sigma}\right)>0\right) \tag{2.34}$$

where μ is the location parameter, $\sigma>0$ is the scale parameter and ξ is the shape parameter.

Atkinson and Shi [97, 98] have suggested using the Generalized Pareto Distribution (GPD) in place of the GEV distribution to predict the maximum inclusion size. Both distributions predict that the maximum inclusion size increases with increasing specimen volume. Unlike a GEV estimate, which increases indefinitely, a GPD estimate is more realistic, as it reaches an upper limit. The GPD is often used to more accurately model the tail (exceedences over a threshold) of another distribution (such as normal). The GPD cumulative distribution function is

$$c(x)=\begin{cases}1-\left(1+\dfrac{\zeta(x-\mu)}{\sigma}\right)^{-1/\zeta} & (\zeta<0 \quad , \quad \mu\le x\le \mu-\dfrac{\sigma}{\zeta})\\ 1-e^{\left(\frac{x-\mu}{\sigma}\right)} & (\zeta=0)\end{cases} \tag{2.35}$$

where μ is the location parameter, $\sigma>0$ is the scale parameter and ξ is the shape parameter. The GPD has three basic forms, each corresponding to a limiting distribution of exceedence data from a different class of underlying distributions.

1. Distributions whose tails decrease exponentially, such as the normal, lead to a generalized Pareto shape parameter of $\zeta = 0$.
2. Distributions whose tails decrease as a polynomial, such as Student t, lead to a positive shape parameter of $\zeta > 0$.
3. Distributions whose tails are finite, such as the beta, lead to a negative shape parameter of $\zeta < 0$.

To date, the application of GEV and GPD families of distributions to HCF has mainly been limited to the inclusion size distribution. Nevertheless, experimental literature suggests that besides inclusion size and shape, other morphological attributes can play a key role in determining the high cycle fatigue (HCF) resistance of alloys with primary inclusions. Such attributes may include surface irregularities, inclusion clustering, proximity to the free surface, inclusion orientation with respect to neighboring inclusions, and loading direction relative to inclusion/cluster orientation.

In this thesis, we will use the GEV distribution to fit the FE simulation data and interpolate various parameters of interest.

2.4 Techniques used in creating the finite element models

In order to efficiently automate the repetitive tasks associated with the parametric finite element studies, we utilize the ABAQUS Scripting Interface [49] to develop modules that perform FE model creation, analysis, and post-processing, as shown in Figure 2-5. These modules can be linked with other analysis tools, thus contributing to the methodologies that seek to extend the life expectancy of existing alloys or tailor their microstructures to achieve improved HCF resistance.

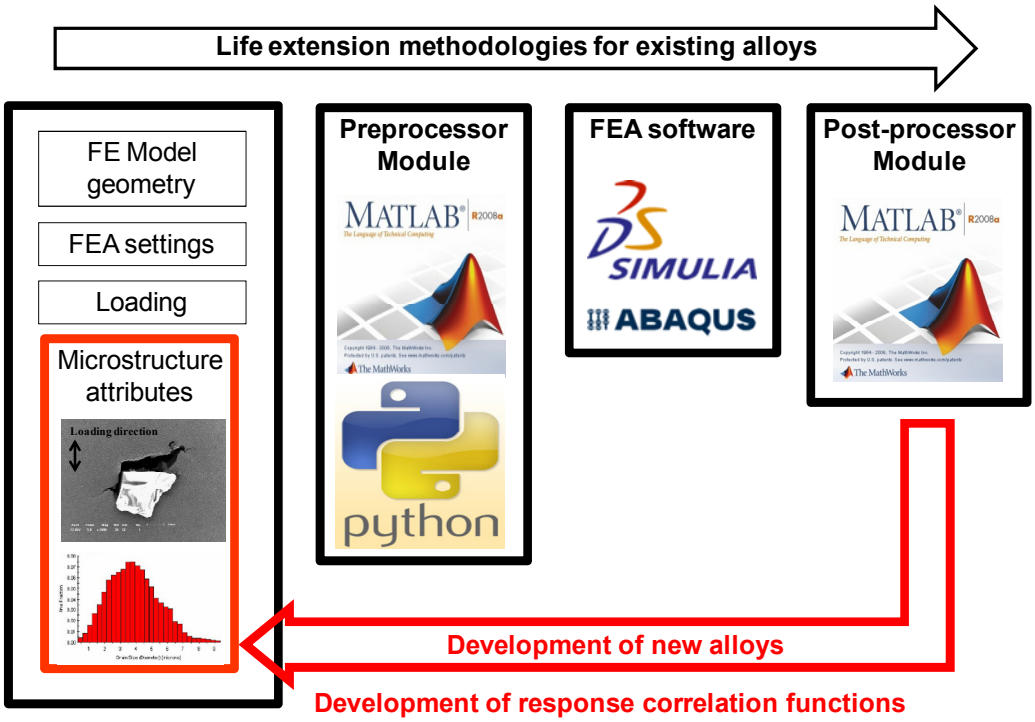

Figure 2-5: FE model creation modules.

ABAQUS scripts are based on the Python object-oriented programming language. The meshing capabilities of ABAQUS/CAE can also be accessed from the scripts. This

enables us to create FE grains with smooth boundaries, alleviating the stress singularities associated with modeling grain boundaries that have zigzagged geometry.

2.4.1 Generalized plane strain (GPS) elements

Except limited 3D finite element simulations in Section 8.3, the remaining FE simulations in this thesis utilize two-dimensional generalized plane strain (GPS) elements [49]. GPS formulation offers a computationally efficient alternative to 3D elements in which 2D finite elements are endowed with the kinematics of a 3D continuum [99]. Finite element simulations utilizing GPS elements are often referred to as 2.5D simulations.

The generalized plane strain theory used in ABAQUS [49] assumes that the model lies between two bounding planes that may move as rigid bodies with respect to each other, thus causing strain in the thickness direction (i.e., z axis in our study) of the model. It is assumed that the deformation of the model is independent of position with respect to this thickness direction, so the relative motion of the two planes causes a direct strain of the thickness direction only. Out-of-plane shear deformation is not included in the element formulation.

In the finite element simulations, grains are meshed with quadratic triangular elements (i.e., 6 nodes and 3 integration points per element) of type CPEG6M [49], with full integration algorithm, hourglass control, and generalized plane strain formulation. This element type uses a quadratic approximation of the displacement distribution, resulting in a linear distribution of stress/strain over the element domain.

2.4.2 Simulating FE grains around inclusions and pores

In the finite element simulation of polycrystals, Voronoi tessellation provides a useful mathematical foundation for defining grains [100-102]. Voronoi tessellation refers to a method of uniquely subdividing a domain into bounded convex polygons (polyhedral for 3D domain), called Voronoi or Dirichlet cells [103]. This subdivision is based on the spatial distribution of a set of constructor sites/seeds such that each and every Voronoi cell contains only one Voronoi seed, and each and every cell consists of all points closer to this seed than to any other site [104].

To better fit the experimentally-characterized polycrystal attributes, such as the distribution of grain size, spacing, and shape, several researchers [51, 105-107] have used an iterative scheme based on the simulated annealing algorithm that seeks an optimized spatial distribution of Voronoi seeds. The Voronoi seeds are often restrained from being too close to each other. We use a similar approach in this thesis to construct a Voronoi diagram representing the polycrystal Ni-base superalloy, IN100.

At low applied uniaxial strain amplitudes ($R_\varepsilon = -1$) examined in this thesis, plastic deformation is constrained to the few grains at the notch root of the inclusion/pore. Away from the inclusion, grains deforms elastically. We coarsen the grains in this region to speed up the FE model creation such that the mean grain size in the critical region at the notch root of the inclusion/pore is 2 μm and away from it is 4 μm. It should be noted that we do not intend to suggest that the actual material has a graded (increasing) grain size distribution around inclusions/pores. This measure is taken to increase the computational efficiency and does not affect the response parameters of interest.

Additionally, in order to better represent the grains adjacent to the inclusion (or pore) and to improve the convergence of the FE analysis, several additional modifications are made to the Voronoi diagram:

- Artificial Voronoi seeds are introduced for those neighbouring grains having seeds that are closer than $0.3 \times d_{gr}$ ($d_{gr} = 2$ μm) to the interface of the inclusion/pore with the matrix, where d_{gr} is the mean grain size. For those seeds that are closer to the inclusion than this distance, artificial Voronoi seeds are placed at their mirror sites with respect to the inclusion-matrix (or pore-matrix) interface.
- Voronoi vertices that are no more than $0.05 \times d_{gr}$ outside of the inclusion-matrix interface are shifted to their mirror location inside the inclusion-matrix interface contour. This prevents the creation of FE grains that are drastically different from the Voronoi idealization of realistic grains.
- Small Voronoi boundary segments result in the generation of finite elements of odd aspect ratio (as shown in Figure 2-6 middle), which may cause solution convergence issues and irregularities in the solution variables. The mesh at these locations can be corrected when the user inspects the FE mesh, but in order to automate the correction process, those Voronoi boundary segment vertices that are closer to each other than $0.2 \times t_{min}$, are both replaced by a Voronoi vertex located halfway on the corresponding boundary segment. Here, t_{min} is the finest element size used for all grains that are within R/4 (R is the inclusion/pore size) from the inclusion-matrix (or pore-matrix) interface. The value of R/4 is

approximately equal to $t_{min} = 0.25 \times d_{gr}$. The mesh due to this adjustment is shown in Figure 2-6 left.

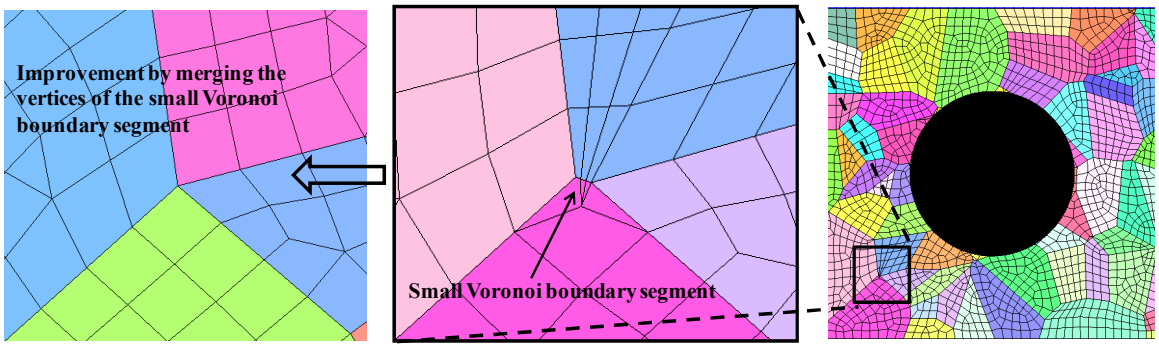

Figure 2-6: Improvements for Voronoi tessellation around inclusion.

The above-mentioned modifications are considered as time-efficient methods for enhancing the mesh quality, and they generate a more natural-looking Voronoi diagram with the presence of an inclusion/pore; they are not based on a rigorous mathematical foundation. The selected parameters are based on trial-and-error and are not unique; they are chosen by visually monitoring the Voronoi diagram. The coordinates of the Voronoi vertices are then entered into the ABAQUS/CAE Python script to partition the matrix region into Voronoi cells.

2.4.3 Monotonic stress strain response of the 2.5D FE model

The experimentally-obtained homogenous material properties are not suitable for idealized 2.5D simulations. As such, we estimate these parameters by simulating the stress strain relationship of polycrystalline aggregates using crystal plasticity and 2.5D generalized plane strain element formulations. However, the crystal plasticity model parameters are still calibrated to the experimentally obtained stress strain response.

The stress and strain components are volume averaged over the polycrystalline aggregates, to comprise a statistically representative number of grains; this prevents the size of the polycrystalline aggregate from affecting the predictions of the homogenized material properties of interest. The grain aggregate is modeled with the same finite element type and subjected to the same boundary conditions as the simulations with the embedded inclusions, discussed later in this chapter.

Figure 2-7 is a 2.5D FE model (see Section 2.4.1) showing the polycrystalline aggregate used for averaging the simulated stress and strain data. To alleviate the boundary effects in a computationally-efficient manner, the crystal plasticity region is embedded within a larger region, consisting of (1) a transitioning polycrystalline region, modeled with a fully anisotropic elastic material model and (2) a far-field homogenous region, modeled with a fully isotropic elastic material model, filled out using properties obtained via a recursive analysis starting with the initial values found in the literature [108].

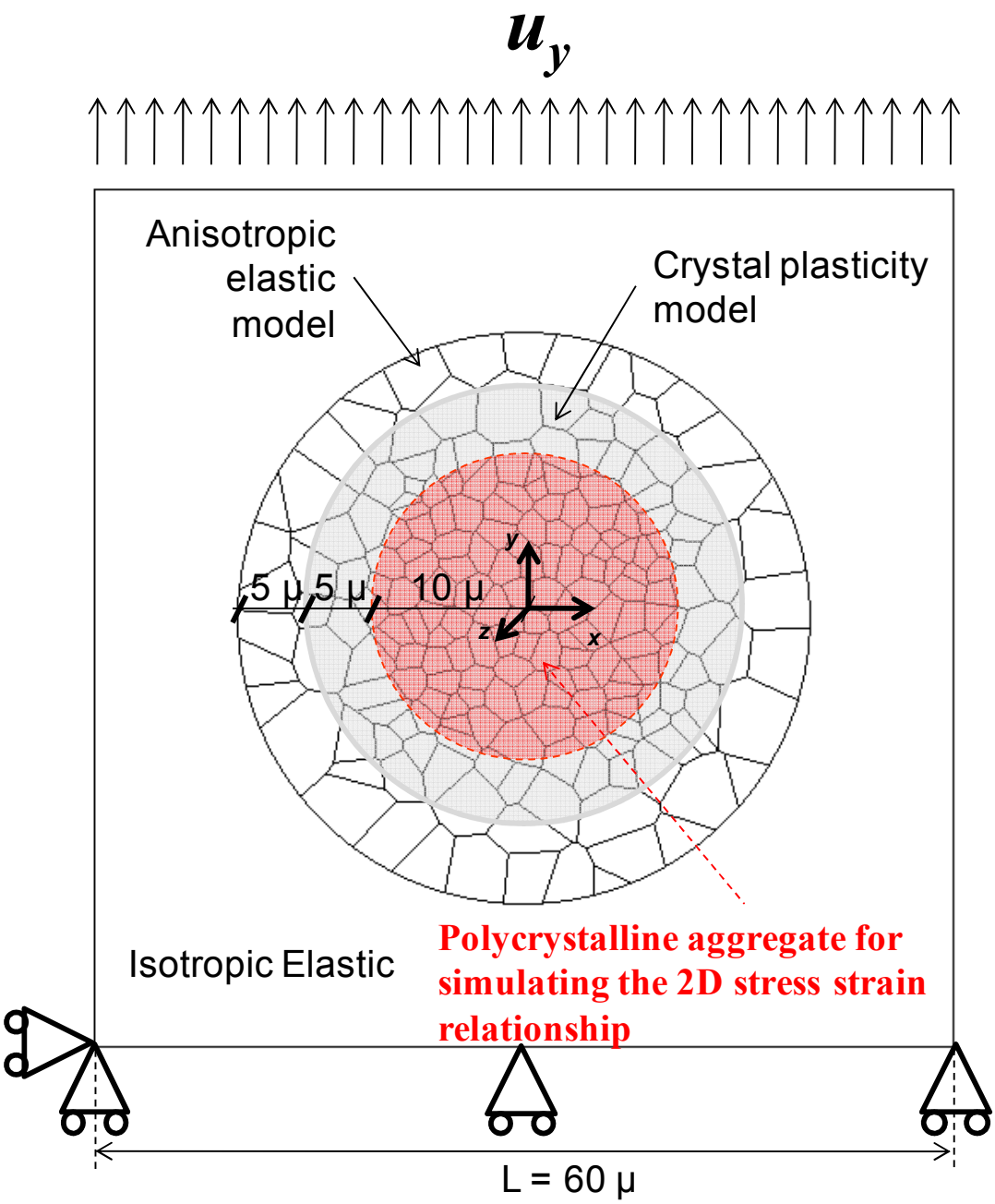

Figure 2-7: The FE model for simulating the 2.5D stress strain relationship.

The following boundary conditions are enforced, assuming the origin of the *xyz* coordinate system is at the center of the crystal plasticity region:

1. The traction free boundary condition is enforced for the entire length of the model's left and right edges (x = -L/2, L/2 and -L/2 < y < L/2).
2. The y-symmetry boundary condition (u_y = 0) is enforced for the entire length of the model's bottom edge (y = -L/2 and - L/2 < x < L/2).
3. The z-symmetry boundary condition (u_z = 0) is enforced to the reference point of the GPS model.
4. A monotonic uniaxial displacement $u_y = 0.01 \times L$ is applied to the entire length of the model's top edge (y = L/2 and - L/2 < x < L/2) at the uniform rate of 0.002 s^{-1}.

Ten realizations of the polycrystalline microstructure with random grain orientation distribution were simulated; Voronoi seed spatial distribution as well as grain orientation distribution was varied within these microstructure realizations. We use two-dimensional generalized plane strain (GPS) elements [49], often referred to as 2.5D, and the fully 3D crystal plasticity material model (see Section 2.1.2). Each grain was meshed with 60-100 quadratic triangular elements of type CPEG6M (see Section 2.4.1). The FE mesh coarsens away from the polycrystalline aggregate.

Figure 2-8 plots the volume-averaged stress strain response for 5 of the simulated realizations. The polycrystalline aggregates typically consist of about 150 grains. Virtually equivalent plots are obtained, indicating that the polycrystalline aggregates are sufficiently large to be statistically representative for the assessment of the overall stress strain response.

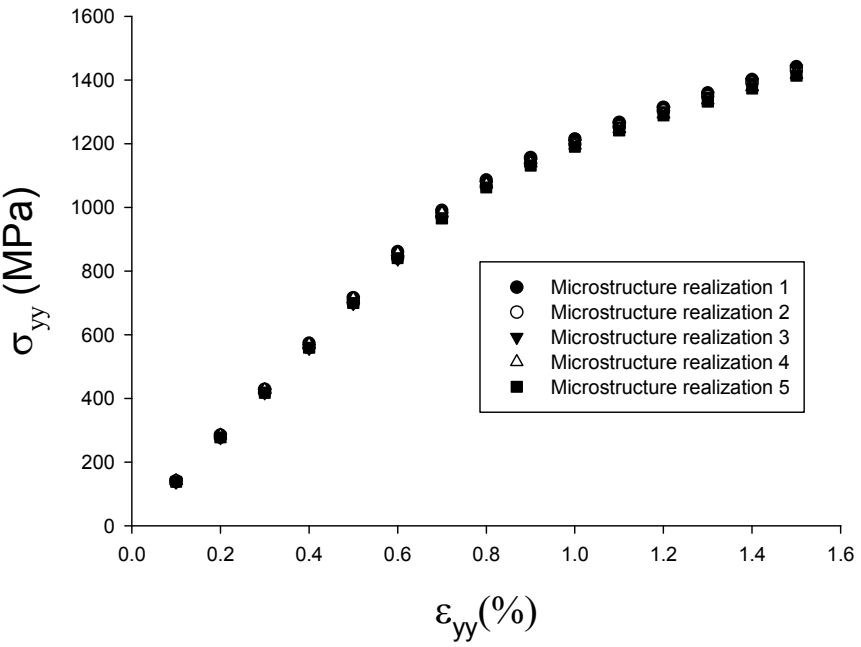

Figure 2-8: Uniaxial stress strain response (averaged over the polycrystalline aggregate).

The linear elastic portions of these plots were used to obtain the homogenized Young's modulus, E^m = 142 GPa, and Poisson's ratio, ν^m = 0.25, of the isotropic fully elastic response for the purposes of 2.5D generalized plane strain FE simulations. Figure 2-9 (top) illustrates the plastic strain (yy) component, averaged over the polycrystalline aggregate, versus the applied total (yy) strain component for the same 5 of the 10 microstructure realizations. The horizontal dashed lines correspond to the 0.1% and 0.2% plastic strain levels. Figure 2-9 (bottom) illustrates the yy stress component, averaged over the polycrystalline aggregate, versus applied total (yy) strain component for 4 of the 10 microstructure realizations.

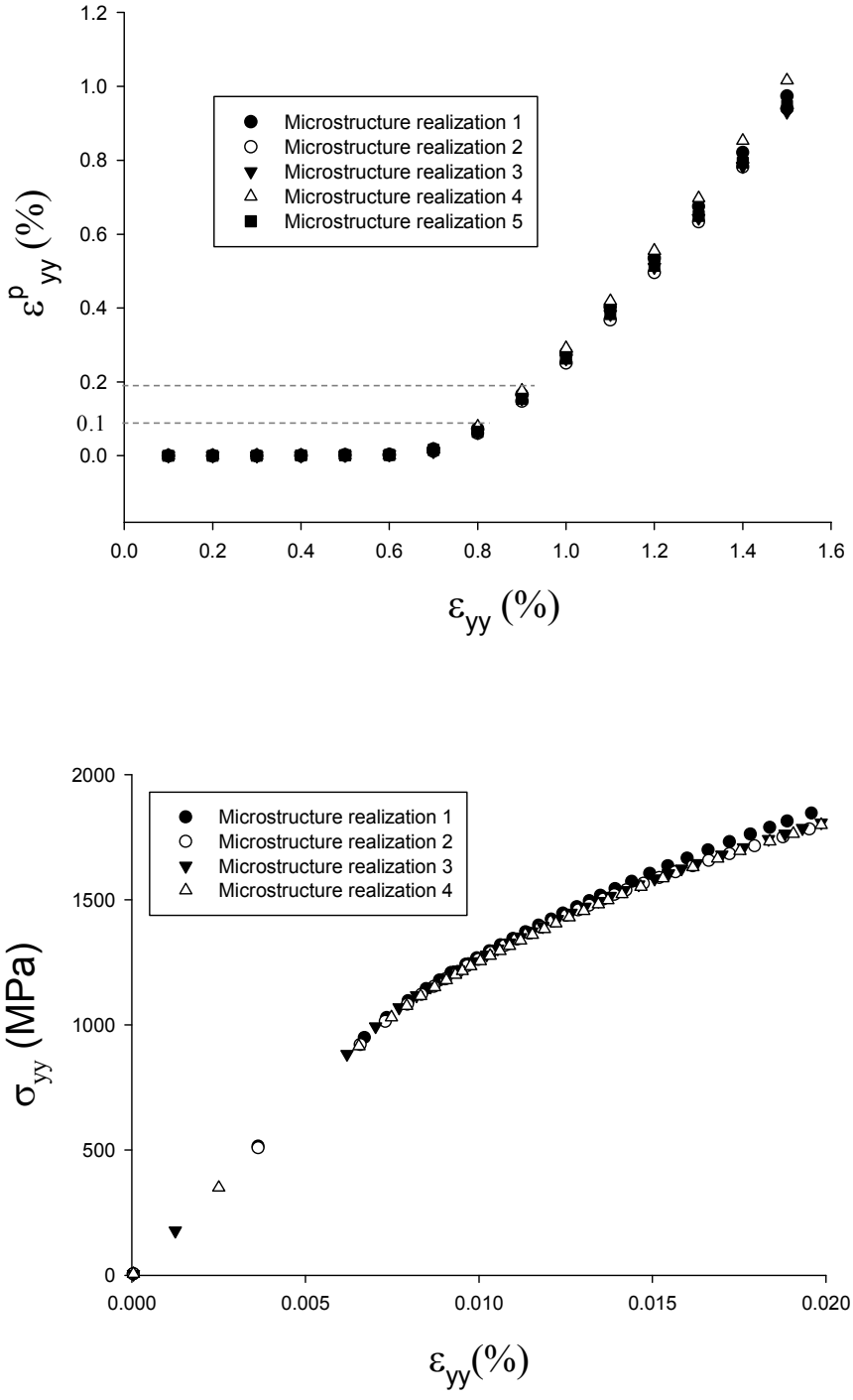

Figure 2-9: (top) ε^p_{yy} (averaged over the polycrystalline aggregate) vs. applied ε_{yy}; (bottom) σ_{yy} vs. ε_{yy} (both averaged over the polycrystalline aggregate).

The remote applied strain required to impose ε^{p}_{yy} = 0.1% plastic strain in the polycrystalline aggregate is defined as the remote yield strain and is calculated as ε_{ys} = 0.007. The 0.1% plastic strain is chosen as the offset yield point, since it more closely corresponds to the yield stress σ_{ys} ≈ 1000-1050 MPa, reported in the experimental literature for fine-grained subsolvus IN100 at the intermediate temperature range of 600-700°C [108].

2.4.4 Cyclic crystal plasticity FE model for embedded inclusions and pores

Our finite element models use a two-dimensional generalized plane strain element formulation to calculate the response parameters of interest around cylindrical primary inclusions. For computational efficiency, the matrix region is divided into 3 regions with different constitutive models, as shown in Figure 2-10: (1) a ring-shaped region, adjacent to the inclusion, (2) an intermediary ring-shaped region, and (3) the far-field region.

One of the potential difficulties in the multiphase FE simulation is the inconsistency of material properties at the boundary between the two regions, which leads to discontinuities and solution convergence issues. We take the following measures to minimize such effects.

1. In region 1, grains are modeled using Voronoi tessellation (c.f. 2.4.1). Crystal Plasticity FE formulation is used to model the deformation behavior of grains with various sizes and orientations. The thickness of this region is chosen such that the plastic deformation around the inclusion does not go beyond region 1 at the highest simulated applied uniaxial strain amplitude (R_{ε} = -1).

2. In region 2, grains are modeled using an extension of the Voronoi diagram from region 1. In contrast to the material behavior of region 1, individual grains of region 2 are simulated using fully anisotropic elastic material behavior. The elastic material properties are kept the same as those of region 1 in order to preserve a smooth transition across regions.
3. The far-field region is modeled with homogenous isotropic fully elastic material properties defined by two material constants, Young's modulus E^m = 142 GPa and Poisson's ratio ν^m = 0.25. These parameters were obtained in Section 2.4.3 from the volume averaged stress strain relationship of polycrystalline aggregates with statistically representative numbers of grains, such that increasing the polycrystalline aggregate size does not affect the predictions of these material properties. The grain aggregate was modeled using the same element type and the same boundary conditions that were used in the simulations with the embedded inclusion (c.f. 2.4.3).

Half and quarter of the complete model are shown, respectively, in red and blue dashed lines in Figure 2-10. We simulate the full model throughout this study. Since the grain structure and orientation distribution are random, we cannot simulate half or quarter of the complete model instead. Simulating the full model also helps to alleviate the boundary effects.

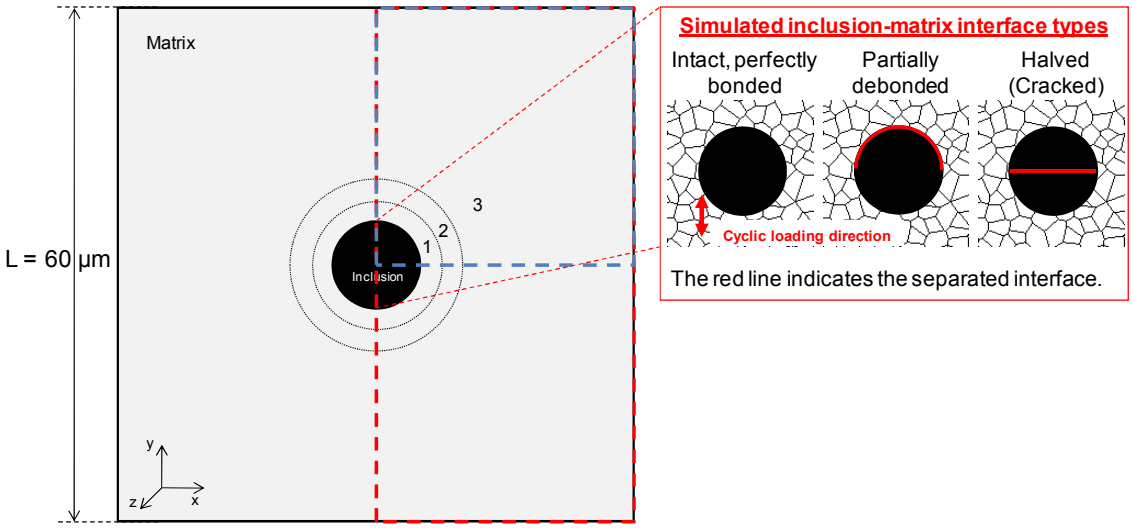

Figure 2-10: Matrix subdivisions showing half and quarter of the complete model and the simulated inclusion-matrix interface types.

The following boundary conditions are enforced, assuming the origin of the *xyz* coordinate system is at the center of the inclusion/pore:

1. The traction free boundary condition is enforced for the entire length of the model's left and right edges (x = -L/2, L/2 and -L/2 < y < L/2).
2. The y-symmetry boundary condition (u_y = 0) is enforced for the entire length of the model's bottom edge (y = -L/2 and - L/2 < x < L/2).
3. The z-symmetry boundary condition (u_z = 0) is enforced to the reference point of the GPS model.
4. A cyclic uniaxial displacement u_y is applied to the entire length of the model's top edge (y = L/2 and - L/2 < x < L/2) at the uniform rate of 0.002 s^{-1}.

For intact, perfectly bonded inclusions, the slip-intensified matrix region is located at the inclusion's top and bottom poles ($x = 0$, $y = \pm R$). To that end, the nonlocal FIP averaging is performed at these regions, as shown in Figure 2-11 (a). In contrast, for halved (cracked) inclusions, debonded inclusions, and pores, the slip-intensified matrix region is located at the inclusion's right and left poles ($x = \pm R$, $y = 0$). The nonlocal FIP averaging region for these simulations is shown in Figure 2-11 (b).

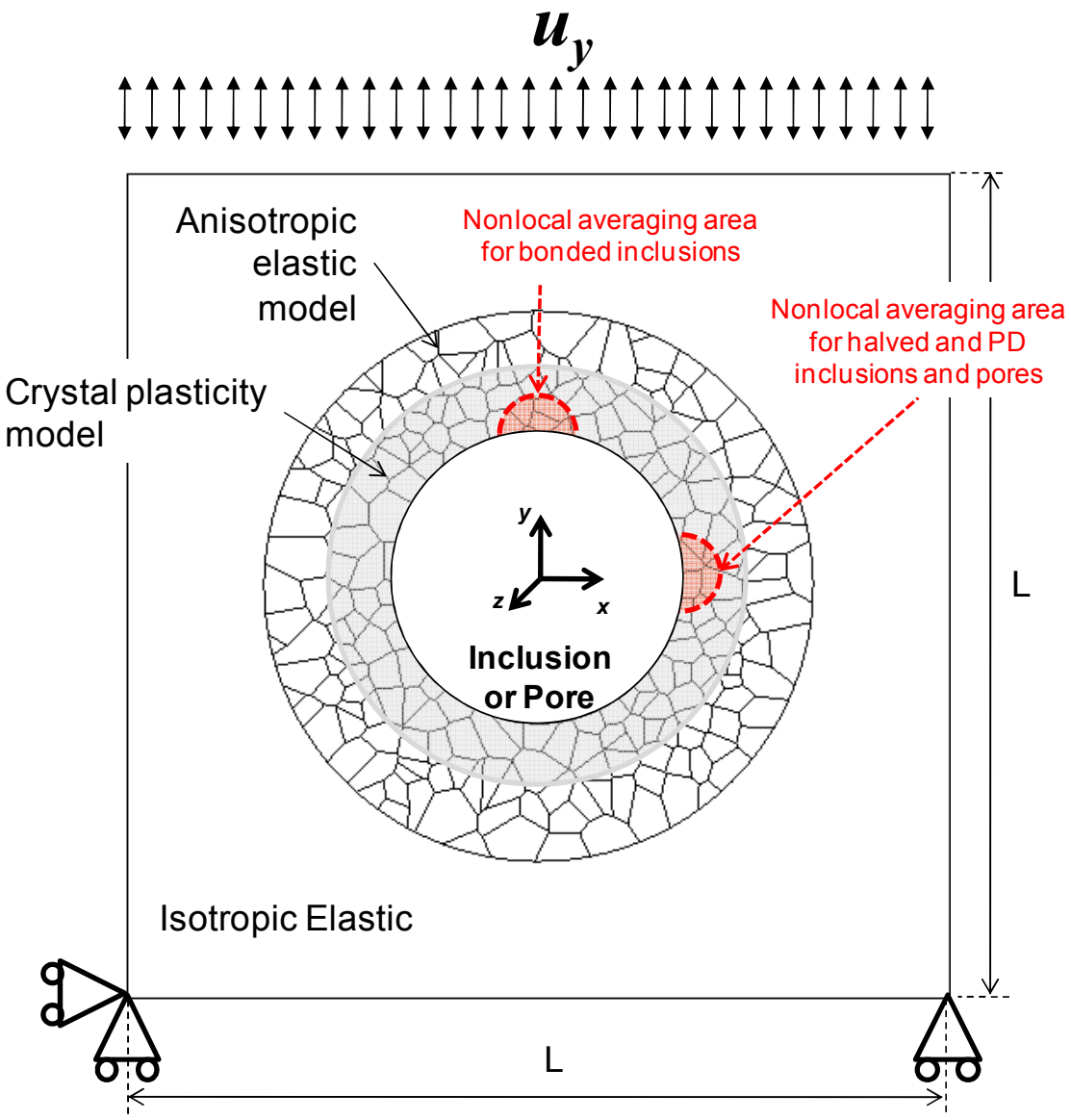

Figure 2-11: The FE model and location of the nonlocal FIP averaging region.

2.4.5 Stabilized load cycle

The time duration of a cyclic FE analysis is proportional to the number of load cycles being simulated. A minimum of three simulated cycles is recommended to allow for early shakedown and to capture a steady FIP for a similar IN100 microstructure under comparable loading conditions. To further investigate this matter, we monitor variation in the nonlocal maximum range of plastic shear strain, $\Delta\gamma^{*}_{p,\max}$, with changes in the loading cycle at a notch root of a pore.

The FE model, shown in Figure 2-11, is examined where the following boundary conditions are enforced; assuming the origin of the *xyz* coordinate system is at the center of the inclusion/pore:

1. The traction free boundary condition is enforced for the entire length of the model's left and right edges (x = -L/2, L/2 and -L/2 < y < L/2).
2. The y-symmetry boundary condition ($u_y = 0$) is enforced for the entire length of the model's bottom edge (y = -L/2 and - L/2 < x < L/2).
3. The z-symmetry boundary condition ($u_z = 0$) is enforced to the reference point of the GPS model.
4. Cyclic uniaxial displacement $u_y = \varepsilon_{yy} \times L$ is applied to the entire length of the model's top edge (y = L/2 and - L/2 < x < L/2) at the applied strain amplitudes ε_{yy} = 0.5, 0.6, and 0.7 ε_{ys} (ε_{ys} = 0.7 % (c.f. 2.4.3)), strain ratio R_ε = -1, and uniform strain rate of 0.002 s^{-1}.

The FIP is calculated for 10 simulated loading cycles. Two nonlocal averaging regions are studied: (1) grains, located at inclusion notch root and (2) a semicircular region, located at the slip-intensified region of the inclusion notch root, as shown in Figure 2-11. Only one inclusion radius (R = 10 μm) is examined in this section. The averaging area is 5% of the size of the inclusion [109], and L = 60 μm.

Figure 2-12 shows the variation of $\Delta\gamma^*_{p,\max}$ for two nonlocal averaging regions, the grain with the highest $\Delta\gamma^*_{p,\max}$ value and the semicircular region at the inclusion notch root. A significant portion of the shakedown seems to have taken place upon completion of the 3rd loading cycle for both cases.

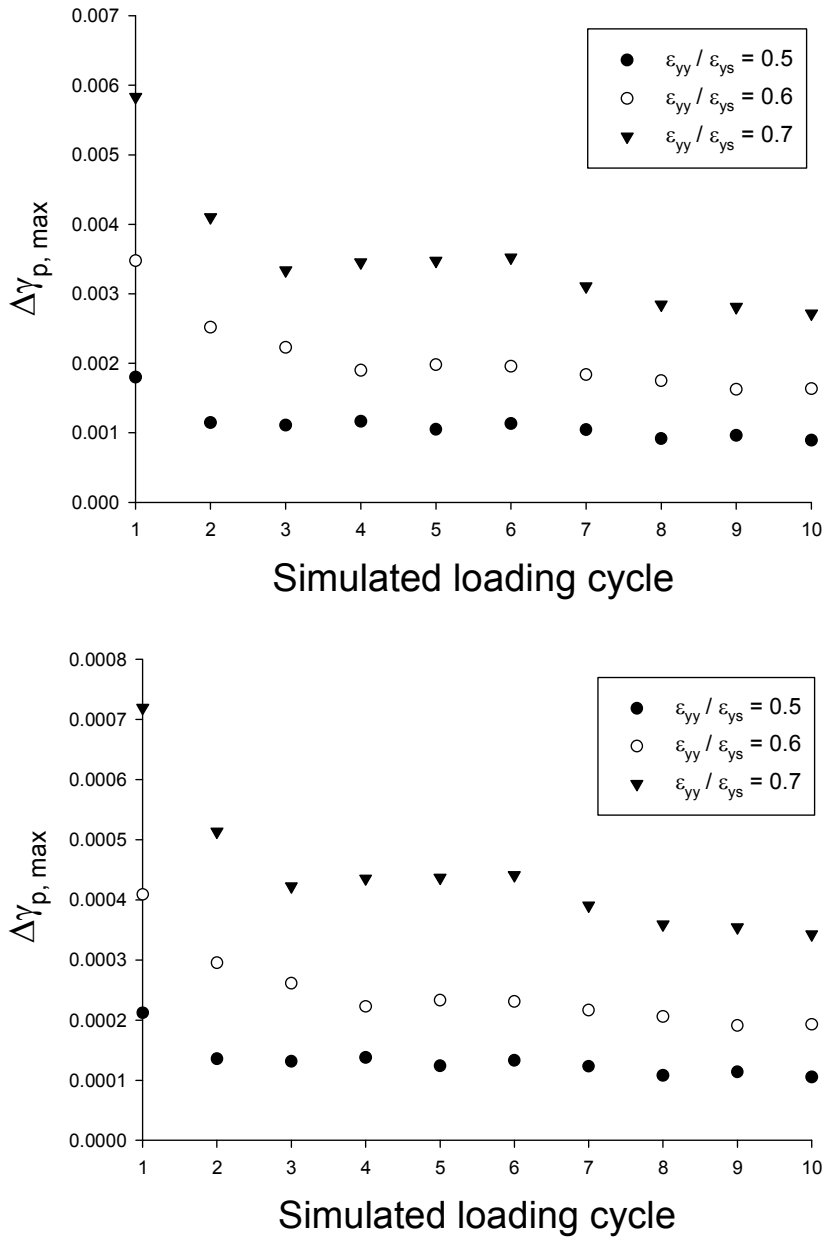

Figure 2-12: $\Delta\gamma^*_{p,\max}$ vs. loading cycle (R = 10 μm; L = 60 μm; ε_{ys} = 0.7 %; R_ε = -1). Top: nonlocal averaging regions = grains (Grain with the highest $\Delta\gamma^*_{p,\max}$ is shown). Bottom: nonlocal averaging regions = the semicircular region at the inclusion notch root.

The beginning and end of the load reversals in the 3rd loading cycle are labeled in Figures 2-13 (a) and 2-14 (a). In both cases, B → C is the proper trajectory for computing the shear-based FIPs explained in Section 2.2.

Figure 2-13 (b) shows the variation of the averaged stress strain at the notch root of a pore with R = 6 μm for three loading cycles ($\varepsilon_{yy}/\varepsilon_{ys}$ = 0.6 and R_ε = -1). Figure 2-14 (b) shows the same plot for a partially debonded inclusion. The averaged stress strain plots in Figures 2-13 (b) and 2-14 (b) may appear as closed cycles of elastic reversed deformation. Nevertheless, the plots of averaged stress versus plastic strain, shown in Figure 2-13 (c) for a pore and Figure 2-14 (c) for a partially debonded inclusion, indicate a state of plastic shakedown [91]. Therefore, three cycles of loading will be simulated throughout this thesis unless specified otherwise.

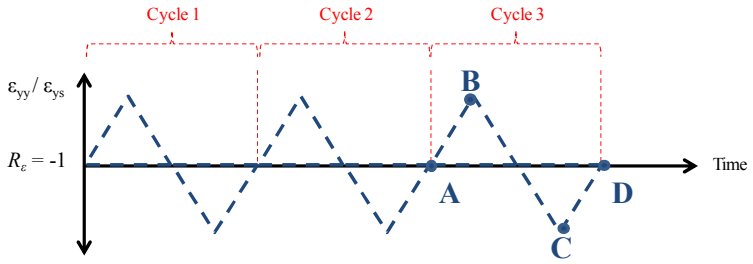

(a)

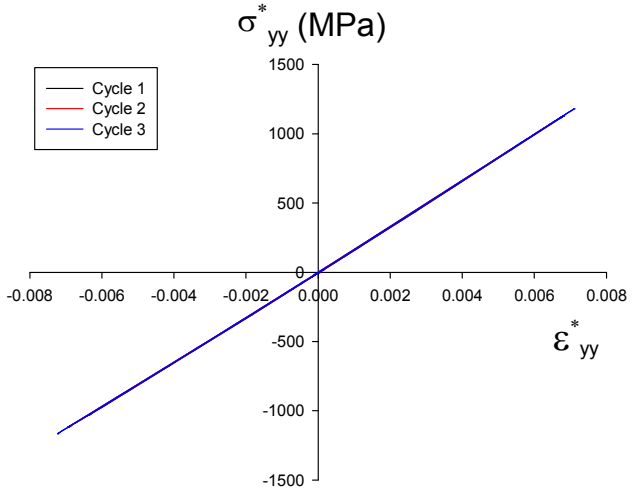

(b)

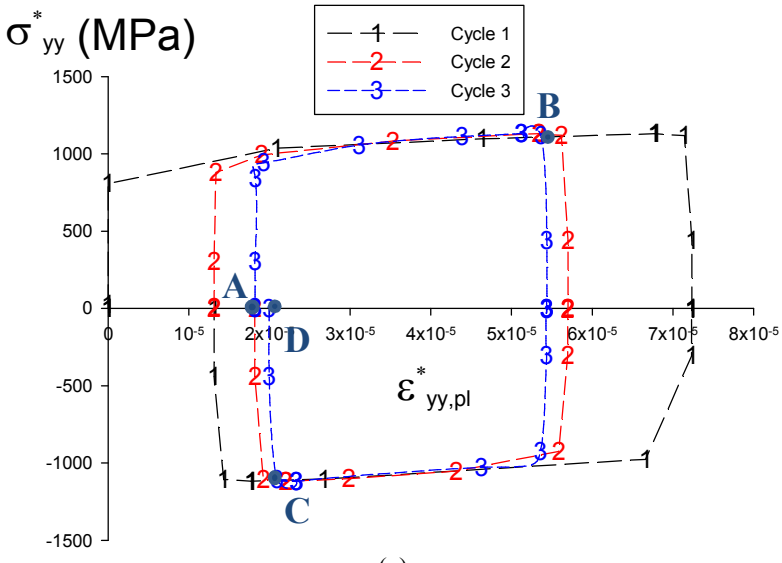

(c)

Figure 2-13: (a) Load reversals (b) σ^*_{yy} vs. ε^*_{yy} and (c) σ^*_{yy} vs. ε^{p*}_{yy} at the pore notch root (R = 6 µm; L = 60 µm; ε_{yy} = 0.6 ε_{ys}; ε_{ys} = 0.7 %; R_ε = -1).

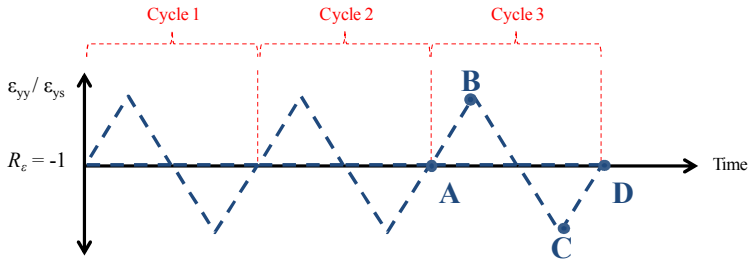

(a)

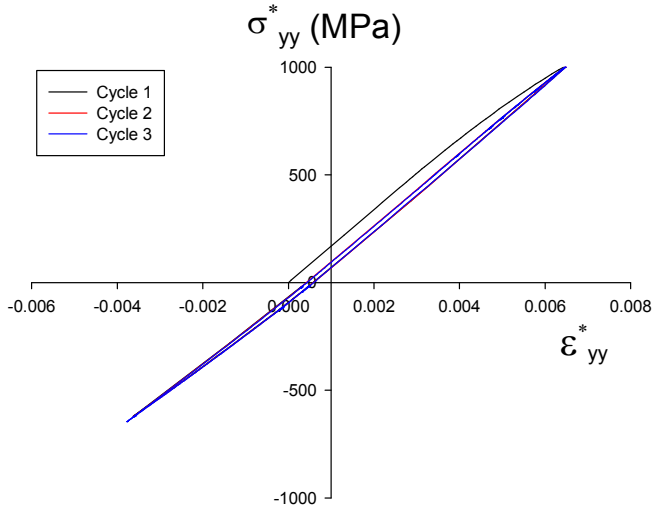

(b)

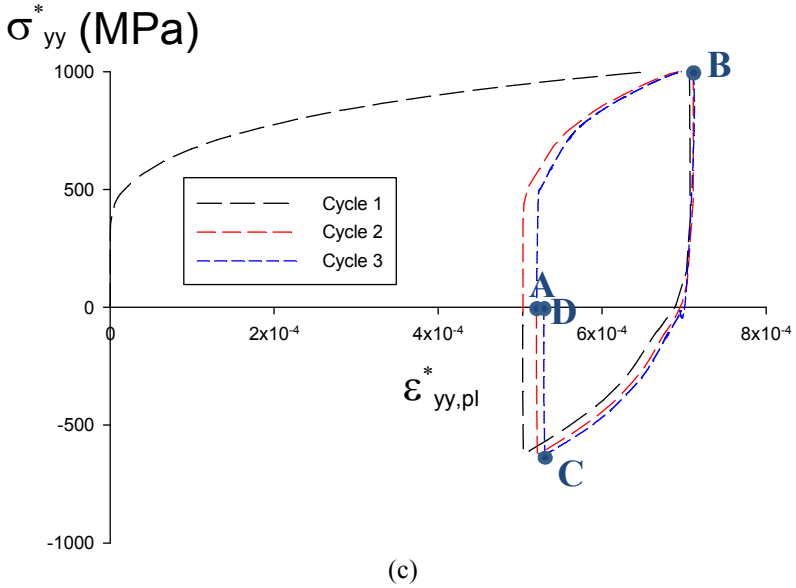

(c)

Figure 2-14: (a) Load reversals (b) σ^*_{yy} vs. ε^*_{yy} and (c) σ^*_{yy} vs. ε^{p*}_{yy} at the inclusion notch root (R = 6 μm; L = 60 μm; ε_{yy} = 0.6 ε_{ys}; ε_{ys} = 0.7 %; R_ε = -1).

It should be noted that the number of simulation loading cycles, needed to achieve a stable nonlocal FIP, depends on a myriad of factors such as loading conditions (i.e., strain amplitude and strain ratio), microstructure attributes, and selected averaging area for calculation of the nonlocal FIP. Therefore, a different number of loading cycles may need to be simulated to achieve a stable response in other scenarios.

2.4.6 Choice of element size

The FIP averaging procedure helps to ensure computationally consistent and objective results by regularizing to avoid mesh-size dependence. Nevertheless, we still need to control the element size to ensure solution accuracy and convergence. Simulation time is also reduced by using a sufficiently, yet not needlessly, fine mesh density. The ideal element size depends on a myriad of factors that influence the solution convergence [110]. As such, a host of simulation techniques such as adaptive meshing algorithms [111-114] have been developed to warrant the optimal mesh density for a given finite element simulation.

To examine to what degree the element size affects the simulation time, the FE model, shown in Figure 2-11, with a center pore ($R = 10\ \mu m$) is examined. The following boundary conditions are enforced; assuming the origin of the *xyz* coordinate system is at the center of the inclusion/pore:

1. The traction free boundary condition is enforced for the entire length of the model's left and right edges (x = -L/2, L/2 and -L/2 < y < L/2).

2. The y-symmetry boundary condition ($u_y = 0$) is enforced for the entire length of the model's bottom edge (y = -L/2 and - L/2 < x < L/2).
3. The z-symmetry boundary condition ($u_z = 0$) is enforced to the reference point of the GPS model.
4. Cyclic uniaxial displacement $u_y = \varepsilon_{yy} \times L$ is applied to the entire length of the model's top edge (y = L/2 and - L/2 < x < L/2) at the applied strain amplitudes $\varepsilon_{yy} = 0.6\ \varepsilon_{ys}$ (ε_{ys} = 0.7 % (c.f. 2.4.3)), strain ratio R_ε = -1, and uniform strain rate of 0.002 s^{-1}.

The mean grain size is (d_{gr} = 2 μm). A mesh with element size t_{min}, is used to discretize grains that are within R/4 distance, i.e., $0 < d < R/4$, from the pore notch root, located at $(x = R, y = z = 0)$, as shown in Figure 2-15. We maintain the fine mesh in this region because the deformation is mainly localized here. Beyond $d = R/4$, the element size is increased linearly with increasing distance (i.e., d) from the pore notch root in order to reduce the computational cost. Figure 2-15 illustrates the element size variation for two fine mesh densities $t_{min} = 0.1$ and $0.2\ \mu m$. Figure 2-15 also illustrates the actual finite element discretization for $t_{min} = 0.1\ \mu m$ for inclusions/pores of radius $R = 10\ \mu m$.

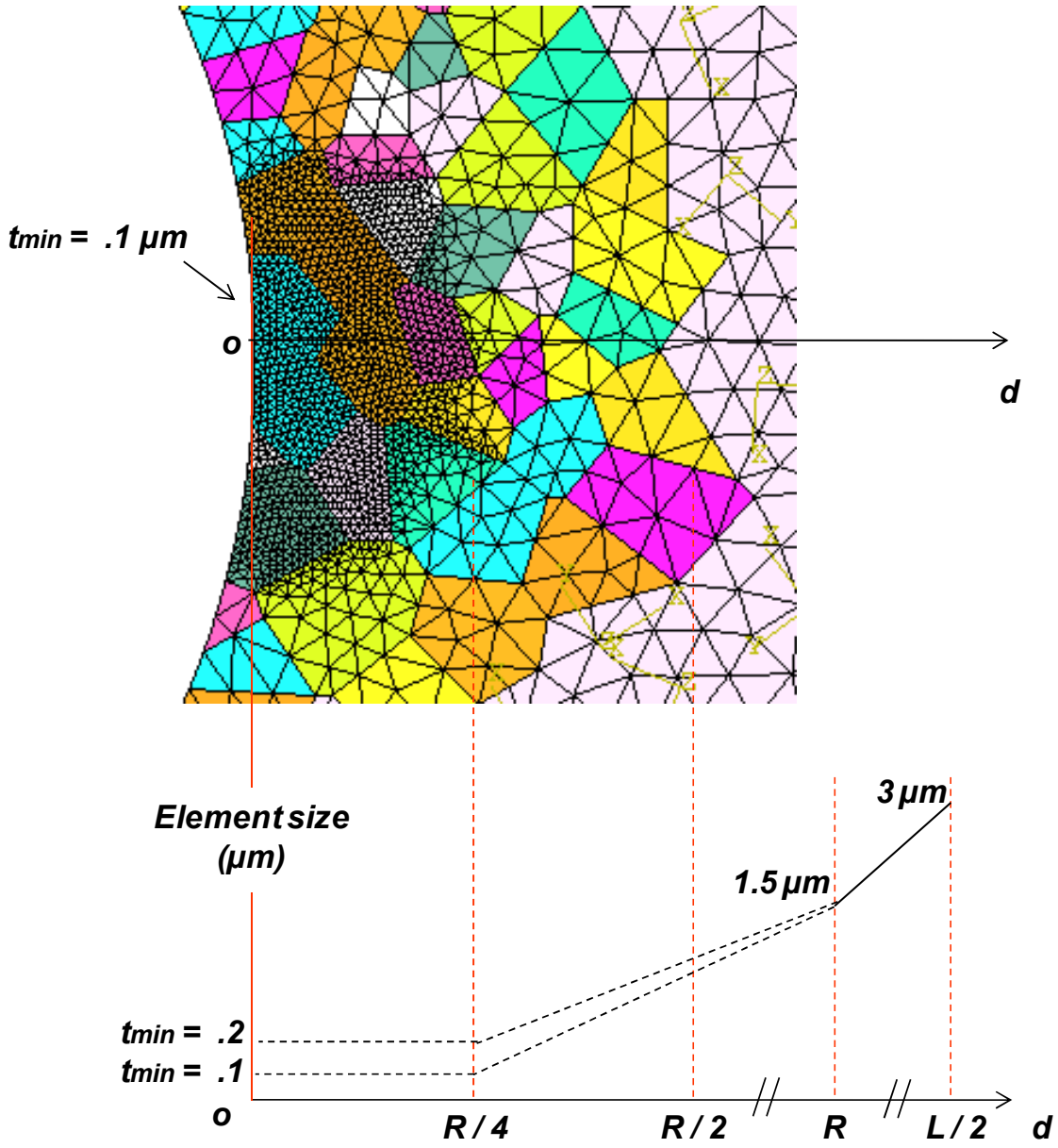

Figure 2-15: The element size variation as a function of distance (i.e., *d*) from the notch root. The mean grain size is (d_{gr} = 2 µm).

Figure 2-16 shows the 3rd cycle contour plots of local $\Delta\gamma_{p,\max}$ (i.e., computed at the element integration points) for t_{min} = *0.1, 0.2, 0.3, 0.4,* and *0.5 µm.* In these

simulations, a constant microstructure realization (constant Voronoi diagram and grain orientation distribution) around a pore with radius $R = 10\ \mu m$ is examined.

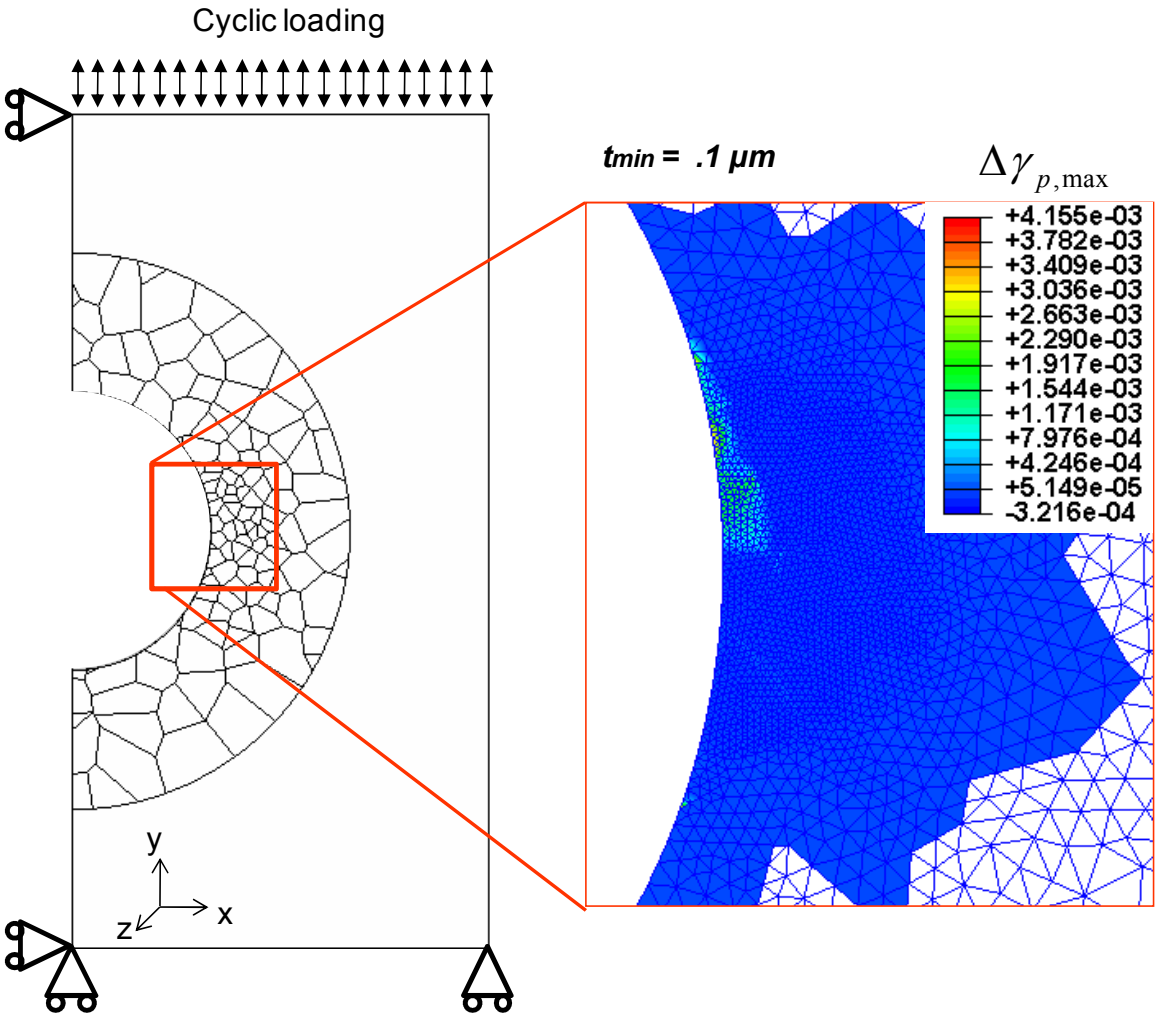

Figure 2-16: The 3rd cycle contours of the local $\Delta\gamma_{p,\max}$, computed at the element integration points (R = 10 µm; $\varepsilon_{yy} = 0.6\ \varepsilon_{ys}$; $\varepsilon_{ys} = 0.7$ %; $R_\varepsilon = -1$). The mean grain size is ($d_{gr} = 2$ µm).

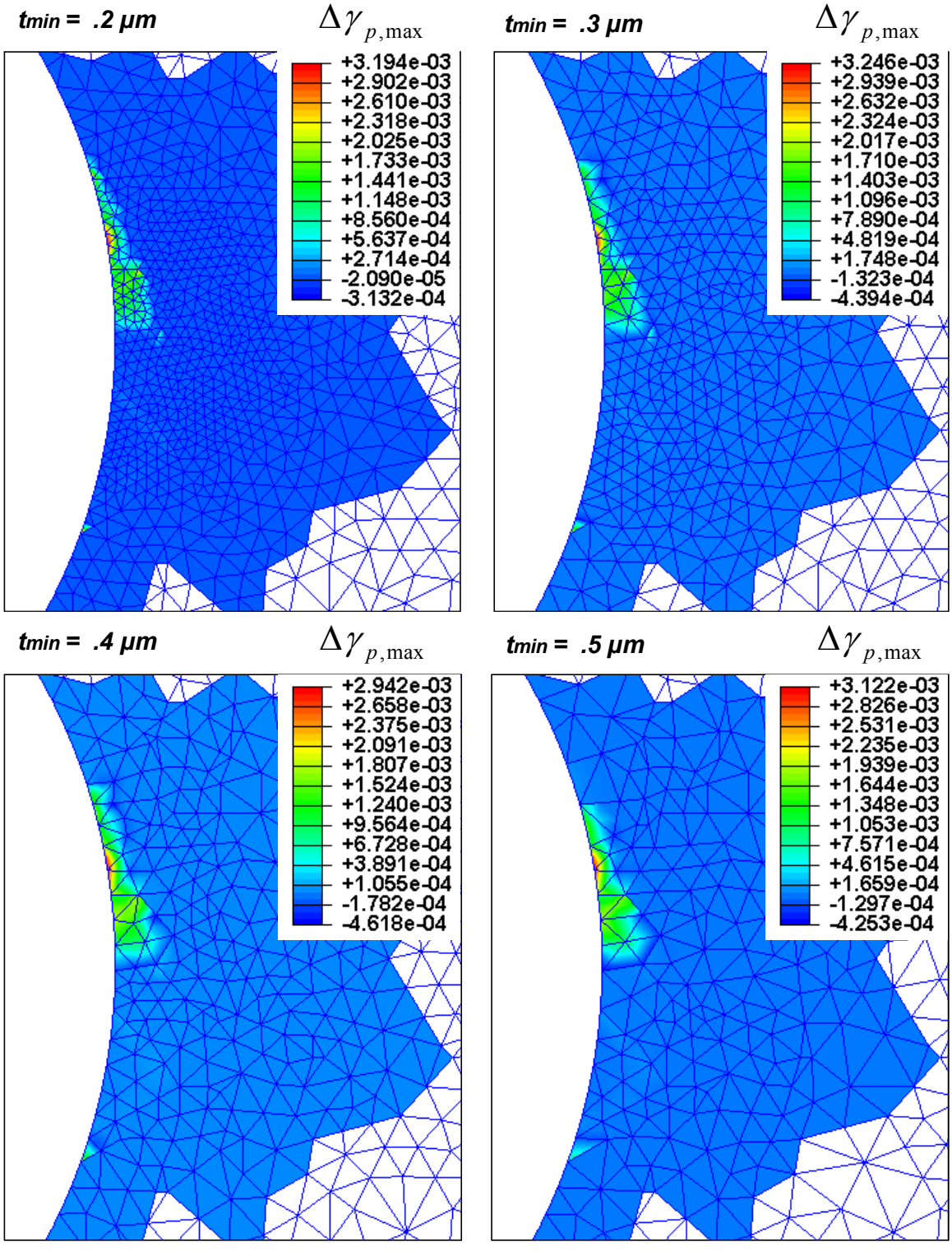

Figure 2-16 Continued.

Relative to the case with the finest mesh (i.e., $t_{min} = 0.1\ \mu m$), coarser mesh scenarios expectedly underpredict the magnitude of local $\Delta\gamma_{p,\max}$ but seem to capture the location of the hot spot with the highest local $\Delta\gamma_{p,\max}$. Table 6 shows the decrease in the simulation time as the mesh coarsens (t_{min} increases).

Table 6: Simulation time versus minimum finite element size.

t_{min} (μm)	0.1	0.2	0.3	0.4	0.5	0.6
Simulation time (s)	20528	4187	3186	2000	1686	828

To examine the effect of mesh density on the nonlocal FIP calculations, we compare the FIP predictions using these choices of minimum finite element size, t_{min}. The particular FIP is the maximum range of plastic shear strain, $\Delta\gamma^{*}_{p,\max}$, averaged over individual grains. For this analysis, grains are a natural option for averaging $\Delta\gamma_{p,\max}$; each grain encompasses a large number of elements for all the examined values for t_{min}.

The five grains with the highest grain-averaged magnitude of $\Delta\gamma^{*}_{p,\max}$, as suggested by the simulation with $t_{min} = 0.1\ \mu m$, are considered. The FIP predictions for these five grains (from the remaining mesh density scenarios) are normalized with respect to the prediction of the finest mesh, i.e. $t_{min} = 0.1\ \mu m$, and plotted in Figure 2-17.

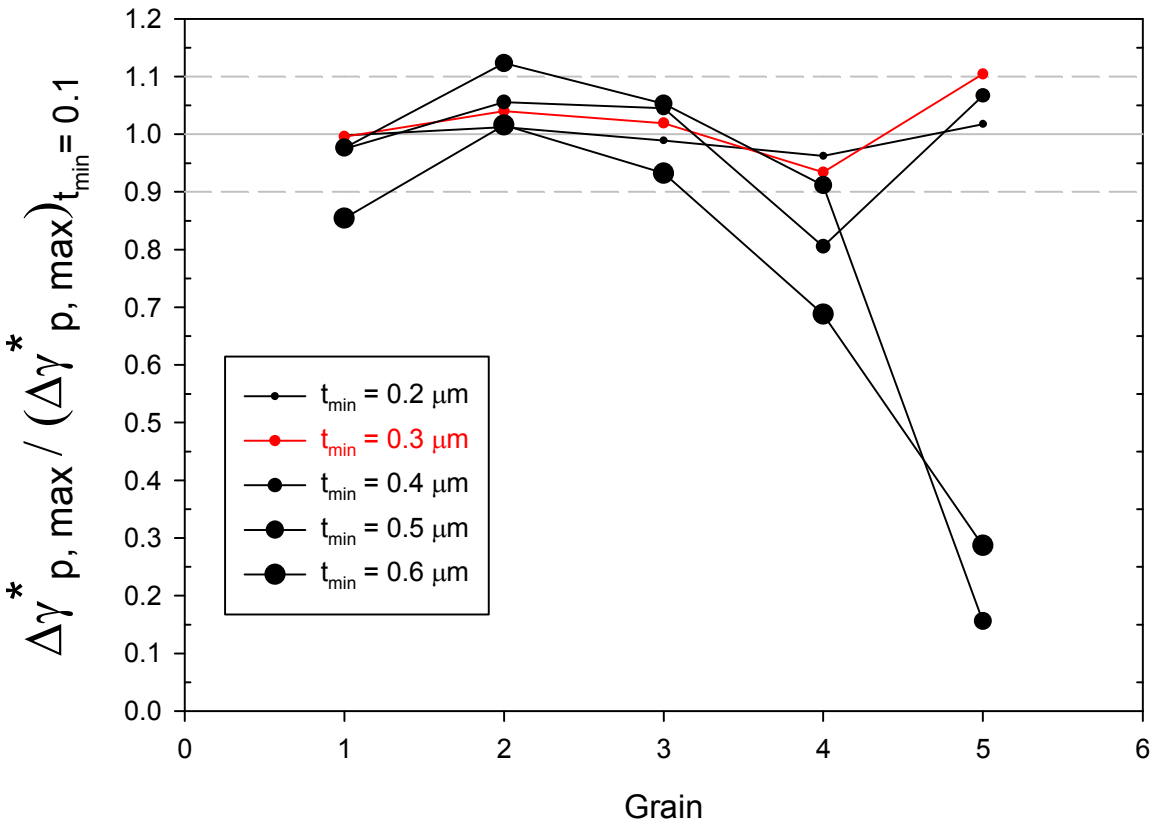

Figure 2-17: Normalized $\Delta\gamma^*_{p,\max}$ for the five grains with the highest grain-averaged values (R = 10 μm; $\varepsilon_{yy} = 0.6\ \varepsilon_{ys}$; $\varepsilon_{ys} = 0.7$ %; $R_\varepsilon = -1$).

The mesh density with $t_{min} = 0.3\ \mu m$ (plotted in red) seems to predict the grain-averaged $\Delta\gamma^*_{p,\max}$ within ±10 % of the best predictions based on the finest mesh examined; however, this result required only 15% of the simulation time required by the finest mesh. Thus, we can consider the $t_{min} = 0.3\ \mu m$ mesh density a pragmatic middle ground for our simulations.

3 HCF crack formation potency of inclusions and pores in PM Ni-base superalloys: A comparative study of FIPs

3.1 Introduction

The origin of fatigue failure in superalloys has been an important subject of experimental research programs over the past few decades. In engine applications, there are often two components to this problem: (1) low cycle fatigue (LCF), which results from relatively large cycles associated with the ground-air-ground cycles of the gas turbine engine, and (2) high cycle fatigue (HCF), associated with cyclic loading during service. HCF, in particular, has been recognized as the single largest cause of engine failures in military aircraft [115]. Representative experimental observations of inclusion-controlled fatigue failure in common PM Ni-base supealloys are presented in this section.

Hyzak and collaborators [116-118] used a precision sectioning technique to investigate fatigue crack initiation in two subsolvus high strength PM Ni-base superalloys, AF-115 and AF2-IDA, at T = RT, 649°C, and 760°C (R_ε = -1). For the latter alloy, with lower concentrations of inherent pores and inclusions, it was observed that the primary mechanism for fatigue crack formation was the debonding of bulk non-metallic inclusions such as MgO particles, followed by formation of crystallographic cracks in large adjacent grains (so called “facet” initiation). The inclusions were observed to have ellipsoidal shape. At room temperature, crack formation was attributed to surface crystallographic cracking along intense planar slip bands at approximately 45 degrees to the tensile axis for all applied strain amplitudes, indicating Stage I initiation. However, as the strain amplitude decreased at elevated temperatures, there was a transition of initiation sites from near surface non-metallic inclusions and grains to bulk non-metallic

inclusions. Figure 3-1 shows one such bulk crack initiation at a non-metallic inclusion in AFZ-IDA [117].

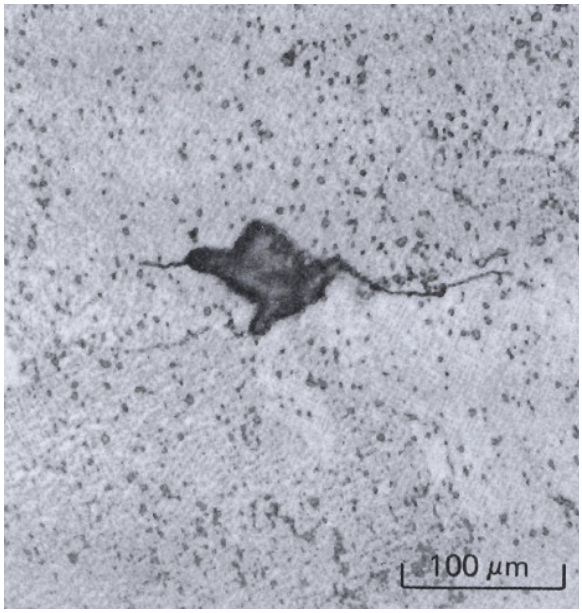

Figure 3-1: Formation of crystallographic cracks in large grains adjacent to debonded bulk MgO inclusions in AFZ-IDA [117] ($R_\varepsilon = 0$, T = 649°C).

Gayda and Miner [119, 120] examined modes of fatigue crack formation and early growth of several Ni-base superalloys under pure cycling and cycling with dwell periods at 650°C ($R_\varepsilon = -1$). They concluded that in the higher strength alloys without tensile dwell, crack initiation was transgranular and frequently associated with porosity or non-metallic inclusions. These sites were usually located near the surface, except for tests at low total strain ranges where large, internal (bulk) pores or inclusions often initiated fatigue cracks.

They also reported that in alloys with grain sizes less than 15 μm, fatigue crack formation and early crack growth was transgranular and became intergranular as the crack grew away from the inclusion. This transition was environmentally-assisted and did not occur for subsurface cracks until the crack broke through to the atmosphere. In the two coarse-grained alloys Waspaloy and Astroloy, Gayda and Miner did not report any of the internal crack initiation events that were observed in the fine-grained, high strength alloys in the plastic strain range of $\Delta\varepsilon_p$ = 0. 01% and strain ratio of R_ε = -1. Since large grain Waspaloy and Astroloy are not strictly cleaner than the other alloys of their study, grain size, rather than inclusion-assisted crack formation, was considered to be the main cause of Stage I crack formation and early crack growth within persistent slip bands [119].

De Bussac [121] performed LCF experiments on specimens of N18 superalloy, a French patented PM Ni-base superalloy [122] at T = 450°C and T = 650°C and $\Delta\varepsilon/2$ = 0.4% (R_ε = -1). They reported fatigue crack formation at surface and bulk inclusions. They identified the dependence of surface and bulk fatigue crack initiation probabilities on specimen size and oxidation effects based on experiments.

Huron and Roth [123] performed low cycle fatigue experiments on specimens of René 88DT, also a polycrystalline PM Ni-base superalloy, at T = 204°C (ε_{max} = 0.52% and 0.72%, R_ε = 0) and T = 650°C (ε_{max} = 0.60% and 0.80%, R_ε = 0). The specimens were either seeded with inclusions or unseeded. They observed that fatigue cracks formed exclusively at internal ceramic inclusions at 650°C and at crystallographic facets within surface grains at 204°C. The data showed an increased tendency for internal initiation at elevated temperatures, with surface initiation becoming prevalent only at high stress

amplitudes. They pointed out that the majority of sites for fatigue crack formation corresponded to large crystallographic facets in grains with sizes ranging from 60μm to 120μm, which are much larger than the average grain size of 26μm. In the presence of large grains, non-metallic inclusions corresponded to less than 5% of all the fatigue crack formation sites. Thus, the shift from inclusion-related to crystallographic failure modes is expected when grains are quite large.

Xie *et al.* [124] performed fatigue tests at T = 20°C and σ_{max} = 600 MPa (R_σ = 0.1) with in-situ SEM to trace the entire process of crack initiation, propagation, and fracture in Al_2O_3-seeded PM Rene'95 superalloy. Their observations, shown in Figure 3-2, confirmed that the main fatigue crack initiation mechanism was crystallographic crack initiation in grains adjacent to debonded bulk non-metallic inclusions.

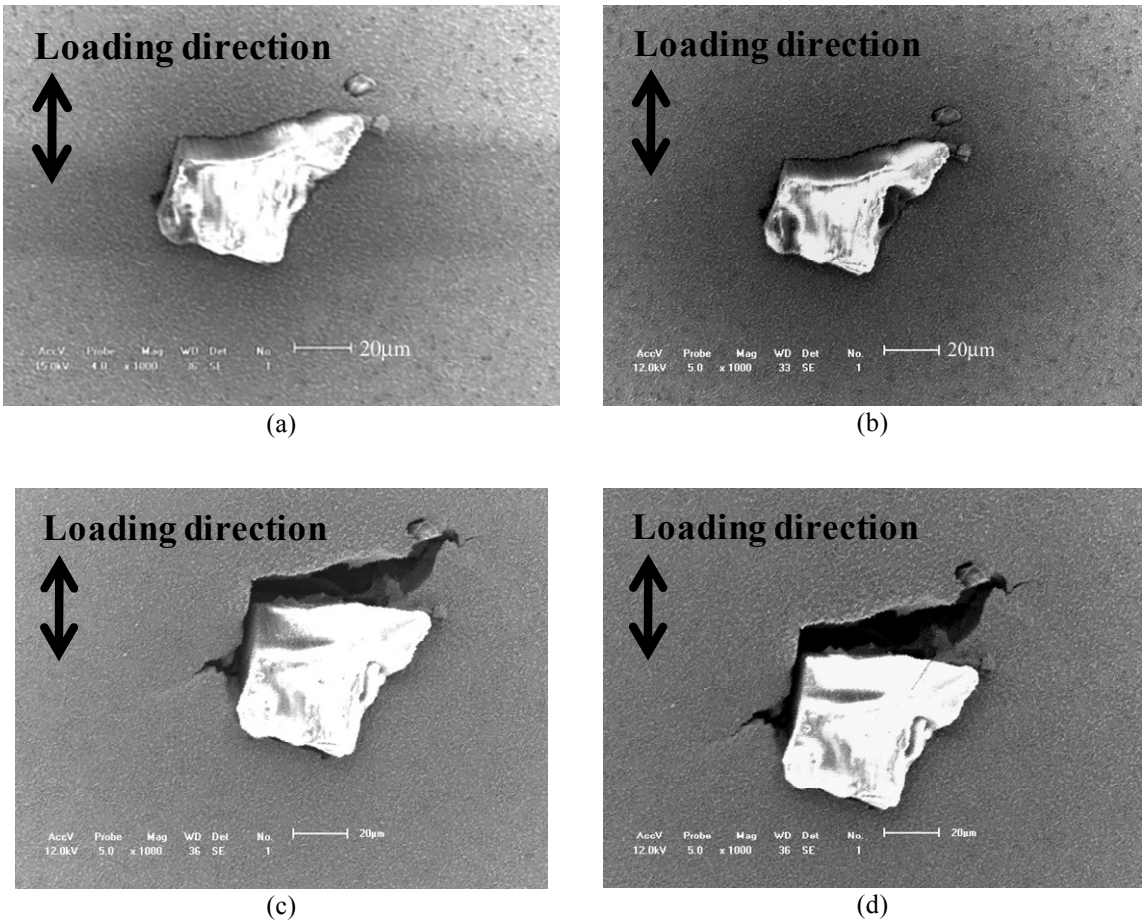

Figure 3-2: Fatigue crack initiation from a debonded inclusion in Al_2O_3-seeded PM Rene'95 superalloy; (a) N=0, (b) N=101335, (c) N=116316, (d) N=158116 (σ_{max}=600MPa, R_σ = 0.1, T = 20°C) [124].

Findley and Saxena [53] examined fatigue crack formation mechanisms in René 88DT for total strain range $\Delta\varepsilon$ = 0.66%, 0.79%, 0.94%, and 1.15% (R_ε = 0) as well as $\Delta\varepsilon$ = 0.66%, 0.75%, and 1.50% (R_ε = -1) at temperature T = 650°C. They reported that large grains, rather than non-metallic inclusions, were the dominant initiation sites.

Cashman [125, 126] examined fatigue crack failure mode in René 95, a polycrystalline PM Ni-base superalloy at T = 399°C and 538°C (R_ε = 0). He noted that fatigue cracks formed at small ceramic inclusions with diameters ranging from 20 to 127

microns. Cashman also identified competing modes of surface and bulk inclusion initiated fatigue crack formation. He noted dramatically different fatigue lives, even for comparable stress amplitudes, for surface and internally initiated fatigue cracks, with the internal sites associated with longer lives, nominally by a factor of eight.

Miao *et al.* [127] performed ultrasonic fatigue experiments under σ_{max} = 600 MPa and 940 MPa (R_σ = 0) at room temperature and T = 593°C for a supersolvus heat treatment René 88DT. They noted increased variability of fatigue life with decreasing stress amplitude. Their analyses of the fracture surfaces indicated that at room temperature, cracks formed at the surface where slip bands form, whereas at 593°C, all fatigue cracks formed internally. Both experiments were performed at low stress amplitudes in the VHCF regime.

More recently, and with reference to a fine-grained, subsolvus PM IN100 Ni-base superalloy, Wusatowska *et al.* [108] (σ_{max} = 568-811 MPa, R_σ = 0.05, and T = 426°C and 621°C) and Jha *et al.* [14] (σ_{max} = 1000-1200 MPa, R_σ = 0.05, and T = 650°C) noted the dominant role of ceramic inclusions in initiating fatigue cracks. Jha *et al.* [24] categorized the total fatigue lifetimes in terms of two populations, life-limiting and mean-controlling. They noted increased separation of the two lifetime data populations with decreasing stress amplitude, and attributed this increased divergence to the differing degree to which each of the relevant controlling mechanisms responds to the change of stress amplitude.

Fatigue cracks were observed to originate from ceramic inclusions in both scenarios, with the surface and bulk inclusions governing the life-limiting and mean-controlling lifetime populations, respectively. Table 7 summarizes the experimental

observations of fatigue crack initiation mechanisms in PM Ni-base superalloys associated with non-metallic particles.

Table 7: Experimental observations of fatigue crack initiation mechanisms in PM Ni-base superalloys.

Reference	Material	Test Conditions	Notes regarding crack initiation mechanism
[116]	AF-115 & AF2-IDA	$R_\varepsilon = 0$, T = RT, 649°C, 760°C $\sigma_y^{760°C} = 1069\ MPa$ $\Delta\varepsilon = 0.55,0.7,0.9,1.1\ (\%)$	Transition from surface inclusions and grains at RT to bulk inclusions at HT at low strain amplitudes. This transition is also observed in vacuum tests.
[119]	Several alloys	$R_\varepsilon = -1$, T = 650°C $\Delta\varepsilon_p = 0.01\%$	For fine grain alloys, initiation from porosity or inclusions. Shift to bulk defects at low strain ranges.
[123]	René 88DT Seeded	$R_\varepsilon = 0$, T = 204°C, 649°C $\varepsilon_{max}^{204°C} = 0.52,\ 0.72\ \%$ $\varepsilon_{max}^{649°C} = 0.6,\ 0.8\ \%$	At 204°C, fatigue cracks initiate from crystallographic facets within surface grains while at 649°C, they form from bulk inclusions. Grain size: ASTM 7/8 ALA 4
[12]	René 88DT	$R_\sigma = 0.05$, T = 593°C $\sigma_{max} = 940 - 1400\ MPa$ $\sigma_{y(0.2\%)}^{593°C} = 985\ MPa$	All bulk, crystallographic facets at longer lives and inclusions at shorter lives. More crystallographic failures than inclusion failures at 940 and 1000 MPa, Grain size: 10-40 μm
[53]	René 88DT	$R_\varepsilon = 0$ & -1, T = 650°C $\Delta\varepsilon^{R=0} = 0.66,0.79,0.94,1.15\ (\%)$ $\Delta\varepsilon^{R=-1} = 0.66,0.75,1.5\ (\%)$	Large surface grains when grain size is large (~20 μm) and bulk debonded inclusions for microstructures with finer grains averaging 6 μm.
[127, 128]	René 88DT	$R_\sigma = 0.05$, T = 593°C $\sigma_{max} = 500 - 760\ MPa$ $\sigma_y^{593°C} = 940\ MPa$	95% from large (60-120 μm) bulk grain and 5% from large inclusions. Oxidation may retard surface initiation at HT. Mean grain size is 26μm.
[108]	IN100	$R_\sigma = 0.05$, T = 426°C, 621°C $\sigma_{max} = 568 - 811\ MPa$ $\sigma_y^{20°C} = 1041\ MPa$ $\sigma_y^{400°C} = 1002\ MPa$ $\sigma_y^{600°C} = 1023\ MPa$	The majority of failures initiated from oxides inclusions. Ceramic inclusion size: 7-57 μm
[14]	IN100	$R_\sigma = 0.05$, T = 650°C $\sigma_{max} = 1000 - 1200\ MPa$ $\sigma_y^{650°C}$ = not mentioned	Surface non-metallic particles at lower lives and a mixture of subsurface NMP-initiated and surface pore- initiated failures at higher lives. Median γ-grain size: 4 μm

The following conclusions can be drawn from the experimental findings cited above:

1. Ceramic inclusions and pores are the dominant HCF crack initiation sites in fine-grained Ni-base superalloys. In coarse-grained Ni-base superalloys, large grains can be more critical than inclusions and pores.
2. Regardless of specimen size, non-metallic inclusions are generally more critical than grains of comparable size with regard to their potency to assist formation of fatigue cracks.
3. Inclusion-matrix debonding is prevalent. Experimental studies of inclusion related fatigue failures in PM Ni-base superalloys reveal that the majority of inclusions were in fact debonded [116-118, 124].

It is commonly believed that the HCF and VHCF fatigue crack initiation (formation and early growth) mechanisms are irreversible deformation accumulation on active slip systems acting at a slower rate than that in the LCF regime. Inclusions behave as micronotches that raise the local stress field, yet the nature of this notch effect has not been adequately defined, particularly with respect to the nature of the inclusion-matrix interface.

Computational studies of cast Al-Si alloys [76] and martensitic gear steels [78] have shown that the driving force for fatigue crack initiation in the matrix, surrounding the inclusions, depends strongly on the nature of the inclusion-matrix interface. Both studies suggest that inclusions with partially debonded interfaces provide higher driving

forces for fatigue crack initiation in the surrounding matrix than do intact, perfectly bonded and cracked inclusions.

For PM Ni-base superalloys, however, similar computational studies regarding the effects of the inclusion-matrix interface are lacking. Characterizing such effects can play a significant role in explaining experimental observations that the majority of critical inclusions in Ni-base superalloys were debonded [116, 124]. In this Chapter, we calculate and compare three candidate FIPs around intact, halved, and partially debonded inclusions as well as pores.

3.2 Finite element model

We utilize the FE model shown in Figure 2-11 for all inclusion-matrix interface types, as well as pores of the same size, to maintain consistency. The FE models for halved and partially debonded inclusions are replicated, respectively, in Figures 3-3 and 3-4 to emphasize the designation of inclusion-matrix interface associated with them. In simulations with halved and partially debonded inclusions, contact between the interacting surfaces is assumed to be frictionless.

We use two-dimensional generalized plane strain (GPS) elements [49] (see Section 2.4.1), often referred to as 2.5D, and the fully 3D crystal plasticity material model (see Section 2.1.2). The crystal plasticity material model constants and microstructure parameters are listed in Table 3 and Table 4, respectively. Properties assigned for the fully isotropic elastic inclusion include Young's modulus E^i = 400 GPa and Poisson's ratio ν^i = 0.3. Quadratic triangular elements of type CPEG6M are used to mesh the FE model (see Section 2.1.2).

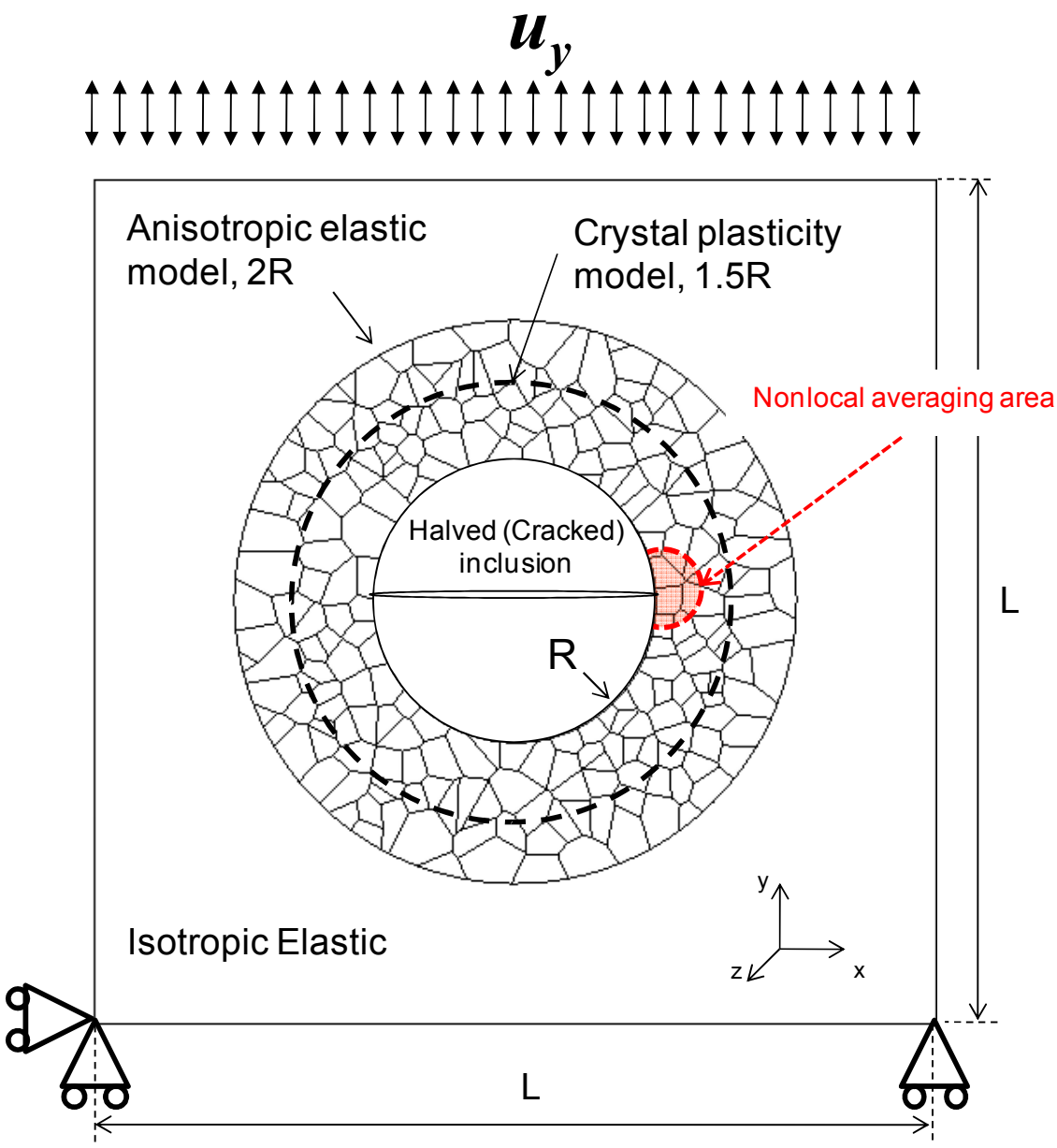

Figure 3-3: FE model for simulations of halved inclusions.

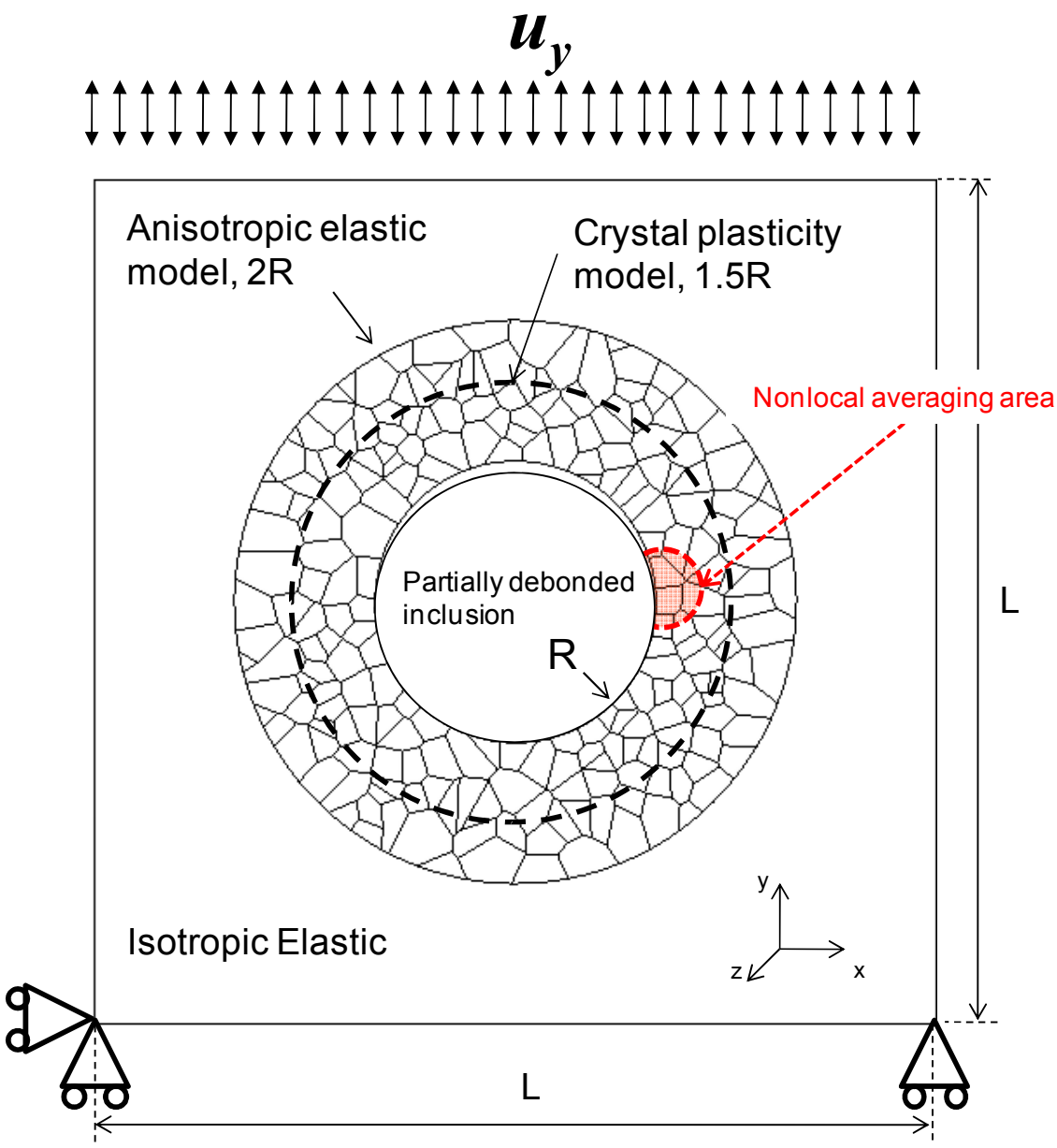

Figure 3-4: FE model for simulations of partially debonded inclusions.

The three candidate FIPs under study are the maximum range of plastic shear strain $\Delta\gamma^{*}_{p,\max}$, the Fatemi-Socie P_{FS}, and the cumulative equivalent plastic strain P_P parameters (c.f. Section 2.2). The inclusion radius is R = 10 μm for all cases and L = 60 μm. Two sizes of the semicircular FIP averaging region with radii equal to R/5 (2 μm) and R/√10 (3 μm) are considered, corresponding to averaging regions that are 2% and 5% of the inclusion/pore size [109]. The FIP averaging region is located in the slip-intensified region of the inclusion/pore notch root. The element with the maximum local magnitude of FIP determines the center of the semicircular FIP averaging region within the slip-intensified region.

The following boundary conditions are enforced; assuming the origin of the *xyz* coordinate system is at the center of the inclusion/pore:

1. The traction free boundary condition is enforced for the entire length of the model's left and right edges (x = -L/2, L/2 and -L/2 < y < L/2).
2. The y-symmetry boundary condition (u_y = 0) is enforced for the entire length of the model's bottom edge (y = -L/2 and - L/2 < x < L/2).
3. The z-symmetry boundary condition (u_z = 0) is enforced to the reference point of the GPS model.
4. Cyclic uniaxial displacement $u_y = \varepsilon_{yy} \times L$ is applied to the entire length of the model's top edge (y = L/2 and - L/2 < x < L/2) at the applied strain amplitudes ε_{yy} = 0.5, 0.6, 0.7, and 0.8 ε_{ys} (ε_{ys} = 0.7 % (c.f. 2.4.3)), strain ratio R_ε = -1, and uniform strain rate of 0.002 s^{-1}.

The FIPs are calculated for three simulated loading cycles. A total of 20 randomly assigned polycrystalline orientation distributions (realizations) are simulated for each applied strain amplitude and inclusion-matrix interface type. The Voronoi tessellation diagram is the same and only grain orientations (random) vary across these realizations. As such, only different grain orientations distinguish the microstructure realizations.

A case pointer, of the *A#-#* format, is used to refer to each simulation scenario where A can be I, H, PD, or P for intact, perfectly bonded inclusions, halved (cracked) inclusions, partially debonded inclusions, and pores, respectively. The first and second numeric characters, separated by a hyphen, refer to the polycrystalline orientation distribution and the normalized applied strain amplitude (i.e., $\varepsilon_{yy}/\varepsilon_{ys}$), respectively. For instance, the case pointer *H5-0.5* refers to the simulation scenario where the inclusion is halved, the grain orientations are from polycrystalline orientation distribution 5, and the applied strain amplitude $\varepsilon_{yy} = 0.5\ \varepsilon_{ys}$. As such, 320 simulations (Figure 3-5) were performed (R = 10 μm for all of them) to assess these candidate FIPs around non-metallic inclusions and pores.

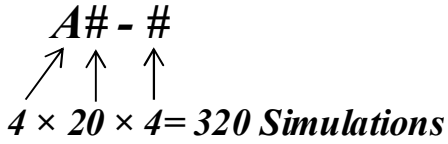

Figure 3-5: Simulation case pointer format.

3.3 Results and discussion

Figure 3-6 relates the variation of the maximum range of the nonlocal plastic shear strain, the Fatemi-Socie parameter and the cumulative equivalent plastic strain to the applied strain amplitude for intact, perfectly bonded inclusions, halved (cracked) inclusions, partially debonded (PD) inclusions, and pores. Each data point corresponds to the mean value of 20 simulated polycrystalline orientation distributions. For each FIP, the two nonlocal averaging regions that are 2% and 5% of the inclusion projected area are plotted in hollow and solid symbols, respectively. As expected the smaller FIP averaging area results in higher predicted FIP values due to the highly localized nature of deformation at the notch root.

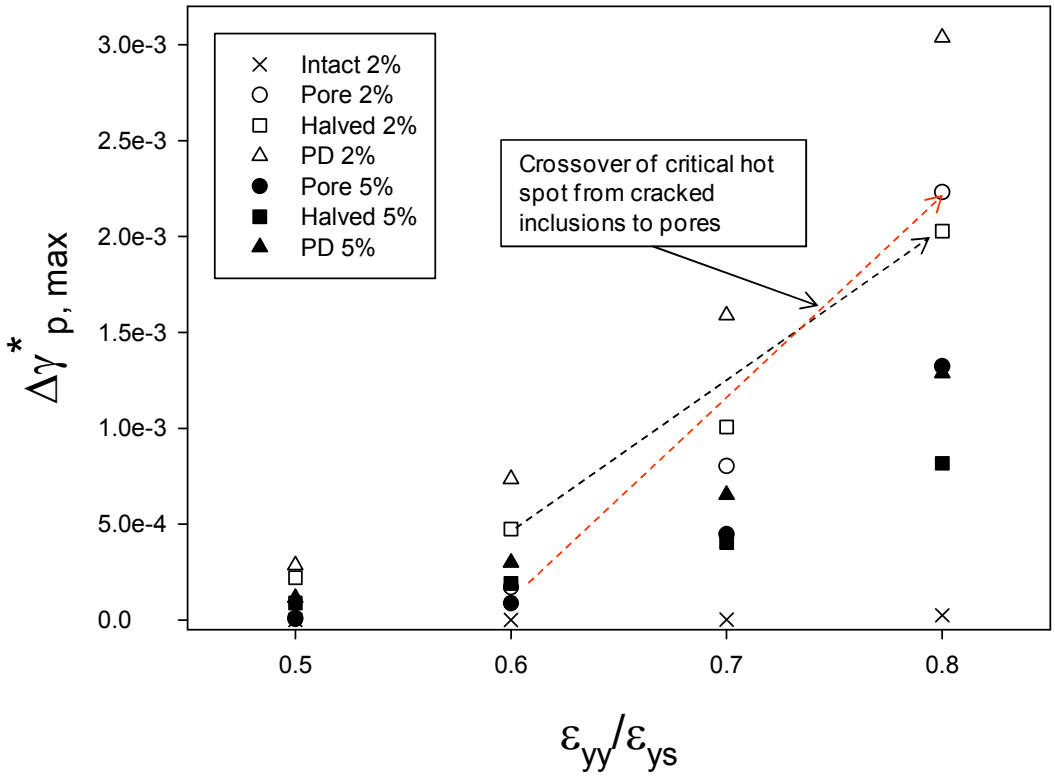
Intact 2%
Pore 2%
Halved 2%
PD 2%
Pore 5%
Halved 5%
PD 5%
Crossover of critical hot spot from cracked inclusions to pores
3.0e-3
2.5e-3
2.0e-3
1.5e-3
1.0e-3
5.0e-4
0.0
0.5
0.6
0.7
0.8
$\Delta\gamma^*_{p,max}$
$\varepsilon_{yy}/\varepsilon_{ys}$

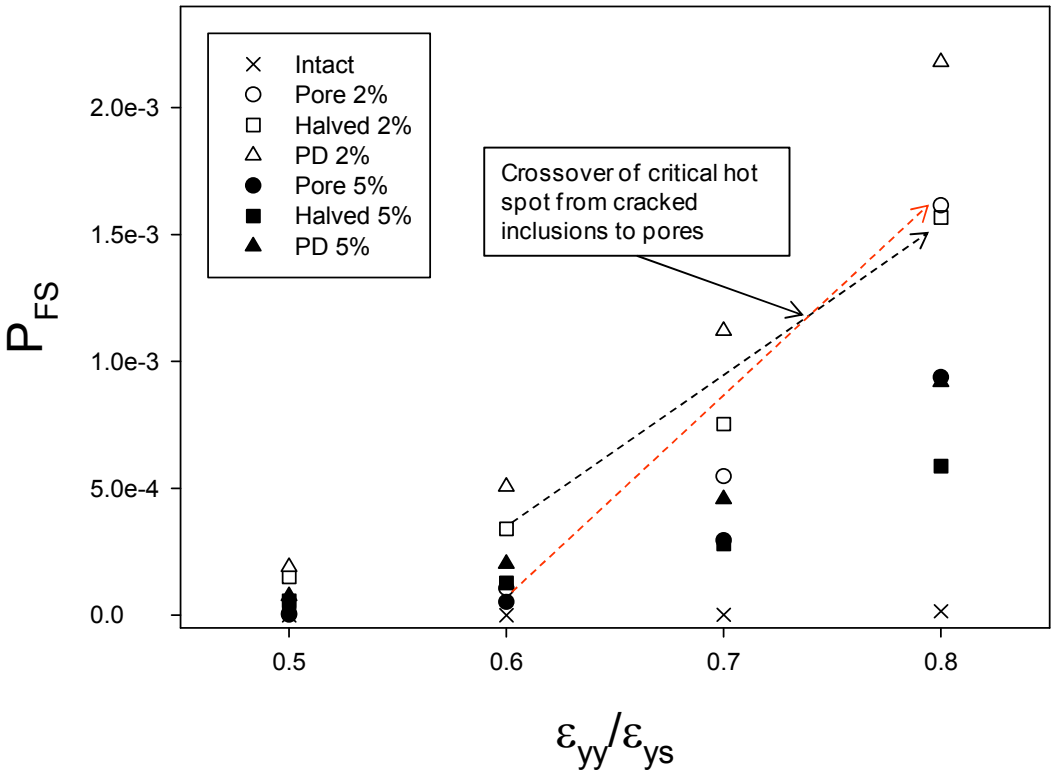
Intact
Pore 2%
Halved 2%
PD 2%
Pore 5%
Halved 5%
PD 5%
Crossover of critical hot spot from cracked inclusions to pores
2.0e-3
1.5e-3
1.0e-3
5.0e-4
0.0
0.5
0.6
0.7
0.8
P_{FS}
$\varepsilon_{yy}/\varepsilon_{ys}$

Figure 3-6: Comparison of FIPs vs. the applied strain amplitude (ε_{ys} = 0.7 %, R_ε = -1; R = 10 μm).

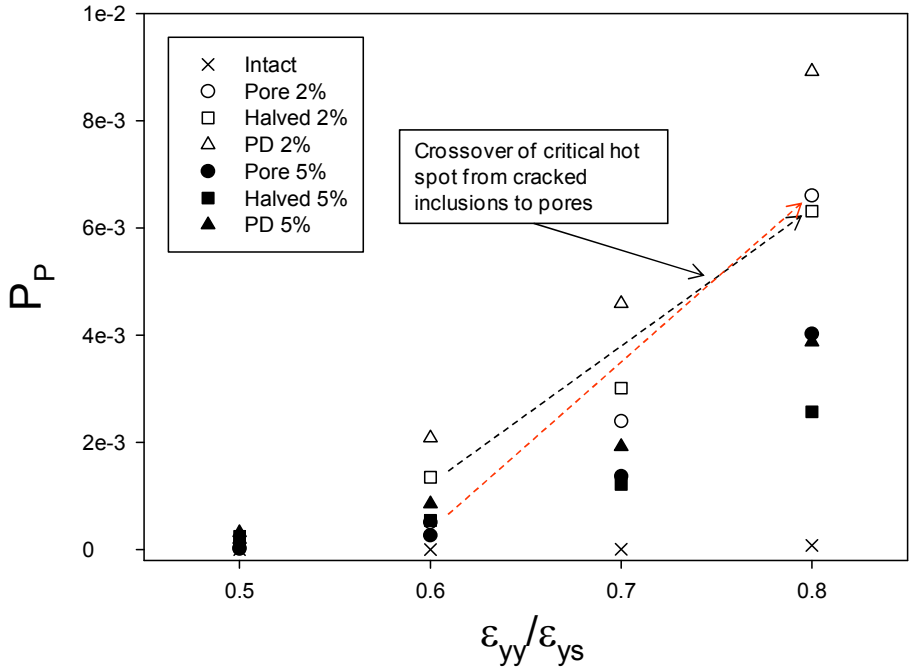

Figure 3-6 Continued.

As seen in Figure 3-6, all three FIPs under study suggest that damaged inclusions and pores are more significant than intact, perfectly bonded inclusions. Moreover, between the two types of damaged inclusions studied, partially debonded inclusions are more critical than halved inclusions and pores at all applied uniaxial strain amplitudes studied. For instance, based on an averaging region that is 2% of the inclusion projected area:

1. Partially debonded inclusions are 45 ~ 55 % more critical than halved inclusions at all applied strain amplitudes studied.

2. Partially debonded inclusions are about three times, twice, and 30% more critical than pores at $\varepsilon_{yy}/\varepsilon_{ys}$ = 0.6, 0.7, and 0.8, respectively.

FIPs for inclusions increase proportionally (i.e., with the same pace) with respect to the applied strain amplitude. However, the FIPs for pores appear to increase at a different rate. Therefore, pores are less critical than halved inclusions at lower applied strain amplitude (i.e., $\varepsilon_{yy}/\varepsilon_{ys}$ = 0.5, 0.6, and 0.7), but they become as critical as, or more critical than, halved inclusions at the higher applied strain amplitude of $\varepsilon_{yy}/\varepsilon_{ys}$ = 0.8. This is shown in Figure 3-6 by the crossover of critical hot spots from inclusions to pores at higher applied strain amplitudes.

Plastic deformation around pores is not as concentrated as that around damaged, especially halved, inclusions. As a result, around pores, more slip systems experience the effects of increased applied strain amplitude, which explains the higher rate of increase in FIPs for pores than for damaged inclusions. This effect is shown in Figure 3-7 via contour plots of the Fatemi-Socie P_{FS} parameter (i.e., computed at the element integration points) around a pore and a halved inclusion having the same polycrystalline orientation distribution and loaded at $\varepsilon_{yy}/\varepsilon_{ys}$ = 0.6 and 0.8. The P_{FS} contour limits are set to 0 and 1×10^{-5}; the black-shaded and grey-shaded regions corresponds to finite element integration points having $P_{FS} \geq 10^{-5}$ and $P_{FS} \leq 0$, respectively. By definition, the Fatemi-Socie parameter P_{FS} should be positive. However, the contour plots indicate regions with negative values for this FIP; these negative regions represent the ABAQUS Viewer's extrapolation of the FIP values calculated at integration points, which are positive, to nodal values. Figure 3-7 indicates that as the applied uniaxial strain amplitude (R_ε = -1) increases (from $\varepsilon_{yy}/\varepsilon_{ys}$ = 0.6 to 0.8), the critical region (with $P_{FS} \geq 10^{-5}$) at the pore notch

root grows to affect a larger region than the critical region at the notch root of the cracked inclusion.

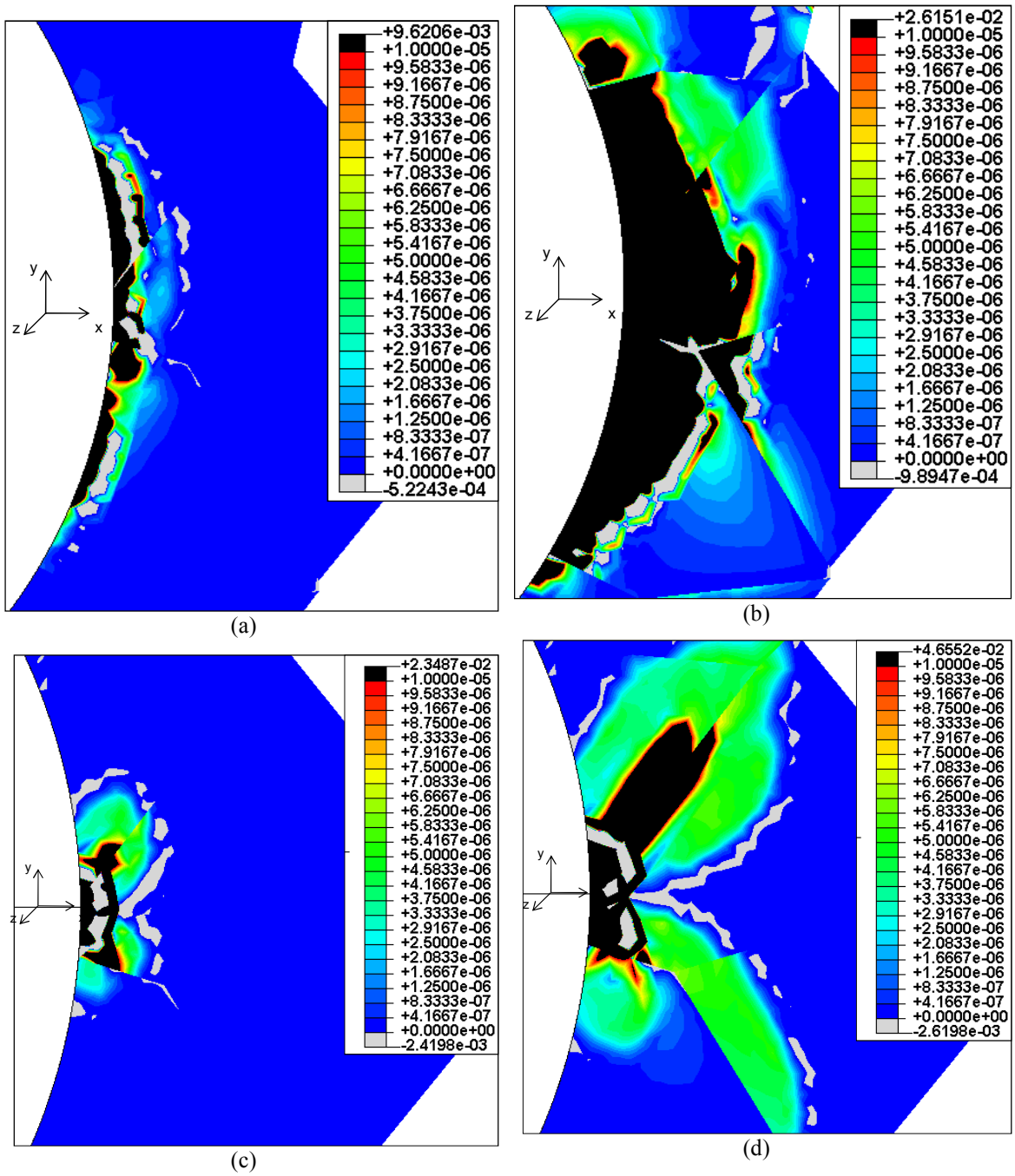

Figure 3-7: Contour plots of local P_{FS} parameter (computed at the element integration points) for (a) pore $\varepsilon_{yy}/\varepsilon_{ys} = 0.6$, (b) pore $\varepsilon_{yy}/\varepsilon_{ys} = 0.8$, (c) cracked inclusion $\varepsilon_{yy}/\varepsilon_{ys} = 0.6$, and (d) cracked inclusion $\varepsilon_{yy}/\varepsilon_{ys} = 0.8$

(ε_{ys} = 0.7 %, R_ε = -1; R = 10 μm).

The crossover of most critical hot spots from inclusions to pores at higher applied strain amplitudes can help to explain experimental findings by Wusatowska *et al.*, [108] who noted the dominant role of oxide inclusions for $\sigma_{yy} / \sigma_{ys} < 0.7$ ($R_\sigma = 0.05$) and Jha *et al.*, [14] who attributed the fatigue crack origin to a mixture of inclusions and pores at $\sigma_{yy} / \sigma_{ys} > 0.7$ ($R_\sigma = 0.05$). The material for both studies was a fine-grained, subsolvus PM IN100 Ni-base superalloy tested at elevated temperatures. However, sufficient experimental data are lacking to conclusively describe such experimental observations by the simulated FIP trends.

Figure 3-8 shows the nonlocal P_{FS} parameter around intact and damaged inclusions as well as pores at $\varepsilon_{yy}/\varepsilon_{ys}$ = 0.5 and 0.6; all of these are 10 μm in radius. The scatter bars indicate the standard deviation of the P_{FS} parameter distribution for the 20 simulated polycrystalline orientation distributions. The Voronoi tessellation diagrams are kept the same for these cases; only the grain orientations vary across these microstructure realizations. For $\varepsilon_{yy}/\varepsilon_{ys}$ = 0.6, a downward triangular symbol represents the maximum value of FIP amongst the 20 realizations around a halved inclusion. Similarly, an upward triangular symbol represents the minimum value of FIP amongst the 20 realizations around a debonded inclusion.

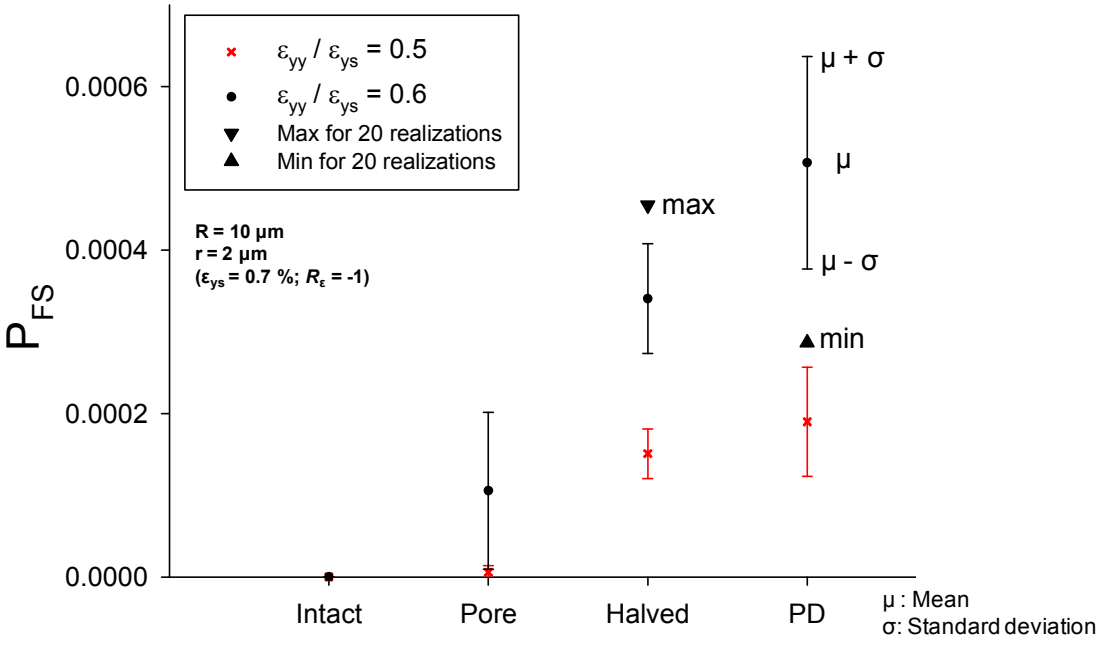

Figure 3-8: P_{FS} parameter around inclusions and pores, 20 µm in diameter (ε_{ys} = 0.7 %; R_ε = -1).

As seen in Figure 3-8, the FIP variation due to the orientation of adjacent grains is of the same order of magnitude as that due to the type of damaged inclusion (i.e., halved versus debonded). Our approach to the surface to bulk transition of HCF initiation sites in Chapter 6 accounts for the fact that the effect of grain orientation distribution and the type of damaged inclusion can be equally significant in terms of variability.

Since the scatter bars in Figure 3-8 correspond to absolute values, they do not directly compare the degree of scatter amongst FIP distributions. To address this, we plot the coefficient of variation (CV) for each P_{FS} parameter distribution in Figure 3-9. CV is a normalized measure of dispersion of a probability distribution defined as the ratio of the standard deviation, σ, to the mean, µ, i.e.,

$$CV = \frac{\sigma}{\mu} \tag{3.1}$$

Figure 3-9 is a bubble chart of the P_{FS} parameter around intact and damaged inclusions as well as pores, all 20 μm in diameter. Results for four macroscopic remote applied strain amplitudes of $\varepsilon_{yy}/\varepsilon_{ys}$ = 0.5, 0.6, 0.7, and 0.8 are shown. The CV for FIP distributions of 20 simulated polycrystalline orientation distributions determines the size of each bubble.

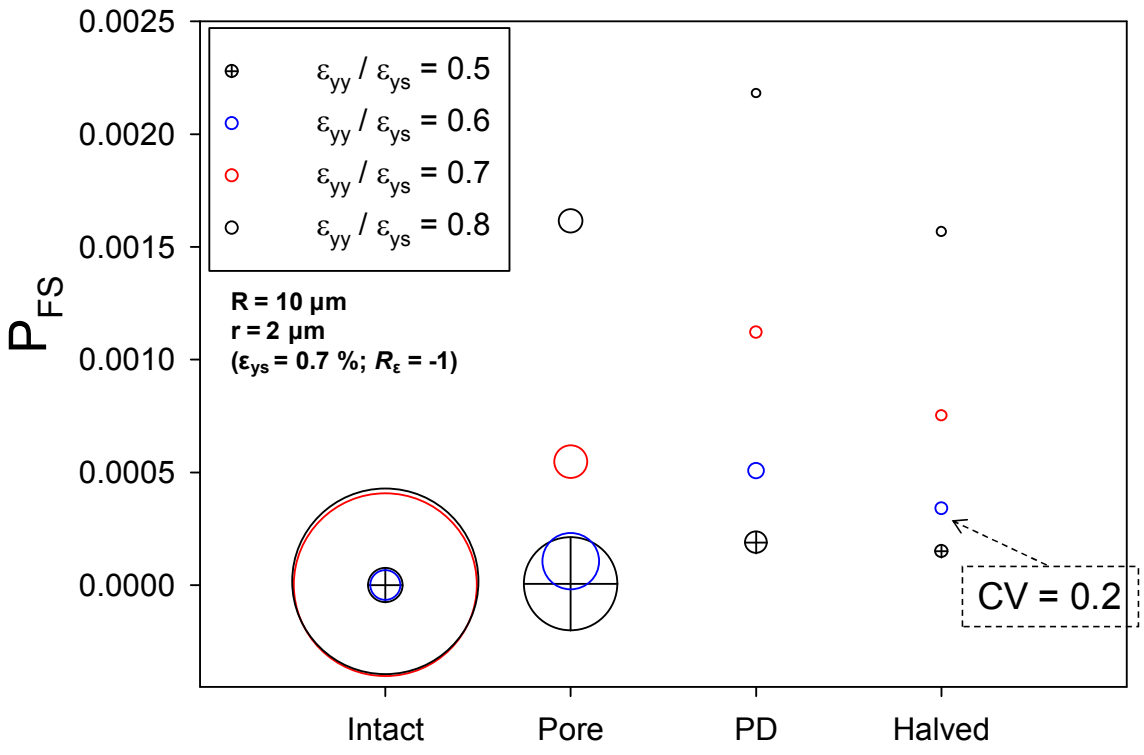

Figure 3-9: P_{FS} parameter around inclusions and pores, 10 μm in radius (ε_{ys} = 0.7 %; R_{ε} = -1).

As suggested by the smaller bubbles in Figure 3-9, the normalized FIP scatter is less among the microstructure realizations at higher applied uniaxial strain amplitudes, due to the more homogenous slip activity in the nonlocal FIP averaging region. Also, as the deformation becomes increasingly localized, FIP scatter decreases. The deformation is most localized for the halved inclusions, followed by partially debonded inclusions and then pores.

The extreme value $\left(\Delta\gamma^{*}_{p,\max}\right)$ parameter is plotted in Figure 3-10 for partially debonded and halved inclusions as well as pores. The horizontal scatter bars correspond to the variation in this parameter among the simulated polycrystalline orientation distributions. The type I cumulative extreme value distribution, known as the Gumbel distribution (cf. Section 2.3) is fitted to this scatter data and plotted in red for each applied strain amplitude. The location and scale parameters of the Gumbel distribution fits are calculated using the maximum likelihood (MLE) [92] estimation method.

Figure 3-10 indicates that the mean and variability in the absolute value of FIPs increase as the applied uniaxial strain amplitude (R_ε = -1) increases. Whereas, the coefficient of variation, which is regarded as a normalized measure of FIP variability, was shown in Figure 3-9 to decrease as the applied uniaxial strain amplitude increased. The variability in the absolute value of FIPs increases as the applied strain amplitude increases because the nonlocal averaging region for the calculation of FIPs is taken to be of a constant size r = 2 μm. As such, increasing the applied strain amplitude increases the stress intensity in this averaging region and magnifies the variability in the distribution of FIPs for the simulated matrix realizations (grain orientation distributions).

These plots are presented in this section as representative plots of the kind used in Chapter 7 to assess the surface fatigue crack initiation probability under HCF and VHCF. In Chapter 7, we will utilize the cumulative generalized extreme value distribution (GEV), described in Section 2.3, to fit the simulated FIP data. The scale parameter of the fitted GEV distribution accounts for the increases statistical dispersion of the FIP data. GEV distribution includes the Gumbel distribution as a special case so that the data can decide which extreme value distribution type is more appropriate. The variation of the parameters of the fitted GEV distribution versus the applied uniaxial strain amplitude (R_ε = -1) and inclusion radius will be further examined for partially debonded inclusions in Chapter 7.

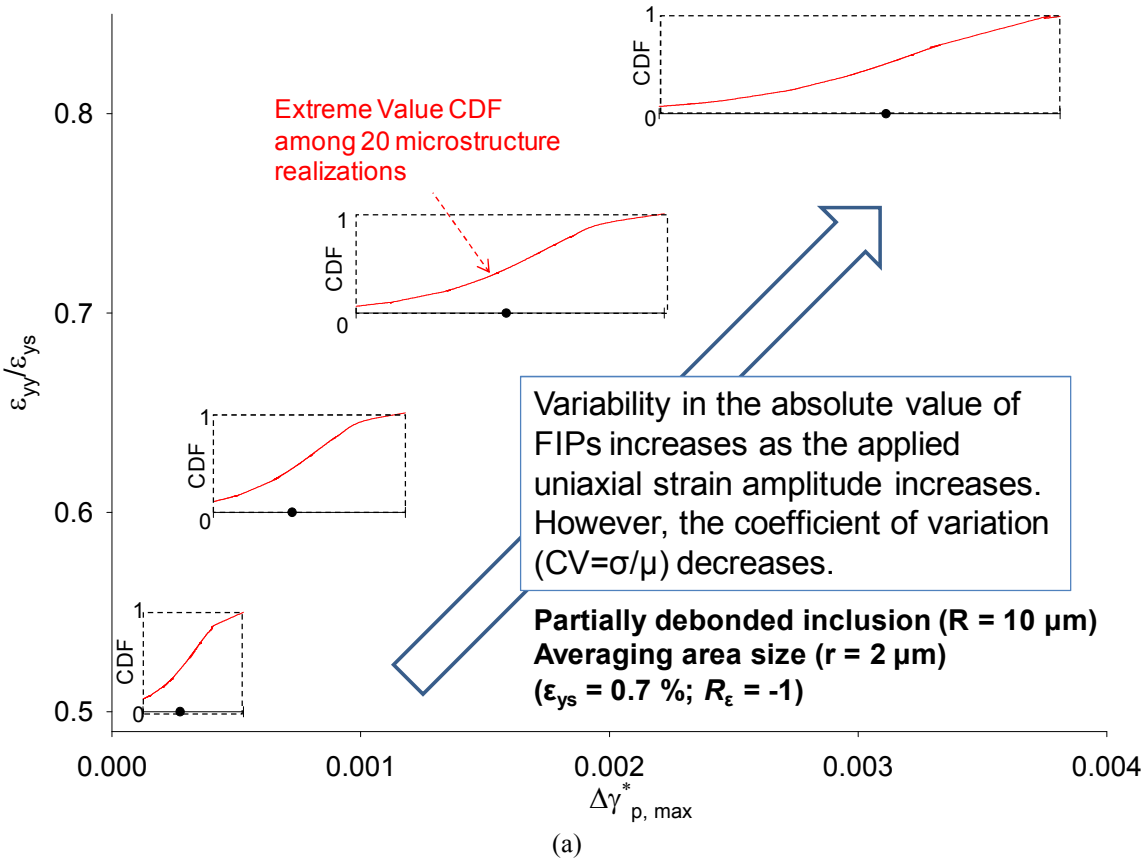

(a)

Figure 3-10: The Gumbel distribution fit of extreme value $\Delta\gamma^{*}_{p,\max}$ (ε_{ys} = 0.7 %; R_{ε} = -1). (a) partially debonded inclusions, (b) halved inclusions, and (c) pores (R = 10 μm).

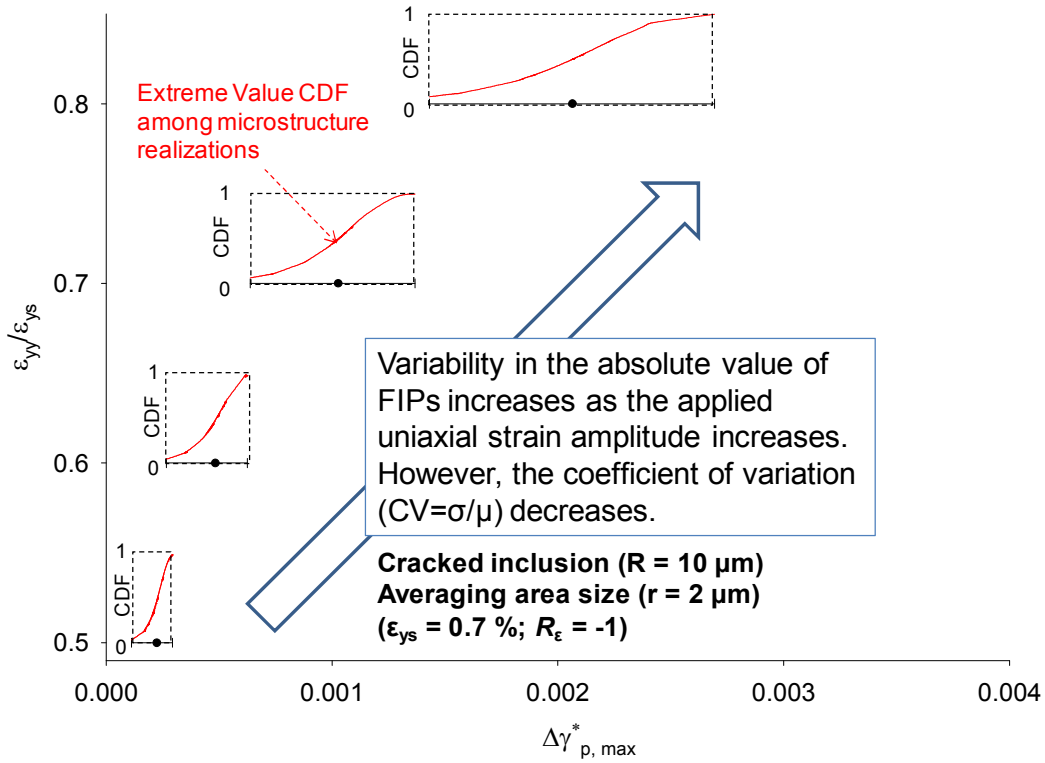

(b)

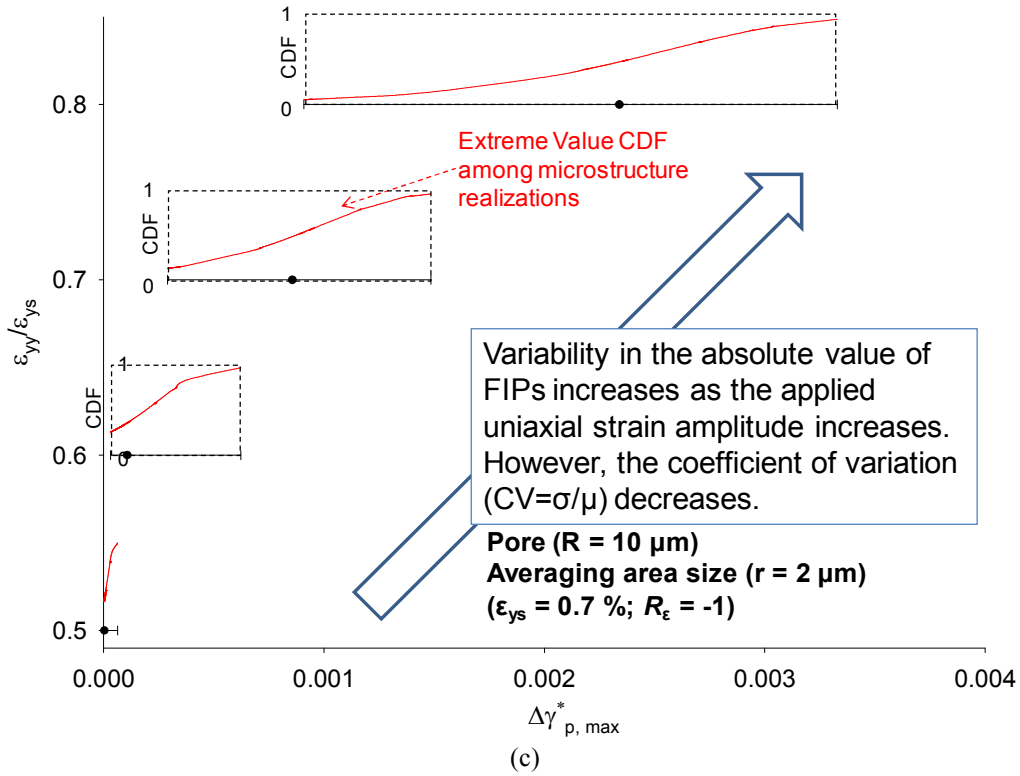

(c)

Figure 3-10 Continued.

3.4 Summary

The distributions of three shear-based FIPs were examined for intact, perfectly bonded inclusions, halved (cracked) inclusions, partially debonded (PD) inclusions, and pores. For each case, 20 simulated polycrystalline orientations (realizations) were simulated at four different applied strain amplitudes corresponding to the HCF and LCF regimes.

Due to the dominating role of inclusions/pores in localizing the deformation, the spatial distributions of all three FIPs were found to be similar. The studied FIPs collectively indicated that:

1. Damaged inclusions and pores are significantly more critical than intact, perfectly bonded inclusions.
2. Partially debonded inclusions are often more critical than halved inclusions and pores at all applied uniaxial strain amplitudes. Nevertheless, a halved inclusion or pore may surpass the partially debonded inclusion, if it is next to a favorably oriented (particularly large) grain.

As expected, FIPs increased at higher applied strain amplitudes. However, the rate of increase in FIPs for pores was found to be higher. This is because plastic deformation around pores is not as concentrated as that around damaged inclusions, and more slip systems experience the effects of increased applied strain amplitude. Interestingly, pores can become as critical as or more critical than halved inclusions at higher applied strain amplitudes, which can help to explain the similar trends seen in experiments by

Wusatowska *et al.*, [108] who noted the dominant role of oxides inclusions for $\sigma_{yy} / \sigma_{ys} < 0.7$ ($R_\sigma = 0.05$) and Jha *et al.*, [14] who attributed the fatigue crack origin to a mixture of inclusions and pores at $\sigma_{yy} / \sigma_{ys} > 0.7$ ($R_\sigma = 0.05$). The degree of scatter in FIPs among microstructure realizations was found to depend on the:

1. Applied strain amplitude: The coefficient of variation (CV) in the distribution of FIPs for the simulated grain orientation distributions was shown in Figure 3-9 (CV was shown by the bubble size) to decrease as the applied uniaxial strain amplitude increases. CV is regarded as a normalized measure of FIP variability. However, Figure 3-10 indicates that the mean and variability in the absolute value of FIPs increase as the applied uniaxial strain amplitude ($R_\varepsilon = -1$) increases. The variability in the absolute value of FIPs increases as the applied strain amplitude increases because the nonlocal averaging region for the calculation of FIPs is taken to be of a constant size r = 2 μm. As such, increasing the applied strain amplitude increases the stress intensity in this averaging region and magnifies the variability in the distribution of FIPs for the simulated matrix realizations (grain orientation distributions).
2. Inclusion-matrix interface type: As the deformation becomes increasingly localized, FIP scatter decreases. The deformation is most localized for the halved inclusions followed by partially debonded inclusions and pores.

4 Inclusion-matrix debonding probability to stress amplitude

4.1 Introduction

In Chapter 3, we cited experimental studies that support the dominant role of inclusions in initiating fatigue cracks in various PM processed Ni-base superalloys, and we concluded that partially debonded inclusions are more critical than other damaged inclusions and pores.

It is instructive to study the likelihood and location of inclusion-matrix interface separation at various remote applied uniaxial strain amplitudes. To that end, parametric finite element simulations are performed in this Chapter to assess the interface traction and the modified interface traction parameters (cf. 2.2.4). The findings are used in Chapter 7 to study the inclusion-matrix debonding effect on the ratio of probabilities of surface to bulk fatigue crack initiation.

Although halved (fractured) inclusions can theoretically generate FIPs comparable to those for partially debonded inclusions, we assume that critical inclusions are debonded in the remainder of our study. This is not because they result in higher average FIPs (cf. Figure 3-9) but because:

1. Inclusion-matrix debonding is prevalent. Experimental studies of inclusion related fatigue failures in PM Ni-base superalloys reveal that the majority of inclusions were in fact debonded [116-118, 124].
2. Computational studies suggest that the stress distribution in halved inclusions is likely to cause debonding of the inclusion-matrix interface [76].

3. Intuitively, inclusion-matrix interface debonding is more likely to occur than inclusion fracture. This is because the surfaces are of two different materials (i.e., inclusion and matrix). Most often the inclusion-matrix interface is not deliberately strengthened.

In this Chapter, we introduce a probabilistic-mechanics approach to explore how the likelihood of inclusion-matrix debonding may decrease as the applied remote stress amplitude decreases.

The interface traction (T_{int}) and the modified interface traction parameter (P_T) (see Section 2.2.4) are used as indicators for assessing the driving force for the inclusion-matrix interface separation. Parameters T_{int} and P_T are calculated for each grain, located at the inclusion-matrix interface, as shown in Figure 2-4. The inclusion-matrix interface unit normal vector $\left(n^{incl}\right)$ is unique for each grain, determined based on the location of the grain relative to the inclusion center.

We define $c_R^{\omega}(x)$ as the cumulative probability that an inclusion with radius R results in parameter FIP smaller than x (an averaged quantity) in magnitude under the applied uniaxial strain amplitude $\omega = \varepsilon_{yy} / \varepsilon_{ys}$ for R_ε = -1. The indicator parameter could be T_{int} or P_T.

Since c_R^{ω} depends on the inclusion radius, the probability that an arbitrary inclusion, regardless of its size, results in an indicator parameter smaller than x in magnitude under the applied strain amplitude ω can be expressed as

$$C^{\omega}(x) = \int P_R \; c_R^{\omega}(x) \; dR \tag{4.1}$$

where the variable P_R refers to the inclusion radius distribution such that

$$\int P_R \, dR = 1 \tag{4.2}$$

Thus, the probability that this inclusion debonds under these circumstances can be expressed as

$$P^{\omega}_{debond} = 1 \text{ - } C^{\omega}(x^*) \tag{4.3}$$

where x^* is a material-specific threshold parameter.

In this chapter, we simulate several polycrystalline orientation distributions at various applied strain amplitudes to construct the empirical cumulative distribution functions (CDFs) of extreme value FIP parameters in order to model c^{ω}_R.

4.2 Finite element model

Finite element simulations utilize two-dimensional generalized plane strain elements [49], and the full model, shown in Figure 4-1, is utilized to mitigate any boundary effects. We use two-dimensional generalized plane strain (GPS) elements [49] (see Section 2.4.1), often referred to as 2.5D, and the fully 3D crystal plasticity material model (see Section 2.1.2). The crystal plasticity material model constants and microstructure parameters are listed in Table 3 and Table 4, respectively. Properties assigned for the fully isotropic elastic inclusion include Young's modulus E^i = 400 GPa and Poisson's ratio ν^i = 0.3. Quadratic triangular elements of type CPEG6M are used to mesh the FE model (see Section 2.1.2).

The following boundary conditions are enforced; assuming the origin of the *xyz* coordinate system is at the center of the inclusion:

1. The traction free boundary condition is enforced for the entire length of the model's left and right edges (x = -L/2, L/2 and -L/2 < y < L/2).
2. The y-symmetry boundary condition (u_y = 0) is enforced for the entire length of the model's bottom edge (y = -L/2 and - L/2 < x < L/2).
3. The z-symmetry boundary condition (u_z = 0) is enforced to the reference point of the GPS model.
4. Cyclic uniaxial displacement $u_y = \varepsilon_{yy} \times L$ is applied to the entire length of the model's top edge (y = L/2 and - L/2 < x < L/2) at the applied strain amplitudes ε_{yy} = 0.5, 0.6, and 0.7 ε_{ys} (ε_{ys} = 0.7 % (c.f. 2.4.3)), strain ratio R_ε = -1, and uniform strain rate of 0.002 s^{-1}.

A total of 20 polycrystalline orientation distributions are simulated at each applied strain amplitude and inclusion radii R = 4, 6, 8 and 10 μm. The Voronoi tessellation diagram is same across these realizations and only grain orientations vary.

Upon the completion of the 3rd cycle, the parameters T_{int} and P_T are calculated as the indicator parameters (see Section 2.2.4) for each inclusion radius, polycrystalline orientation distribution, and applied strain amplitude. For discrete values of the applied strain amplitude and the inclusion radii, Eq. 4.1 can be approximated as

$$C^{\omega} = \sum_{i=1,2,\ldots,n} P_{R_i}\ c_R^{\omega}\ \Delta R_i \qquad\qquad \omega = 0.5, 0.6, 0.7, 0.8 \tag{4.4}$$

where n and ΔR_i are the number and the size of bins used to discretize the inclusion radius distribution. Since we are simulating inclusions with radii R = 4, 6, 8 and 10 μm, n = 4. We restricted this study to inclusions up to 10 μm in radius due to computational time constraints and consider this as a limitation of this study.

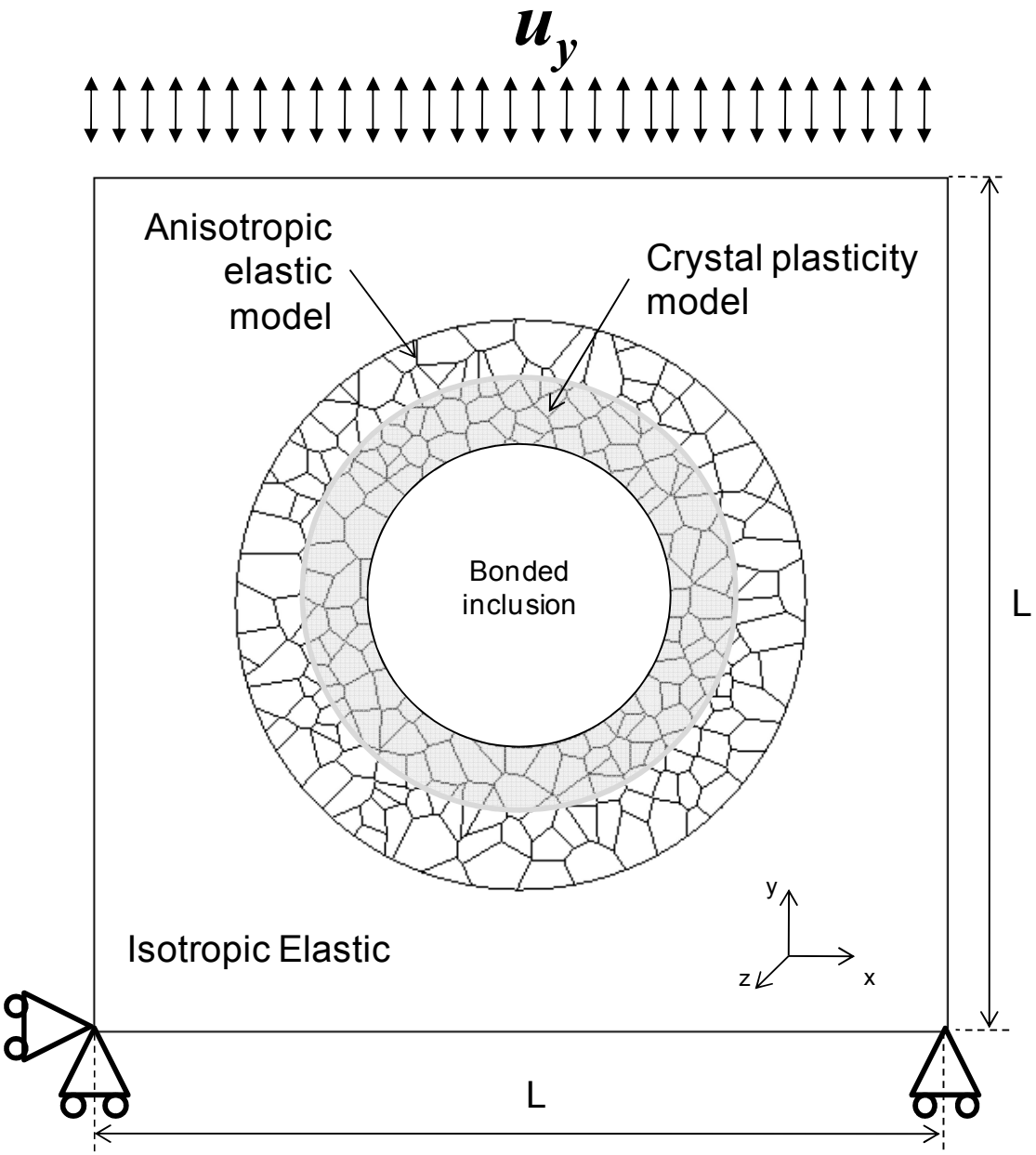

Figure 4-1: Full model for simulations of intact, perfectly bonded inclusions.

4.3 Results and discussion

Figure 4-2 shows the *yy* stress contours of an intact, perfectly bonded inclusion for $\varepsilon_{yy} = 0.5\ \varepsilon_{ys}$ and $R_\varepsilon = -1$. They are plotted for polycrystalline orientation distribution #1 and at the peak applied uniaxial strain amplitude in the third cycle (point A in the cyclic load history, shown in Figure 4-2). As expected, the *yy* stress component peaks in the north and south poles of the inclusion, two regions outlined in red dashed lines.

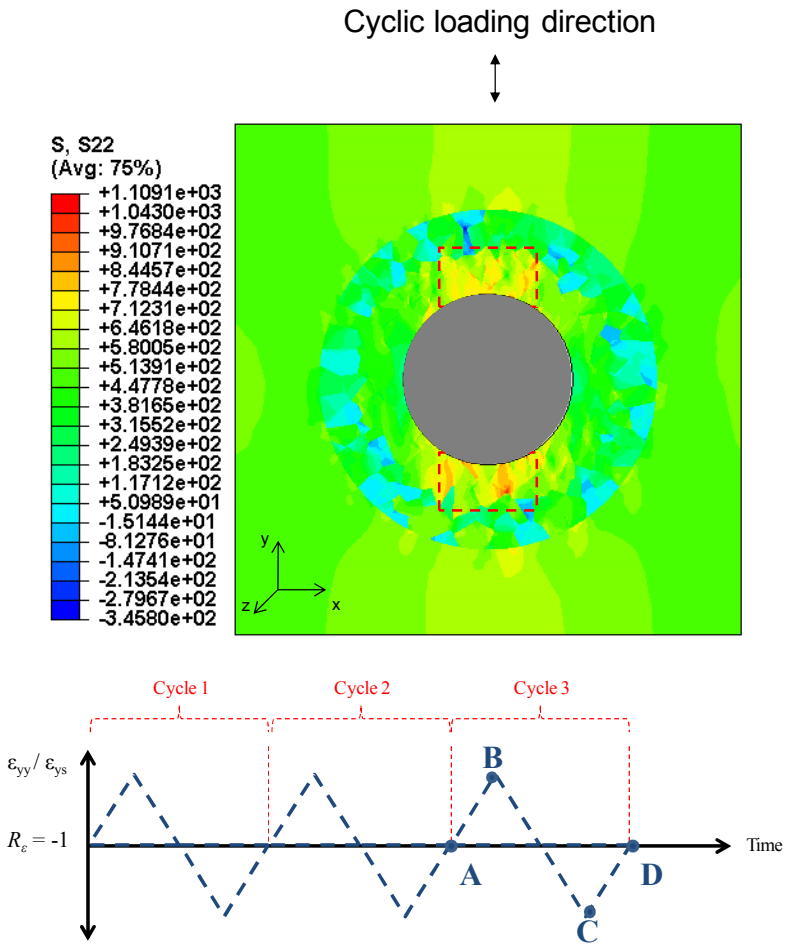

Figure 4-2: yy stress contours of a intact, perfectly bonded inclusion plotted at point A ($\varepsilon_{ys} = 0.7$ %; $R_\varepsilon = -1$).

The grains that produce the highest magnitudes of P_T were most frequently located at these sites, as marked with "+" and "o" symbols in Figure 4-3.

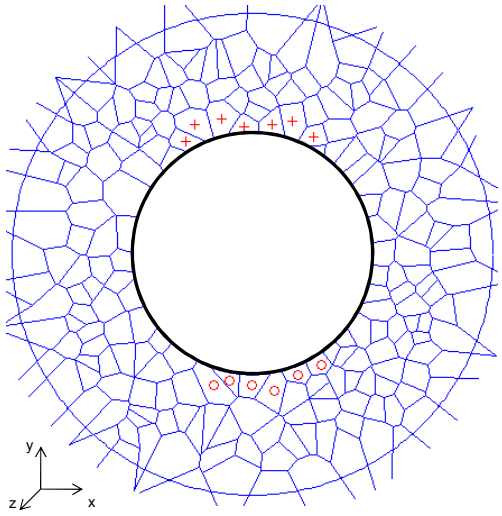

Figure 4-3: Grains for the FIP averaging regions at the north and south poles of the inclusion.

The empirical cumulative distribution functions (CDFs) of extreme value nonlocal P_T parameter are plotted in black symbols in Figure 4-4 for $\varepsilon_{yy} = 0.5\ \varepsilon_{ys}$ and $R_\varepsilon = -1$. These CDFs represent $c_R^{\omega=0.5}(P_T)$. The red dashed line represents the simulated $C^{\omega = 0.5}(P_T)$ (see Eq. 4.4) for the inclusion radius distribution shown in Figure 4-5. The dashed lines in Figure 4-5 correspond to inclusion sizes that are out of the range examined in the simulations of this thesis.

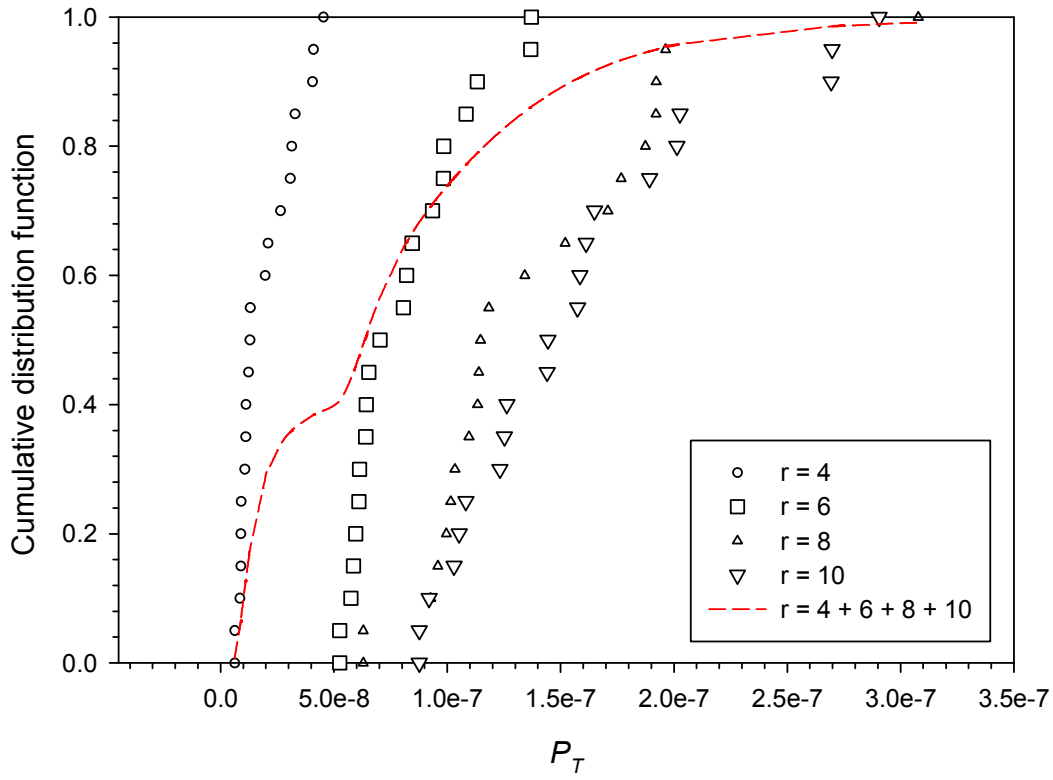

Figure 4-4: CDFs of extreme value nonlocal P_T parameter.

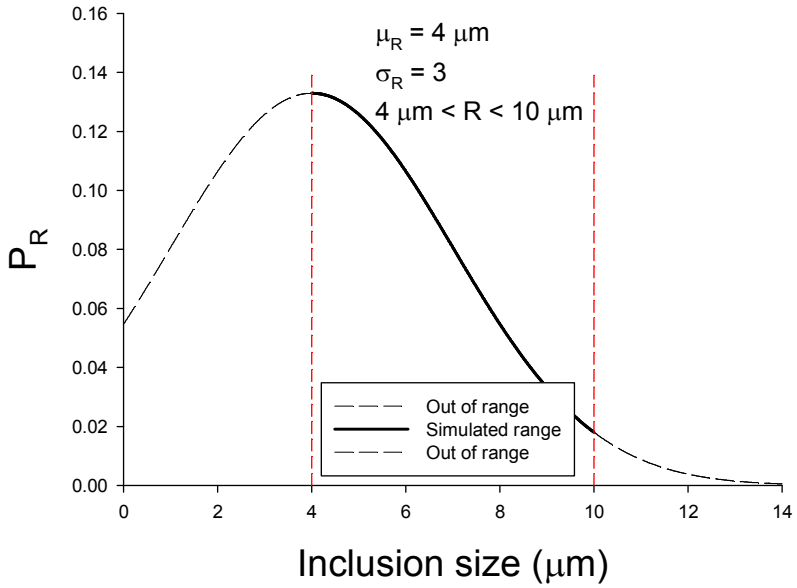

Figure 4-5: Inclusion radius distribution. Out of the range examined in the simulations of this thesis.

The simulated $C^{\omega}(P_T)$ distributions are shown in Figure 4-6 for the applied strain amplitudes ω = 0.5, 0.6, 0.7, and 0.8. The experimental data needed to calibrate the material-specific threshold parameter P_T^* are lacking. As such, to estimate P_T^*, we assume that the applied uniaxial strain amplitude of ω = 0.8 is high enough such that, 95% of all inclusions debond. This can, of course, be modified to accord with available experimental observations. We can then estimate P_T^* by solving $C^{\omega=0.8}\left(P_T^*\right)=0.05$.

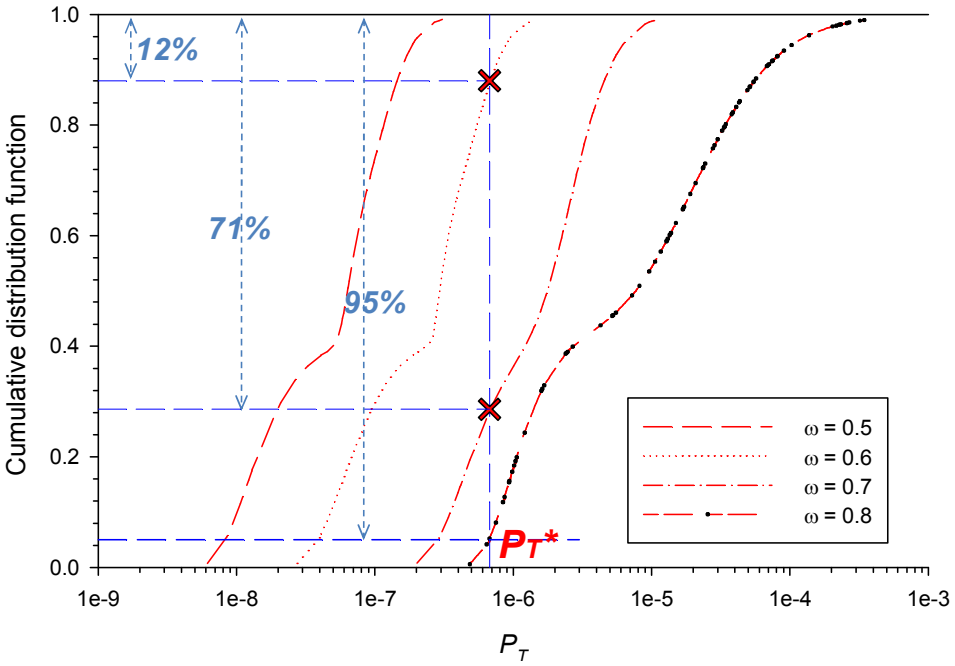

Figure 4-6: Simulated C^{ω} and estimation of P_T^*.

We are now able to solve Eq. 4.3 to obtain P_{debond}^{ω} at the applied strain amplitudes ω = 0.5, 0.6, 0.7, as 0%, 12%, and 71%, respectively. Figure 4-7 shows the

variation of P_{debond}^{ω} versus the applied macroscopic strain amplitudes. The following two-term power series is fit to the data using the maximum likelihood (MLE) [92] estimation method:

$$P_{debond}^{\omega} = 1.189 - 0.07478\omega^{-5.209} \tag{4.5}$$

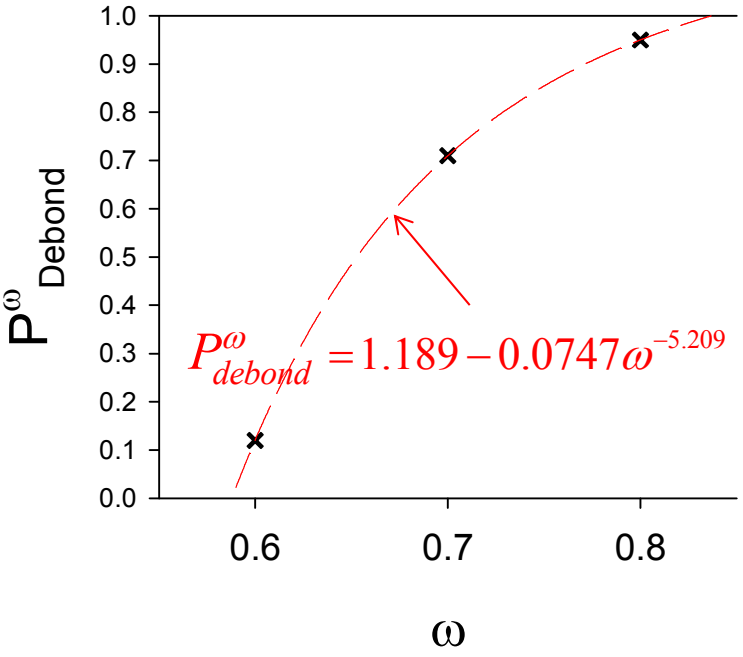

Figure 4-7: The variation of P_{debond}^{ω} versus the applied strain amplitude based on the P_T parameter.

Similarly, the computed cumulative distribution functions (CDFs) of extreme value nonlocal T_{int} parameter are plotted in Figure 4-8. These trends represent the simulated $C^{\omega}(T_{\text{int}})$ for ω = 0.5, 0.6, 0.7, and 0.8. The inclusion radius distribution is shown in Figure 4-5. Again, in order to estimate T_{int}^{*} for the case study in Chapter 7, we

assume that at ω = 0.8, 95% of all inclusions would likely debond. As such, we can estimate T_{int}^{*} by solving $C^{\omega=0.8}\left(T_{\text{int}}^{*}\right)=0.05$. Figure 4-9 shows the variation of P_{debond}^{ω} versus the applied strain amplitude. The following linear fit to the data is obtained using the maximum likelihood (MLE) [92] estimation method:

$$P_{debond}^{\omega}=2.28\omega-0.837 \tag{4.6}$$

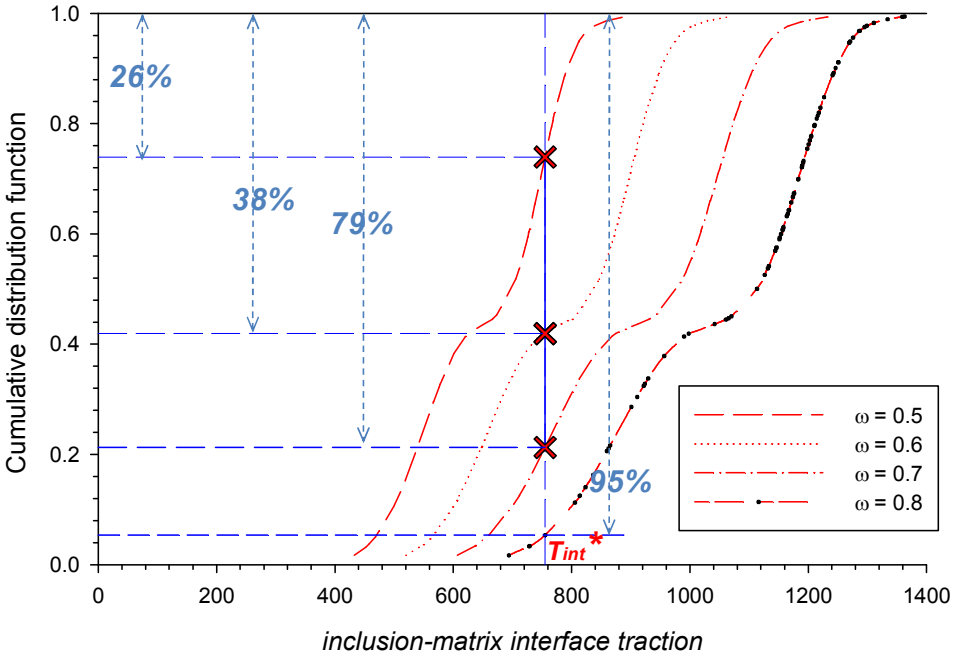

Figure 4-8: CDFs of extreme value nonlocal T_{int} parameter.

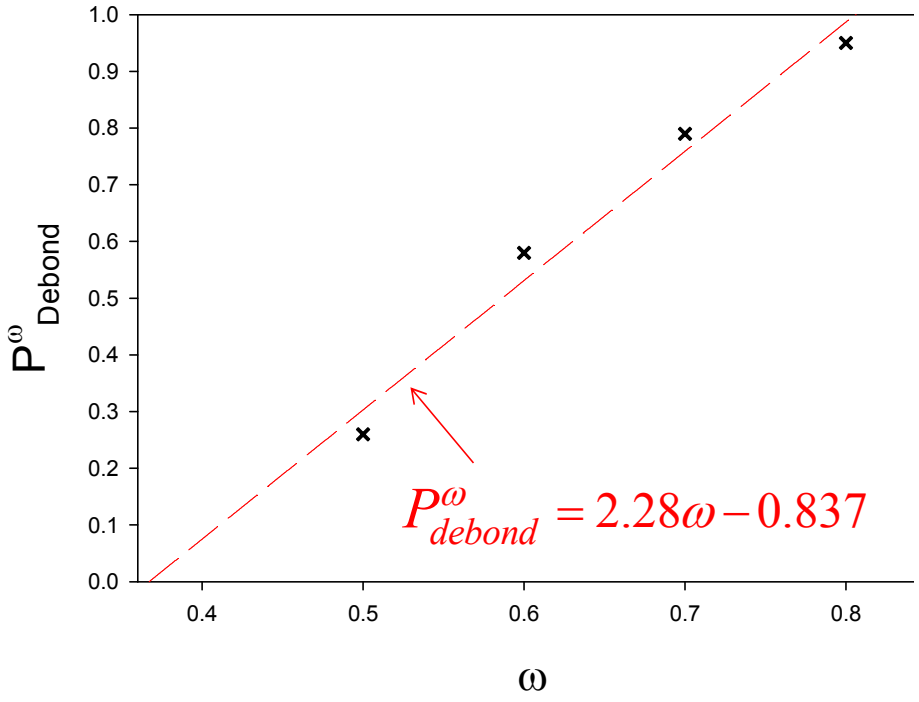

Figure 4-9: The variation of P^{ω}_{debond} versus the applied strain amplitude based on the T_{int} parameter.

4.4 Summary

Inclusion-matrix interface debonding is mainly due to the residual stresses resulting from prior processing. Most inclusions could be already debonded before the application of cyclic loading. Nevertheless, Even if a small percentage of inclusions debond during fatigue loading, this percentage decreases as the cyclic stress/strain amplitude decreases. Thus, this mechanism decreases the surface initiation probability.

The modified interface traction parameter, P_T, is used as an indicator for assessing the driving force for the inclusion-matrix interface separation. The north and south poles of the inclusion (aligned with the loading direction) are the two most likely regions for inclusion-matrix interface separation for all polycrystalline orientation distributions studied. Based on the cumulative distribution function of the extreme value P_T parameters, the probability of inclusion-matrix debonding is expressed as a function of the applied strain amplitude, $\varepsilon_{yy}/\varepsilon_{ys}$. This expression will be used to account for the effect of inclusion-matrix debonding on the change in the ratio of probabilities of surface to bulk fatigue crack initiation in Chapter 7.

5 Residual stress relaxation at primary inclusions and pores

5.1 Motivation

The dependence of surface fatigue crack initiation probability, p_s, on the stress amplitude can be partially due to the retention of beneficial residual stresses. The reasoning is based on two well-established phenomena:

1. Compressive stresses reduce the propensity of cracks to initiate at surface inclusions in PM processed Ni-base superalloys [129, 130].
2. Cyclic strains and overstrains can eliminate compressive stresses [131-135]. The residual stresses can relax significantly due to mechanical loading even under normal operating conditions.

As such, for a given R ratio and as the stress amplitude decreases, compressive residual stresses might not relax at some of the inclusions even though these stresses would otherwise relax at the higher stress amplitudes. These compressive residual stresses can effectively suppress fatigue crack initiation at some of the inclusions.

In Chapter 6, we will further discuss and mathematically formulate this effect. In this Chapter, we use a simulation-based approach to examine the residual stresses around idealized inclusions and pores. The relaxation of these stresses due to cyclic loading is also studied for several cyclic uniaxial strain amplitudes and initial residual stress values.

5.2 Introduction

Compressive residual stresses induced by mechanical surface treatments such as shot peening, laser shock peening, autofretage, hole expansion, and low-plasticity burnishing can be highly beneficial to fatigue resistance [131]. In general, such processes have shown potential to reduce crack initiation at surface inclusions in PM processed Ni-base superalloys [129, 130]. In implementing these processes, various issues should be considered, including:

1. Harmful tensile residual stresses are present in the interior of surface-treated specimens as a consequence of the compressive residual stresses that are applied near the surface to maintain static equilibrium. This can result in higher mean strain and stress at bulk inclusions during fatigue cycling.
2. To suppress cracking at large surface inclusions, cost-efficient surface treatment processes such as shot peening may produce so much cold work, lapping, and other material damage near the surface as to override the benefits of compressive residual stresses. Alternative surface enhancement processes such as low plasticity burnishing [134] should be assessed in such situations. These processes potentially offer compressive residual stresses to a greater depth and with less cold work than shot peening, but they can be more costly.
3. Some surface treatment processes such as shot peening and laser shock peening can break up the inclusions, producing inclusion clusters, having lengths up to twice the maximum lengths of the original inclusions [136, 137]. Theses inclusion

clusters can be more critical than the original inclusions if their relative placement results in enhanced potency for fatigue crack formation and growth.

4. Thermal relaxation can greatly reduce the magnitude and beneficial effects of the compressive residual stresses [134, 138-140]. Such effects are not examined in this study, since our objective is the study of surface to bulk transition as the applied stress/strain amplitude decreases.

In addition to thermal loading, cyclic loading is believed to eliminate compressive stresses [131-135]. Mattson and Coleman [141] were among the first researchers who reported cyclic residual stress relaxation, as shown in Figure 5-1.

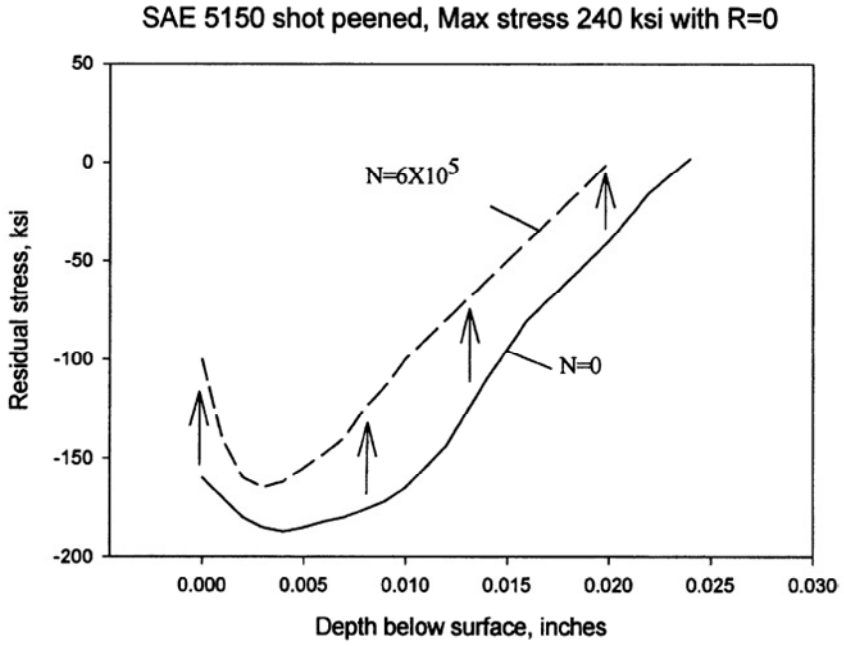

Figure 5-1: Residual stress relaxation before and after cyclic loading at room temperature [141].

Extensive research efforts were undertaken to predict the dependence of residual stress relaxation on the magnitude and distribution of the residual stress, the degree of cold work, the applied alternating and mean stresses, and the number of applied loading cycles. Morrow and Sinclair [142] conducted strain-controlled fatigue tests and proposed a relationship between mean stress and load cycle, i.e.,

$$\frac{\sigma_m^N}{\sigma_m^1} = \frac{\sigma_y - \sigma_a}{\sigma_m^1} - \left(\frac{\sigma_a}{\sigma_y}\right)^b \log(N) \tag{5.1}$$

where $\sigma_m{}^N$ is the mean stress at the Nth cycle, $\sigma_m{}^1$ is the mean stress at the first cycle, σ_a is the alternating stress amplitude, σ_y is the material yield strength, and b is a constant dependent on material softening and applied strain range $\Delta\varepsilon$.

Following Morrow's work, it has been commonly accepted that residual stress effects on fatigue can be assessed by the relaxation of the mean stress [133]. For instance, Jhansale and Topper [143] proposed a logarithmic linear relationship between mean stress relaxation against axial strain-controlled cycles. Alternative equations have also been proposed based on the relaxation of the surface residual stress instead of mean stress value [144].

Figure 5-2 shows the relaxation of compressive residual stresses due to cyclic strains in the experimental studies of Barrie *et al.* [129] on subsolvus PM processed seeded Udimet® 720.

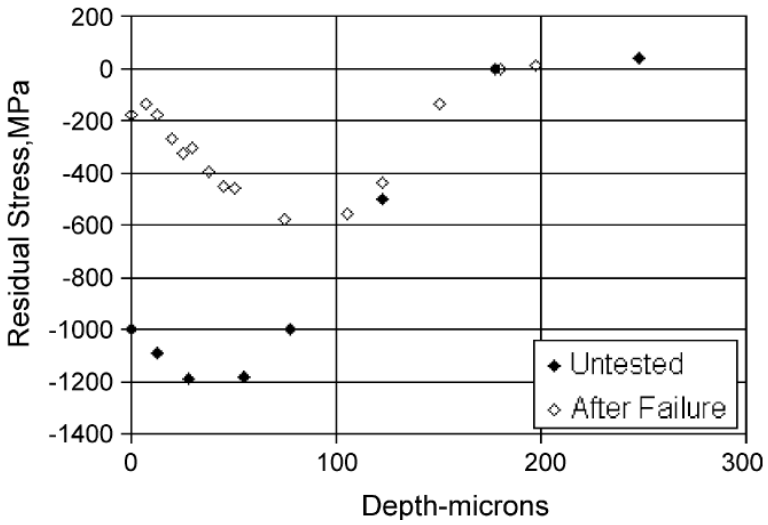

Figure 5-2: Axial residual stresses of shot peened PM processed Udimet® 720 specimen before and after testing at T = 650°C, $\Delta\varepsilon_t$ = 0.8% and R_ε = 0; N_f is not mentioned for this specific case but should be around 10^4 [129].

The rate of residual stress relaxation depends strongly on mean stress and stress amplitude among other factors, as shown in the numerical predictions of Figure 5-3.

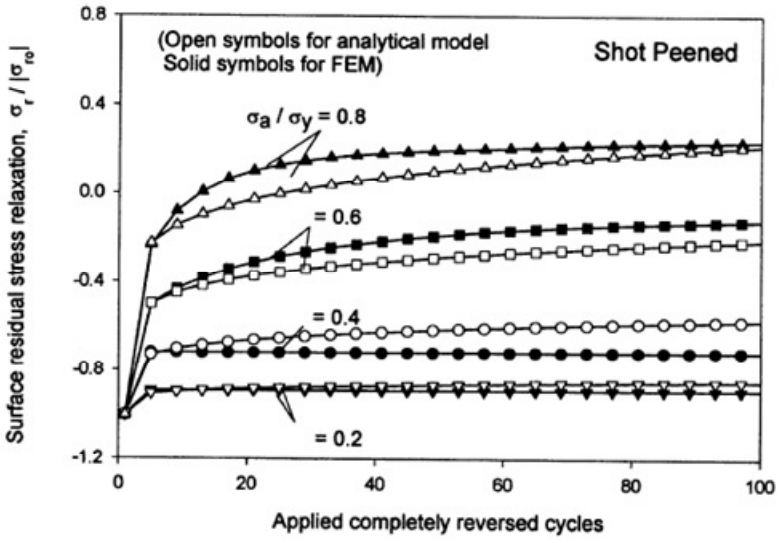

Figure 5-3: Effect of stress amplitude on residual stress relaxation (R_σ = -1) [131].

Despite considerable research [145], there is insufficient experimental knowledge concerning the effect of fatigue cycling on residual stresses around inclusions and pores because:

1. There remains the technical challenge of accurately measuring the residual stress relaxation and redistribution under cyclic mechanical and thermal load [146].
2. Residual stresses and their relaxation behavior are expected to differ around inclusions and pores.

To that end, there is considerable interest in predictive models for the state and relaxation of residual stresses [147, 148]. Computational modeling such as finite element analysis offers a useful platform to investigate the effects of process history (including residual stresses) on the fatigue resistance of components [78].

5.3 Simulation-based methodology for imposing the residual stresses

In this Chapter, we adopt a simulation-based approach to study the degree of local residual stress relaxation around primary inclusions and pores. In this approach, a uniform state of equiaxial compressive stress is imposed prior to fatigue simulations using a simplified yet practical methodology developed by Prasannavenkatesan *et al.* [78, 149]. The use of this methodology is justified because:

- We seek to qualitatively compare the degree of residual stress relaxation under several applied uniaxial strain amplitudes ($R_\varepsilon = -1$) and for several initial residual stress values in order to draw conclusions regarding the dependency of the number of fatigue hot spots (referred to as Ψ in this thesis) on the applied strain amplitude. In lieu of the comparative nature of our study, the inherent inaccuracies of this simplified approach are not significant.
- Common mechanical surface treatment processes produce a state of residual stress that does not vary significantly over a domain of the order of primary inclusion size in fine grained PM processed Ni-base superalloys.
- Parameters for equations of residual stress relaxation such as Eq. 5.1 are lacking for the material of this study.

We summarize this simplified approach in the following. A detailed explanation of this approach is given in [78, 149] and the references therein. It should be noted that this simplified approach imparts an equiaxial state of compressive residual stress that may exist in a subsurface region due to a variety of mechanical surface treatments.

Therefore, it is not limited to simulations of a specific process, e.g., shot peening. Also, changes to the material properties (crystal plasticity model parameters), due to the peening process, are neglected in this study.

A subsurface element is considered which is small enough, relative to the gradient of the residual stress field along the specimen depth, that a uniform distribution of residual stress can be assumed over its domain, as shown in Figure 5-4.

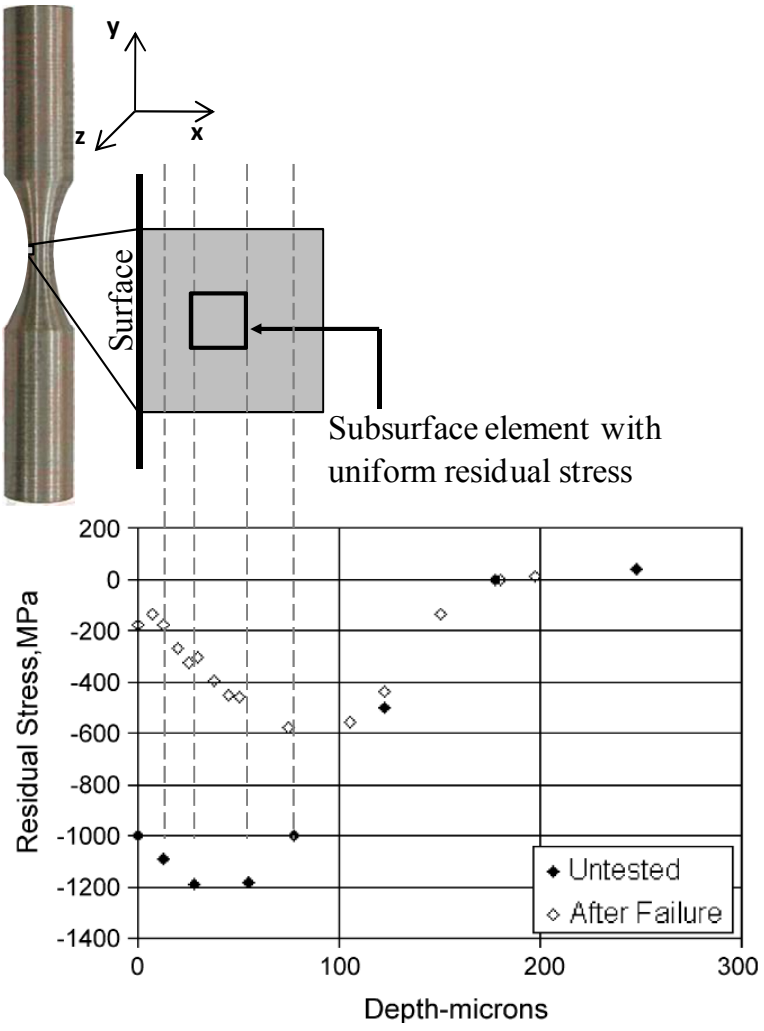

Figure 5-4: A subsurface element with uniform compressive residual stresses [78, 131, 149]. Failure is defined as fracturing the specimen.

A uniform state of equiaxial residual stress over a subsurface domain is imparted by a two step strain-controlled (ε_{xx}^{load} and ε_{xx}^{final}) loading in the depth direction, as shown in Figure 5-5 for the 2.5D case. The following direction convention holds for all subsequent calculations:

- Direction of impact (shot peening) – along the x direction
- Equibiaxial residual stress state – along y and z directions
- Cyclic loading – along the y direction

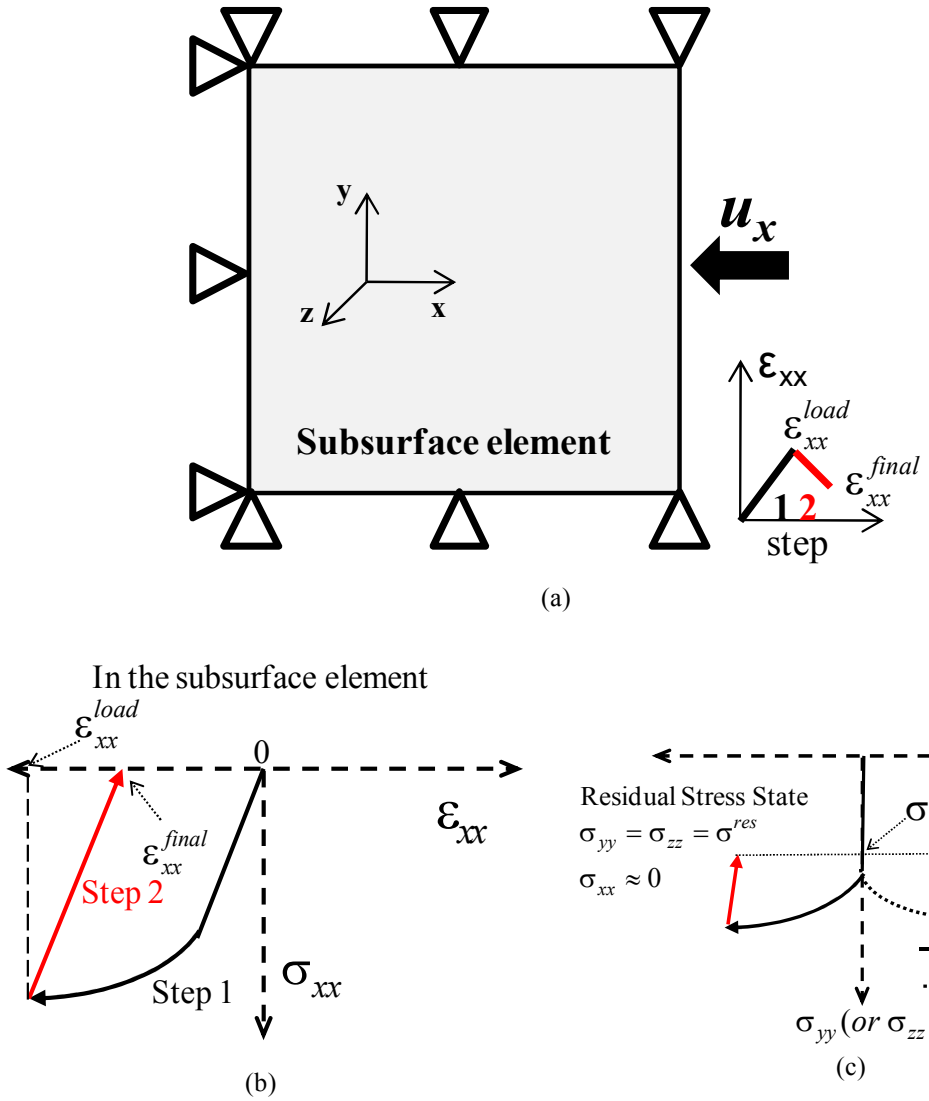

Figure 5-5: (a) Boundary conditions for imparting the equiaxial state of stress (b) two step compression in the x direction, (c) strain variation in the subsurface element [78, 149].

For a simple initially homogenous material model with pure nonlinear kinematic hardening, a closed form solution to the magnitude of compressive strains, ε_{xx}^{load} and ε_{xx}^{final}, is derived in terms of the magnitude of residual stress by Zhang *et al.* [149]. However, due to the intricacies of the IN100 crystal plasticity material model, the strains ε_{xx}^{load} and ε_{xx}^{final} are estimated iteratively in this section using incremental polycrystal

plasticity calibrated to the macroscopic stress-strain response of IN100 Ni-base superalloys (see Section 2.4.3). For imposing the residual stress, the following boundary conditions are enforced (shown in Figure 5-6 (a)):

1. The x-symmetry boundary condition ($u_x = 0$) is enforced for the entire length of the model's left edge (x = -L/2 and -L/2 < y < L/2).
2. The y-symmetry boundary condition ($u_y = 0$) is enforced for the entire length of the model's top and bottom edges (y = -L/2, L/2 and - L/2 < x < L/2).
3. The z-symmetry boundary condition ($u_z = 0$) is enforced to the reference point of the GPS model.

Upon application of compressive residual stresses, cyclic simulations are performed to calculate and compare FIPs for the case without initial compressive residual stresses. For the cyclic loading simulations, the boundary conditions are relaxed such that assuming the origin of the xyz coordinate system is at the center of the inclusion/pore (shown in Figure 5-6 (b)):

1. The traction free boundary condition is enforced for the entire length of the model's left and right edges (x = -L/2, L/2 and -L/2 < y < L/2).
2. The y-symmetry boundary condition ($u_y = 0$) is enforced for the entire length of the model's bottom edge (y = -L/2 and - L/2 < x < L/2).
3. The z-symmetry boundary condition ($u_z = 0$) is enforced to the reference point of the GPS model.

4. Cyclic uniaxial displacement is applied to the entire length of the model's top edge (y = L/2 and - L/2 < x < L/2).

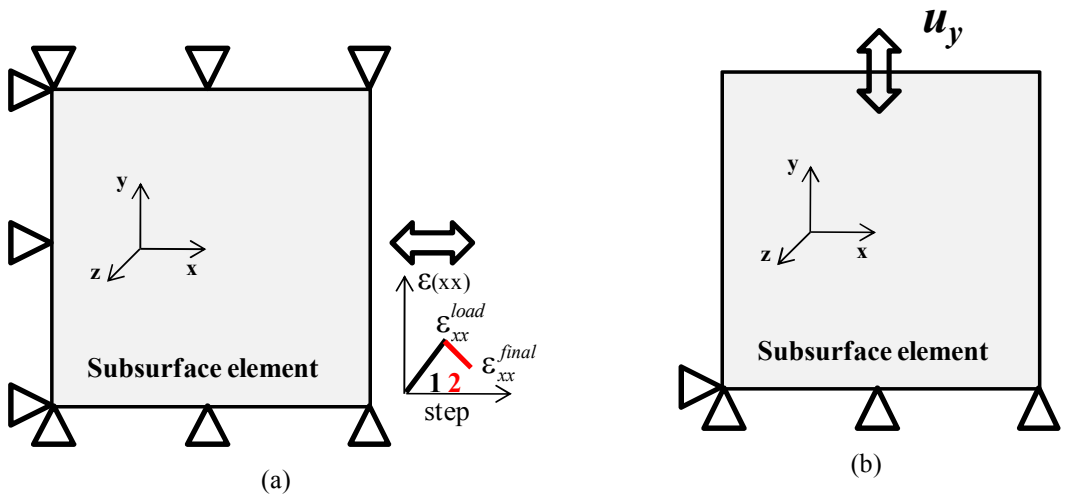

Figure 5-6: Loading and boundary conditions: (a) imposing an equiaxial state of stress and (b) subsequent cyclic loading.

5.4 Imposing the compressive residual stresses without inclusion or pores

The finite element simulations utilize two-dimensional generalized plane strain (GPS) elements [49] (see Section 2.4.1), often referred to as 2.5D, and the fully 3D crystal plasticity material model (see Section 2.1.2). The crystal plasticity material model constants and microstructure parameters are listed in Table 3 and Table 4, respectively. The full model, shown in Figure 5-7, is utilized to mitigate any boundary effects. Grains are randomly oriented, and each grain is meshed with 10-20 quadratic triangular elements of type CPEG6M (see Section 2.1.2), using the reduced integration algorithm.

While the strains ε_{xx}^{load} and ε_{xx}^{final} are applied in terms of displacement to the right edge (i.e., x = L/2) of the model to achieve a uniform strain rate of 0.001 s^{-1}, all stress and strain components are averaged over a circular averaging area with the radius of 10 μm (see Figure 5-7). This averaging area consists of about 100 grains. The averaged *yy* stress component, σ^{*}_{yy}, upon the completion of ε_{xx}^{final} is considered as the imposed residual stress, σ^{res}. The magnitude of σ^{*}_{yy} turns out to be different than the averaged *zz* stress component, σ^{*}_{zz}, mainly because:

1. Two-dimensional generalized plane strain idealization is used. Out-of-plane shear deformation is not included in the element formulation.
2. Grains are randomly oriented, and fully anisotropic material properties are assigned to them.

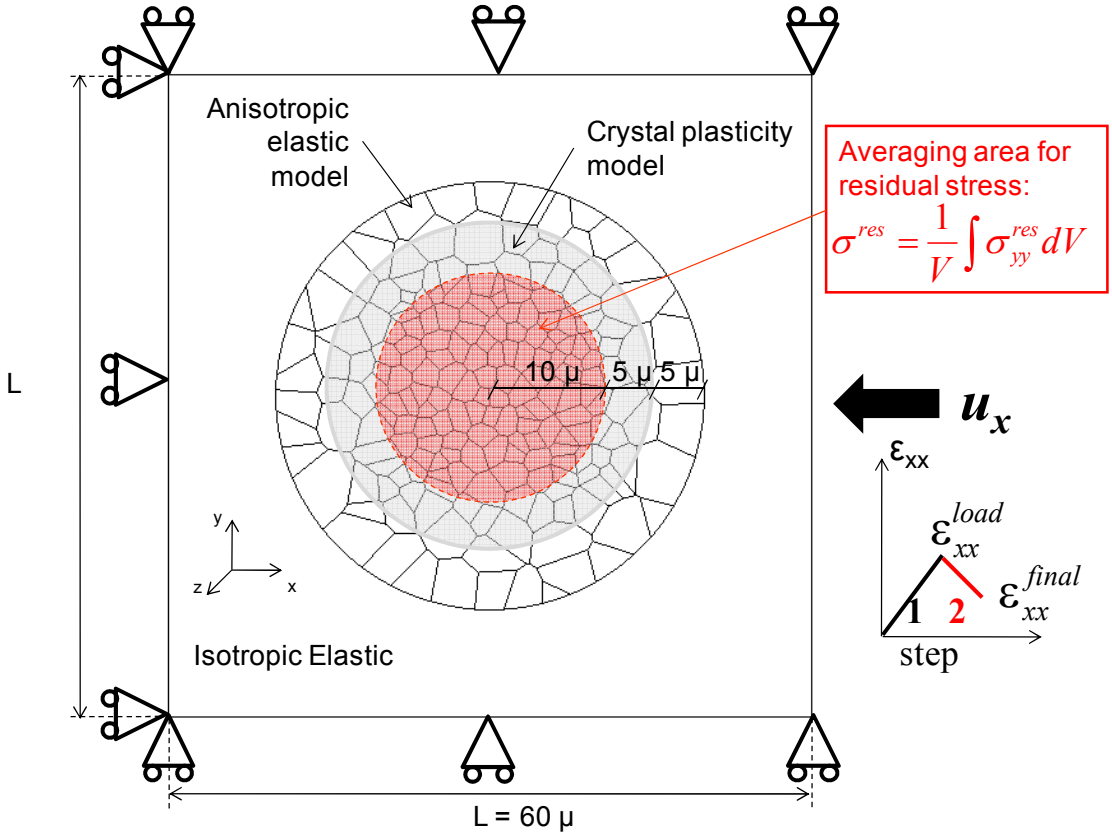

Figure 5-7: Full FE model for prediction of ε_{xx}^{load} *and* ε_{xx}^{final}.

Several pairs of values for ε_{xx}^{load} and ε_{xx}^{final} are tested, amongst which cases A, B, and C (see Table 1) are chosen for further analysis. The imparted σ^{res} values for cases A, B, and C correspond to experimentally measured residual stresses of shot peened PM processed Udimet® 720 [129] (see Figure 5-2) below the surface to the bulk transition depth, d_t = 100 μm, as suggested by de Bussac [121] (see Figure 6-13). Here, simulating the residual stress distribution with depth is not of primary importance, and the exact depths corresponding to cases A, B, and C are not the key issue here. The key issue is that fatigue crack initiation origins at these depths are considered to be surface-originated.

Table 8: The imposed σ^{res} values for cases A, B, and C.

Case Pointer	ε_{xx}^{load}	ε_{xx}^{final}	σ^{res} (σ^{res}_{yy})
	0.02	0	-400 MPa
A	**0.02**	**0.01**	**-900 MPa**
	0.03	0	-650 MPa
B	**0.03**	**0.005**	**-1070 MPa**
C	**0.02**	**0.015**	**-1170 MPa**
	0.03	0.01	-1400 MPa

Figure 5-8 shows the contours of σ_{yy} upon the completion of ε_{xx}^{final} in the circular averaging area, where $\varepsilon_{xx}^{load} = 0.03$ and $\varepsilon_{xx}^{final} = 0$. The σ_{yy} stress component appears to be fairly evenly distributed throughout this area, suggesting that its average, σ^{res}, is relatively independent of the microstructure realization. Still, multiple microstructure realizations were considered in estimating the shot peening strain levels required to match the measured initial residual stress. The Voronoi tessellation diagram and polycrystalline orientation distribution vary across these realizations. Virtually equivalent values of σ^{res} were obtained, indicating that the polycrystalline aggregates, typically consisting of about 100 grains, are sufficiently large to be considered as RVE for the purposes of estimating residual stresses.

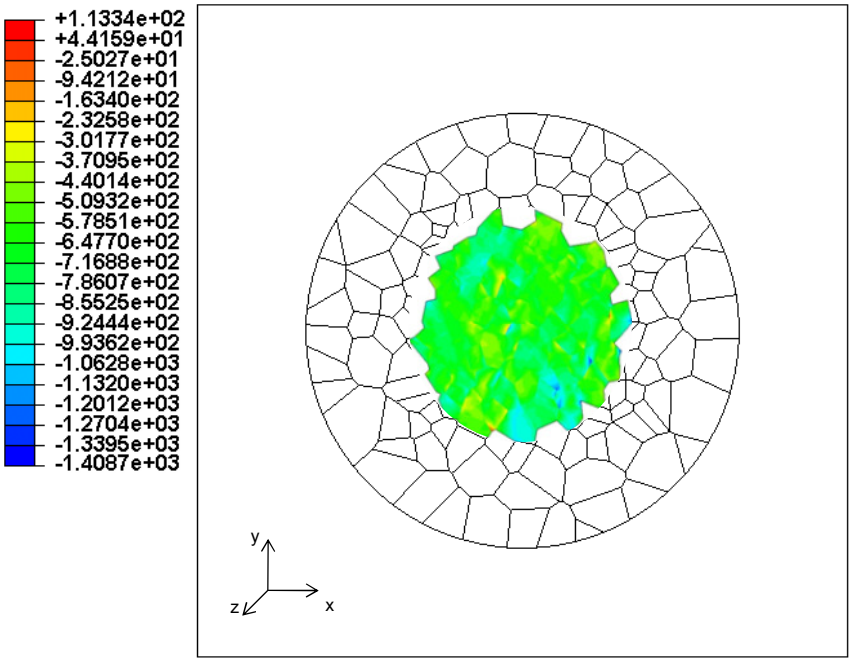

Figure 5-8: Contours of σ_{yy} upon the completion of ε_{xx}^{final} ($\varepsilon_{xx}^{load} = 0.03$ and $\varepsilon_{xx}^{final} = 0.03$).

Figure 5-9 shows the variation of σ^*_{yy} versus the elastic, $\varepsilon^*_{yy,el}$, and plastic, $\varepsilon^*_{yy,pl}$, parts of the averaged total *yy* strain component, ε^*_{yy}, while the strains $\varepsilon_{xx}^{load} = 0.02$ followed by $\varepsilon_{xx}^{final} = 0.01$ are applied by displacing the right edge (i.e., x = L/2) of the model.

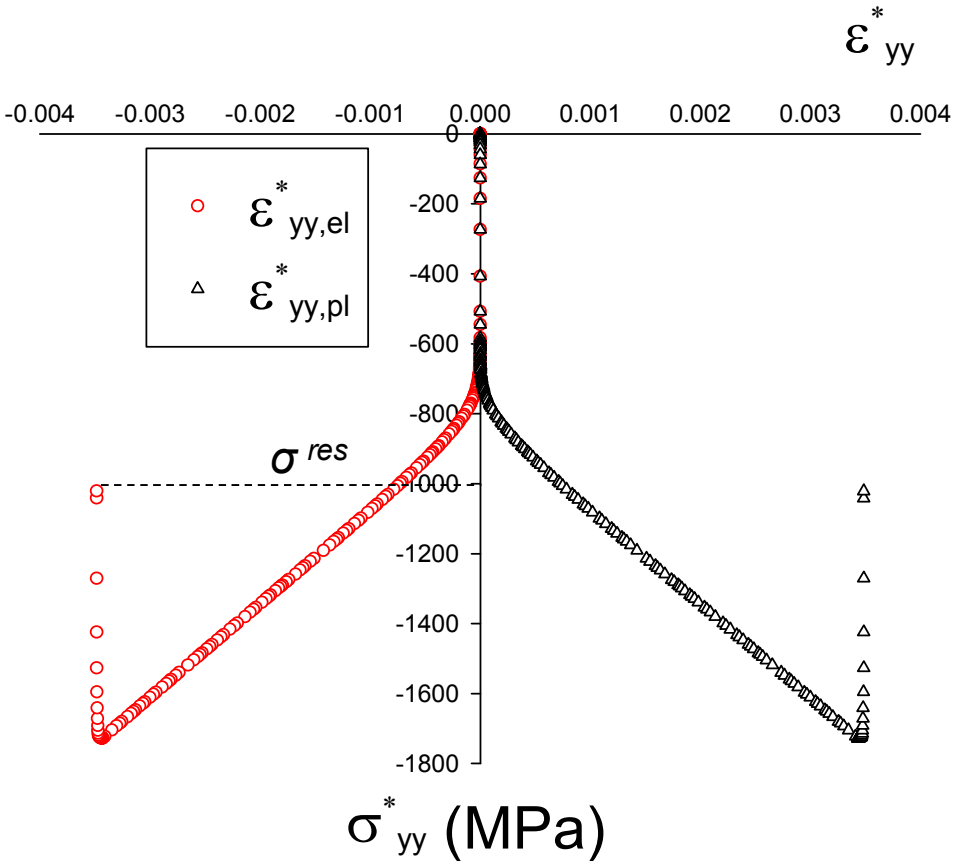

Figure 5-9: Variation of σ^*_{yy} vs. $\varepsilon^*_{yy,el}$ and $\varepsilon^*_{yy,pl}$ (ε_{xx}^{load}= 0.02 & ε_{xx}^{final} = 0.01).

5.5 The influence of an embedded inclusion/pore

The imparted residual stresses are different in the local neighborhood of an inclusion or a pore. To study the inclusion effect, we simulate inclusions that are assumed to be already debonded at the beginning of the shot peening process as a means of assessing their influence on the local residual stress state and the fatigue crack formation potency. In simulations with partially debonded inclusions, contact between the interacting surfaces is assumed to be frictionless.

Pores and partially debonded inclusions with radii R = 4, 6, 8, and 10 μm are embedded in the full FE model, as shown in Figure 5-10. Except for the embedded inclusion/pore, this model is similar to the one shown in Figure 5-7. Properties assigned for the fully isotropic elastic inclusion include Young's modulus E^i = 400 GPa and Poisson's ratio ν^i = 0.3.

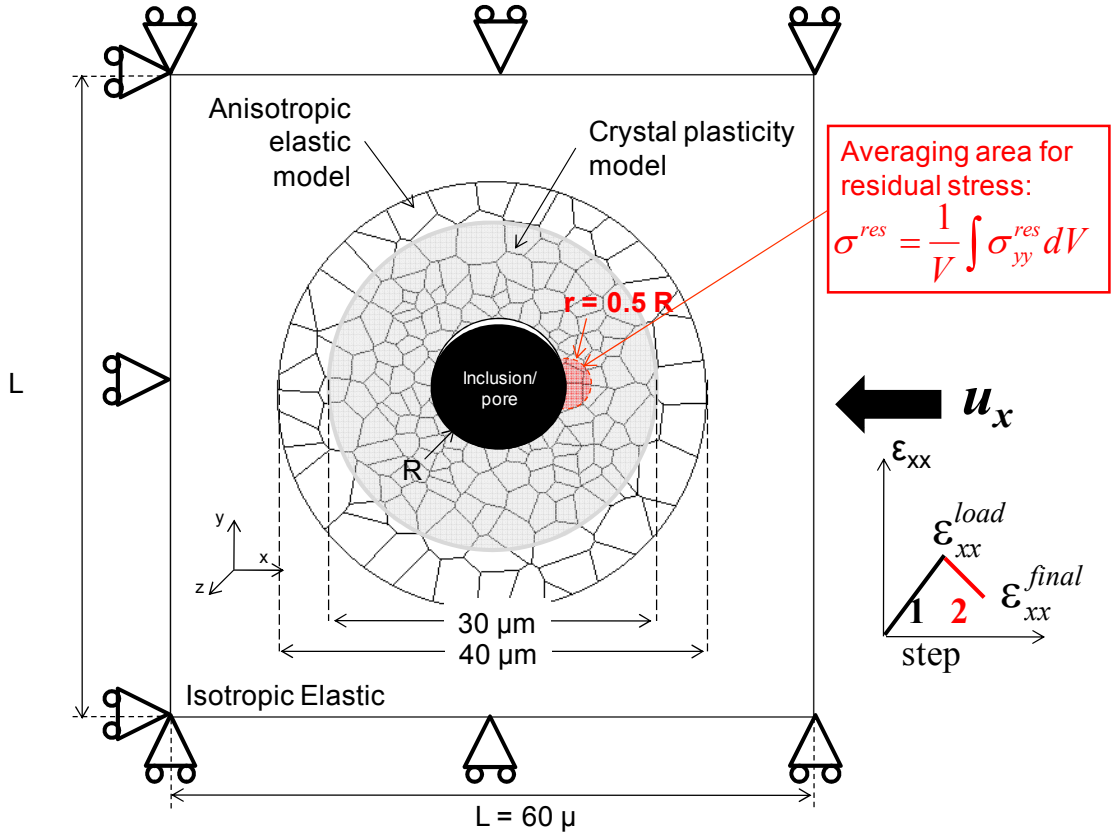

Figure 5-10: The application of ε_{xx}^{load} *and* ε_{xx}^{final} in the full FE model with embedded inclusion/pore.

Figure 5-11 shows the contours of local σ_{yy} (computed at the element integration points) upon the completion of ε_{xx}^{final} in the crystal plasticity modeled region. A partially debonded inclusion and a pore with radii R = 6 μm were embedded in Figures 5-11 (a) and (b), respectively. Figures 5-12 (a) and (b) show the same contour plots for a partially debonded inclusion and a pore with radii R = 10 μm. The grey-colored contours in both figures correspond to the regions where the absolute value of the residual stresses exceeds 80% of the absolute value of the reference residual stress value for the case without an embedded inclusion/pore (i.e., $\sigma_{yy} \geq 0.8 \cdot \sigma_{ref}^{res}$; $\sigma_{ref}^{res} = 1170\ MPa$ for case C). In this region, the beneficial compressive residual stresses are comparable to the case

without an embedded inclusion/pore. Thus, we can say this region has not been negatively affected by the presence of inclusion/pore.

The red-colored contours correspond to the regions where the absolute value of the residual stresses is less than 50% of the absolute value of the reference residual stress value (i.e., $\sigma_{yy} \le 0.5 \cdot \sigma_{ref}^{res}$; $\sigma_{ref}^{res} = 1170\ MPa$). In this region, we have significant loss of beneficial residual stress due to the presence of inclusions/pores.

As seen in these contour plots, pores result in a more widespread decrease in the beneficial residual stress. Figure 5-12 (b) shows that the affected region is larger as the pore size increases, whereas, increasing the radius of the partially debonded inclusion decreases the size of the red-shaded area.

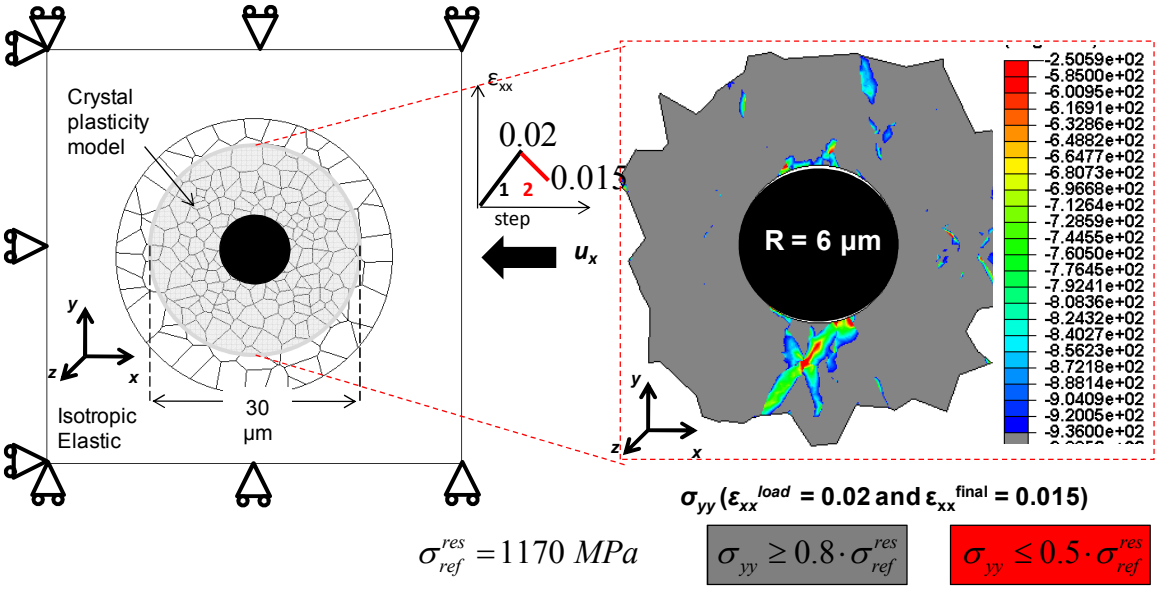

(a)

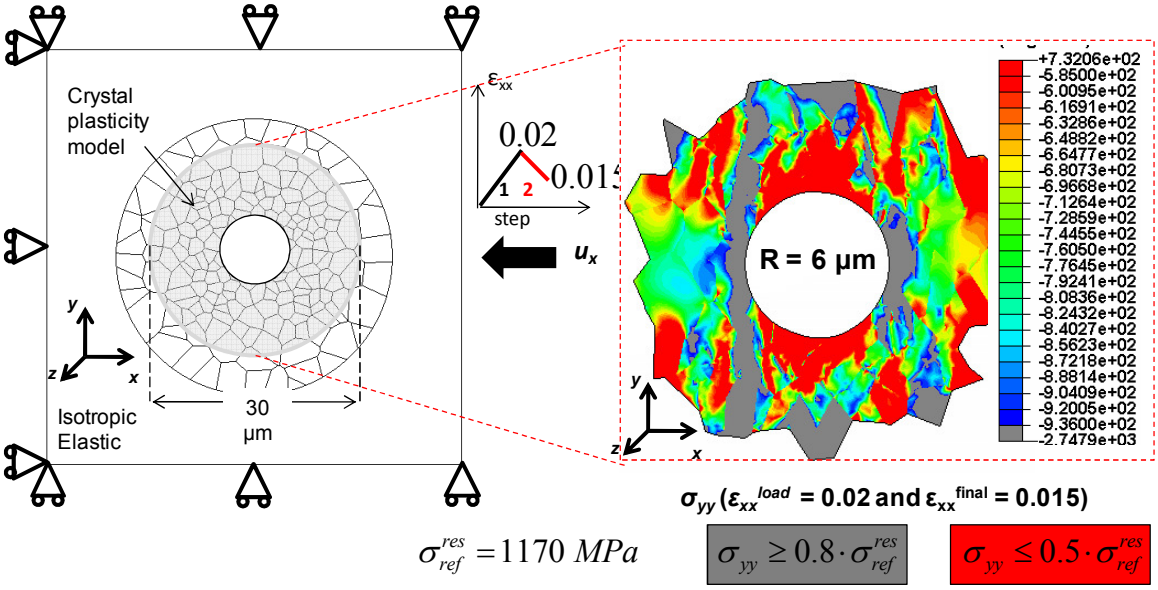

(b)

Figure 5-11: Contours of σ_{yy} at the completion of ε_{xx}^{final}, (a) debonded inclusion and (b) pore (case C, R = 6 μm).

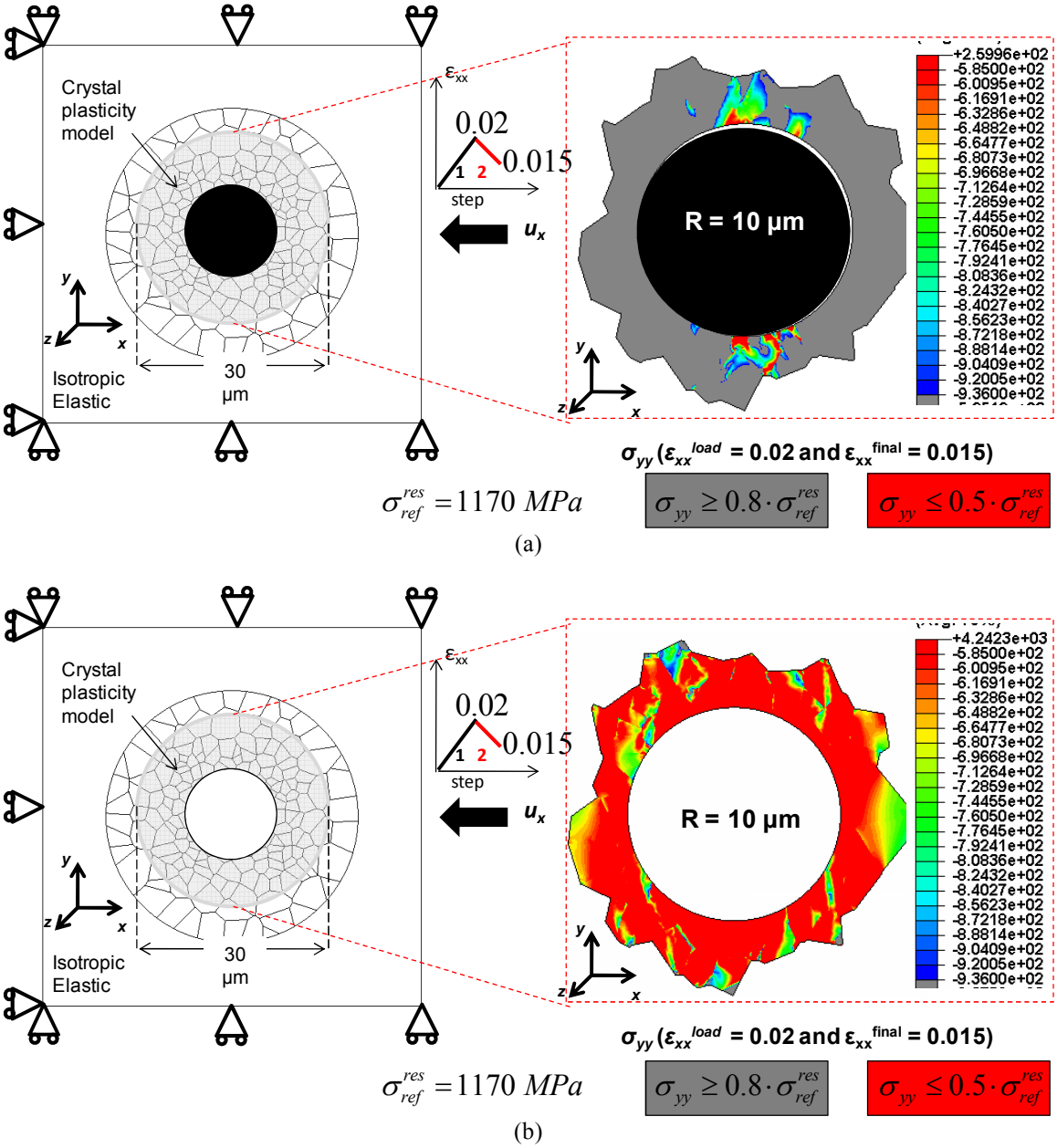

(a)

(b)

Figure 5-12: Contours of σ_{yy} at the completion of ε_{xx}^{final}, (a) debonded inclusion and (b) pore (case C, R = 10 μm).

To study the change in the residual stresses at the inclusion/pore notch root due to presence of an inclusion/pore, a semicircular region with radius r = R/2 (R = inclusion/pore radius) is used as the residual stress averaging area. The averaging region

is located in the slip-intensified region of the inclusion/pore notch root (see Figure 5-10). This averaging region contains 3 ~ 4 grains for the smallest inclusion/pore examined, i.e., R = 4 μm. At R = 10 μm, it comprises 15 ~ 20 grains. Examining a statistically representative number of simulations is crucial for the embedded inclusion/pore case because the averaging region is smaller than that of the case with no inclusion/pore (see Figure 5-7). The nonlocal residual stress value is obtained by averaging σ_{yy} over this area upon the completion of ε_{xx}^{final}:

$$\sigma_{yy}^{res} = \frac{1}{V}\int \sigma_{yy} dV \tag{5.2}$$

The strains ε_{xx}^{load} and ε_{xx}^{final} from cases A, B, and C (see Table 8) are examined for the partially debonded inclusion. For brevity, only case C is considered for pores. Ten different polycrystalline orientation distributions (realizations) are simulated for each loading case and inclusion/pore size. The Voronoi tessellation diagram is the same and only grain orientations vary across these realizations. Table 9 lists median nonlocal imparted σ_{yy}^{res} values across simulated polycrystalline orientation distributions (realizations) for embedded inclusions and pores. A modest variation between different realizations is observed.

Table 9: Median imparted σ_{yy}^{res} values across simulated polycrystalline orientation distributions (realizations) for embedded inclusions and pores.

Inclusion					
R →		4 μm	6 μm	8 μm	10 μm
Residual stress case	A	-1328 (MPa)	-1384 (MPa)	-1546 (MPa)	-1670 (MPa)
	B	-1334 (MPa)	-1359 (MPa)	-1588 (MPa)	-1702 (MPa)
	C	**-1456 (MPa)**	**-1480 (MPa)**	**-1701 (MPa)**	**-1790 (MPa)**
Pore					
R →		4 μm	6 μm	8 μm	10 μm
	C	**-1368 (MPa)**	**-1001 (MPa)**	**- 733 (MPa)**	**- 539 (MPa)**

For case C, the median imparted σ_{yy}^{res} for the case with embedded inclusion/pore, highlighted in bold in Table 9, is normalized by the value corresponding to the case without an inclusion/pore (i.e., $\sigma_{ref}^{res} = 1170\ MPa$ for case C). We reiterate that for the case with an embedded inclusion/pore, the residual stress averaging area is a semicircular region with radius r = R/2 (R = inclusion/pore radius), located at the inclusion/pore notch root (see Figure 5-10). Whereas, for the case without an inclusion/pore, the residual stress averaging area is a circular area with the radius of 10 μm (see Figure 5-7). Figure 5-13 shows the variation in the ratio $\sigma_{yy}^{res} / \sigma_{ref}^{res}$ versus the inclusion/pore radius.

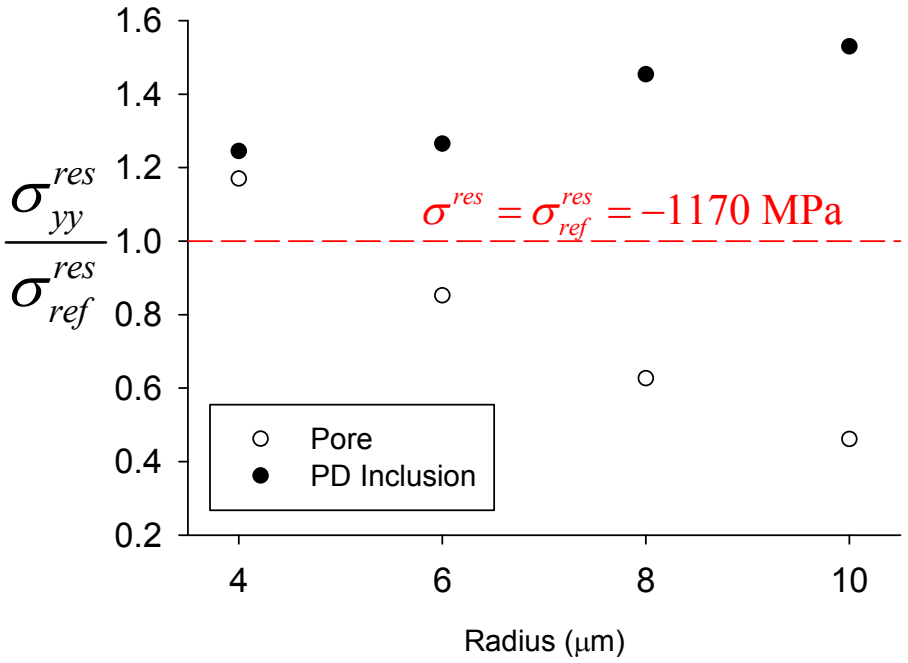

Figure 5-13: Variation in the ratio $\sigma_{yy}^{res} / \sigma_{ref}^{res}$ versus the inclusion/pore radius.

The embedded partially debonded inclusions (shown with filled symbols in Figure 5-13) seem to have a higher averaged (at their notch root) compressive residual stress than the case with no inclusions/pores. For instance, for a partially debonded inclusion with R = 10 μm, the compressive residual stress averaged at the inclusion notch root (over the semicircular region with radius r = 5 μm) is substantially more (~ 50%) than the reference compressive residual stress for the case with no inclusion/pore. Larger inclusions enhance the local compressive stresses by a higher percentage.

The embedded pores on the other hand can have mixed effects, whereby small pores have higher local compressive stresses relative to the case with no pores, and large pores decrease the local compressive stresses. Next, averaged residual stresses are

monitored for embedded inclusions and pores throughout the application of cyclic loading to explore the degree of their relaxation.

5.6 Applying the cyclic loading after shot peening

Upon achieving the target σ_{yy}^{res}, cyclic loading simulation is performed on the same FE model. The residual stresses imposed in the shot peening simulation serve as initial conditions for subsequent cyclic loading. For brevity, only the initial residual stresses of case C are examined. Moreover, for any simulated inclusion radius (R = 4, 6, 8 and 10 μm), only one polycrystalline orientation distribution is simulated. The examined realization has an initial σ^{res} value that is closest to the median of all the simulated polycrystalline orientation distributions (realizations). For the cyclic loading simulations, the boundary conditions are relaxed such that assuming the origin of the *xyz* coordinate system is at the center of the inclusion/pore:

1. The traction free boundary condition is enforced for the entire length of the model's left and right edges (x = -L/2, L/2 and -L/2 < y < L/2).
2. The y-symmetry boundary condition (u_y = 0) is enforced for the entire length of the model's bottom edge (y = -L/2 and - L/2 < x < L/2).
3. The z-symmetry boundary condition (u_z = 0) is enforced to the reference point of the GPS model.
4. Cyclic uniaxial displacement is applied to the entire length of the model's top edge (y = L/2 and - L/2 < x < L/2).

Here, we report the residual stress relaxation in the y and z directions (y = cyclic loading direction) for the initial three simulated loading cycles. We monitored these stresses throughout the application of fifteen loading cycles and observed negligible

variation upon application of three loading cycles. Table 10 lists the averaged *yy* and *zz* residual stress components at the end of three initial loading cycles, N = 1, 2, and 3 for partially debonded inclusions. The beginning of cyclic loading (end of shot peening) is indicated as N = 0. The negative values correspond to a shift from compressive to tensile stress state.

Table 10: averaged *yy* and *zz* residual stress components at the end of three initial loading cycles, N = 1, 2, and 3 for partially debonded inclusions.

yy residual stress component for partially debonded inclusions																
	R = 4 μm				R = 6 μm				R = 8 μm				R = 10 μm			
N = 0	1449				1478				1726				1790			
$\varepsilon_{yy}/\varepsilon_{ys}$	0.5	0.6	0.7	0.8	0.5	0.6	0.7	0.8	0.5	0.6	0.7	0.8	0.5	0.6	0.7	0.8
N = 1	635	590	542	496	670	630	587	537	793	735	669	593	911	856	796	729
N = 2	629	585	543	504	664	625	583	537	785	727	662	591	904	850	792	725
N = 3	626	582	539	500	661	622	580	533	781	722	658	587	900	846	788	720
zz residual stress component for partially debonded inclusions																
	R = 4 μm				R = 6 μm				R = 8 μm				R = 10 μm			
N = 0	1799				1666				1795				1848			
$\varepsilon_{yy}/\varepsilon_{ys}$	0.5	0.6	0.7	0.8	0.5	0.6	0.7	0.8	0.5	0.6	0.7	0.8	0.5	0.6	0.7	0.8
N = 1	433	424	418	412	456	447	442	435	486	494	482	469	567	561	554	546
N = 2	431	417	385	337	453	440	423	393	481	481	454	411	564	552	532	502
N = 3	431	415	380	328	451	438	419	386	479	478	447	400	562	549	526	493

Figure 5-14 shows the relaxation of σ_{yy}^{res} and σ_{zz}^{res} for a partially debonded inclusion (4 μm in radius) versus the applied uniaxial strain amplitudes ε_{yy} = 0.5, 0.6, and 0.7 ε_{ys} (ε_{ys} = 0.7 % (c.f. 2.4.3)) for strain ratio R_ε = -1 and uniform strain rate of 0.002 s^{-1}.

The residual stresses are normalized relative to their initial values at the onset of cyclic loading, listed in Table 10 at N = 0 for case C.

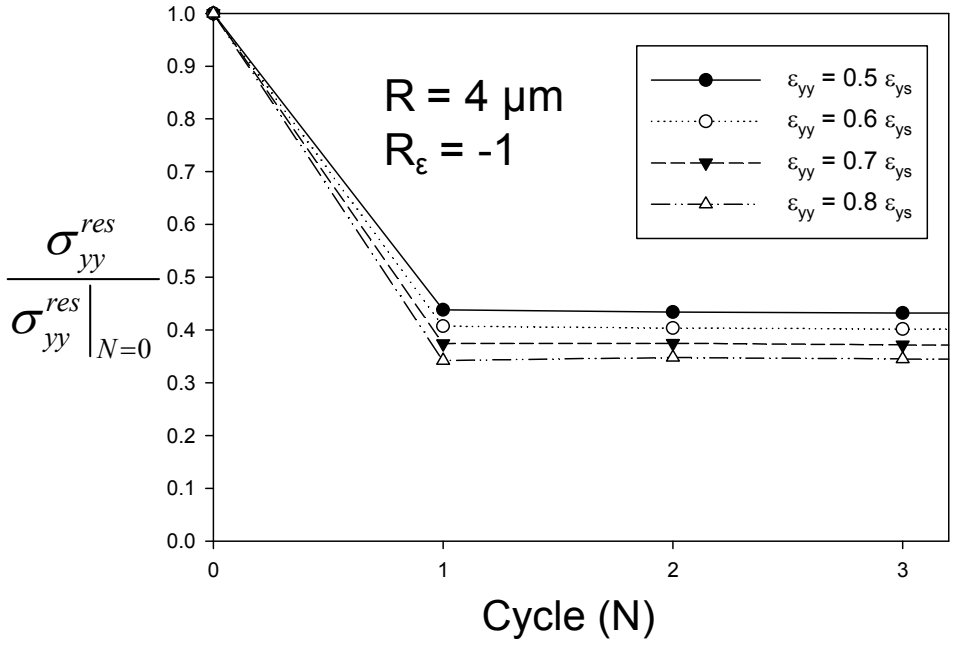

Figure 5-14: Relaxation of nonlocal (averaged over r = 2 μm) σ_{yy}^{res} (top) and σ_{zz}^{res} (bottom) at the notch root of a partially debonded inclusion (radius R = 4 μm) versus the applied uniaxial strain amplitude (ε_{ys} = 0.7 %; R_ε = -1).

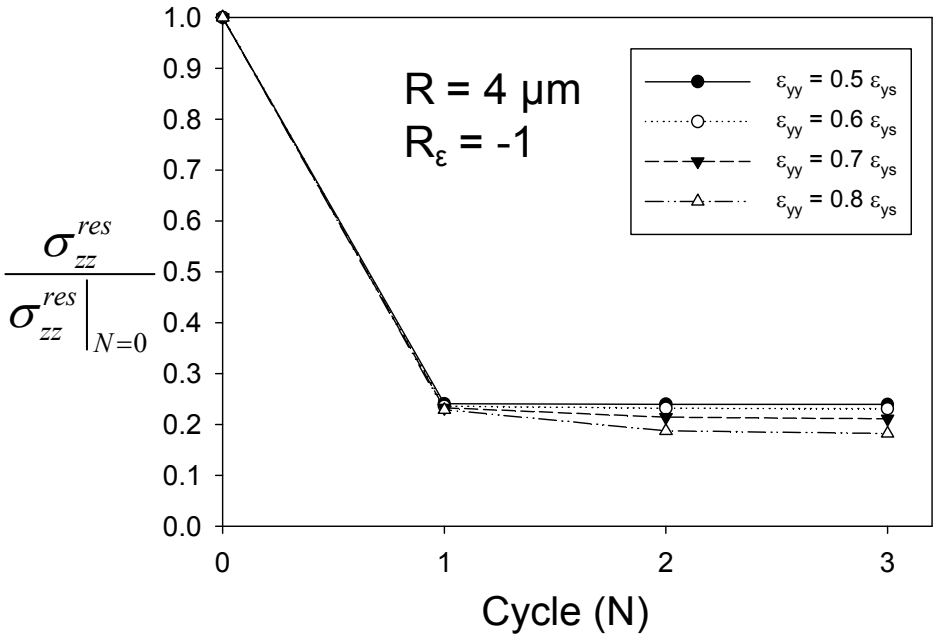

Figure 5-14 Continued.

Similar to Figure 5-14 for R = 4 μm, Figures 5-15 and 5-16 show the relaxation of σ_{yy}^{res} and σ_{zz}^{res} for partially debonded inclusions with radii, respectively, equal to R = 6 μm and R = 10 μm versus the applied uniaxial strain amplitudes ε_{yy} = 0.5, 0.6, and 0.7 ε_{ys} (ε_{ys} = 0.7 % (c.f. 2.4.3), R_ε = -1, and strain rate 0.002 s^{-1}).

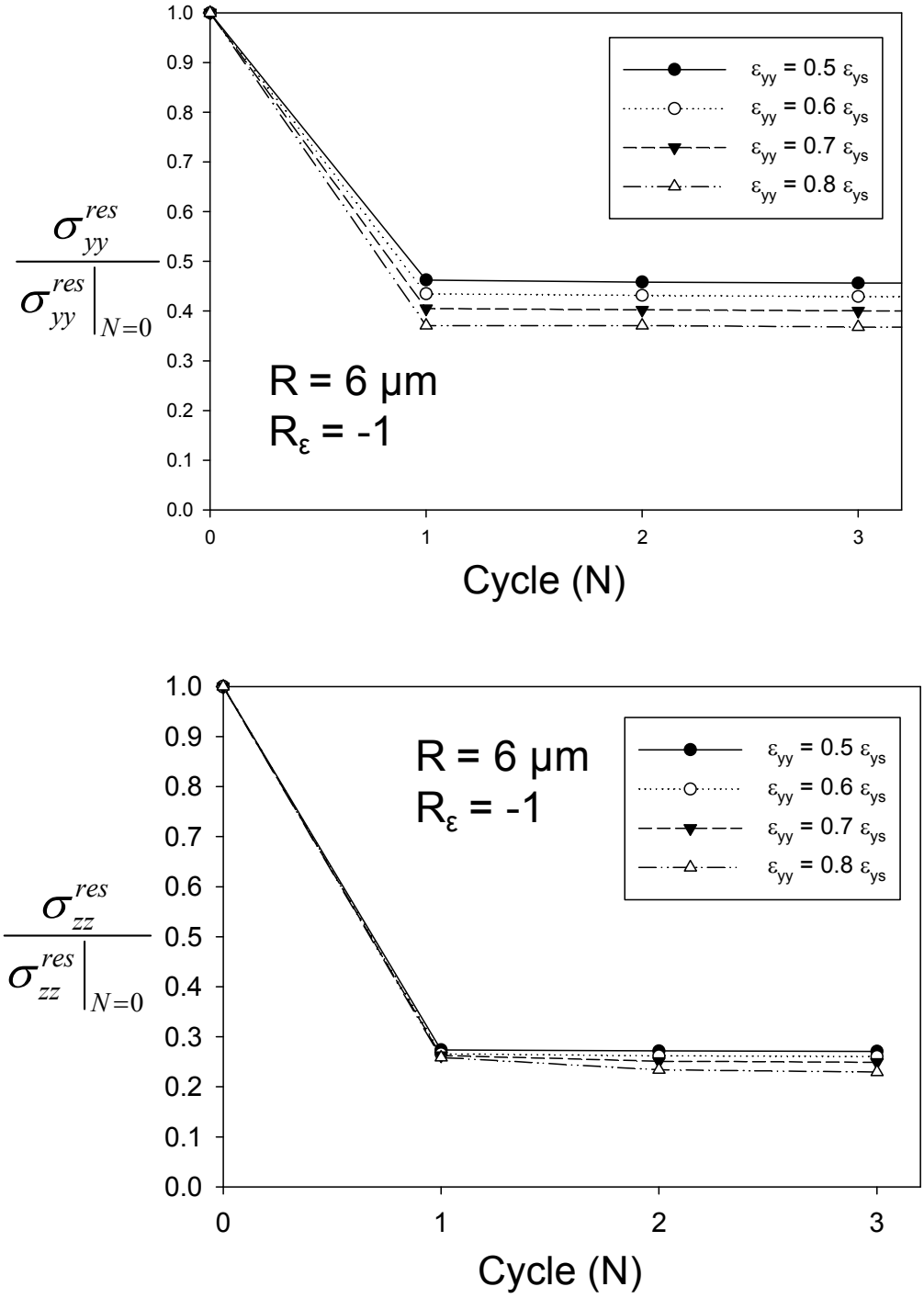

Figure 5-15: Relaxation of nonlocal (averaged over r = 3 μm) σ_{yy}^{res} (top) and σ_{zz}^{res} (bottom) at the notch root of a partially debonded inclusion (radius R = 6 μm) versus the applied uniaxial strain amplitude (ε_{ys} = 0.7 %; R_ε = -1).

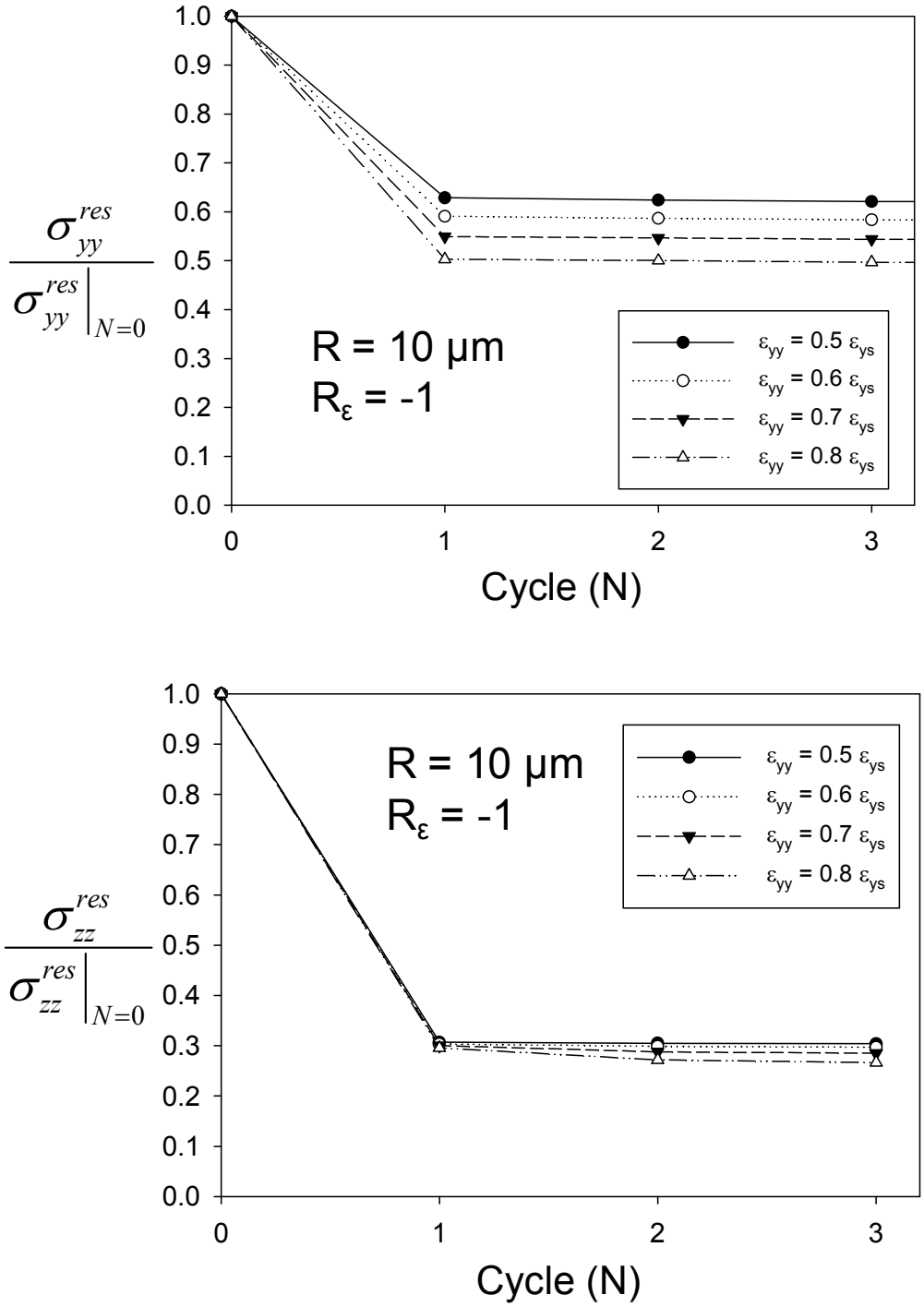

Figure 5-16: Relaxation of nonlocal (averaged over r = 5 μm) σ_{yy}^{res} (top) and σ_{zz}^{res} (bottom) at the notch root of a partially debonded inclusion (radius R = 10 μm) versus the applied uniaxial strain amplitude (ε_{ys} = 0.7 %; R_ε = -1).

As seen in Figures 5-14, 5-15, and 5-16 the compressive residual stresses (*yy* as well as *zz* components) at the inclusion notch root reduce to 35-65% of their initial value with the application of cyclic loading. A substantial amount of beneficial compressive residual stresses (in *y* and *z* directions) would be retained for the case of PD inclusions. The inclusion size influences the degree (percentage) of relaxation. The initial compressive residual stress is higher for large inclusions, as is the decrease in the magnitude of residual stress due to subsequent cyclic loading. The combined effect is a higher magnitude of retained compressive residual stress, relative to their initial value, for larger inclusions.

Cyclic microplasticity is the primary driver for the relaxation of residual stresses in favorably oriented grains under HCF [91] loading conditions. This explains why the highest degree of residual stress relaxation occurs at $\varepsilon_{yy}/\varepsilon_{ys} = 0.8$, for all sizes of inclusions (the same will be shown to hold for pores).

In order to examine the additional residual stress retained upon the application of cyclic loading at lower applied strain amplitudes, we consider the difference in the magnitude of residual stresses at $\varepsilon_{yy}/\varepsilon_{ys} = 0.5$, 0.6, 0.7, and 0.8 relative to their minimum value at $\varepsilon_{yy}/\varepsilon_{ys} = 0.8$, $\left(\sigma^{res}\right)_{\omega=0.8}$. The residual stress values at the end of the third loading cycle are examined. This difference in the magnitude of residual stress is then normalized by $\left(\sigma^{res}\right)_{\omega=0.8}$ and plotted as a percentage in Figure 5-17 for inclusions with R = 4, 6, 8, and 10 μm.

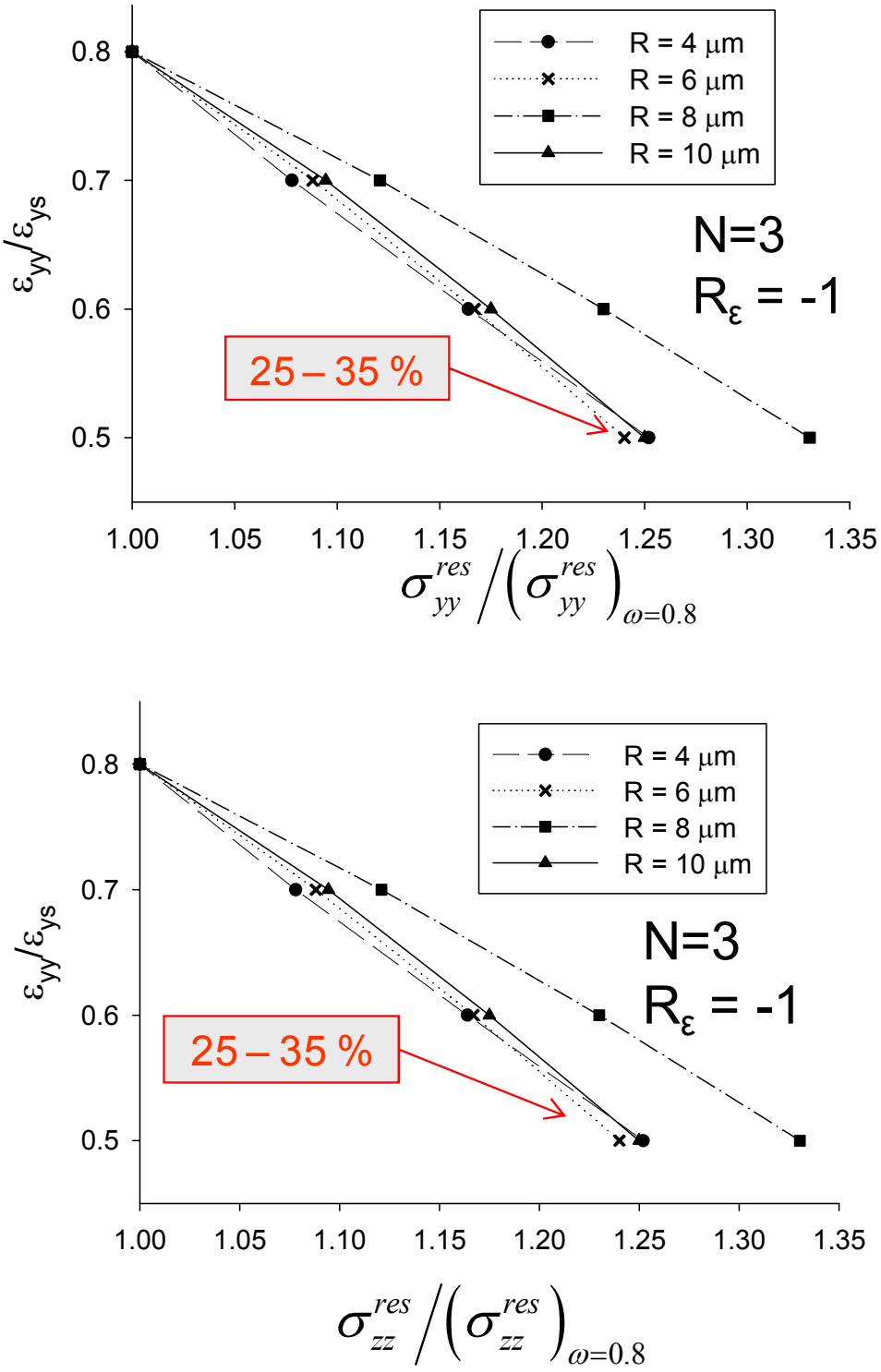

Figure 5-17: Applied uniaxial strain amplitude versus $\sigma_{yy}^{res} \Big/ \left(\sigma_{yy}^{res}\right)_{\omega=0.8}$ (top) and $\sigma_{zz}^{res} \Big/ \left(\sigma_{zz}^{res}\right)_{\omega=0.8}$ (bottom) for partially debonded inclusions, $R_\varepsilon = -1$.

According to Figure 5-17, up to 25-35% more of the beneficial residual stresses (in *y* as well as *z* directions) can be retained when the applied strain amplitude decreases from $\varepsilon_{yy}/\varepsilon_{ys} = 0.8$ to $\varepsilon_{yy}/\varepsilon_{ys} = 0.5$. This is aligned with our original hypothesis as to how the decrease in the degree of residual stress relaxation at lower stress amplitudes can be partially responsible for the dependence of surface fatigue crack initiation probability, p_s, on the stress amplitude (see Section 5.1).

Similar to Table 10 for partially debonded inclusions, Table 11 lists the averaged *yy* and *zz* residual stress components at the end of three initial loading cycles, N = 1, 2, and 3 for pores. The beginning of cyclic loading (end of shot peening) is indicated as N = 0. The negative values correspond to a shift from compressive to tensile stress state.

Table 11: averaged *yy* and *zz* residual stress components at the end of three initial loading cycles, N = 1, 2, and 3 for pores.

yy residual stress component for pores																
	R = 4 μm				R = 6 μm				R = 8 μm				R = 10 μm			
N = 0	1368				1001				733				539			
$\varepsilon_{yy}/\varepsilon_{ys}$	0.5	0.6	0.7	0.8	0.5	0.6	0.7	0.8	0.5	0.6	0.7	0.8	0.5	0.6	0.7	0.8
N = 1	364	237	103	-38	52	-3	-72	-151	-71	-116	-168	-233	-223	-217	-208	-206
N = 2	356	231	102	-28	48	-7	-68	-120	-73	-112	-149	-203	-222	-214	-201	-192
N = 3	352	227	99	-29	46	-9	-70	-119	-75	-113	-148	-200	-222	-213	-199	-190
zz residual stress component for pores																
N = 0	613				481				361				539			
$\varepsilon_{yy}/\varepsilon_{ys}$	0.5	0.6	0.7	0.8	0.5	0.6	0.7	0.8	0.5	0.6	0.7	0.8	0.5	0.6	0.7	0.8
N = 1	152	135	121	108	-14	-17	-23	-31	-50	-68	-90	-118	-103	-111	-128	-144
N = 2	151	134	116	87	-14	-19	-33	-69	-53	-76	-109	-150	-103	-116	-138	-161
N = 3	150	132	112	76	-15	-19	-36	-76	-53	-78	-112	-155	-103	-117	-140	-164

The retained compressive residual stresses are much lower for pores. Figure 5-18 shows the relaxation of σ_{yy}^{res} and σ_{zz}^{res} for a pore (4 μm in radius) versus the applied uniaxial strain amplitudes ε_{yy} = 0.5, 0.6, and 0.7 ε_{ys} (ε_{ys} = 0.7 % (c.f. 2.4.3)) for strain ratio R_ε = -1 and uniform strain rate of 0.002 s^{-1}. The residual stresses are normalized relative to their initial values at the onset of cyclic loading, listed in Table 11 at N = 0 for case C.

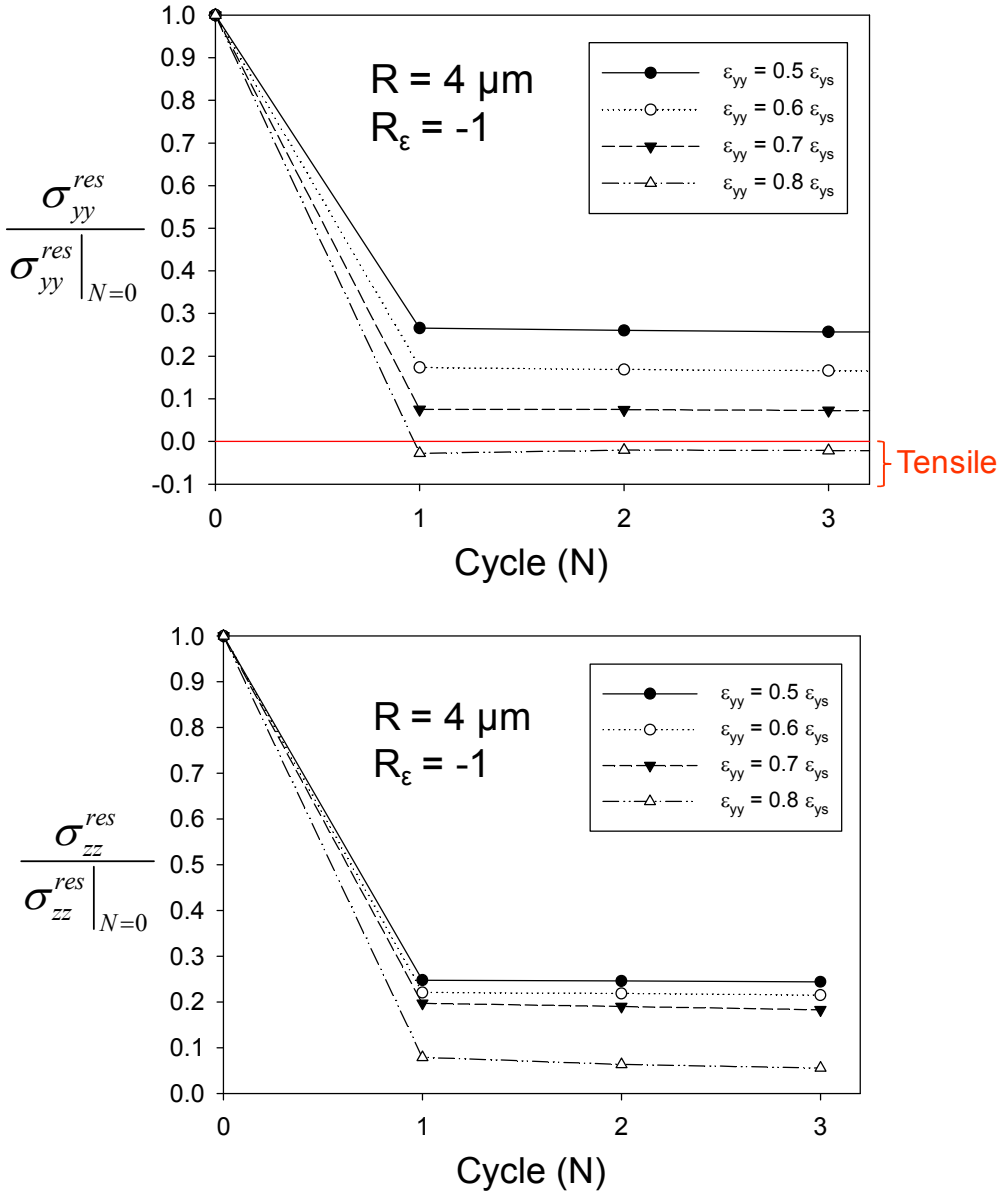

Figure 5-18: Relaxation of nonlocal (averaged over r = 2 μm) σ_{yy}^{res} (top) and σ_{zz}^{res} (bottom) at the notch root of a pore (radius R = 4 μm) versus the applied uniaxial strain amplitude (ε_{ys} = 0.7 %; R_ε = -1).

Similar to Figure 5-18 for R = 4 μm, Figures 5-19 and 5-20 show the relaxation of σ_{yy}^{res} and σ_{zz}^{res} for pores with radii, respectively, equal to R = 6 μm and R = 10 μm versus

the applied uniaxial strain amplitudes ε_{yy} = 0.5, 0.6, and 0.7 ε_{ys} (ε_{ys} = 0.7 % (c.f. 2.4.3), R_ε = -1, and strain rate 0.002 s^{-1}).

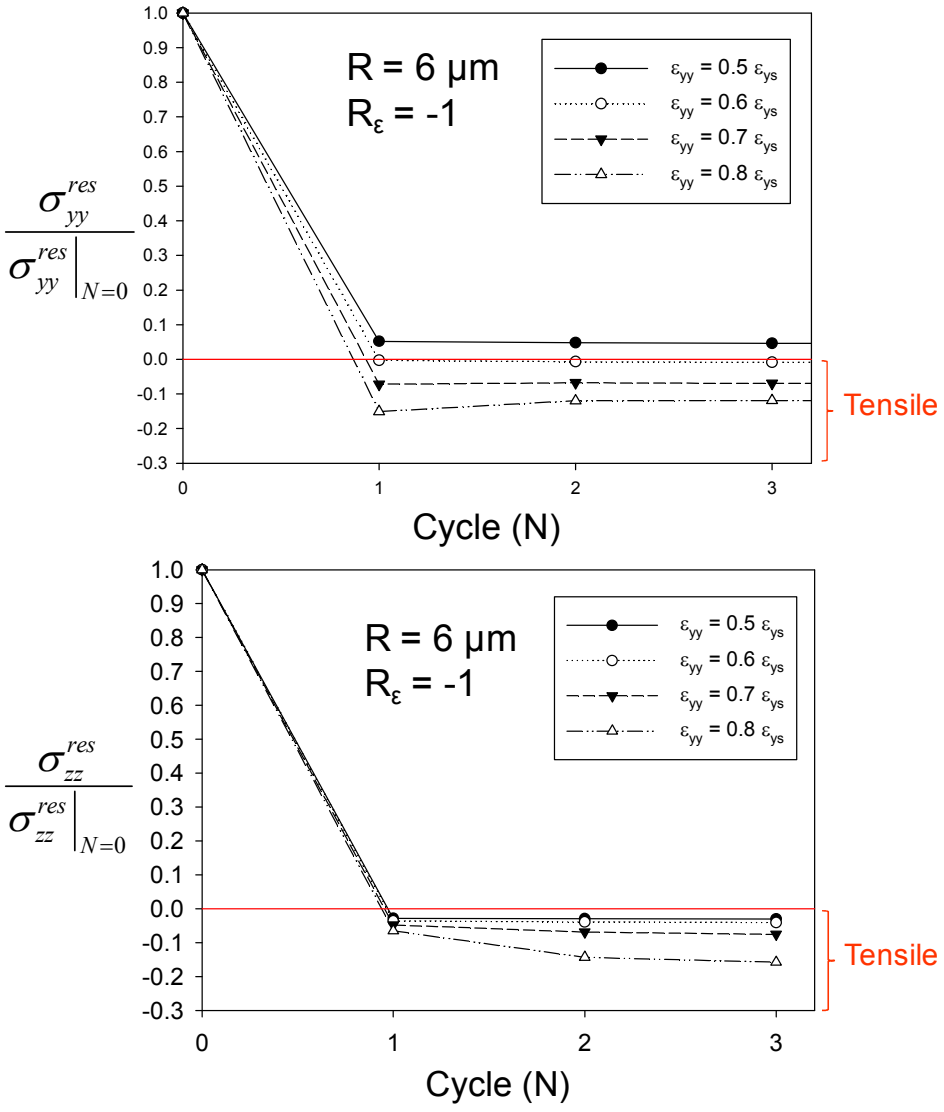

Figure 5-19: Relaxation of nonlocal (averaged over r = 3 µm) σ_{yy}^{res} (top) and σ_{zz}^{res} (bottom) at the notch root of a pore (radius R = 6 µm) versus the applied uniaxial strain amplitude (ε_{ys} = 0.7 %; R_ε = -1).

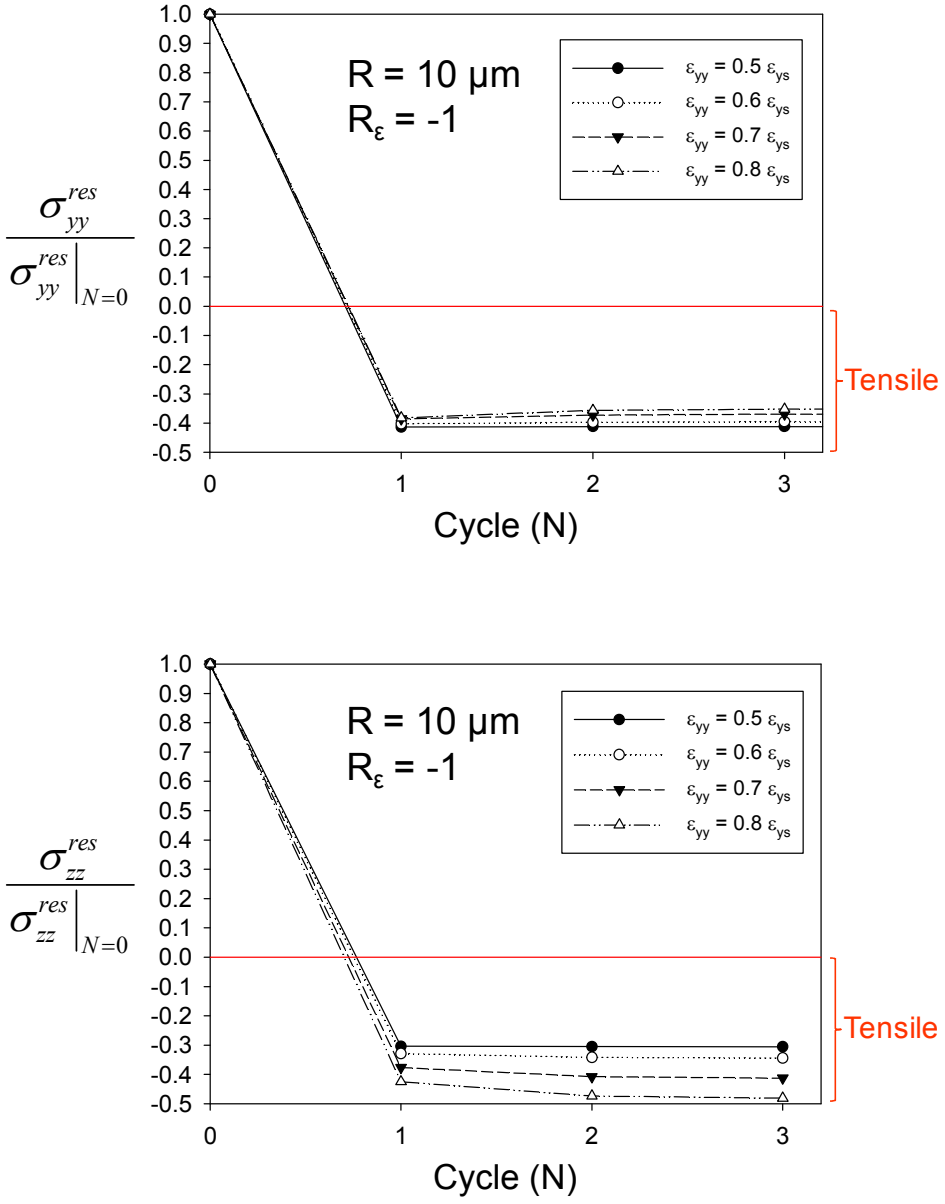

Figure 5-20: Relaxation of nonlocal (averaged over r = 5 μm) σ_{yy}^{res} (top) and σ_{zz}^{res} (bottom) at the notch root of a pore (radius R = 10 μm) versus the applied uniaxial strain amplitude (ε_{ys} = 0.7 %; R_ε = -1).

Upon the first loading cycle, the compressive residual stresses almost completely diminish for all but the smallest pore size studied (R = 4 μm). As seen in Figure 5-18 (a) for R = 4 μm, only around 30% of the initial compressive residual stresses are retained at

the lowest simulated applied strain amplitude of $\varepsilon_{yy}/\varepsilon_{ys} = 0.5$. Most simulated pore sizes result in the initial compressive residual stresses to shift to a tensile state, detrimental to the material's fatigue resistance.

To better understand the different effects of partially debonded inclusions and pores, we monitor the variation of averaged stress versus plastic strain (σ^*_{yy} versus $\varepsilon^*_{yy,pl}$) at the notch root of a pore (Figure 5-21 b) and at a debonded inclusion (Figure 5-21 c) with R = 6 μm after three loading cycles ($\varepsilon_{yy}/\varepsilon_{ys} = 0.6$ and $R_\varepsilon = -1$). The dark, wide black lines show the variations during shot peening.

The beginning and end of load reversals in the first loading cycle are labeled in Figure 5-21 (a). Under fully reversed cyclic loading (i.e., $R_\varepsilon = -1$), extensive cyclic plasticity occurs during the first load reversal (segment BC), resulting in substantial relaxation of compressive residual stresses. As such, for both inclusions and pores, the first loading cycle results in the highest percentage reduction in the magnitude of residual stresses; this agrees with experiments using shot peened Astroloy [150] and IN939 [151] superalloys under cyclic loads. Almer et al. [152] pointed out that microstresses within grains relax rapidly due to this small-scale plastic deformation, while macroscopic stresses relax less rapidly; this can significantly influence fatigue crack formation and growth behavior in HCF [78].

The relatively rigid inclusion plays a significant role in retaining the compressive residual stresses by bearing compressive stresses in the first load reversal (segment BC), thus resulting in a lesser amount of plastic deformation and residual stress relaxation.

Figure 5-21 indicates a state of plastic shakedown where the third cycle can essentially be considered closed cycles of alternating plastic deformation without any

accumulation of plastic strains, i.e., plastic strain ratcheting [91]. The compressive residual stresses around partially debonded inclusions endure the applied cyclic loading over a broader range of inclusion sizes and applied strain amplitudes. Thus, we consider the residual stress effects only for inclusions when we study in Chapter 6 the residual stress relaxation effects on the ratio of probabilities of surface to bulk fatigue crack initiation.

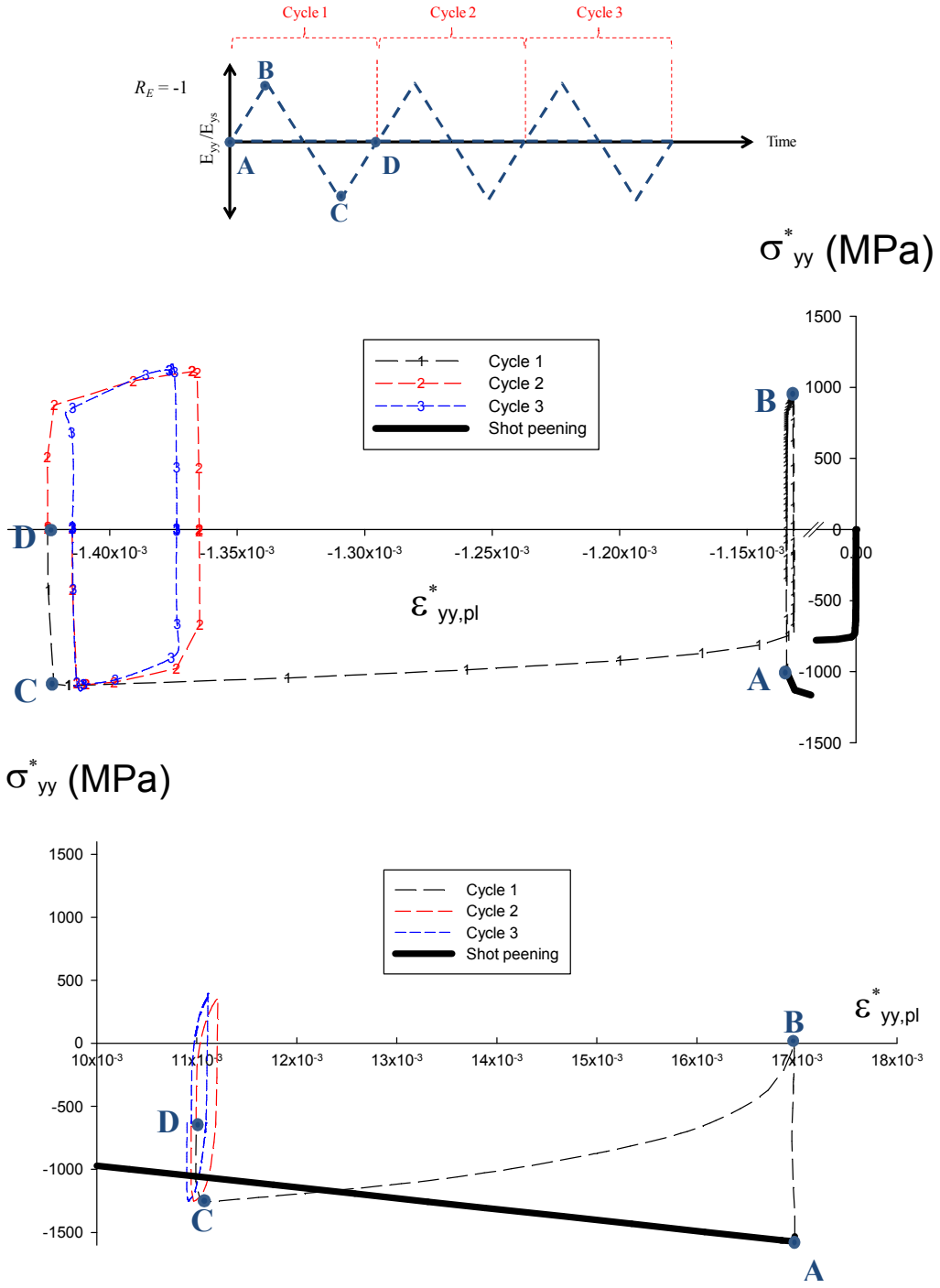

Figure 5-21: (top) load reversals. The variation of σ^*_{yy} vs. ε^{p*}_{yy} at the pore (middle) and debonded inclusion (bottom). R = 6 μm, $\varepsilon_{yy}/\varepsilon_{ys}$ = 0.6 and R_ε = -1. The dark, wide black lines show the variations during shot peening.

5.7 Summary

A simplified methodology developed by Prasannavenkatesan *et al.* [78, 149] was implemented to:

1. Model the residual stress state due to the shot peening process.
2. Study the residual stresses around inclusions/pores.
3. Examine degree of residual stress relaxation around inclusions/pores.

The embedded partially debonded inclusions were found to have increased the local compressive stresses by as much as 80% depending on the inclusions size and the magnitude of initial residual stresses. Relative to the case with no pores, small and large pores, respectively, have higher and lower local compressive stresses.

Next, residual stresses were monitored for embedded partially debonded inclusions and pores throughout the application of cyclic loading. Extensive cyclic plasticity during the first load reversal results in the highest percentage reduction in the magnitude of residual stresses such that the compressive residual stress:

1. Reduces to 35-65% of its initial value at the partially debonded inclusion notch root. Larger inclusions were found to retain compressive residual stresses to a higher degree.
2. Almost completely diminishes at the pore notch root.

It was also found that the degree of residual stress relaxation increases with increased applied uniaxial strain amplitude ($R_\varepsilon = -1$) for all sizes of inclusions and pores. These findings were explained by examining the scale of cyclic microplasticity at the notch root of inclusions and pores. It was found that the relatively rigid inclusions restrict the plastic deformation in the first load reversal, thus resulting in enhanced residual stress retention. Larger amounts of the beneficial residual stresses were retained when the applied strain amplitude decreased. The contribution of this additional amount of retained residual stress to the surface-to-bulk transition of HCF failure origins will be addressed in Chapter 6.

6 Weighted probability approach for modeling surface to bulk transition of HCF failures dominated by primary inclusions and pores

6.1 Introduction: Bimodal fatigue life distribution with surface and bulk sites

Fatigue life variability naturally exists in all fatigue regimes due to variability in the microstructure and to uncontrollable test conditions. Nevertheless, HCF experiments on some advanced metallic alloys, such as Ni-base superalloys, titanium alloys, and high-strength steels, show that fatigue life can be unexpectedly much higher for some specimens [4-18]. The relative number of such observations increases as the stress amplitude decreases in the HCF regime, such that just below the traditional HCF limit, fatigue life data appears to be distributed between two branches. The occurrence of two distinct failure distributions has been referred to as "Competing Failure Modes" [19, 20].

This duplex distribution over drastically different fatigue lives appears as a plateau in the corresponding S-N curve, often referred to as a step-wise or duplex S-N curve. Figure 6-1 (a) shows a step-wise S-N curve in Ti-6-2-4-6 [16]. Similarly, Figure 6-1 (b) shows a step-wise S-N curve in a bearing steel [17]. A bilinear, step-wise, or duplex cumulative distribution function (CDF) of fatigue life refers to the same effect; when two separate normal distribution functions are fitted to the datasets, they appear as two linear segments when CDF is plotted in a logarithmic scale, Figure 6-1 (c). It has been shown that two modes of failure can be separable by statistical analysis, even in circumstances where there may be a high degree of overlap in the fatigue data for the two modes [18].

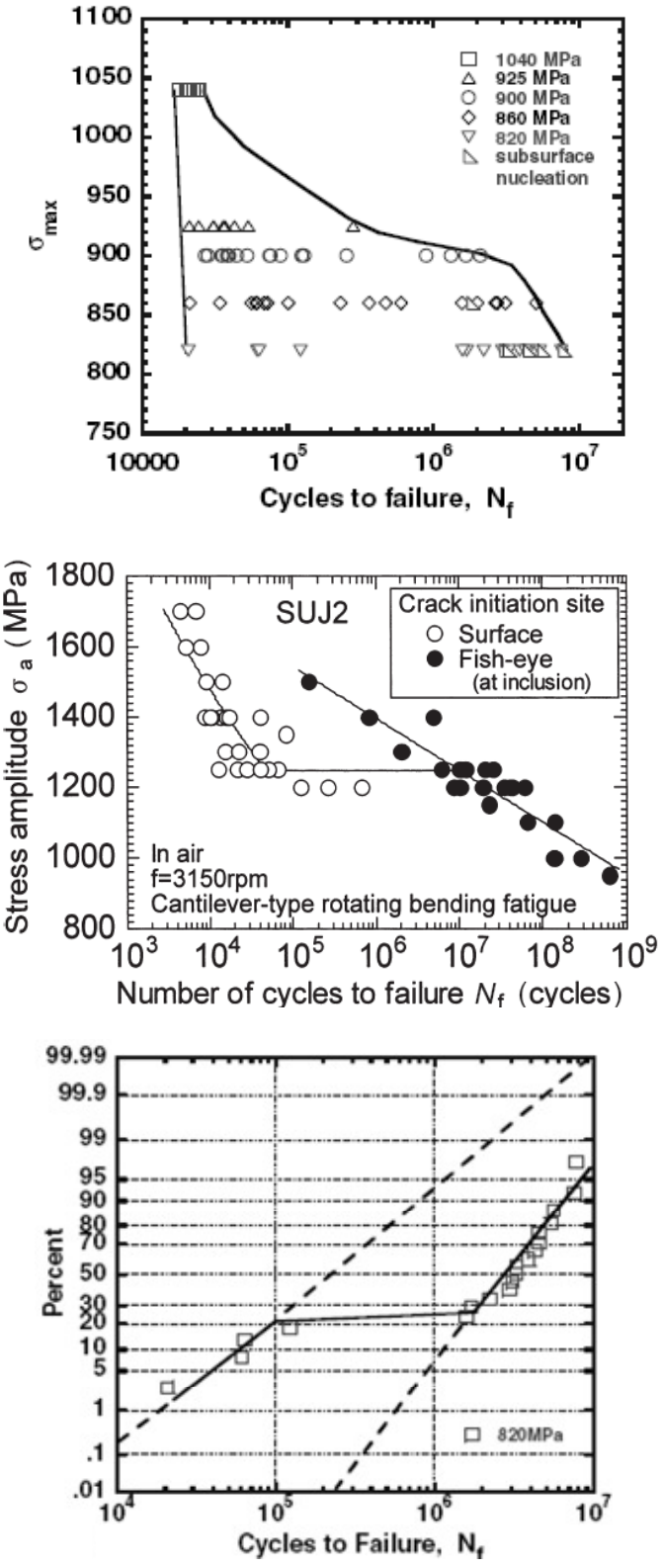

Figure 6-1: Step-wise S-N curve in Ti-6-2-4-6 [16] (top) and a bearing steel [17] (middle); Example of bilinear fatigue life CDF in Ti-6-2-4-6 [16] (bottom).

As the stress amplitude decreases below the traditional endurance limit and into the VHCF regime, the dataset that corresponds to shorter fatigue lives becomes sparsely populated, whereas the other dataset grows in number and thus controls the mean of the entire data population [12-15, 153, 154]. As such, the two datasets are often referred to as (1) life-limiting and (2) mean-controlling, respectively.

At a given stress amplitude, the overall fatigue life variability can be associated with two sources (c.f. Figure 6-2):

1. Variability within each life data population corresponding to *(b)* surface and *(c)* internally originated fatigue failures due to variability in the microstructure and underlying mechanisms.
2. Separation *(a)* between the life data populations due to the:
    a. Environmentally-enhanced cracking at surface sites [18]. Regarding the latter, fatigue crack growth rates in air are significantly faster than those observed in vacuum [119, 120]. In contrast, the bulk initiation mechanisms essentially operate in a quasi-vacuum environment, producing longer fatigue lives.
    b. Lack of constraints on plastic strain localization at sites near the free surface.

Additionally, these life-limiting and mean-controlling datasets broaden and diverge with decreases in the stress amplitude. The *INCREASE* in overall fatigue life

variability due to a decrease in stress from σ to σ' (within the VHCF regime) can be identified, as schematically shown in Figure 6-2.

1. Increased variability *(b<b')* and *(c<c')* within lifetime data populations, corresponding to surface and internally originated fatigue failures [12] that arise due to increased deformation heterogeneity at lower stress amplitudes.
2. Increased separation *(a<a')* between the lifetime data populations, attributed to differences in the failure initiation mechanisms to decreases in the stress amplitude [14, 18].

Here, the fatigue life is defined by the number of cycles to fracture the specimen, N_f, and normal distribution functions are shown for each data population only for illustrative purposes.

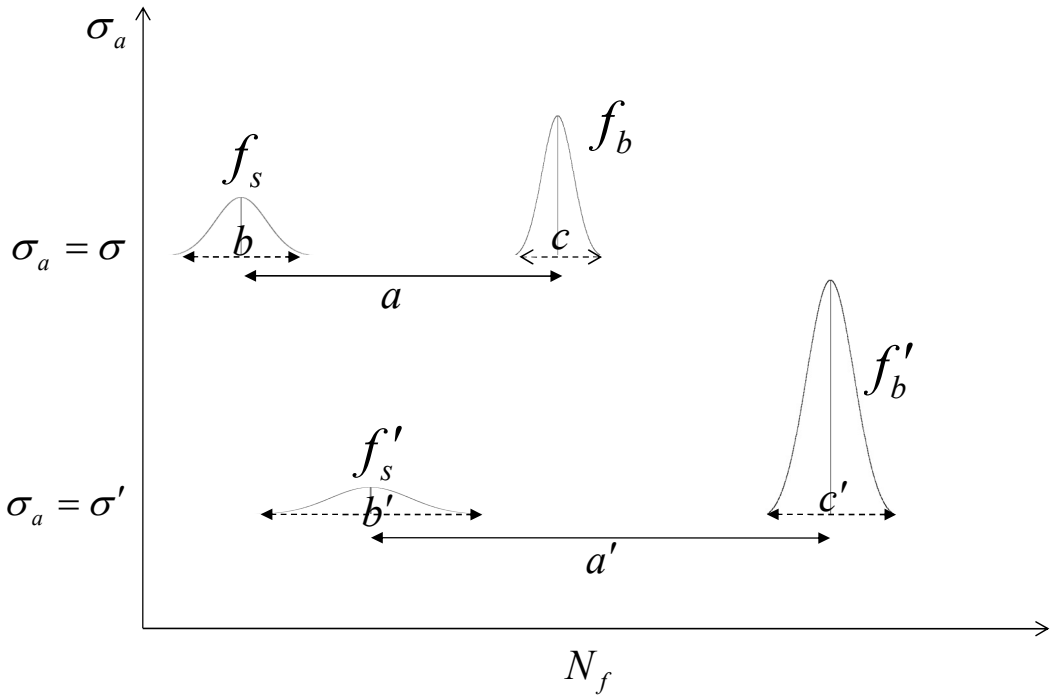

Figure 6-2: Variability in fatigue life for a given applied stress/strain amplitude (symbols are for illustrative purposes and do not represent actual experimental data).

In light of the distinct nature of surface- and bulk-originated failure modes, bimodal representation of the probability distribution function (PDF) of the fatigue life data, *f(x)*, has been suggested as a more accurate fit to the experimental fatigue data [12-14, 16, 126, 155]. In the bimodal representation, two PDFs, f_s and f_b, corresponding to each of the two fatigue life datasets are superimposed as

$$f(x) = p_s f_s(x) + p_b f_b(x) \tag{6.1}$$

Similarly and in terms of the cumulative distribution function (CDF) of the fatigue life data, *c(x)*,

$$c(x) = p_s c_s(x) + p_b c_b(x) \tag{6.2}$$

where c_s and c_b correspond to the CDF of each fatigue life dataset. Statistically-speaking, the weighting parameters, p_s and p_b, are the probabilities that a given data point belongs to the life-limiting dataset (first term) or the mean-controlling dataset (second term).

In clean alloys with inclusions, such as powder processed alloys, the life-limiting (worst-case) characteristics of the HCF and VHCF regimes are governed by extreme value microstructure attributes, which are large non-metallic inclusions. The processes of fatigue crack formation and early growth from surface grains, inclusions, or pores and bulk inclusions govern the scatter within the life-limiting and mean-controlling datasets [156].

Because we are attributing the life-limiting and mean-controlling datasets to the surface and bulk inclusions in PM Ni-base superalloys, the weighting parameters, p_s and p_b of the bimodal fatigue life distribution in Eqs. 6.1 and 6.2 are hereafter referred to as the probability of failure initiation (formation and early growth) from surface and bulk inclusions, respectively.

Physically-based life prediction methodologies that integrate the mechanisms of fatigue variability in Ni-base superalloys are of great interest in life-extension as well as in new alloy development in the gas turbine industry [156-158]. To that end, life-limiting mechanisms of superalloys have received considerable attention [12, 14, 119, 120, 153, 156, 159, 160]. This is because superalloy applications demand a very low probability of failure, for example 0.1% (known as B0.1) in aircraft gas turbine applications.

Many experimental studies seek to enhance the general understanding of fatigue crack formation and early growth behavior by obtaining extensive databases of hard-to-measure fatigue crack growth data, often introducing known populations of artificial

inclusions (seeds) to production powder to intentionally promote surface fatigue failure initiation.

Although a fair level of understanding has been achieved regarding small crack growth behavior, a physically-based predictive tool is lacking, and fatigue crack growth behavior is still the subject of active research. The complexities of this problem are evident in the erratic trends of fatigue crack growth data, as shown in Figure 6-3.

Besides the distribution of the life-limiting dataset, the populations of life-limiting versus mean-controlling distributions (i.e. surface versus bulk initiation probabilities in the PM Ni-Base superalloys), $P=p_s/p_b$, can significantly impact the low failure probability estimate of fatigue life for the bimodal fatigue life distribution. This will be discussed in the next section.

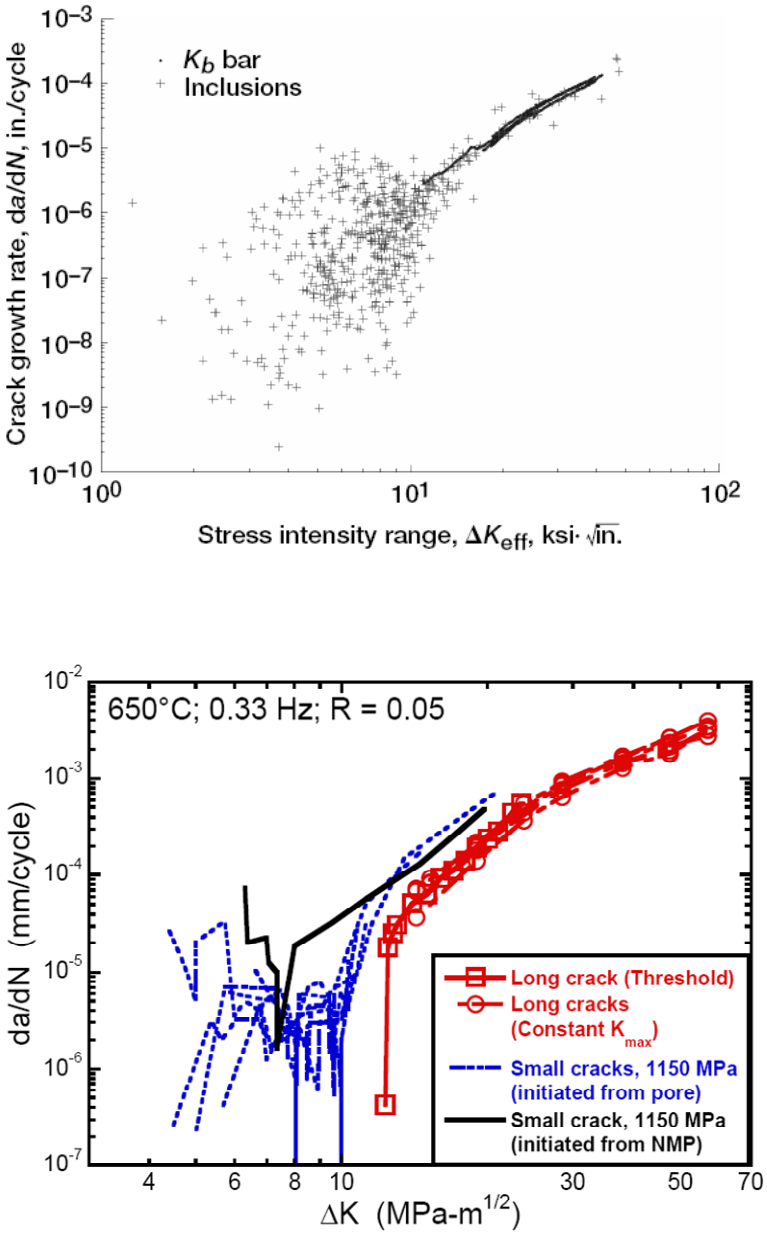

Figure 6-3: Distribution of measured fatigue crack growth rates. Top: Inclusion-initiated cracks in seeded Udimet720 [159]. Bottom: Inclusion- and pore-initiated cracks in IN100 [14]. The test temperature was 650°C.

6.2 The significance of surface and bulk initiation probabilities

To further illustrate the impact of surface initiation probability on the low failure probability estimate of fatigue life, we cite the experimental fatigue data of a study on subsolvus PM IN100 tested at 650°C, f = 0.33 Hz, and $R_\sigma = 0.05$ (stress-controlled) [14].

The Cumulative Distribution Function (CDF) of fatigue life data is shown in blue symbols in Figure 6-4. The fitted CDF to all the fatigue life data points is shown with a continuous blue line. The traditional B0.1 estimate (1 in 1000 probability of failure) is computed by extrapolating this fitted CDF.

The CDF of the simulated life-limiting distribution, i.e., c_s in Eq. 6.2, is shown with a black dashed line in Figure 6-4. In the referenced study, the life-limiting distribution was simulated using the Paris crack growth equation with random parameters. The initial crack size for the inclusion initiated crack was determined based on the diameter of the circle with equivalent projected area. By simulating the distribution c_s, a first-order improvement to the B0.1 estimate is achieved by solving $c_s(N_f) = 0.001$.

However in doing so, an overly conservative B0.1 estimate is obtained, as the contribution of the mean-controlling distribution is not accounted for. As shown in Figure 6-4, a considerable improvement to the B0.1 estimate can be obtained by accounting for the fact that for any surface initiation, there occurs p_b/p_s bulk initiations. This view is justified, as all the bulk initiated failures are known to have longer lives than the surface initiated cases. Thus, one must calculate the B0.1 estimate based on the implicit relation:

$$c_s(N_f) = \frac{0.001}{p_s} \tag{6.3}$$

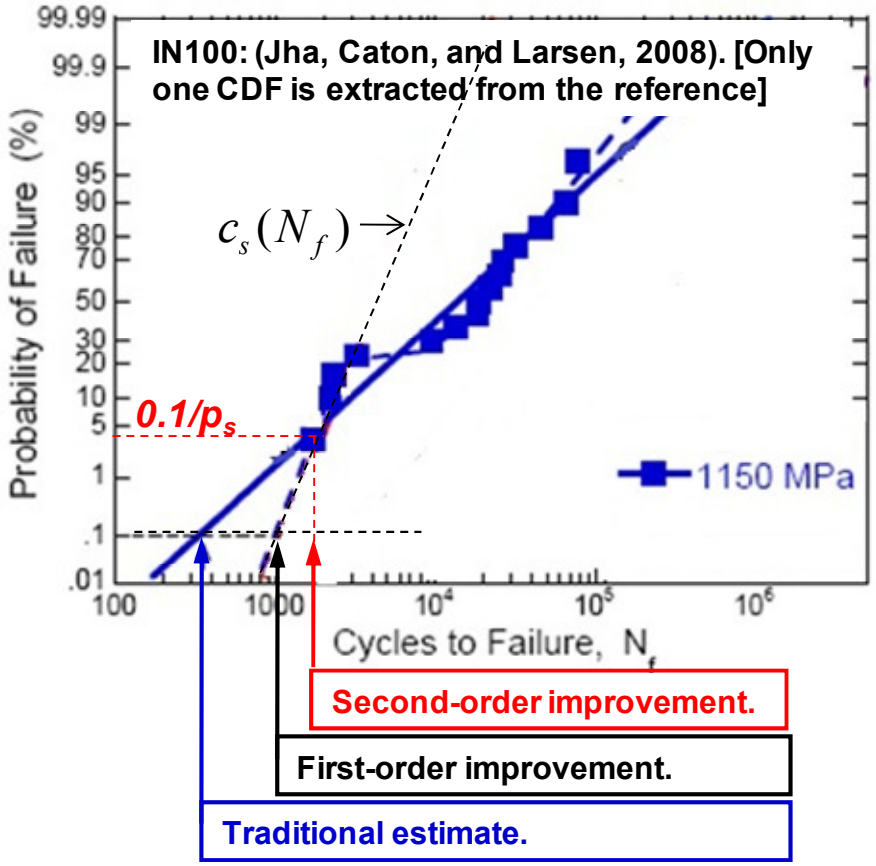

Figure 6-4: Improvements to the B0.1 estimate. The experimental and fitted fatigue life data are shown in blue symbols and line, respectively. The simulated life-limiting distribution (c_s) is shown with a black dashed line [14].

The processes of fatigue crack initiation at bulk sites have previously been studied in the context of surface-treated materials or of damage-tolerant design of large components, where surface initiation is suppressed or where the critical site, often a large inclusion or a cluster of favorably oriented grains, is more likely to exist in the bulk of the material.

Extensive research at the Air Force Research Laboratory (AFRL) [12-15, 153, 154] indicates that even though the life estimate obtained by solving $c_s(N_f) = X$ does not account for a significant number of bulk initiations, it still results in a conservative

estimate with significant improvement to the traditional estimates that are based on the extrapolation of a unimodal life distribution.

6.3 Existing approaches to prediction of surface initiation probability

From experimental data, the weighting parameters can be obtained as the proportions of all experiments that show surface and bulk failure initiation sites, respectively [14], i.e.,

$$\begin{aligned} p_s &= n_s \big/ \left(n_s + n_b \right) \\ p_b &= n_b \big/ \left(n_s + n_b \right) \end{aligned} \tag{6.4}$$

Experimentally obtained values of p_s are sensitive to slight variations in the outcome of limited experimental data, and a prohibitively large number of fatigue experiments is needed to ensure that the experimentally obtained values of p_s vary negligibly upon performing additional experiments.

To further illustrate the dependence of p_s on the variations in the outcome of experimental data, suppose that the actual value of p_s = 0.2 and we intend to perform fatigue experiments to calculate p_s. If we perform 10 fatigue experiments, 2 of the experiments should fail from the surface. Now, suppose that only one surface initiated failure event is substituted by an internally initiated failure event. Thus, the experimentally measured surface initiation probability is calculate as $p_s = \left(2-1\right)\big/10 = 0.1$, resulting in a 50 % error (the actual value was p_s = 0.2). For this example (assuming we now the actual value of p_s = 0.2 a priori), Figure 6-5 illustrates the sensitivity of p_s to the number of experiments used to calculate it.

As observed in this simple example, at least 100 experiments are needed to warrant 95 % confidence in this experimental estimation. This number increases as the actual value of p_s decreases (in VHCF) and the desired confidence level increases.

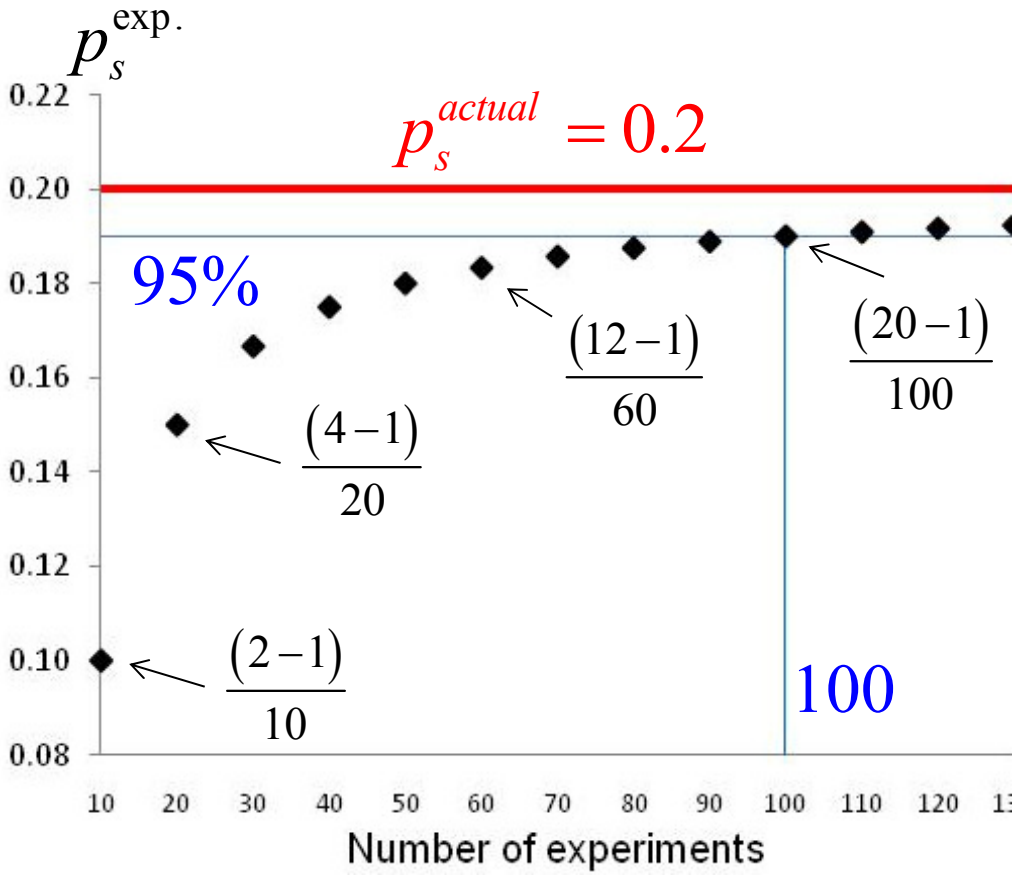

Figure 6-5: Sensitivity of ps to the number of experiments used to calculate it.

It is clear from Figure 6-5 that the size of most experimental studies performed to date is typically far too small for the purpose of accurately estimating p_s. A more practical and accurate assessment of the surface initiation probability is desirable in order to better assess the mean and minimum life modeling of entire population. Without this, the applicability of Eqs. 6.1-6.3 is quite limited (perhaps unusable in practical terms).

Physically-based simulative approaches to predicting surface and bulk fatigue crack initiation probabilities can help to reduce the number of experiments. Such approaches are lacking.

Cashman [125, 126, 155] pursued an analytical methodology, based on the Weibull "Weakest Link" concept [92]. First, he calculated p_s from available experimental data as $p_s = n_s \big/ \left(n_s + n_b \right)$ for various applied uniaxial strain amplitudes. Then, he fitted the binary logistic distribution [161, 162] to the probability of surface initiation as a function of applied loading. The fitted binary logistic distribution is shown in Figure 6-6 for the uniaxial experimental data for PM René 95 [125]. The ordinate is identified as pseudostress amplitude, defined as $\left(E\Delta\varepsilon/2 \right)$; $\Delta\varepsilon$ and E denote the total strain range and the modulus of elasticity, respectively. This is the typical aspect of the method of presenting fatigue life data points in strain-controlled fatigue tests at GE Aviation [19].

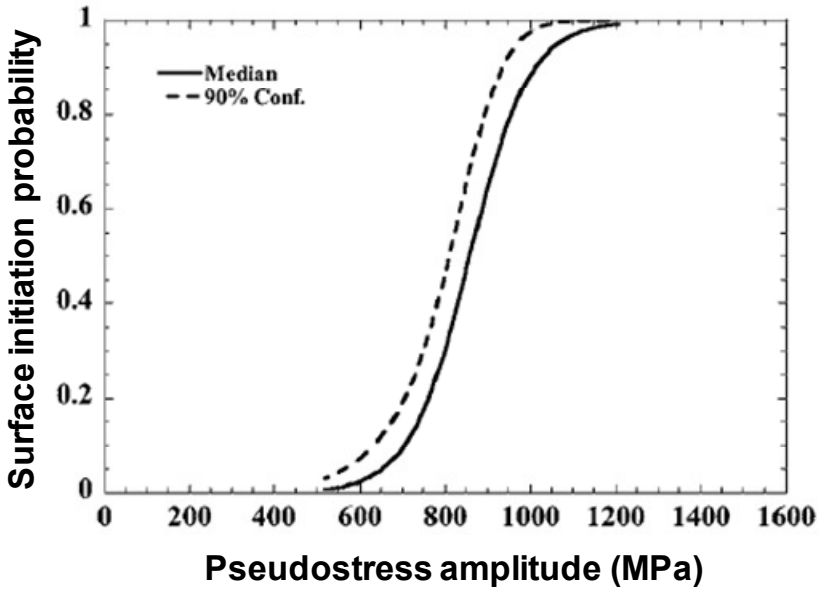

Figure 6-6: The fitted binary logistic distribution to the experimental surface initiation probability vs. pseudostress amplitude in René 95 tested at 538°C [125].

Logistic regression is often used to predict a discrete outcome, such as surface and bulk failure initiation, from a set of variables that may be continuous (e.g., stress amplitude), discrete/categorical (e.g., inclusion versus pore), or a mix of both [162]. Mathematically, the binary logistic model used for the stress-dependence of the surface initiation probability can take the form [126, 161, 163]:

$$p_s = \left[1 + e^{-\left(\frac{\sigma - a}{b}\right)}\right]^{-1} \tag{6.5}$$

where σ is the relevant measure of the loading condition (e.g., stress amplitude/range), and a and b are the model parameters, calculated from the available p_s data for representative loading conditions with maximum likelihood estimation.

Cashman considered small subregions at the inclusion notch root. He then used the estimated cyclic stress intensity factor for each subregion (assumed to be uniform over subregions) as an indicator parameter for fatigue crack initiation in the PM Ni-base superalloy René 95. He simulated p_s by formulating the "Weakest Link" concept for the collection of the small subregions at the inclusion notch root. He then calibrated the parameters of the simulated p_s distribution to the fitted binary logistic distribution of p_s. Cashman's approach is limited because:

- It assumes the inclusion size is constant.
- It relies on the analytical solution of the cyclic stress intensity factor for a homogenous isotropic material. As such, it does not account for the micro

plasticity under HCF and VHCF, nor it accounts for the variability due to the microstructure.

- It is limited to the uniaxial loading condition.

In contrast, the simulation-based methodology developed in this thesis (described in the next section) overcomes these shortcomings as it includes the inclusions size effect and uses crystal plasticity material model (calibrated to experimental data at T = 650°C) to simulate grains around inclusions/pores. Also, we use FIPs (well-suited for fatigue crack formation and early growth under HCF and VHCF regimes) into our probabilistic construct. As such, the model is capable of handling the effects of multiaxial loading conditions (e.g., tension, torsion, rotating bending and plane bending).

6.4 Simulated surface and bulk initiation probabilities

6.4.1 Fatigue hot spot

We relate the probability of fatigue crack initiation in the surface region to the expected number of critical fatigue hot spots in this region, Ψ. The term "fatigue hot spot" refers to a microstructure attribute or collection of attributes (a large favorably oriented grain, an inclusion, a pore, etc.) which, under a given uniaxial loading condition (i.e., $\Delta\varepsilon$ and R_ε) can associate with a sufficient driving force to incubate a fatigue crack. The effects of loading condition, free surface, oxidation, specimen size, as well as the density and size distribution of primary inclusions are incorporated in a single variable Ψ.

A fatigue "hot spot" may have one or more constituent elements. In fine-grained PM Ni-base superalloys, non-metallic inclusions are candidate fatigue hot spots. A less potent inclusion may qualify as a hot spot if it is adjacent to a large grain that is favorably oriented for intense shear deformation. Examples of microstructure configuration that may be fatigue hot spots are shown in Figure 6-7 with added degrees of complexity. If a fatigue experiment were performed at a given stress amplitude under HCF or VHCF, the most potent fatigue hot spot would be the dominant fatigue crack formation site. Other fatigue hot spots might serve as sites for secondary fatigue crack formation.

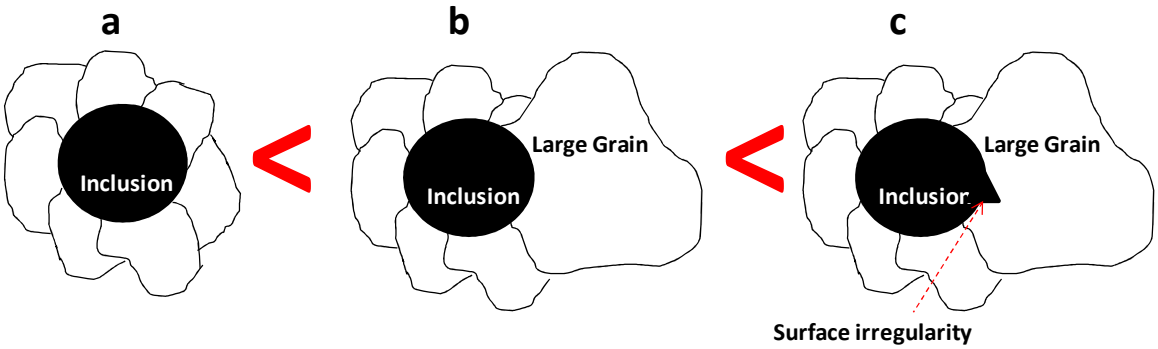

Figure 6-7: Degree of complexity for microstructure configurations. (a) Inclusion, (b) Inclusion next to a large grain, and (c) Inclusion with surface irregularity, next to a large grain.

Hyzak *et al.* [116] noted the significant influence of inclusion shape in the high cycle fatigue regime. They observed that the dominant fatigue cracks initiated from sharp hafnium oxide inclusions in AF-115 alloy despite the existence of other considerably larger but equiaxed non-metallic inclusions.

Wusatowska-Sarnek *et al.* [108] studied LCF crack initiation from oxide inclusions in IN100. Lifetime data corresponding to fatigue cracks incubated from surface inclusions seems to show a regular trend with respect to the equivalent inclusion size, with larger inclusions resulting in shorter lives. However, fatigue cracks seem to result from bulk inclusions of drastically different sizes for the same stress amplitude and fatigue life (Figure 6-8).

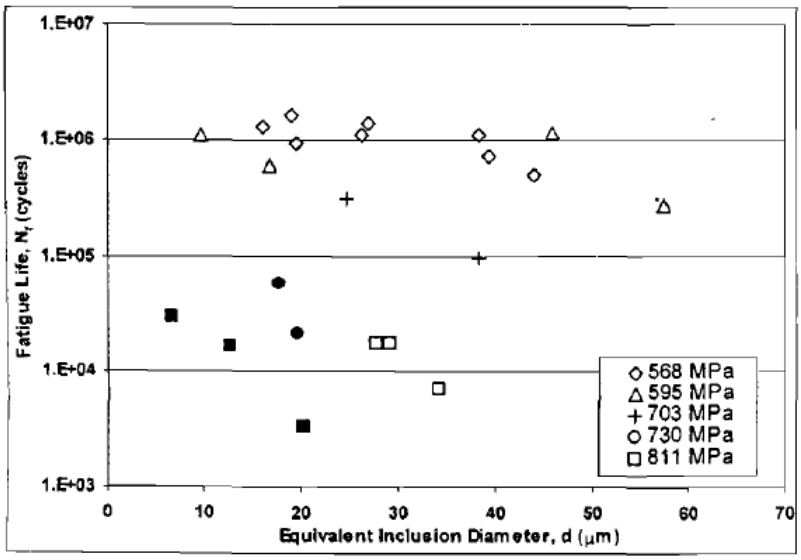

Figure 6-8: Fatigue life vs. the inclusion diameter (R=0.05). Internal and surface inclusions are referred to by open and full symbols, respectively [108].

This implies the influence of other microstructure attributes in addition to the inclusion size on fatigue strength. A similar conclusion can be drawn from Figure 6-9 by looking at the large variation in the crack initiation area of bulk non-metallic particles at constant N_f. The cooperative influence of these attributes can be detrimental to material integrity even if any given attribute by itself is subcritical.

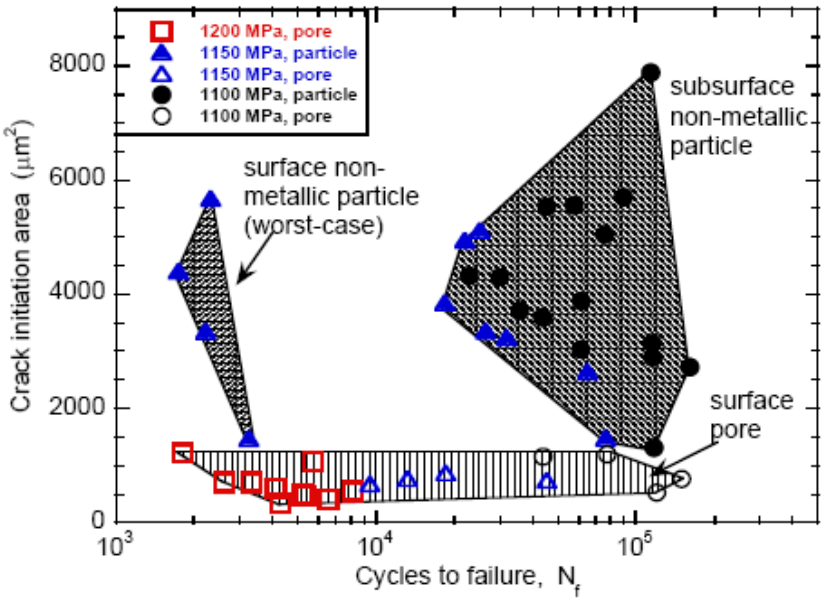

Figure 6-9: Lifetimes for surface and subsurface crack initiation locations in IN100 [14].

At low stress amplitudes, several microstructure attributes may need to work together to generate sufficient driving force for fatigue crack formation and early growth. For instance, a large non-metallic inclusion that can invariably incubate a fatigue crack at high stress amplitudes may need the additional influence of a large favorably oriented neighboring grain, to generate sufficient driving force for fatigue crack formation at low stress amplitudes.

If the expected number of fatigue hot spots for a given material volume, V, (i.e., component, test coupon, or regions therein) at a given stress amplitude is expressed by Ψ, then Ψ is a monotonically increasing function of σ_a, the applied stress amplitude, i.e.,

$$\sigma_1 > \sigma_2 > \cdots > \sigma_i \Rightarrow \Psi_{\sigma_a=\sigma_1} > \Psi_{\sigma_a=\sigma_2} > \cdots > \Psi_{\sigma_a=\sigma_i} \tag{6.6}$$

This is because the probability for a microstructure configuration decreases as it includes more critical microstructure attributes (cf. Figure 6-7).

The existing probabilistic approaches [18, 164] neglect the dependence of the expected number of critical fatigue hot spots on the stress amplitude and R_σ ratio. Thus, they fail to capture the decrease in surface versus bulk initiation probabilities with decreasing stress amplitude. Such frameworks only consider the dependence of surface and bulk initiation probabilities on specimen size and the number density and size distribution of primary inclusions.

6.4.2 Definition of surface versus internal crack initiation

The criterion that defines a surface fatigue crack initiation event is subjective, and no suitable classification currently exists. Initiation sites that under visual inspection of the fracture surface appear in the bulk and on the surface of the test specimen are categorized as internal and surface-originated cases. Figure 6-10 shows low magnification SEM fractographs of fatigue crack initiation from a ceramic inclusion located in the bulk (top) and on the surface (bottom) of the test specimen. The material is a Ni-base superalloy, René 95, tested at elevated temperature in strain control [165]. This classification is performed regardless of the number of fatigue cycles to failure.

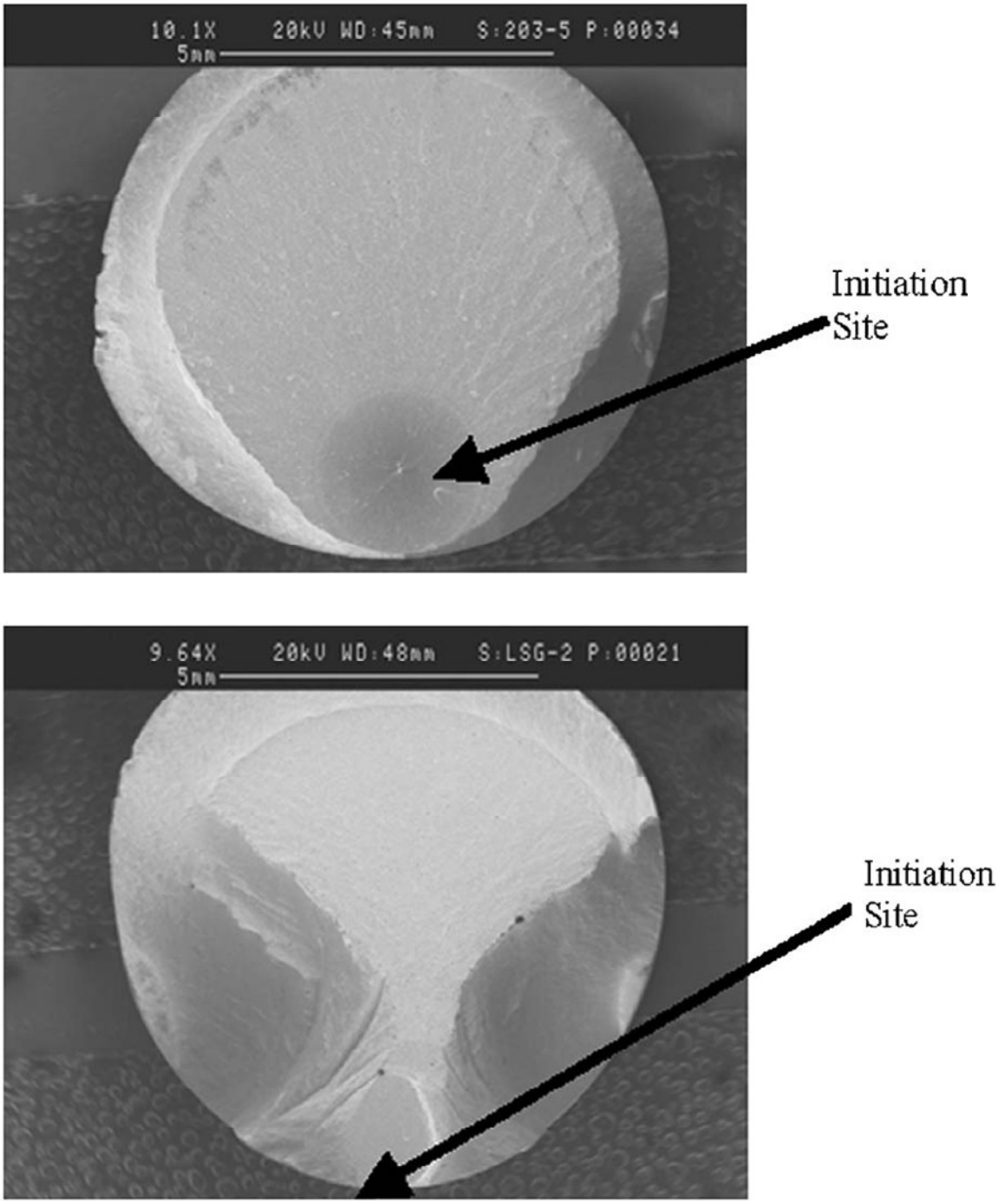

Figure 6-10: Fatigue crack initiation from ceramic inclusions in René 95; (top) internal fatigue initiation site, (bottom) surface initiation site [165].

For near surface initiation sites, a transition depth, d_t, needs to be defined beyond which fatigue failure initiation is considered internal (Figure 6-11).

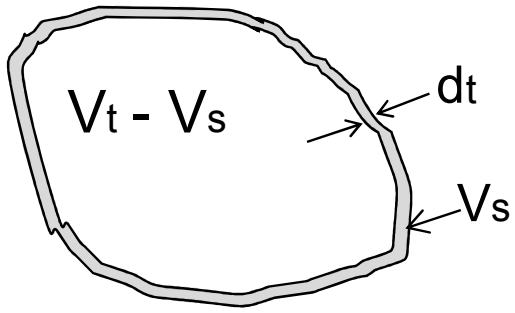

Figure 6-11: d_t = the transition depth; V_t = specimen total volume; V_S = specimen surface volume.

De Bussac [121] performed LCF experiments on specimens of N18 superalloy, a French patented PM Ni-base superalloy [122], and suggested a graphical criterion for defining d_t. He plotted the experimental fractographic measurements of the average size of the fatigue crack origin versus their depth from the free surface. The size of the fatigue crack origin was defined as the equivalent diameter, d_{eq}, of the critical non-metallic inclusion. This equivalent diameter was defined as the square root of the area of the box shown in Figure 6-12, i.e., $d_{eq} = \sqrt{D_{\max} \cdot D_{\perp}}$. The depth of the initiation site was defined as the minimum distance from the crack origin to the specimen free surface.

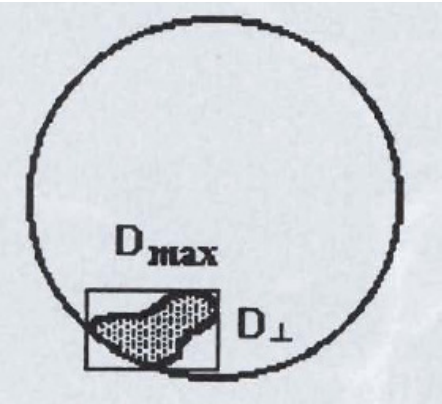

Figure 6-12: The definition of the equivalent diameter. D_{max} is the largest linear dimension of the critical non-metallic inclusion and $D_{\perp}$ is the dimension normal to D_{max} [121].

Figure 6-13 shows the average size of the fatigue crack origin versus their depth from the free surface.

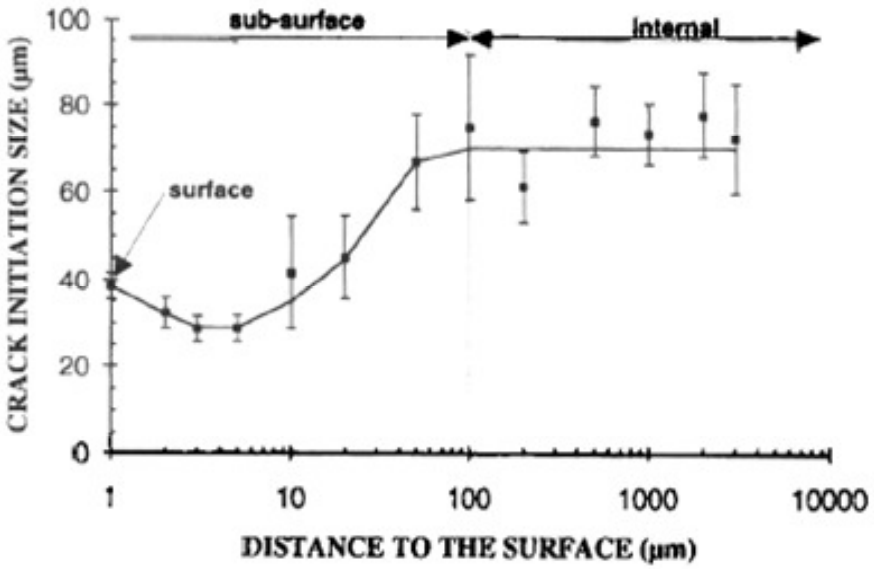

Figure 6-13: Size of the fatigue crack origin vs. its distance to the surface [121].

It can be seen in Figure 6-13 that beyond a critical depth of 100 μm, the average size of the fatigue crack origin remains constant. From this, bulk-originated fatigue failure was defined as crack formation at a depth greater than 100 μm. Between 0 and 100 μm from the surface, fatigue failure is classified as surface-originated. The average grain size for the N18 superalloy under study was 11 μm (9.5 ASTM) with a narrow size range, and the average size of the fatigue crack origins were 20-100 μm.

A particular definition for the transition depth, d_t, should be based on the differences between surface-originated and bulk-originated fatigue failure for the problem at hand. In our study, surface-originated fatigue failure corresponds to drastically shorter fatigue lives. Moreover, since we are considering HCF and VHCF crack failure from ceramic inclusions, fatigue crack formation and early growth are considered to consume most of the total fatigue life. Therefore, if these stages are not considerably influenced by the specimen free surface, the failure can be considered to have initiated internally.

The experimental data needed to define the transition depth, d_t, in the fine-grained IN100 superalloy of our study is lacking. As such, we use the definition by de Bussac [121], i.e., d_t = 100 μm, since the average size for ceramic inclusions and grains in the fine-grained IN100 superalloy of our study is comparable to those of de Bussac. This definition can, of course, be modified to accord with available experimental observations.

6.4.3 Surface initiation probability based on the number of fatigue hot spots

Surface initiation probability depends on the expected number of fatigue hot spots, because the infrequent configurations are more likely to be found in the bulk than

at the surface. To predict the ratio of probabilities of surface to bulk fatigue crack initiation, we must use a probabilistic mechanics framework that incorporates the probabilities that fatigue hot spots exist in the surface versus bulk regions.

Specific crack initiation mechanisms depend on experimental conditions such as loading, temperature, and environment, which pose challenges and opportunities for improvement in service life in the HCF and VHCF regimes. Therefore, an attempt is made in this thesis to maintain the generality of the framework so as to allow for future refinement.

In probability theory and statistics, the binomial distribution is the discrete probability distribution of the number of successes in a sequence of n independent yes/no experiments, each of which yields success with probability i. The probability of getting *exactly* k successes in n trials is given by the probability mass function [166]:

$$g(k) = \binom{n}{k} (i)^k (1-i)^{n-k} \tag{6.7}$$

The underlying assumptions of the binomial distribution are that there is only one outcome for each trial, that each trial has the same probability of success and that each trial is mutually exclusive. We use the binomial distribution to assess the probability distribution for a specific number of fatigue hot spots in the surface region. If Ψ hot spots can potentially initiate a surface originated fatigue crack, i.e., from within volume V_s, the probability mass function of having exactly k number of such fatigue hot spots in the surface region is given by

$$g(k) = \binom{\Psi}{k} \left(\frac{V_s}{V_t}\right)^k \left(\frac{V_t - V_s}{V_t}\right)^{\Psi - k} \tag{6.8}$$

where V_s and V_t are the volume of the surface region and the total volume of the specimen, respectively.

It is assumed that even one fatigue hot spot present in the surface region, V_s, can cause surface originated fatigue failure. In other words, regardless of the hot spot severity (determined by factors such as size, shape, or orientation of inclusions when inclusions are the main hot spots), a surface hot spot prevails over any internal hot spot.

This weakest-link approach is a reasonable way to account for the higher growth rate of surface fatigue cracks due to environment effects and to their higher stress intensity factor [116, 117, 119, 120] and is in agreement with the approach of Ravi Chandran *et al.* [18]. This assumption is particularly well-suited for study of the fine grained IN100 at 650°C chosen for this project, in which grain boundary oxidation has been shown to cause rapid intergranular crack growth [119].

It is possible that a bulk hot spot competes with one in the surface volume of the same specimen, especially for surface treated specimens. For specimens without surface treatment, this scenario is negligibly improbable. Figure 6-14 shows a very rare scenario in which a large internal inclusion has been almost at par with the surface inclusion in a Ni-base superalloy specimen without surface treatment [165]. The material is a Ni-base superalloy, René 95, tested at elevated temperature in strain control. The final failure was still due to the surface inclusion.

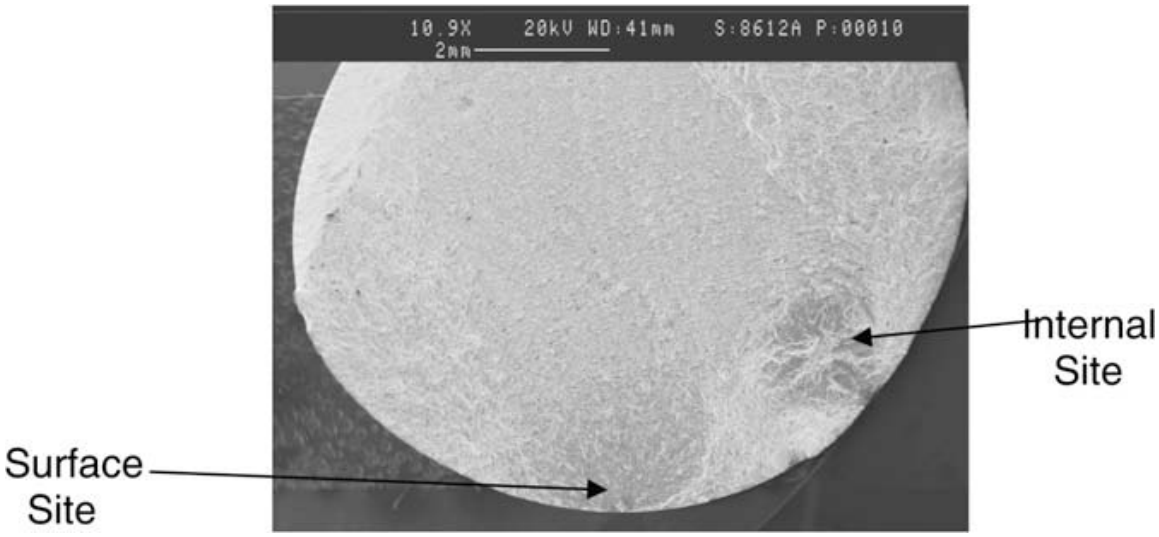

Figure 6-14: Fracture surface demonstrating competing surface and internal initiation sites [165].

The previous paragraph addresses the weak competing effect of bulk versus surface hot spots within the *SAME* specimen. It differs from the more general probabilistic notion of bulk versus surface failure probability, which refers to the outcome of experiments on a *number* of specimens. In the latter context, the bulk failure initiation probability may far exceed that of surface failure initiation in the VHCF regime. The probability of surface fatigue crack initiation, i.e., the probability of having at least one fatigue hot spot in the surface region, is given by

$$p_s = 1 - g(k=0) = 1 - \left(\frac{V_t - V_s}{V_t} \right)^{\Psi} \tag{6.9}$$

Fatigue failure is expected to originate from bulk fatigue hot spots if and only if such hot spots are absent in the specimen surface region. The probability of bulk fatigue

crack initiation, i.e., the probability of having no fatigue hot spot in the surface region, is therefore given by

$$p_b = g(k=0) = \left(\frac{V_t - V_s}{V_t} \right)^{\Psi} \tag{6.10}$$

Now, if at stress amplitudes $\sigma_a = \sigma_1$ and $\sigma_a = \sigma_2$, Ψ_1 and Ψ_2 number of fatigue hot spots can produce sufficient driving force for fatigue crack initiation, then $\sigma_1 > \sigma_2$ renders $\Psi_1 > \Psi_2$, and this in turn results in $p_s(\sigma = \sigma_1) > p_s(\sigma = \sigma_2)$, since $\frac{V_t - V_s}{V_t} < 1$. In other words, as the stress amplitude decreases, so do the expected number of fatigue hot spots, Ψ, and the probability of having a hot spot in the surface relative to the bulk. The problem now is to predict the dependence of Ψ on loading conditions, which are specific to the material of interest.

The methodology proposed in this thesis is appropriate for other advanced alloys, such as titanium alloys and clean steels, by recognition of similar competing mechanisms involving non-metallic particles, large grains, α cluster-defects, or phases that are particularly susceptible to fatigue crack formation. Distributed fatigue crack formation depends not only on microstructure but also on the applied loading/boundary conditions.

Przybyla and McDowell [51] have recently proposed a new microstructure-sensitive extreme value statistical framework. It couples the extreme value distributions of certain fatigue indicator parameters (FIPs), or response functions, to the correlated microstructure attributes that exist at the extreme value locations of these FIPs. By mathematically representing fatigue driving force parameters, or so-called FIPs, in the

space of basis functions used to represent distribution functions of microstructure attributes, this enables identification of hot spot regions that are above a FIP threshold.

It should be noted that the model's variables and parameters depend on the microstructure. Thus, the proposed framework needs to be calibrated to experimental fatigue life data for specific microstructures. The philosophy adopted here is that the formulation (and the simulations therein) should be calibrated to experimental data for selected loading conditions, thereafter providing the capability to assess the sensitivity of fatigue life predictions to variations of microstructure and loading conditions within their calibrated range.

6.5 Suggested physical mechanisms of surface initiation dependence on the stress amplitude in alloys with inclusions

Since the variation of p_s and p_b with respect to the stress amplitude is assessed by studying the stress amplitude dependence of Ψ, several important physical mechanisms that can affect the dependence of Ψ on the stress amplitude are introduced in this section. References are made to fine grained microstructures of PM processed Ni-base superalloys, but these mechanisms can operate in other advanced metallic alloys with primary inclusions controlling fatigue failures.

6.5.1 Inclusion-matrix interface separation

The results of Chapter 4 suggest that as the stress amplitude decreases, a smaller number of inclusions may debond or crack; hence a smaller number of inclusions may produce enough driving force to initiate fatigue cracking in the surrounding matrix. As a result, Ψ decreases with the stress amplitude through the lower probability of inclusion-matrix interface debonding and inclusion cracking.

It should be noted that inclusion-matrix interface debonding is mainly due to the residual stresses resulting from prior processing. Most inclusions could be already debonded before the application of cyclic loading. Nevertheless, Even if a small percentage of inclusions debond during fatigue loading, this percentage decreases as the cyclic stress/strain amplitude decreases. Thus, this mechanism decreases the surface initiation probability.

6.5.2 Residual stress relaxation

The results of Chapter 5 suggest that for a given R ratio and as the stress amplitude decreases, compressive residual stresses do not relax at some of the inclusions (that would otherwise relax at the higher stress amplitudes). These compressive residual stresses can effectively suppress fatigue crack initiation at some of the inclusions. Therefore, statistically speaking, Ψ decreases with decreases in the stress amplitude through retention of beneficial compressive residual stresses. Figure 6-15 shows experimental proof that the initial cyclic plastic strains generated at higher strain ranges and strain ratios apparently reduced the magnitude of shot peening compressive residual stresses sufficiently to promote surface fatigue crack initiation [129].

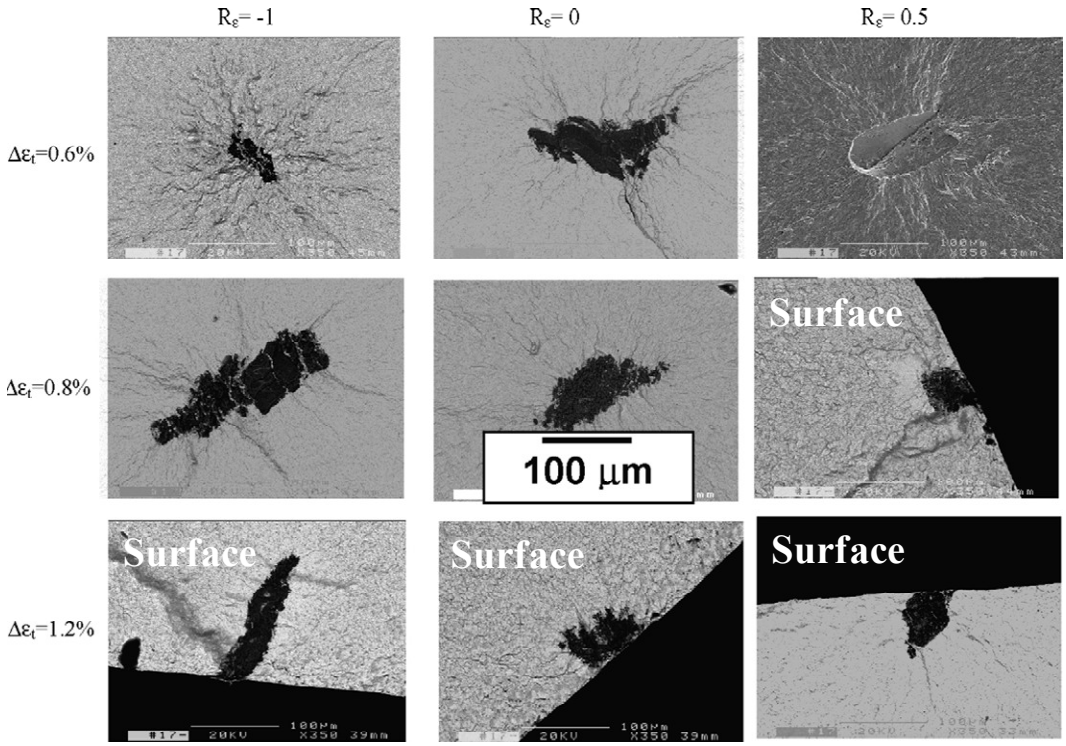

Figure 6-15: Fatigue failure origins of shot peened PM Udimet720 tested at 650 ◦C [129].

6.5.3 *Effect of proximity to the free surface*

The matrix ligament between a near surface inclusion and the specimen free surface experiences increased deformation when a far-field displacement is applied. At the continuum level, this is due to the reduced constraint on the deformation in this region. This effect can explain enhancement of fatigue crack initiation from surface or near surface inclusions in spite of existence of larger inclusions in the bulk.

To illustrate this influence, finite element simulation results are briefly reported here for linear elastic partially debonded inclusions with radii R = 10 and 15 μm located near the free surface, as shown in Figure 6-16. Only one microstructure realization (Voronoi seed spatial distribution and grain orientation distribution) is examined. Inclusion depth is defined as the minimum distance of the inclusion edge from the surface. Contact between the inclusion and matrix in the debonded region is assumed to be frictionless.

We use two-dimensional generalized plane strain (GPS) elements [49] (see Section 2.4.1), often referred to as 2.5D, and the fully 3D crystal plasticity material model (see Section 2.1.2). The crystal plasticity material model constants and microstructure parameters are listed in Table 3 and Table 4, respectively. Properties assigned for the fully isotropic elastic inclusion include Young's modulus E^i = 400 GPa and Poisson's ratio ν^i = 0.3. Quadratic triangular elements of type CPEG6M are used to mesh the FE model (see Section 2.1.2). The elastic properties for the far-field matrix region are Young's modulus, E^m = 142 GPa, and Poisson's ratio, ν^m = 0.25 (see Section 2.4.3).

The following boundary conditions are enforced; assuming the origin of the *xyz* coordinate system is at the center of the model:

1. The traction free boundary condition is enforced for the entire length of the model's right edge (x = L/2 and -L/2 < y < L/2).
2. The x-symmetry boundary condition ($u_x = 0$) is enforced for the entire length of the model's left edge (x = -L/2 and -L/2 < y < L/2).
3. The y-symmetry boundary condition ($u_y = 0$) is enforced for the entire length of the model's bottom edge (y = -L/2 and - L/2 < x < L/2).
4. The z-symmetry boundary condition ($u_z = 0$) is enforced to the reference point of the GPS model.
5. Cyclic uniaxial displacement $u_y = \varepsilon_{yy} \times L$ is applied to the entire length of the model's top edge (y = L/2 and - L/2 < x < L/2) at the peak applied strain amplitude $\varepsilon_{yy} = 0.0015$, strain ratio $R_\varepsilon = -1$, and uniform strain rate of 0.002 s^{-1}.

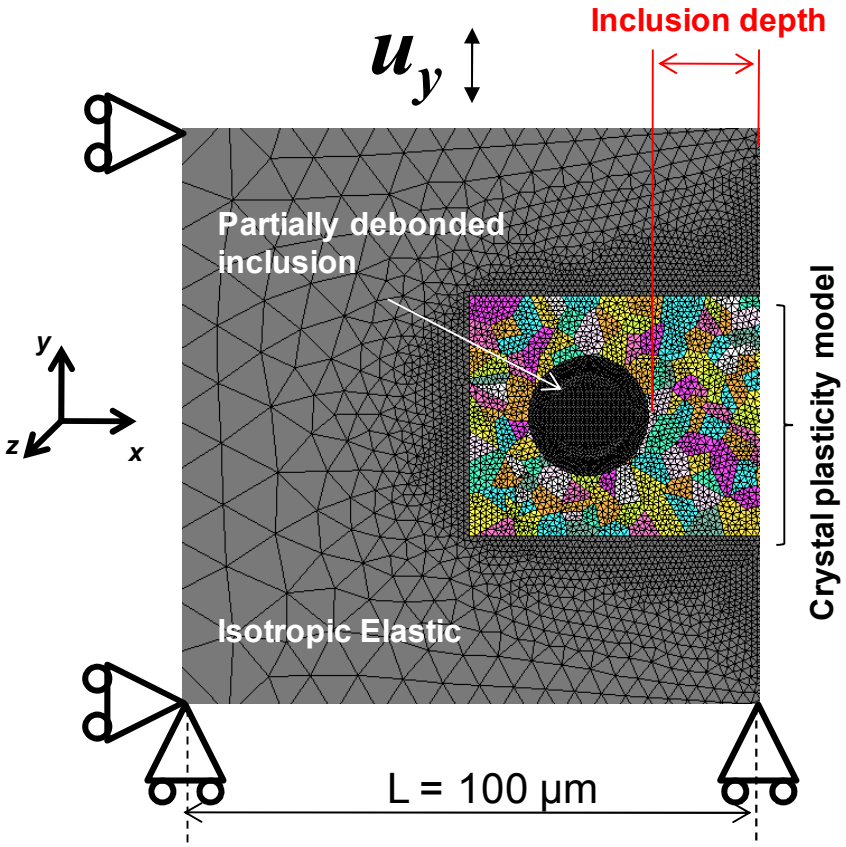

Figure 6-16: FE model for simulations of partially debonded near-surface inclusions. Inclusion depth is defined as the minimum distance of the inclusion edge from the surface.

The Fatemi-Socie P_{FS} parameter (c.f. Section 2.2) is calculated for the 3rd loading cycle. Figure 6-17 shows the variation of P_{FS} parameter versus inclusion depth from the specimen's free surface for partially debonded inclusions with radii R = 10 and 15 μm. As shown in Figure 6-17 for partially debonded inclusions and peak applied strain amplitude ε_{yy} = 0.0015 (R_ε = -1), the P_{FS} parameter may increase substantially when the inclusion depth is smaller than its radius. The simulation-based weighted probabilistic construct developed in this thesis (described in Section 6.6) is capable of handling the

effects of proximity to the free surface. However, we do not include the free surface effect when we examine a case study in Chapter 7.

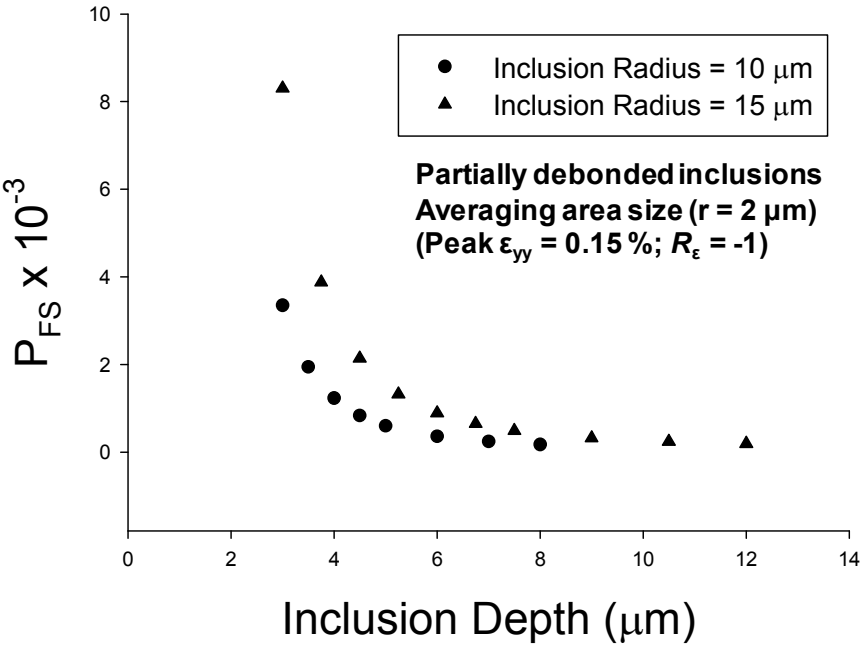

Figure 6-17: Nonlocal Fatemi-Socie P_{FS} parameter around partially debonded inclusions versus inclusion depth for two inclusions with radii of 10 μm and 15 μm (Peak ε_{yy} = 0.15 % and R_{ε} = -1).

6.5.4 Surface oxidation effects

Among other factors, the environment may significantly influence the surface versus bulk fatigue crack initiation probabilities through either environmentally assisted fatigue crack growth at high strain amplitudes or through the formation of protective surface oxide layers at low strain amplitudes.

Mechanically sound surface oxide scales can form at elevated temperatures due to the dynamic equilibrium between continuous microcracking and superimposed oxide-healing processes [167]. It is possible that surface oxidation at elevated temperature retards crystallographic crack incubation at the surface, in which case cyclic strain localization becomes dominant in favorably-oriented, large subsurface grains. This agrees with the observations by Huron and Roth [123], who noted the decreased relative frequency of crystallographic surface fatigue crack formation in the same material at the intermediate temperature of 650°C.

In this thesis, we do not intend to address the mechanisms of surface oxide formation and the detailed analysis of its impact on Ψ. As such, we consider it sufficient to qualitatively discuss a possible scenario in which a sound surface oxide scale can reduce Ψ. Due to addition of alloying elements such as chromium, aluminum, and titanium, most Ni-base superalloys have chromia or alumina rich surface oxides, an example of which is shown in the SEM micrograph of Figure 6-18.

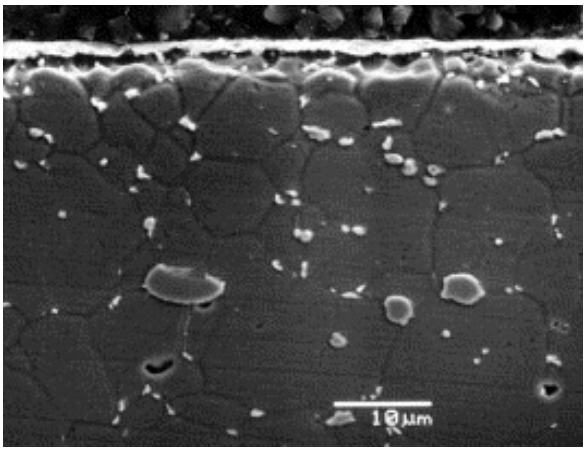

Figure 6-18: SEM micrograph of Haynes 242 alloy cross-section after 60 min of exposure at 900 °C, showing the presence of a chromia oxide layer on the specimen surface [168].

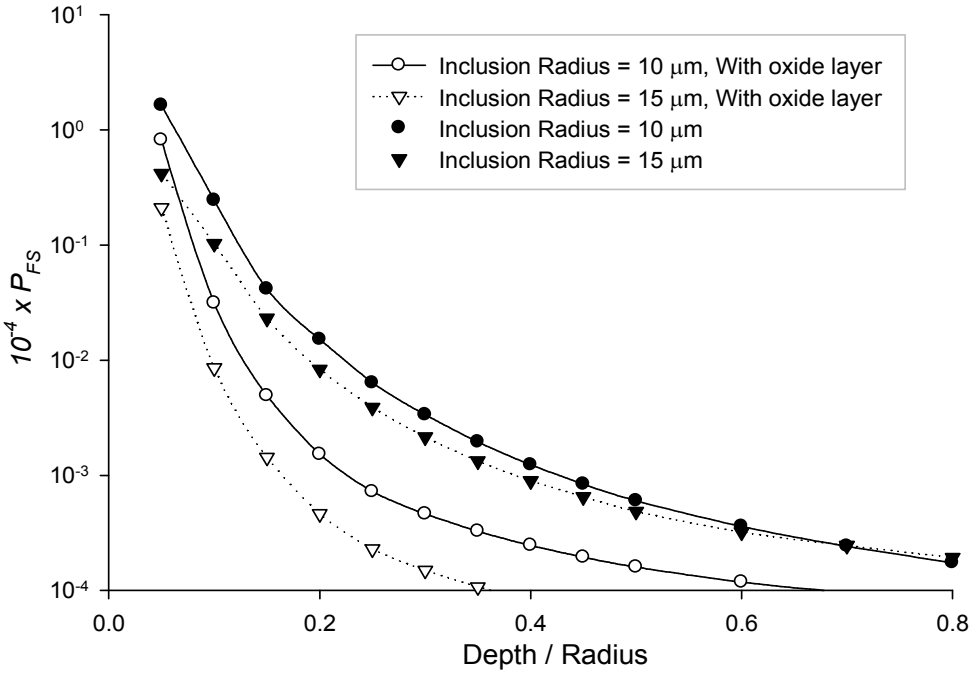

Figure 6-19: Fatemi-Socie parameter P_{FS} vs. normalized inclusion depth from the free surface. (R_ε = -1, ε_{max}=0.15%). Surface oxide layer is 2 µm thick.

Assisted by increased plasticity at elevated temperatures [169], the oxide layer may endure the applied stress in the VHCF regime. In addition to protecting the underlying metal from environmental corrosion, a surface oxide layer can alter the fatigue crack initiation potency of near surface primary inclusions. To illustrate this, the nonlocal Fatemi-Socie parameter P_{FS} (see Section 2.2.2) for cylindrical inclusions located at various depths from the free surface is shown in Figure 6-19 with and without a 2 μm thick intact isotropic linear elastic surface oxide layer. The elastic modulus and Poisson's ratio of the surface oxide layer are assumed to be equal to E = 400 GPa and ν = 0.2, respectively, in these simulations [169]. As seen in Figure 6-19, the surface oxide layer can affect a pronounced decrease in initiation potency of near surface inclusions. Thus, Ψ can decrease when the oxide layer is less likely to fracture at low stress amplitudes.

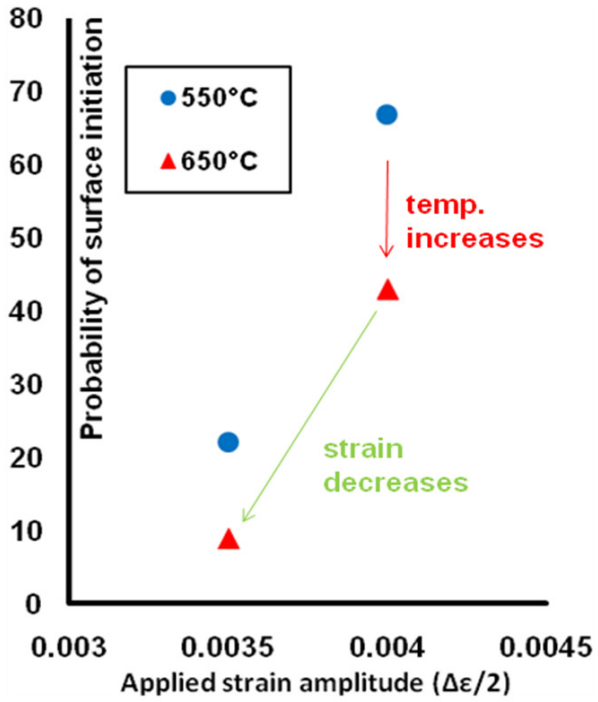

Figure 6-20: Surface initiation probability vs. strain [121].

Figure 6-20 is constructed from experimental fatigue data of N18 PM Ni-base superalloy, reported by de Bussac [121]; it shows the decrease in surface crack initiation probability (increase in bulk initiation probability) as the strain level decreases for tests performed at a constant temperature. For a given strain level, the surface initiation probability decreases for increasing temperature.

Cashman [126] also reported enhanced probability of surface initiation at the higher temperature of 1000°F, compared to the results at 750°F; this is shown in Figure 6-21 by the binary logistic fit [161] to the experimental data of PM René 95. The ordinate is identified as pseudostress amplitude, defined as $\left(E\Delta\varepsilon/2\right)$.

In a recent paper [19], Cashman concludes that the "Competing Modes" effect (i.e., the occurrence of surface and bulk failure among specimens tested under the same conditions) is temperature dependent because of the environmental contribution. They found it puzzling that surface fatigue crack initiation might diminish at higher temperatures. Our hypothesis regarding the formation of protective surface oxide layers can explain this anomalous effect as an enhancement of surface oxidation caused by increased temperature.

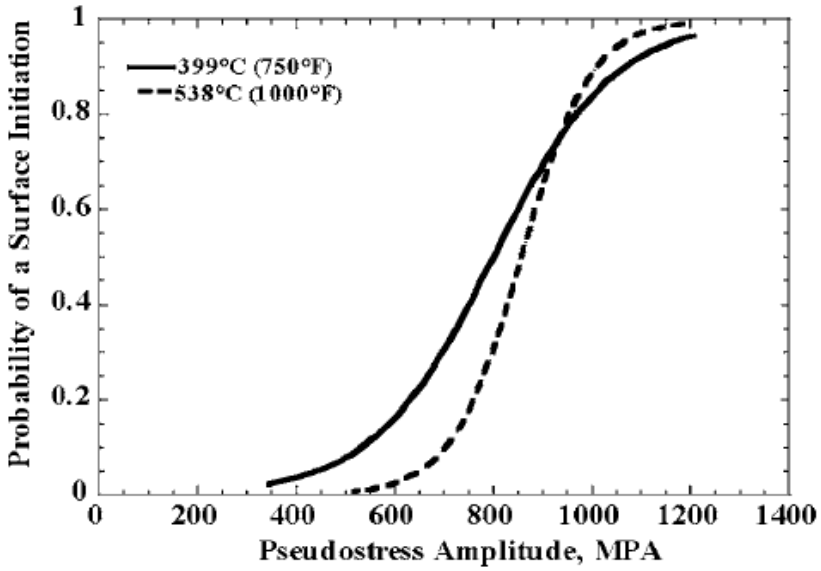

Figure 6-21: Surface initiation probability vs. pseudostress amplitude and temperature [126].

Oxide scale growth has complex effects on the net ratio of probabilities of surface to bulk fatigue crack initiation. For instance, the fatigue crack initiation potency, as measured by the P_{FS} parameter, of a near surface inclusion decreases as the oxide layer grows, as shown in Figure 6-22. However, the mean size of the pores that form in the oxide scale increases during scale growth (see Figure 6-23), and so does the probability of scale failure (because stress intensity at the notch root of the pore increases as the pore size increases).

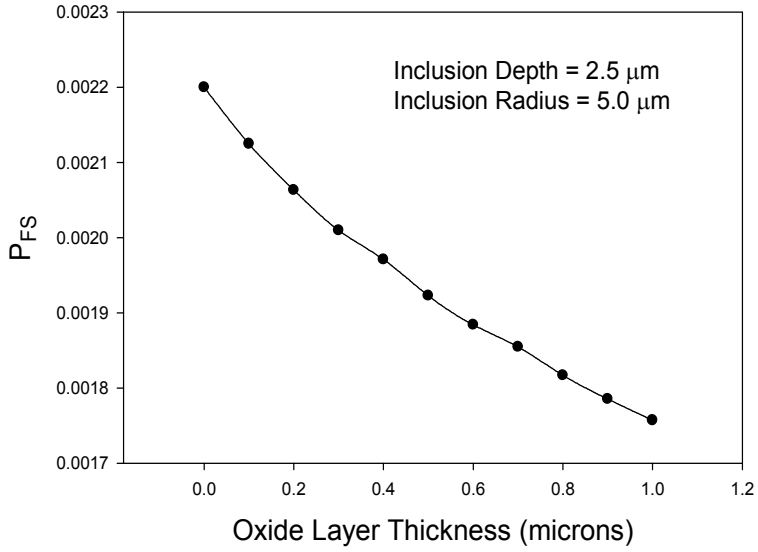

Figure 6-22: Nonlocal P_{FS} parameter vs. oxide layer thickness; symbols are computed data points.

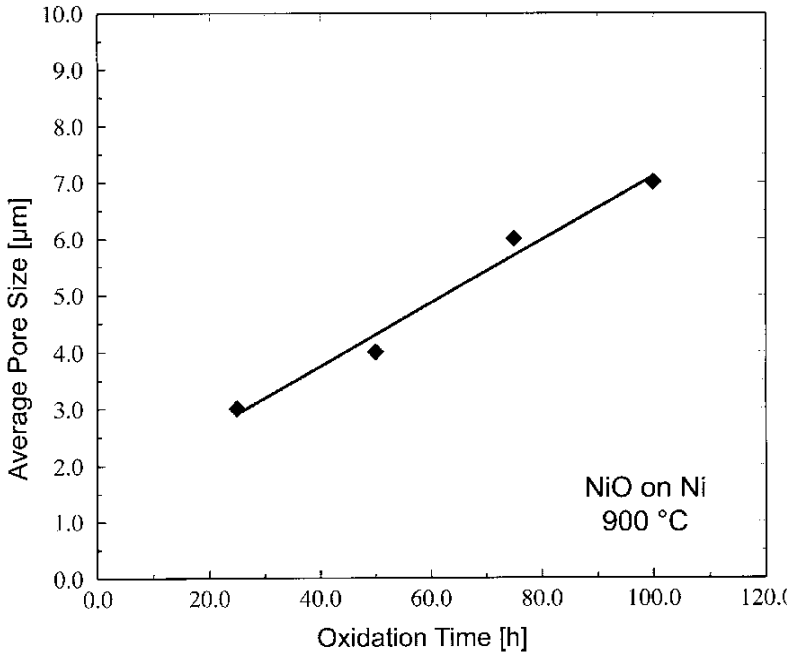

Figure 6-23: Average pore size in the oxide scale vs. oxidation time [170]. Oxide scale is formed on Ni99.6 after oxidation at 900°C in air.

The oxidation behavior of metallic alloys is complex in its own right due to the interplay between heterogeneous oxide growth, oxide interaction, oxide volatilization,

and spalling. The properties of the surface oxide layer depend on many factors, such as stress amplitude, loading history, environment, and oxidation time and temperature to name a few. Unfortunately, there are relatively few techniques available for measuring the mechanical properties of surface oxides, and the properties of the surface oxides formed are invariably different from those of bulk oxides. The surface oxide layer also alters the dislocation activity of the near surface grains, as dislocation motion and formation of extrusions and intrusions are resisted by this layer.

Therefore, detailed study of the influence of an intact protective surface layer is essential, as it will enable more realistic assessment of the contribution that such a layer makes to the surface to bulk transition of mean fatigue behavior. These effects are beyond the scope of this thesis.

6.6 The expected number of fatigue-critical inclusions and pores

Assuming bimodal fatigue crack initiation from inclusions and pores, the expected number of fatigue hot spots can be expressed as

$$\Psi = \Psi_{inclusion} + \Psi_{pore} \tag{6.11}$$

where $\Psi_{\text{inclusion}}$ and Ψ_{pore} are the numbers of inclusion and pore hot spots in a given volume, respectively, determined as

$$\Psi_i = n_i \, P_i^{\sigma} \qquad \text{i = inclusion or pore} \tag{6.12}$$

Here, n_i, is the expected number of inclusions or pores, determined as

$$n_i = \rho_i \, V \qquad \text{i = inclusion or pore} \tag{6.13}$$

where V is the specimen material volume having a uniform stress state and ρ_i is the inclusion/pore density per unit volume.

The stress amplitude-dependent variable P_i^{σ} is the probability that an arbitrary inclusion (or pore) is a fatigue hot spot, i.e., it can produce sufficient driving force to incubate a fatigue crack (see Section 6.4.1). For an arbitrary inclusion, the general form can be expressed via summing a series of weighted probabilities as

$$P_{inclusion}^{\sigma} = \sum_{type} \left\{ \sum_{\text{int}erface} \left[\int P_R^{type} \; P_{(\text{int}erface|R,type,\sigma)} \; C_{(R,type,\text{int}erface)}^{inclusion}(\sigma) \; dR \right] \right\} \tag{6.14}$$

where the summations are performed over all possible inclusion types and inclusion-matrix interfaces. Generally, inclusion types can refer to such attributes as the inclusion

mechanical properties (i.e., soft versus hard or elastic versus elastoplastic) or inclusion morphological features (i.e., round versus elongated).

The variable P_R^{type} refers to the probability distribution of size for an inclusion of certain type. The variable $P_{(\text{int}erface|R,type,\sigma)}$ is the conditional probability of the inclusion interface for an inclusion of certain size and type. For instance, we examined the interface traction in Chapter 4 as one way of characterizing the probability of inclusion-matrix interface debonding for cylindrical ceramic inclusions. Consequently, we derived an expression for P_{debond}^{ω} in Eq. 4.6.

The variable $C_{(R,type,\text{int}erface)}^{inclusion}(\sigma)$ is the conditional probability that this inclusion of certain size, type, and interface characteristics is a fatigue hot spot at a given stress amplitude. For an arbitrary pore, P_i^{σ} can be more simply defined as

$$P_{pore}^{\sigma} = \int P_R^{pore}\ C_R^{pore}(\sigma)\ dR \tag{6.15}$$

where R is the inclusion size (radius), P_R^{pore} refers to the size distribution of pores and $C_R^{pore}(\sigma)$ is the conditional probability that it is a fatigue hot spot at a given stress amplitude. The integrations in Eq. 6.14 and Eq. 6.15 are performed over the inclusion/pore size distribution.

In Chapter 7, we use an extreme value distribution of the simulated Fatemi-Socie parameter to characterize the conditional probability $C_{(R,type,\text{int}erface)}^{inclusion}(\sigma)$ for partially debonded ceramic inclusions in Ni-base superalloy, IN100.

6.7 Summary

The relative paucity of inclusions in PM alloys, compared to their cast and wrought counterparts leads to higher mean fatigue lives but broader distribution of fatigue lives. Consequently, inclusion-initiated failure has a greater impact on variability of the PM processed alloy fatigue life due to its relative cleanness. In fact, PM processing results in such a rare occurrence of relatively large defects that conventional experimental characterization with a limited number of small-volume fatigue test specimens does not adequately sample inclusion-initiated damage to characterize the surface initiation probabilities.

We introduced a simulation-based methodology to characterize the surface initiation probabilities, with an emphasis on the early stages of HCF and VHCF crack initiation mechanisms from inclusions and pores. We calculated the probability of fatigue crack initiation in the surface region by computing the expected number of critical fatigue hot spots in this region. This is done by considering the fatigue crack initiation potency of inclusions/pores for a given loading ratio and stress amplitude. In Chapter 7, we will examine a case study where we assess the fatigue crack initiation potency of partially debonded ceramic inclusions in IN100 by calculating FIPs using the finite element crystal plasticity simulations.

More research needs to be done to incorporate the joint extreme value statistics of key relevant microstructure attributes into analytical life-prediction methodologies that quantify their coupled effects on fatigue life in the HCF and VHCF regimes. These effects depend on applied stress amplitude, mean stress and stress state. One must

characterize the degree of dependence of these effects on the local stress state to realistically assess the surface to bulk transition of HCF crack initiation sites.

7 Case study: Surface initiation probability in Ni-base superalloy, IN100

7.1 Approach

In this case study, we examine the surface initiation probability in uniaxial strain-controlled cyclic loading simulations of round smooth specimens of the fine grained PM processed Ni-base superalloy IN100. We assume that partially debonded alumina inclusions are the main source of fatigue crack initiation (formation and early growth). This assumption is reasonable because:

- Pores are not present in the PM processed IN100 parts. Ceramic inclusions, on the other hand, are a by-product of the PM processing technique (see Section 3.1).
- We concluded in Chapter 3 that partially debonded inclusions are more critical than halved and intact, perfectly bonded inclusions.

Accordingly, the expected number of fatigue hot spots at an applied strain amplitude $\omega = \varepsilon_{yy} / \varepsilon_{ys}$ for (R_ε = -1) is:

$$\Psi = \Psi_{inclusion} = n_{inclusion}\ P^{\omega}_{inclusion} = \rho\ V\ P^{\omega}_{inclusion} \tag{7.1}$$

where V is the volume of the specimen gage section having a uniform stress state and ρ is the inclusion density. Also, Eq. 6.14 reduces to

$$P^{\omega}_{inclusion} = \int P_R\ p^{R,\omega}_{debond}\ C^{R,\omega}_{debonded}\ dR \tag{7.2}$$

where R is the inclusion size (radius) and P_R refers to the size distribution of inclusions. The variable $p_{debond}^{R,\omega}$ is the probability that an inclusion of radius R debonds under the applied strain amplitude ω. According to Chapter 4, it can be calculated as

$$p_{debond}^{R,\omega} = \Pr(T_{int} > T_{int}^*) \tag{7.3}$$

and

$$\Pr(T_{int} > T_{int}^*) = 1 - c_R^{\omega}(T_{int}^*) \tag{7.4}$$

Here, $c_R^{\omega}(T_{int}^*)$ is the cumulative probability that an inclusion with radius R results in an interface separation indicator parameter smaller than a critical threshold T_{int}^* under the applied strain amplitude ω. The interface separation indicator parameter is T_{int} for this case study (see Section 2.2.4). We obtained T_{int}^* by solving $C^{\omega=0.8}\left(T_{int}^*\right) = 0.05$ based on the assumption that the nominal remote applied strain amplitude of ω = 0.8 is high enough that 95% of inclusions would debond. Using the generalized extreme value (GEV) distribution (see Section 2.3), the probability of exceedance can be expressed as

$$\Pr(T_{int} > T_{int}^*) = 1 - \exp\left\{-\left[1 + \xi_{T_{int}}\left(\frac{T_{int}^* - \mu_{T_{int}}}{\sigma_{T_{int}}}\right)\right]\right\}^{\frac{-1}{\xi_{T_{int}}}} \tag{7.5}$$

where $\mu_{T_{int}}$, and $\sigma_{T_{int}}$, and $\xi_{T_{int}}$ are the location, scale, and shape parameters of the GEV distribution, calibrated to the extreme value T_{int} distribution for the particular inclusion radius and the applied strain amplitude.

Similarly, the variable $C_{debonded}^{R,\omega}$ is defined as the conditional probability that a debonded inclusion with radius R is a fatigue hot spot at a given applied strain amplitude. This conditional probability can be expressed as the probability that the P_{FS} parameter, the underlying FIP for this case study, exceeds a material-specific threshold, P_{FS}^{*}.

$$C_{debonded}^{R,\omega} = \Pr(P_{FS} > P_{FS}^{*}) \tag{7.6}$$

Using the GEV distribution, the probability of exceedance can be expressed as

$$\Pr(P_{FS} > P_{FS}^{*}) = 1 - \exp\left\{-\left[1 + \xi_{FS}\left(\frac{P_{FS}^{*} - \mu_{FS}}{\sigma_{FS}}\right)\right]\right\}^{\frac{-1}{\xi_{FS}}} \tag{7.7}$$

where μ_{FS}, and σ_{FS}, and ξ_{FS} are the location, scale, and shape parameters of the GEV distribution, calibrated to the extreme value P_{FS} distribution for the particular inclusion radius and the applied strain amplitude. In the next Section, we use 2.5D crystal plasticity FE analysis to characterize the parameters of their GEV distributions.

7.2 Finite element model

We use two-dimensional generalized plane strain (GPS) elements [49] (see Section 2.4.1), often referred to as 2.5D, and the fully 3D crystal plasticity material model. The crystal plasticity model is calibrated to experimental data at T = 650°C by Shenoy *et al.* [50]. The model constants and microstructure parameters are listed in Table 3 and Table 4, respectively. Properties assigned for the fully isotropic elastic inclusion include Young's modulus E^i = 400 GPa and Poisson's ratio v^i = 0.3.

Quadratic triangular elements of type CPEG6M are used to mesh the FE model (see Section 2.1.2). The full model, shown in Figure 2-7, is utilized to mitigate any boundary effects. We utilize the T_{int} parameter (see Section 2.2.4) distributions for the intact, perfectly bonded inclusions simulated in Section 4.3 to estimate $p_{debond}^{R,\omega}$. For calculating $C_{debonded}^{R,\omega}$, partially debonded inclusions having R = 4, 6, 8, and 10 μm are simulated, with L = 60 μm. In simulations with partially debonded inclusions, contact between the interacting surfaces is assumed to be frictionless. The following boundary conditions are enforced; assuming the origin of the *xyz* coordinate system is at the center of the inclusion/pore:

1. The traction free boundary condition is enforced for the entire length of the model's left and right edges (x = -L/2, L/2 and -L/2 < y < L/2).
2. The y-symmetry boundary condition (u_y = 0) is enforced for the entire length of the model's bottom edge (y = -L/2 and - L/2 < x < L/2).
3. The z-symmetry boundary condition (u_z = 0) is enforced to the reference point of the GPS model.

4. Cyclic uniaxial displacement $u_y = \varepsilon_{yy} \times L$ is applied to the entire length of the model's top edge (y = L/2 and - L/2 < x < L/2) at the applied strain amplitudes ε_{yy} = 0.5, 0.6, 0.7, and 0.8 ε_{ys} (ε_{ys} = 0.7 % (c.f. 2.4.3)), strain ratio R_ε = -1, and uniform strain rate of 0.002 s^{-1}.

A total of 20 polycrystalline orientation distributions are simulated for each applied strain amplitude. The Voronoi tessellation diagram is held constant across these realizations and only grain orientations vary. A fine mesh, with element size equal to 0.5 μm, is used for all grains that are within *R/4* distance from the inclusion, because the deformation is mainly localized in this region. Beyond *d = R/4,* the element size increases linearly with increasing distance from the inclusion, in order to reduce the computation time.

Upon completion of the 3rd cycle, the modified Fatemi-Socie parameter P_{FS} is calculated as the Fatigue Indicator Parameter (see Section 2.2.2) for each inclusion radius, polycrystalline orientation distribution, and applied strain amplitude. The semicircular nonlocal averaging region is taken to be of a constant size r = 3 μm (about 5% of the largest simulated inclusion area, R = 10 μm) in order to account for the size effects. This averaging region is located at the slip-intensified region of the inclusion notch root, as shown in Figure 2-7.

7.3 Model calibration

The GEV distribution (see Section 2.3) is fitted to T_{int} distributions for the 20 polycrystalline orientation distributions simulated in Section 2.2.4. Table 12 lists the parameters of the fitted GEV distributions for the range of simulated inclusion radii and applied strain amplitudes for intact, perfectly bonded inclusions. Here, μ is the location parameter, $\sigma > 0$ is the scale parameter and ξ is the shape parameter.

Table 12: Parameters of the GEV fits to the T_{int} for the intact, perfectly bonded inclusions.

		Remote applied strain amplitude ($\varepsilon_{yy}/\varepsilon_{ys}$); R_ε = -1.											
		0.5			0.6			0.7			0.8		
Inclusion Radius (μm)		μ_{int}	σ_{int}	ξ_{int}	μ_{int}	σ_{int}	ξ_{int}	μ_{int}	σ_{int}	ξ_{int}	μ_{int}	σ_{int}	ξ_{int}
	4	520.48	57.43	-0.4428	624.48	68.11	-0.4442	728.73	79.44	-0.4445	833.16	90.34	-0.4511
	6	727.32	45.64	-0.4075	872.17	54.99	-0.4119	1017.17	63.92	-0.4137	1155.92	67.50	-0.4491
	8	744.34	43.91	-0.0802	892.78	53.10	-0.0935	1041.09	61.08	-0.1106	1175.04	62.95	-0.1603
	10	748.99	31.95	0.2384	898.71	38.28	0.2401	1047.65	43.66	0.2331	1183.82	43.67	0.1830

Furthermore, the GEV distribution is fitted to the extreme value P_{FS} parameter around partially debonded inclusions for the 20 simulated polycrystalline orientation distributions. Table 13 lists the parameters of the fitted GEV distributions for the range of simulated inclusion radii and applied strain amplitudes.

Table 13: Parameters of the GEV fits to the P_{FS} for the partially debonded inclusions.

		Remote applied strain amplitude ($\varepsilon_{yy}/\varepsilon_{ys}$); R_ε = -1.											
		0.5			0.6			0.7			0.8		
Inclusion Radius (μm)		μ_{FS}	σ_{FS}	ξ_{FS}	μ_{FS}	σ_{FS}	ξ_{FS}	μ_{FS}	σ_{FS}	ξ_{FS}	μ_{FS}	σ_{FS}	ξ_{FS}
	4	5.79×10^{-5}	1.99×10^{-5}	0.2029	14.78×10^{-5}	6.32×10^{-5}	-0.0963	36.41×10^{-5}	12.03×10^{-5}	-0.1530	76.30×10^{-5}	22.22×10^{-5}	-0.1513
	6	18.51×10^{-5}	5.57×10^{-5}	0.0702	47.13×10^{-5}	12.52×10^{-5}	-0.1557	102.26×10^{-5}	24.69×10^{-5}	-0.2355	208.17×10^{-5}	41.85×10^{-5}	-0.2936
	8	31.98×10^{-5}	9.38×10^{-5}	-0.0966	79.92×10^{-5}	15.17×10^{-5}	0.0691	169.52×10^{-5}	40.08×10^{-5}	-0.1530	315.37×10^{-5}	66.75×10^{-5}	-0.0449
	10	43.0×10^{-5}	15.3×10^{-5}	-0.1911	98.4×10^{-5}	29×10^{-5}	-0.1189	198.8×10^{-5}	46.5×10^{-5}	-0.0122	412.0×10^{-5}	83.3×10^{-5}	-0.1736

Figures 7-1 and 7-2 show the variation of the fitted P_{FS} GEV distribution parameters versus the applied uniaxial strain amplitude (R_ε = -1) and inclusion size (radius). As shown in Figure 7-1, the location and scale parameters of the fitted P_{FS} GEV distributions increase exponentially as a function of the applied strain amplitude, ω. In contrast, both parameters increase in approximate linear manner as a function of inclusion radius for the simulated applied strain amplitudes, as shown in Figure 7-2.

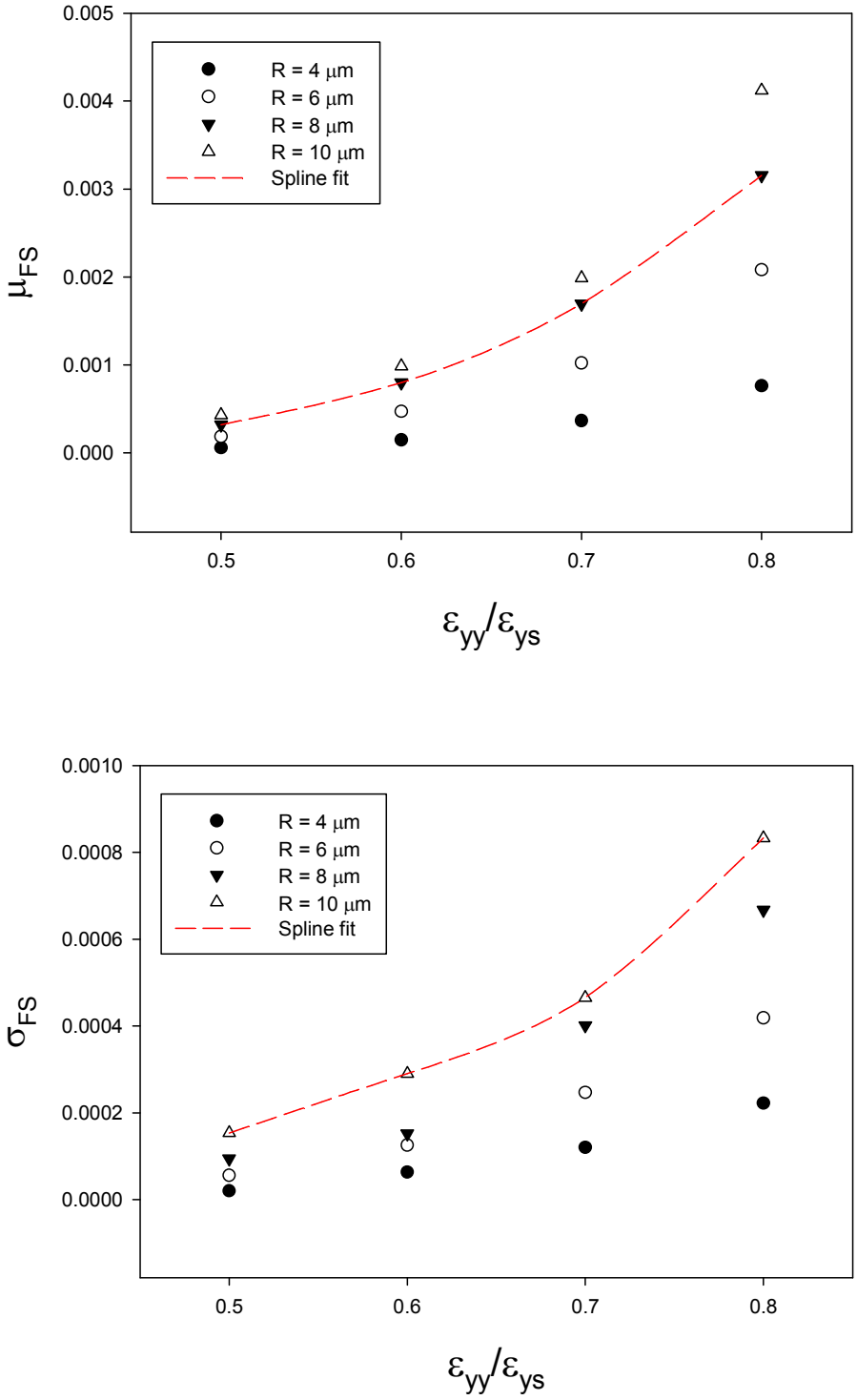

Figure 7-1: Parameters of the P_{FS} GEV distribution fits vs. the applied strain amplitude for partially debonded inclusions (ε_{ys} = 0.7 %; R_{ε} = -1).

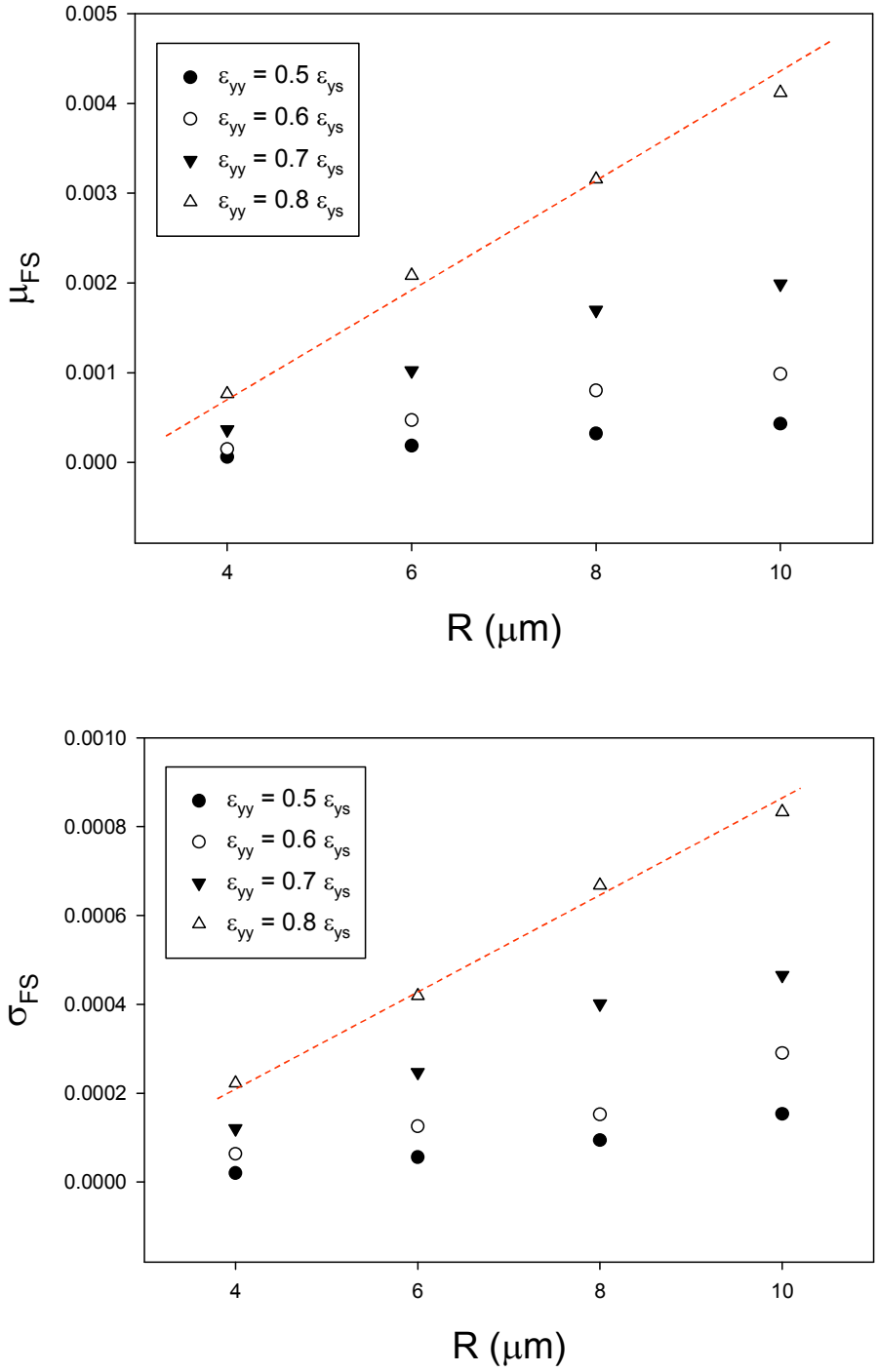

Figure 7-2: Parameters of the P_{FS} GEV distribution fits vs. the inclusion radius for partially debonded inclusions (ε_{ys} = 0.7 %; R_{ε} = -1).

Figure 7-3 shows the bivariate dependence of the P_{FS} GEV distribution parameters on the applied strain amplitude and inclusion size (radius) for $R_\varepsilon = -1$.

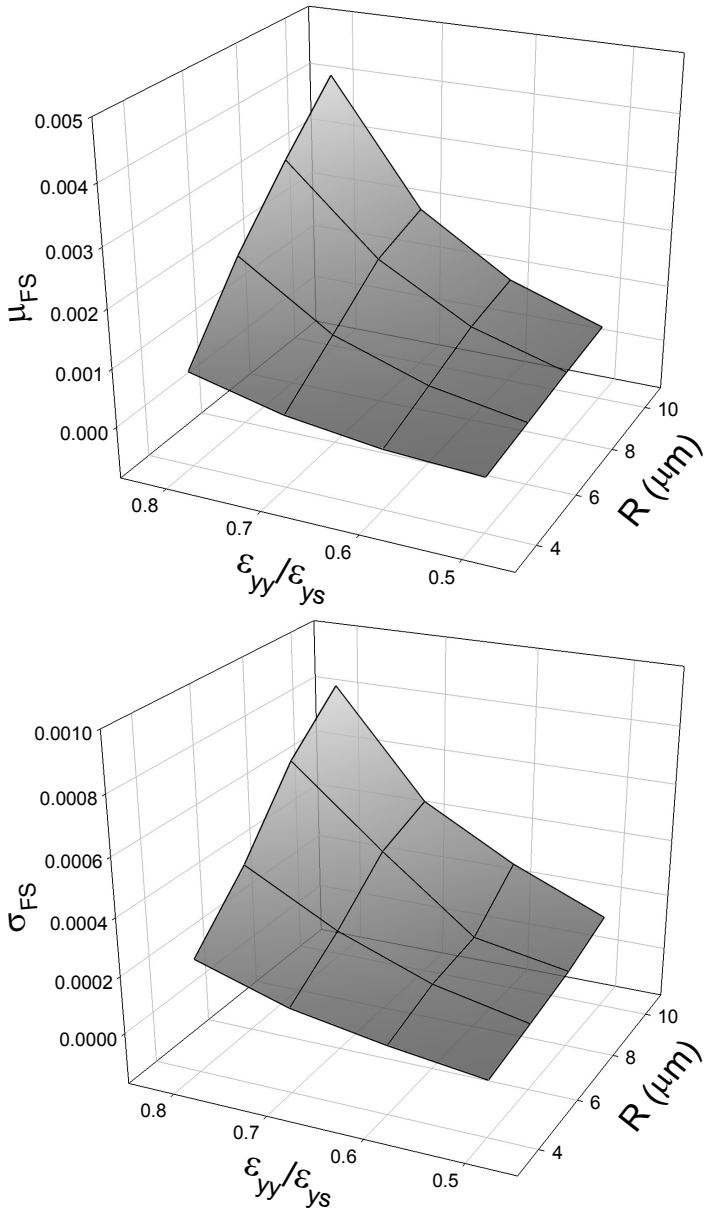

Figure 7-3: The dependence of the parameters of the P_{FS} GEV distribution fits on the applied strain amplitude and inclusion radius for partially debonded inclusions (ε_{ys} = 0.7 %; R_ε = -1).

For the intact, perfectly bonded inclusion, Figure 7-4 shows the bivariate dependence of the T_{int} GEV distribution parameters on the applied strain amplitude and inclusion size (radius) for $R_\varepsilon = -1$. Figure 7-4 indicates that the scale parameter decreases as R (inclusion radius) increases. The scale parameter value determines the statistical dispersion of the data. If it is large, then the distribution will be more spread out; if it is small then the distribution will be more concentrated. As R increases, the dispersion of the extreme value T_{int} data decreases because the number of sampled grains for the calculation of the maximum value of T_{int} increases.

In contrast, the scale parameter for the fitted P_{FS} GEV distribution increases as R (inclusion radius) increases (shown in Figure 7-2). This is because the nonlocal averaging region for the calculation of the P_{FS} parameter is taken to be of a constant size r = 3 μm (about 5% of the largest simulated inclusion area, R = 10 μm). As such, increasing the inclusion radius increases the stress intensity in this averaging region and magnifies the variability in the P_{FS} distribution for the simulated matrix realizations (grain orientation distributions).

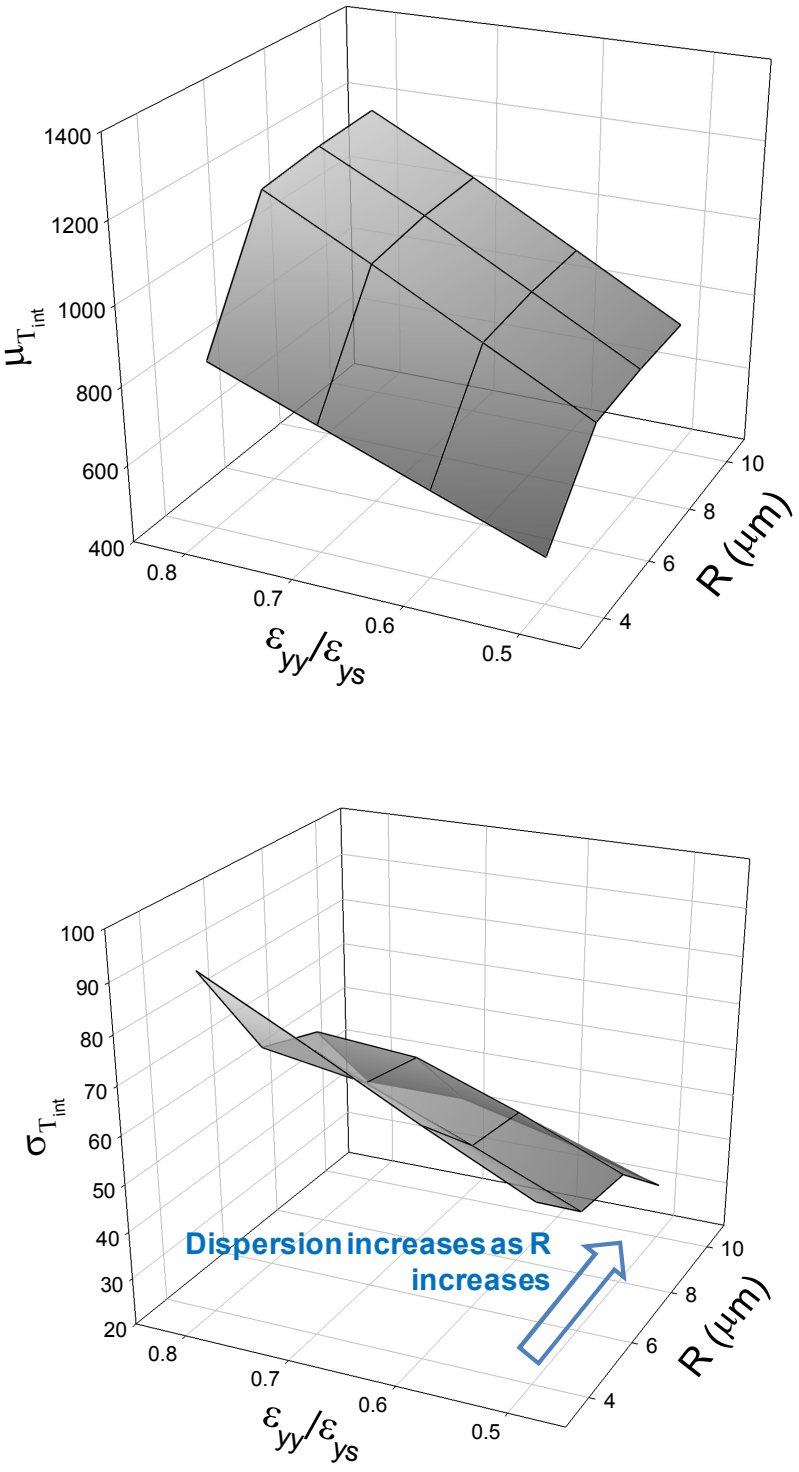

Figure 7-4: The dependence of the parameters of the T_{int} GEV distribution fits on the applied strain amplitude and inclusion radius for the intact, perfectly bonded inclusions (ε_{ys} = 0.7 %; R_ε = -1).

The multivariable Taylor series expansion is truncated to approximate the GEV distribution parameters for intermediate applied strain amplitudes and inclusion radii as

$$\begin{aligned}
\mu_{FS}(R,\omega) &\approx \mu_{FS}(R^*,\omega^*) + \frac{\partial \mu_{FS}}{\partial R}(R-R^*) + \frac{\partial \mu_{FS}}{\partial \omega}(\omega-\omega^*) \\
\sigma_{FS}(R,\omega) &\approx \sigma_{FS}(R^*,\omega^*) + \frac{\partial \sigma_{FS}}{\partial R}(R-R^*) + \frac{\partial \sigma_{FS}}{\partial \omega}(\omega-\omega^*) \\
\xi_{FS}(R,\omega) &\approx \xi_{FS}(R^*,\omega^*) + \frac{\partial \xi_{FS}}{\partial R}(R-R^*) + \frac{\partial \xi_{FS}}{\partial \omega}(\omega-\omega^*)
\end{aligned} \tag{7.8}$$

where μ_{FS}, σ_{FS}, and ξ_{FS} are the location, scale, and shape parameters, respectively, and $\omega = E_{yy}/E_{ys}$ denotes the applied strain amplitude. Similarly, for the T_{int} parameter:

$$\begin{aligned}
\mu_{T_{\text{int}}}(R,\omega) &\approx \mu_{T_{\text{int}}}(R^*,\omega^*) + \frac{\partial \mu_{T_{\text{int}}}}{\partial R}(R-R^*) + \frac{\partial \mu_{T_{\text{int}}}}{\partial \omega}(\omega-\omega^*) \\
\sigma_{T_{\text{int}}}(R,\omega) &\approx \sigma_{T_{\text{int}}}(R^*,\omega^*) + \frac{\partial \sigma_{T_{\text{int}}}}{\partial R}(R-R^*) + \frac{\partial \sigma_{T_{\text{int}}}}{\partial \omega}(\omega-\omega^*) \\
\xi_{T_{\text{int}}}(R,\omega) &\approx \xi_{T_{\text{int}}}(R^*,\omega^*) + \frac{\partial \xi_{T_{\text{int}}}}{\partial R}(R-R^*) + \frac{\partial \xi_{T_{\text{int}}}}{\partial \omega}(\omega-\omega^*)
\end{aligned} \tag{7.9}$$

For the nearest point having $R = R^*$ and $\omega = \omega^*$, these GEV distribution parameters are listed in Tables 12 and 13, respectively, for the T_{int} and P_{FS} parameters. Upon substituting Eq. 7.3 - Eq. 7.9 in Eq. 7.2, we numerically integrate Eq. 7.2 over the inclusions size distribution to calculate $P^{\omega}_{inclusion}$. Subsequently, the variable $P^{\omega}_{inclusion}$ is substituted in Eq. 7.1 to calculate Ψ which in turn is substituted in Eq. 6.9 to calculate the surface initiation probability. These equations are summarized in Table 14.

Table 14: Equations for calculating the surface initiation probability.

Eq.6.9: $$p_s = 1 - \left(\frac{V_t - V_s}{V_t} \right)^{\Psi}$$

Eq.7.1: $\Psi = \rho V P_{inclusion}^{\omega}$, where $\omega = \varepsilon_{yy} / \varepsilon_{ys}$

Eq.7.2: $P_{inclusion}^{\omega} = \int P_R \; p_{debond}^{R,\omega} \; C_{debonded}^{R,\omega} \; dR$ (P_R = inclusion size distribution)

Eq.7.3 - Eq.7.5: $$p_{debond}^{R,\omega} = \Pr(T_{tr} > T_{tr}^*) = 1 - c_R^{\omega}(T_{tr}^*) = 1 - \exp\left\{ -\left[1 + \xi_{tr} \left(\frac{T_{tr}^* - \mu_{tr}}{\sigma_{tr}} \right) \right] \right\}^{\frac{-1}{\xi_{tr}}}$$

Eq.7.6 & Eq.7.7: $$C_{debonded}^{R,\omega} = \Pr(P_{FS} > P_{FS}^*) = 1 - \exp\left\{ -\left[1 + \xi_{FS} \left(\frac{P_{FS}^* - \mu_{FS}}{\sigma_{FS}} \right) \right] \right\}^{\frac{-1}{\xi_{FS}}}$$

Eq.7.8:
$$\begin{cases} \mu_{FS}(R,\omega) \approx \mu_{FS}(R^*,\omega^*) + \dfrac{\partial \mu_{FS}}{\partial R}(R - R^*) + \dfrac{\partial \mu_{FS}}{\partial \omega}(\omega - \omega^*) \\ \sigma_{FS}(R,\omega) \approx \sigma_{FS}(R^*,\omega^*) + \dfrac{\partial \sigma_{FS}}{\partial R}(R - R^*) + \dfrac{\partial \sigma_{FS}}{\partial \omega}(\omega - \omega^*) \\ \xi_{FS}(R,\omega) \approx \xi_{FS}(R^*,\omega^*) + \dfrac{\partial \xi_{FS}}{\partial R}(R - R^*) + \dfrac{\partial \xi_{FS}}{\partial \omega}(\omega - \omega^*) \end{cases}$$

Eq.7.9:
$$\begin{cases} \mu_{T_{\text{int}}}(R,\omega) \approx \mu_{T_{\text{int}}}(R^*,\omega^*) + \dfrac{\partial \mu_{T_{\text{int}}}}{\partial R}(R - R^*) + \dfrac{\partial \mu_{T_{\text{int}}}}{\partial \omega}(\omega - \omega^*) \\ \sigma_{T_{\text{int}}}(R,\omega) \approx \sigma_{T_{\text{int}}}(R^*,\omega^*) + \dfrac{\partial \sigma_{T_{\text{int}}}}{\partial R}(R - R^*) + \dfrac{\partial \sigma_{T_{\text{int}}}}{\partial \omega}(\omega - \omega^*) \\ \xi_{T_{\text{int}}}(R,\omega) \approx \xi_{T_{\text{int}}}(R^*,\omega^*) + \dfrac{\partial \xi_{T_{\text{int}}}}{\partial R}(R - R^*) + \dfrac{\partial \xi_{T_{\text{int}}}}{\partial \omega}(\omega - \omega^*) \end{cases}$$

7.4 Study of the p_s dependence on the specimen size

To study the effects of specimen size on the surface initiation probability, virtual specimens are assumed to have a cylindrical gage section 15.2 mm long, similar to the specimens in [14], and gage section radii equal to 5, 10, and 15 mm. Figure 7-5 shows the variation of p_s versus the applied strain amplitude for these specimens. The intersection of the horizontal dashed line, having p_s = 50%, with plots of p_s marks the surface to bulk transition applied strain amplitude (R_ε = -1). This transition occurs at lower applied strain amplitudes when specimen size increases.

It is expected that larger specimens have shorter HCF lives. Our model simulates such specimen size effects. As shown in Figure 7-5, larger specimens have a higher surface to bulk HCF failure initiation probability at all applied strain amplitudes. This higher surface initiation probability corresponds to shorter fatigue lives (see Section 6.1).

Increasing the specimen size increases the probability of bulk defects. The trend shown in Figure 7-5 of increasing surface probability with specimen size does not contradict this fact. This trend results from the weakest-link approach, stipulating that a surface hot spot prevails over any internal hot spot, due to the higher growth rate of surface fatigue cracks (see Section 6.4.3). It is assumed that even one fatigue hot spot present in the surface region can cause surface originated fatigue failure.

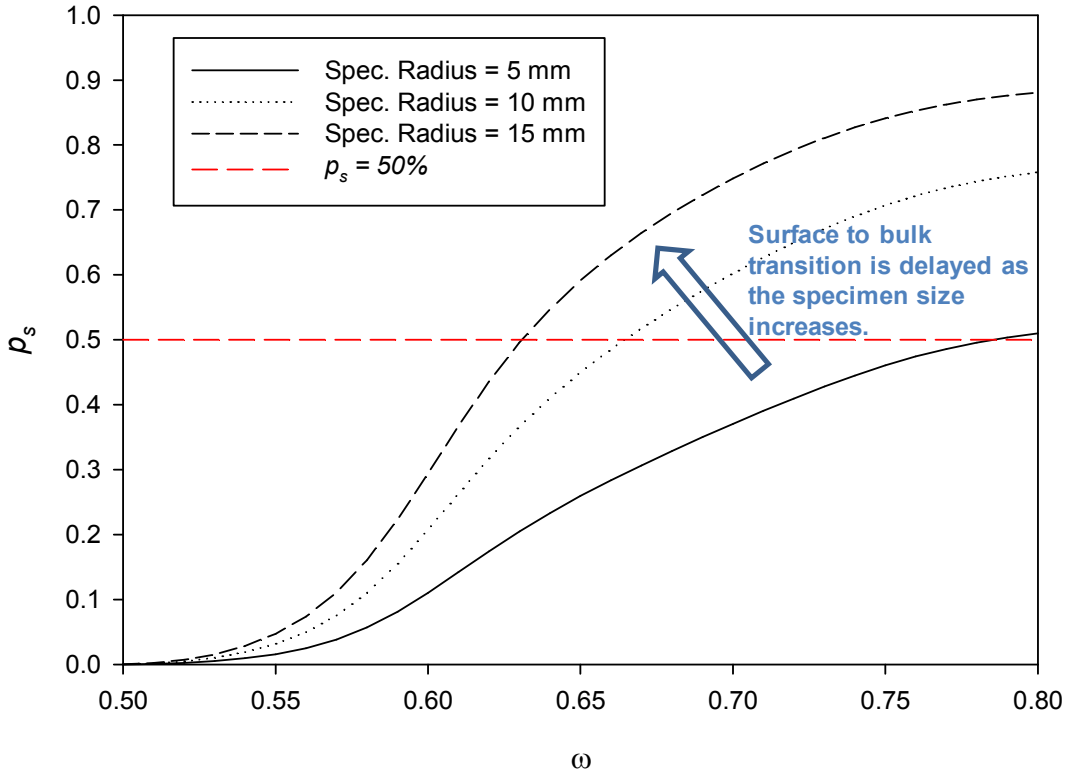

Figure 7-5: p_s dependence on the specimen size.

7.5 Study of the p_s dependence on the inclusion population attributes

Attributes of the inclusion population such as number density, inclusion radius distribution, and inclusion-matrix interface strength can greatly alter the surface initiation probability. If we assume that the second-order inclusion-inclusion interaction effects are negligible, inclusion number density effects are expected to be similar to those of specimen size, discusses in Section 7.4. This is because, similar to enlarging the specimen, increasing the inclusion number density raises the expected number of fatigue hot spots, Ψ, thus enhancing the likelihood of surface failure initiation (see Section 6.4.3).

In order to verify our model's prediction of inclusion number density effects, three values for the inclusion volume density equal to ρ = 1, 2, and 3 ($\times 10^{-9}$) are examined in this case study. Figure 7-6 shows the variation of p_s versus these simulated inclusion densities. As seen in Figure 7-6, the surface initiation probability increases with increases in the inclusion number density for all applied strain amplitudes.

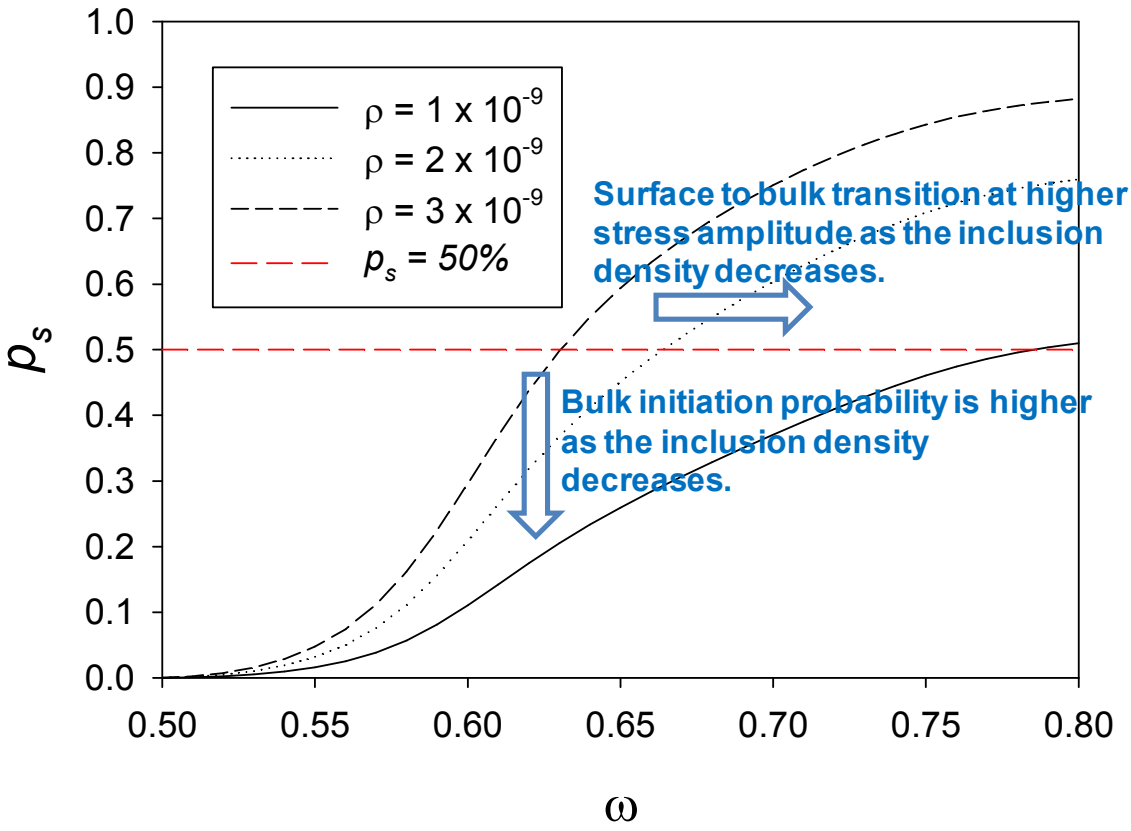

Figure 7-6: p_s dependence on the inclusion density.

To examine the dependence of p_s on the inclusion size (radius) distribution, we consider four different probability distribution functions (PDFs), shown in Figure 7-7, in order to represent the inclusion population. These normal PDFs share a common scale parameter σ_R = 3 but have different mean values equal to μ_R = 4, 6, 8, and 10 µm. Inclusion radius varies from 4 µm to 10 µm in all simulated inclusion populations.

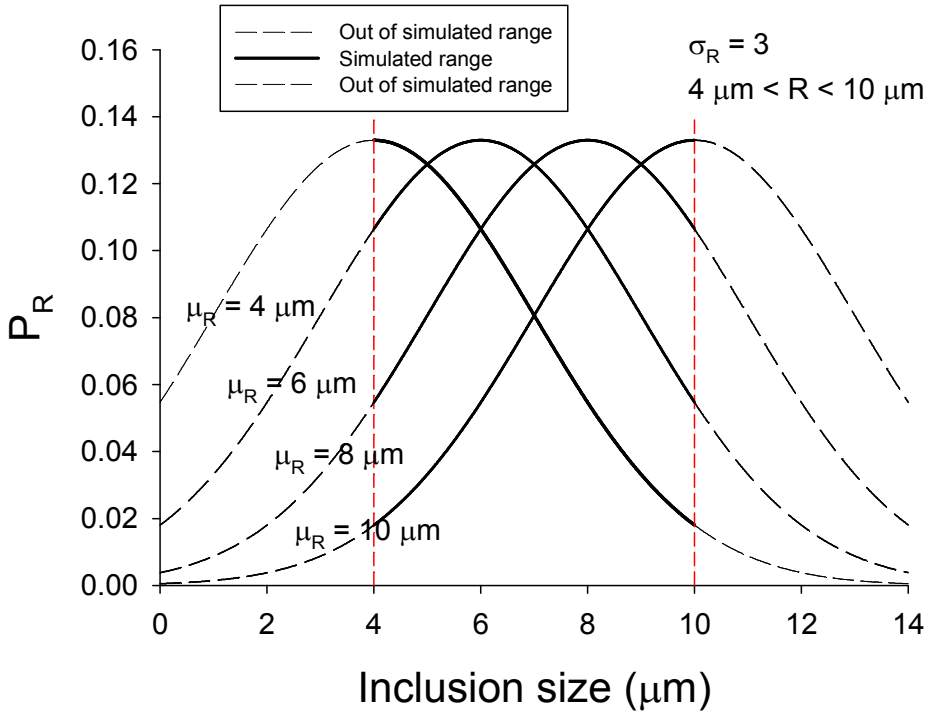

Figure 7-7: The simulated inclusion radius distributions.

We assume that each specimen contains an average of 20 inclusions. Therefore, inclusion volume density increases with increasing μ_R. We previously estimated T^*_{int} by solving $C^{\omega=0.8}(T^*_{int}) = 0.05$ based on the assumption that the applied uniaxial strain amplitude of ω = 0.8 is high enough that, as a result, 95% of all inclusions would likely debond. This T^*_{int} estimate was obtained for μ_R = 4 μm. Since $C^{\omega}(T_{int})$ depends on the inclusion radius distribution (see Eq. 4.1), $C^{\omega=0.8}(T^*_{int})$ is expected to be different than 5% for μ_R = 6, 8, and 10 μm.

Figure 7-8 shows the CDFs of the extreme value T_{int} parameter at ω = 0.8 and the $C^{\omega=0.8}(T^*_{int})$ estimates. As seen in these plots at ω = 0.8, the probability of inclusion

debonding at a constant applied strain amplitude, calculated as (1 - $C^{\omega=0.8}(T^*_{int})$), increases when the mean inclusion radius (i.e. μ_R) increases.

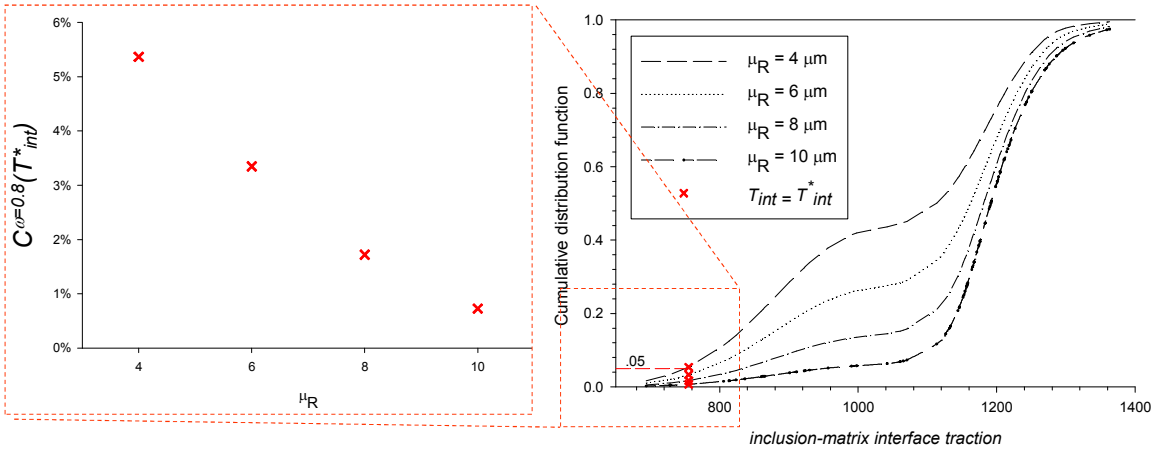

Figure 7-8: CDFs of extreme value T_{int} showing the variation of $C^{\omega=0.8}(T^*_{int})$ vs. the mean inclusion radius.

Similarly, we construct the CDFs of the extreme value P_{FS} parameter at ω = 0.8 (i.e., $C^{\omega=0.8}(P_{FS})$) and plot the variation of $C^{\omega=0.8}(P^*_{FS})$ versus the mean inclusion radius in Figure 7-9.

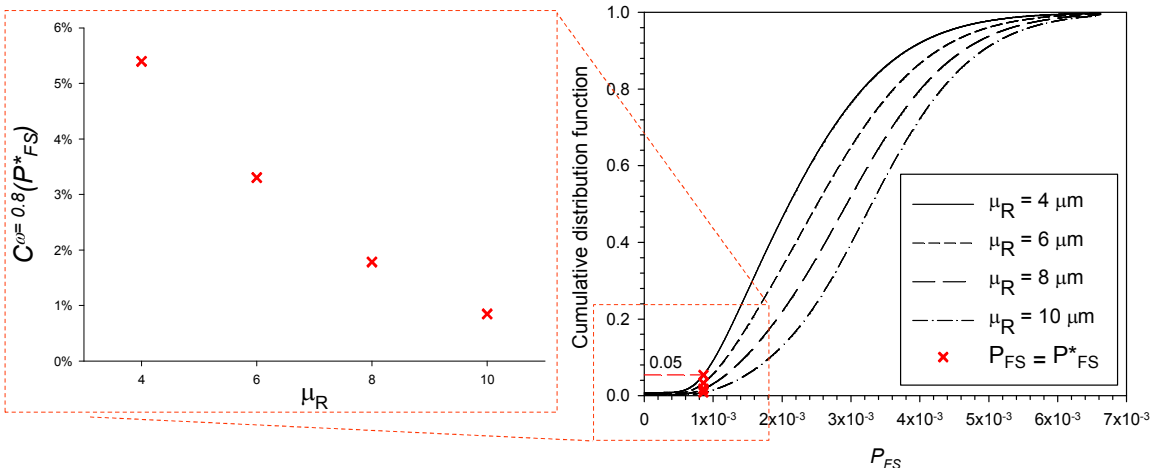

Figure 7-9: CDFs of extreme value P_{FS} showing the variation of $C^{\omega=0.8}(P^*_{FS})$ vs. the mean inclusion radius.

As shown in Figure 7-10, alloys with smaller inclusions have a lower surface initiation probability. This greater tendency towards bulk initiation means that the surface to bulk transition occurs at higher applied uniaxial strain amplitudes. Since bulk initiation corresponds to longer fatigue lives, decreasing the mean inclusion radius is expected to enhance the HCF life expectancy of the material.

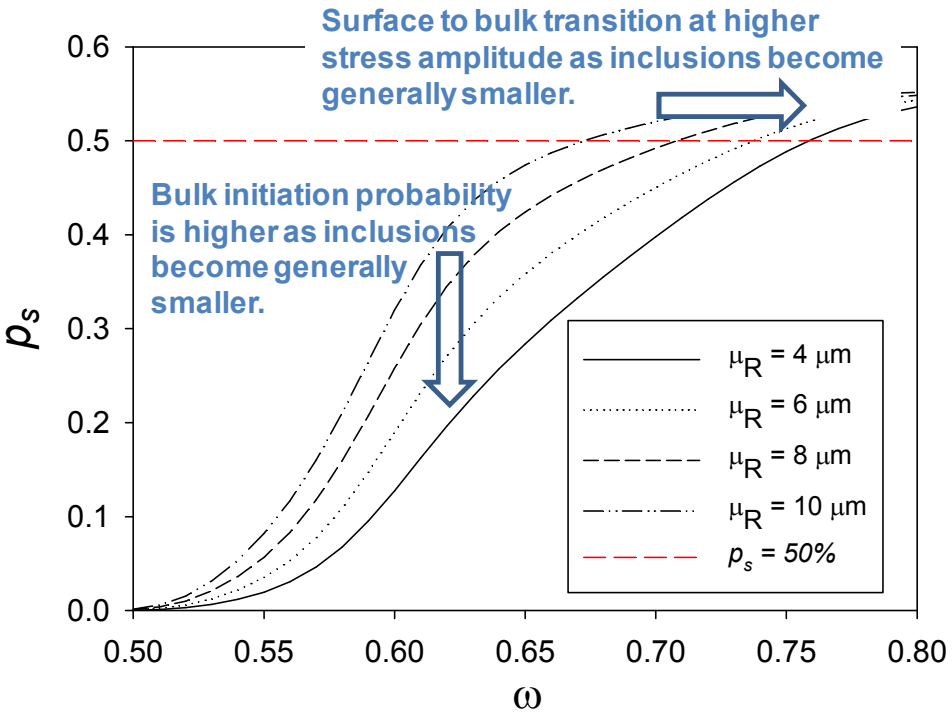

Figure 7-10: p_s dependence on μ_R.

In order to study the effects of inclusion-matrix interface strength, we compare the trends of p_s versus ω for four different values of T^*_{int}. Absent direct experimental data regarding the interface bonding properties, T^*_{int} can be indirectly approximated by solving $C^{\omega=a}(T^*_{int}) = 1 - b$ for known values of inclusion-matrix interface debonding, b, at the applied uniaxial strain amplitude of $\omega = a$.

Let us suppose that the probability of inclusion-matrix interface debonding at $\omega = 0.8$ reduces from 95% to 89%, 86%, and 80% as the interface bonding is increasingly strengthened. Under these conditions, as illustrated in Figure 7-11, T^*_{int} is obtained by solving $C^{\omega=0.8}(T^*_{int}) = 1 - b$ and tabulated in Table 15.

Table 15: T^*_{int} approximated from known inclusion debonding probabilities.

ω	b	T^*_{int} (MPa)
0.8	95%	755.3
0.8	89%	805.8
0.8	59%	997.9
0.8	50%	1113.3

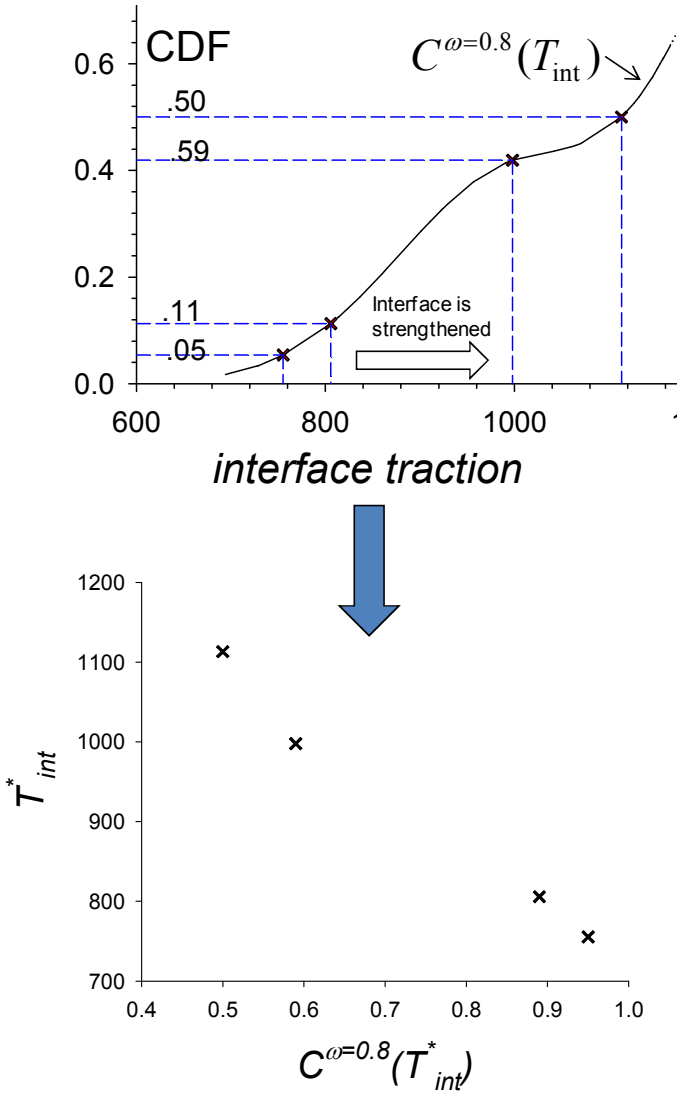

Figure 7-11: Calculating T^*_{int} from inclusion debonding probabilities.

Figure 7-12 shows the trends of p_s versus ω for four different values of T^*_{int}. Improving the inclusion-matrix bonding, to the extent that instead of 95%, only 50% of all inclusions debond at $\omega = 0.8$, can significantly reduce the surface initiation probability at all applied uniaxial strain amplitudes. This greater tendency towards bulk initiation translates into enhancements in the HCF life expectancy of the material.

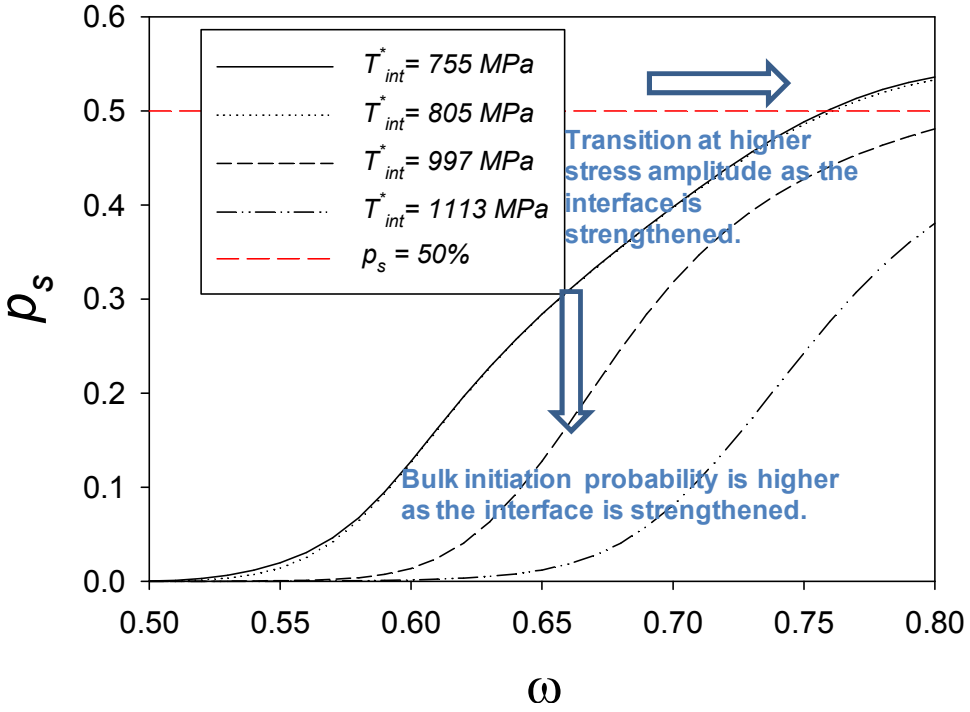

Figure 7-12: p_s dependence on T^*_{int}.

7.6 Summary

In Section 6.2, we discussed the significance of surface initiation probabilities for improving the design for very low probability of failure. We explained that the B0.1 estimate (1 in 1000 probability of failure) is currently obtained by extrapolating the cumulative surface initiation probability distribution, and we showed that this is done by solving $c_s(N_f) = 0.001$.

However in doing so, an overly conservative B0.1 estimate is obtained, as the contribution of the bulk initiation probability is not accounted for in the existing approaches. We argued that a considerable improvement to the B0.1 estimate can be obtained by accounting for the fact that for any surface initiation event, there occur p_b/p_s bulk initiation events; thus we suggested calculating N_f by solving $c_s(N_f) = 0.001/p_s$.

As a case study, we assessed the surface initiation probabilities for virtual cylindrical fatigue specimens, emphasizing the early stage crack initiation mechanisms from partially debonded inclusions in HCF and VHCF. We computed the expected number of fatigue critical inclusions by using finite element crystal plasticity simulations to calculate the critical plane fatigue indicator parameter P_{FS} around the inclusions.

By virtue of microstructure scale simulations, grain-level microplasticity is incorporated in calculations of the underlying fatigue indicator parameter. Therefore, important physical mechanisms that control the HCF response of the material are accounted for in an integrated approach that also accounts for the multiaxial state of local stresses.

For the case study, we verified our model's prediction of surface initiation probability for specimens having different gage radii as well as microstructures having

different inclusion-related attributes such as inclusion density, inclusion radius distribution, and inclusion-matrix interface strength. The inherent idealizations of our computational approach, as well as our incomplete knowledge of mechanisms that conspire to initiate a fatigue crack, prevent us from confidently calculating the surface initiation probability. However, our philosophy is that such idealized simulations shed light on the dependence of surface initiation probability on the specimen size, microstructure attributes, and loading conditions. These simulations help to delineate the trends and compare scenarios, supporting decisions in materials design and development/improvement.

8 Finite element simulation of shielding/intensification effects of primary inclusion clusters in high strength steels

8.1 Introduction

Casting and mechanical alloying processes for advanced metallic alloys often introduce undesirable non-metallic inclusions that are considerably larger than the mean grain size [9, 78, 171, 172]. These inclusions often fracture into smaller inclusions during primary deformation processing or manufacturing, leading to inclusion stringers or clusters, as shown in Figure 8-1. These clusters are high probability sites of fatigue failure origination [21]. The mechanisms of crack nucleation and early growth from inclusions involve either cracking of the inclusion or debonding of the inclusion/matrix interface, concentrating cyclic plastic shear strain in the surrounding matrix [173-177].

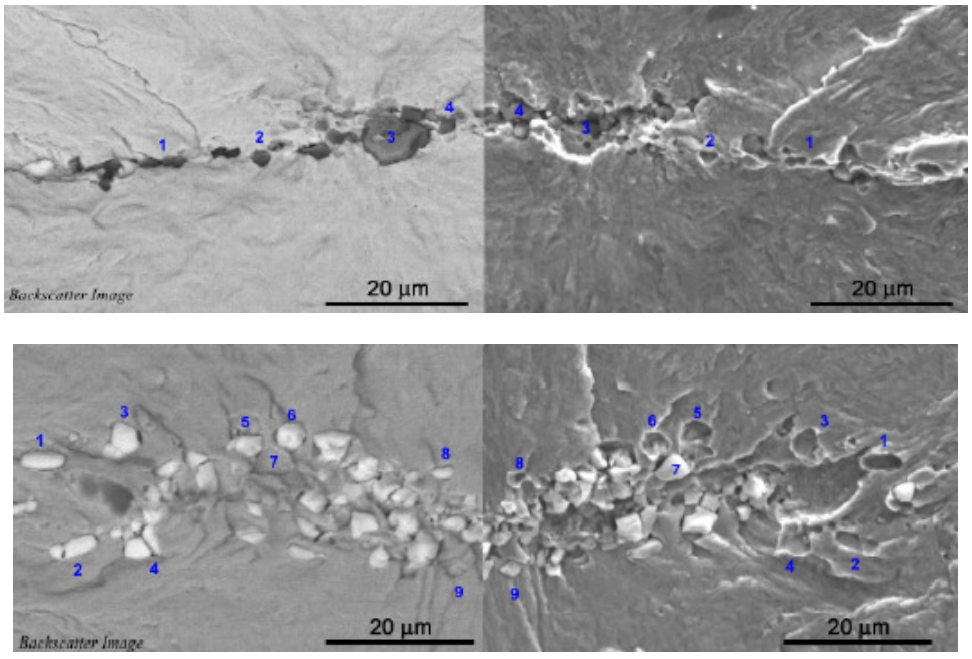

Figure 8-1: Backscatter SEM image of Al_2O_3 (top) and La_2O_2S (bottom) inclusion clusters [21].

Due to the greater volume of application of high strength steels than of Ni-base superalloys, more research studies have examined the critical role of non-metallic inclusions in these alloys [4-6, 9, 10, 21, 94, 95, 173, 175, 176, 178-182]. Second phase particles have often been reported to serve as crack nuclei in different grades of steel [21, 173, 175, 178, 181, 183].

Cyclic bending experiments [21] on shot peened Ferrium® C61 revealed that minimum fatigue strength is controlled by subsurface fatigue crack formation at inclusion clusters, still in the compressive residual stress field. Alumina (Al_2O_3) and lanthanum oxy-sulfide (La_2O_2S) inclusion clusters were observed to originate fatigue cracks. Both inclusion types appeared in clusters of individual particles, each between 1 and 10 μm in diameter, aligned along the hot working direction of the billets from which the gears are manufactured. Figure 8-1 shows SEM micrographs of both classes of inclusions, as seen on the tooth fracture surfaces, as well as the corresponding mating fracture surfaces of the failed spur gear.

The cluster morphology is somewhat different between Al_2O_3 and La_2O_2S classes. Al_2O_3 clusters are generally composed of fewer individual inclusion particles tightly concentrated along a single line. In contrast, La_2O_2S clusters are composed of numerous particles and have a much larger cluster width. The overall size of the inclusion clusters is not significantly different for Al_2O_3 and La_2O_2S inclusions, but the nature of the individual particles within them does show significant differences. La_2O_2S particles appear on both mating fracture surfaces, with individual particles primarily de-cohering from the opposing fracture surface, leaving behind a concavity. Some single particles

show signs of fracture, such as the annotated particle 4 in Figure 8-1. Al_2O_3 particles, in contrast, do not show discernable signs of particle fracture.

Prasannavenkatesan *et al.* [78, 149, 182] developed a computational framework that considered the gradients from the surface of residual stress distribution, bending stress, and carburized material properties. They performed three-dimensional FE simulations to parametrically explore the fatigue crack formation potency at subsurface primary inclusions in carburized and shot peened martensitic gear steels including Ferrium® C61. They conducted systematic parametric studies to investigate the spatial interaction of inclusions in order to frame a method for estimating the critical inclusion spacing for minimal interaction in fatigue. They calculated two FIPs, namely the nonlocal average maximum shear plastic strain range, $\Delta\gamma^{*}_{p,\max}$ (cf. 2.2.1), and the Fatemi-Socie (cf. 2.2.2) parameters around idealized (i.e., ellipsoidal) inclusions. They predicted a strong propensity for crack formation at subsurface depths (i.e., ranging from 75 μm to 300 μm below the surface) for both isolated inclusions and for inclusion clusters. The simulation predictions are consistent with the cyclic bending experimental data of [21].

In the HCF regime, crack nucleation and early stages of microstructurally small crack (MSC) growth within the inclusion cluster consume most of the total fatigue life and hence control the inherent scatter in the HCF life [6, 9, 11, 171, 179, 184]. As inclusion clustering is evident in Ferrium® C61, it is of prime importance to discern the relative short range shielding/enhancement effects of the neighboring inclusion on the fatigue crack formation potency.

The intensification/shielding effect of an elastic inclusion on the range of stress intensity factor of an adjacent crack has also been investigated [185-188]. However, it is

important to define the interaction effect of a neighboring inclusion on the formation and early growth of a fatigue crack at non-metallic, partially debonded inclusions in metals. Though research on this problem is lacking in the literature, such valuable understanding will contribute to the design of fatigue-resistant microstructures and will enhance the methods and processes by which one can improve the fatigue performance.

This Chapter investigates the way a neighboring inclusion causes changes in the high cycle fatigue (HCF) crack nucleation potency of non-metallic primary inclusions in Ferrium® C61 [22] martensitic gear steel. This investigation is conducted using two- and three- dimensional elasto-plastic finite element (FE) analyses. Fatigue Indicator Parameters (FIPs) are computed in the proximity of the inclusion and are used to compare the crack nucleation potency of various scenarios.

FE simulations suggest significant intensification of plastic shear deformation, and hence higher FIPs, when the inclusion pair is aligned perpendicular to the uniaxial stress direction. Relative to the reference case with no neighboring inclusion, FIPs decrease considerably when the inclusion pair aligns with the applied loading direction.

These findings shed light on the anisotropic HCF response of alloys whose primary inclusions have been arranged in clusters by virtue of the fracture of a larger inclusion during deformation processing. Materials design methodologies may also benefit from such cost-efficient parametric studies that explore the relative influence of microstructure attributes on the HCF properties and suggest strategies for improving the HCF resistance of alloys.

In the HCF and VHCF regimes (i.e., total fatigue life >> 10^6), crack growth beyond the influence of the critical inclusion (inclusion cluster) is known to contribute

negligibly to total fatigue life [11, 171]. This is the regime on which the present study focuses. We build on the work of Prasannavenkatesan *et al.* to simulate the shielding/intensification effects of primary inclusion clusters in Ferrium® C61.

HCF and especially VHCF crack formation processes are rare event phenomena, otherwise known as extreme value problems [10, 189-191]. The life-limiting (worst-case) characteristics of the VHCF regime are governed by extreme value microstructure attributes, which in turn depend on material processing, loading history, etc. The small occurrence rate of the VHCF-controlling microstructure attributes results in increased scatter in fatigue life data, as well as specimen size effects.

Accordingly, a very large number of experiments is required to obtain a statistically representative distribution of fatigue life in this regime. Even with the advent of high-frequency fatigue testing methods [6, 192, 193], statistically representative experimental characterization of the VHCF regime is not yet practical due to time and cost limitations. Therefore, the contribution of modeling and simulation to understanding the variability in fatigue lifetime may assist in reducing the number of costly fatigue experiments that must be conducted to obtain a specific confidence level.

8.2 Finite element model

We consider a fully martensitic gear steel (low carbon content) matrix (c.f. 1.3.2) with hard non-metallic inclusions that are partially debonded. Contact between the interacting surfaces is assumed to be frictionless. The initial debonding could occur during processing as well as service (over) loading. We use a homogeneous rate-independent plasticity model with nonlinear kinematic hardening [48, 49] to simulate the matrix material (c.f. 2.1.1). This model is included in the ABAQUS standard material model library [49]. Pure kinematic hardening is employed to simulate a cyclically stable response in parametric studies. Model parameters are chosen to mimic the cyclic deformation behavior of the candidate low carbon high strength martensitic steel at room temperature as elaborated elsewhere [77]. Unlike crystal plasticity, this constitutive model has no size effects; relevant size effects are described only by the inclusion size and spacing, i.e., the ratio R/d, and the scale of averaging the FIPs.

Idealized cylindrical inclusions with homogeneous linear elastic isotropic material properties are considered to be partially debonded, the worst-case scenario for HCF crack nucleation [75, 76, 78], as experimentally observed for similar systems [4, 5, 7, 177]. Inclusion-matrix interfaces are simulated using a frictionless contact penalty algorithm within the commercial finite element software, ABAQUS [49].

The material investigated is a Ferrium® C61 martensitic gear steel [22] subjected to carburization and tempering. The microstructure consists predominantly of tempered lath martensite. A detailed description of the heat treatment, surface treatment and composition of the material are presented elsewhere [21]. The material constitutive behavior and parameters are presented in Section 1.3.2. The parameters are typical values

for carburized and tempered low carbon martensitic steels intended for HCF applications [21].

Figure 8-2 shows a schematic of a nested three-phase finite element model in which two elastic inclusions are embedded in a near field elasto-plastic matrix that is surrounded in turn by a far field matrix region simulated as having isotropic elastic properties. Generalized plane strain (see Section 2.4.1) FE simulations were performed to study the variation in FIPs for the non-metallic inclusion of interest with minimum spacing *d* relative to the neighboring inclusion; these are shown, respectively, in dark and light shades in Figure 8-2. Inelastic strain occurs only near the inclusion at remote applied strain below macroscopic yield. Figure 8-2 also elaborates the dimensions of the FE domains, the boundary conditions, and the loading direction enforced in the simulations.

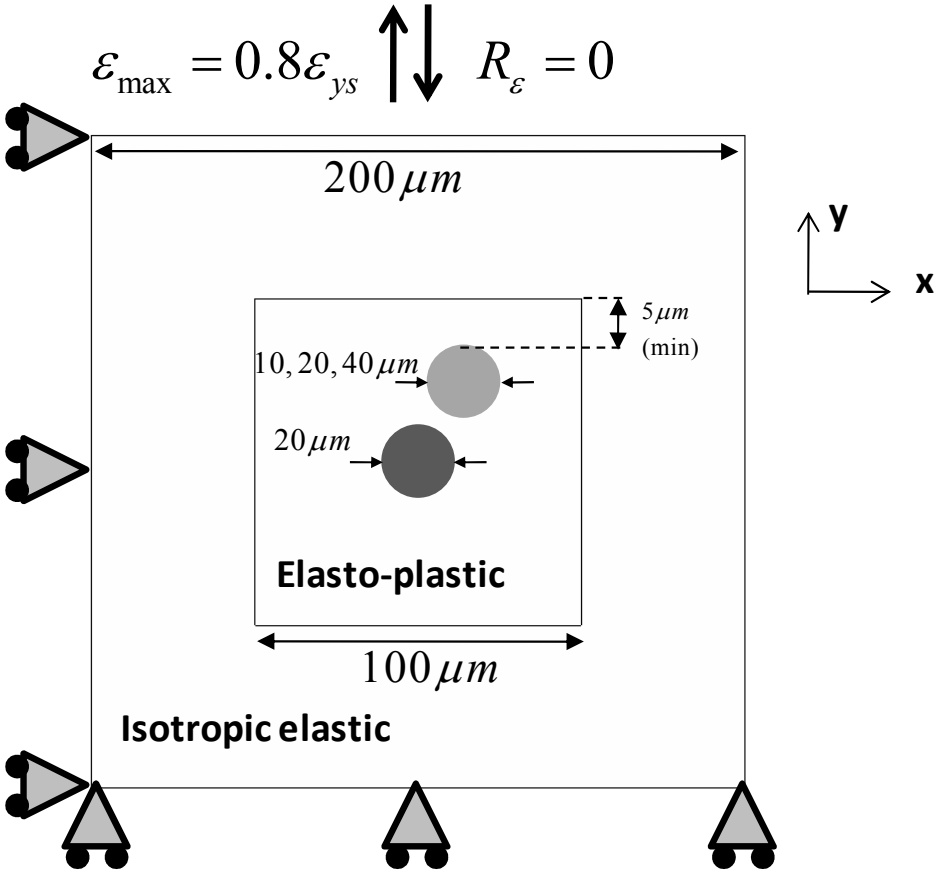

Figure 8-2: Schematic of the two-dimensional finite element model.

Minimum inclusion spacing and the inclusion pair orientation with respect to the far field applied displacement direction are defined by *d* and *(90 – θ°)*, respectively, as shown in Figure 8-3.

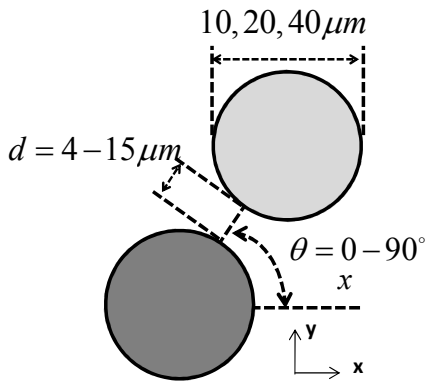

Figure 8-3: Inclusion spacing and orientation.

The two candidate FIPs under study are the maximum range of plastic shear strain and the Fatemi-Socie (c.f. Section 2.2), assuming k_{FS} = 0.6 [78]. The nonlocal averaging region is taken to be of constant size (3 × 3 μm^2) to account for effects such as inclusion size and spacing.

We focus on parametric studies of the shielding/intensification effect exerted by a neighboring inclusion within a two-inclusion cluster, compared to the changes in magnitude of FIPs in a reference case having no neighboring inclusion. One may use modified Coffin-Manson laws to relate such FIPs to fatigue crack formation or to the initiation life of a crack within the influence domain of the primary inclusion [79, 80, 194, 195]; however, we do not pursue that here.

Three cycles of uniaxial cyclic strain, with applied strain ratio of $R_\varepsilon = \varepsilon_{min}/\varepsilon_{max}$ = 0, are applied in the y direction in terms of displacement, as shown in Figure 8-2. A macroscopic peak strain of $\varepsilon_{max} = 0.8\ \varepsilon_{ys}$ is applied, where ε_{ys} = 0.75 % is the matrix yield strain in 2.5D plane strain.

Limited representative cases are simulated at $\varepsilon_{max}/\varepsilon_{ys}$= 0.4, 0.5, 0.6, 0.7, and 0.8 (R_ε = 0) to investigate the effect of remote applied loading relevant to both HCF and VHCF regimes. The diameter of the inclusion of interest is 20 μm in all cases, and the dimension of the elasto-plastic region is 100 μm. A fine mesh is employed close to the inclusion (element size about 0.5 μm) to capture the details of deformation around the inclusion, fanning out with a coarse mesh away from the inclusion.

All 2.5D simulations were performed using 3-node GPS triangular elements in ABAQUS. Figure 8-4 magnifies the FE mesh in the elasto-plastic region for a neighboring inclusion of 20 μm in diameter with d = 4 μm and θ = 60º. Inclusions are assumed to be debonded over their top half interface with the matrix, and frictionless contact is assumed along debonded regions. Inclusions are deemed bonded over their bottom half interface with the matrix region; the ABAQUS *Tie command is used to enforce continuous displacement across these interfaces.

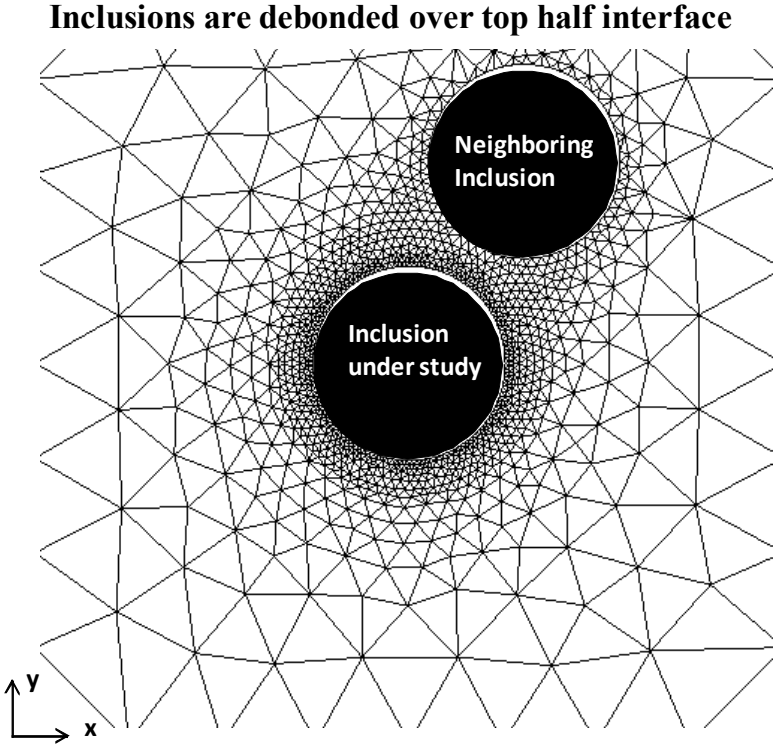

Figure 8-4: Detailed view of the FE mesh.

Properties assigned for the fully isotropic elastic inclusion include Young's modulus E^i = 380 GPa and Poisson's ratio ν^i = 0.2 [174]. The third cycle is used for the calculation of the FIPs over several averaging regions near the inclusion debond notch root to identify the area that yields the highest average parameters. The averaging procedure also helps to achieve computationally consistent results by regularizing to avoid mesh-size dependence, and it accounts for the fact that cracks physically form over a finite region, as noted in other studies [75, 76]. In this study, in 2D geometries (3D constitutive model), the averaging area is taken to be 3 × 3 μm^2. We define normalized nonlocal $\Delta\gamma^*_{pl,max}$ and P_{FS} parameters as

$$\Delta\gamma^{N} = \frac{\Delta\gamma^{*}_{pl,max}}{\left(\Delta\gamma^{*}_{pl,max}\right)^{ref}} \tag{8.1}$$

and

$$\Delta\Gamma^{N} = \frac{\Delta\Gamma}{\left(\Delta\Gamma\right)^{ref}} \tag{8.2}$$

where the reference values, $(\Delta\gamma^{*}_{pl,max})^{ref}$ and $(\Delta\Gamma)^{ref}$ are obtained for an identical simulation in each case, i.e., the same geometry and remote applied boundary conditions are used for a single inclusion without the neighboring inclusion. Accordingly, shielding and intensification effects due to a neighboring inclusion correspond, respectively, to $\Delta\gamma^{N}$ and $\Delta\Gamma^{N}$ values below and above unity.

8.3 Results and Discussion

Figure 8-5 shows the 2.5D finite element predictions of $\Delta\gamma^N$ dependence on the inclusion pair orientation with respect to the transverse direction, θ (see Figure 8-3), for several values of inclusion spacing, d. The macroscopic remote applied strain amplitude and strain ratio for these simulations are $\varepsilon_{max} = 0.8\ \varepsilon_{ys}$ and $R_\varepsilon = 0$, respectively.

Three schematics are overlaid on this figure to illustrate the relative placement of the two inclusions (both 20 μm in diameter) with respect to the applied loading for $d = 4$ μm and $\theta = 0$, 45, and 90 degrees, the cases exhibiting the highest intensification and shielding effects. For the inclusion interface under study, $\Delta\gamma^N$ can increase several fold for small inclusion spacing when the inclusion pair is aligned normal to the loading direction, i.e., $\theta = 0^o$.

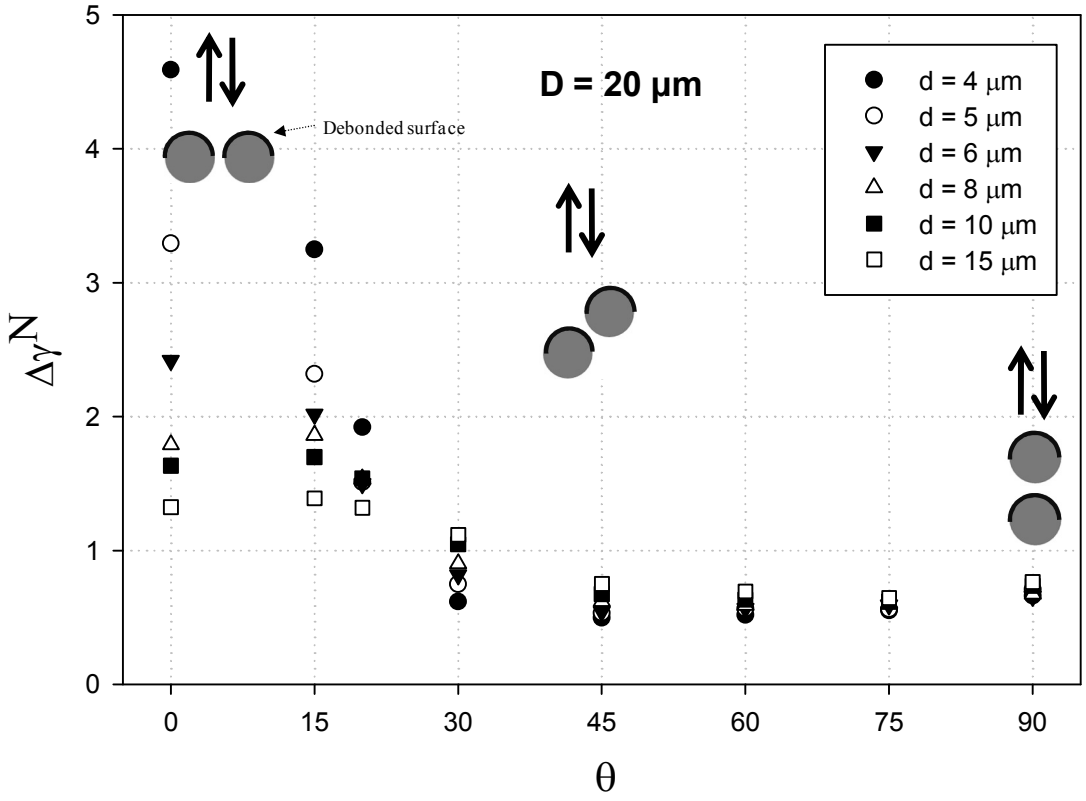

Figure 8-5: $\Delta\gamma^N$ dependence on inclusion pair orientation, with inclusion diameter D = 20 μm (for both inclusions) at various θ.

The inclusion interaction and thus $\Delta\gamma^N$ intensification, for this orientation weakens exponentially for increasing inclusion spacing, as shown in Figure 8-6, in which neighboring inclusion diameters are 10 μm, 20 μm, and 40 μm. With regard to the nucleation potency, the detrimental intensification effect of the neighboring inclusion almost completely diminishes, i.e., $\Delta\gamma^N$ = 1, for particle spacing on the order of neighboring inclusion diameter and beyond.

However, particle distances less than the inclusion diameter are quite common when a primary inclusion fractures into smaller pieces during processing (Figure 8-1).

Neighboring inclusions whose spacing is greater than their diameter are still likely to adversely affect the fatigue resistance of the alloy, as they promote enhanced propagation.

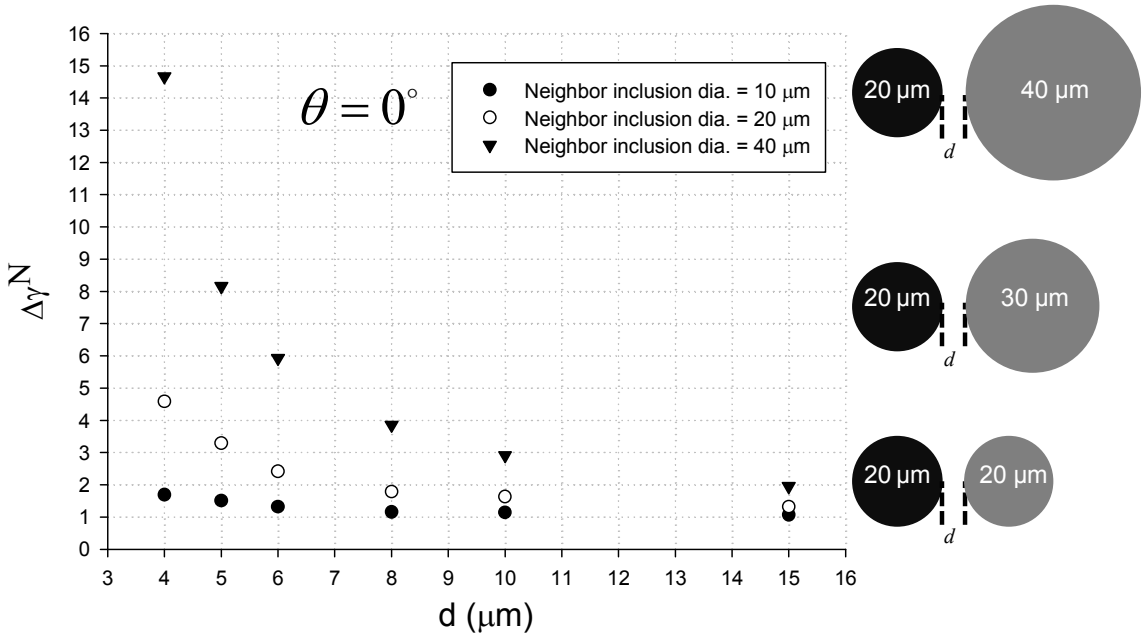

Figure 8-6: $\Delta\gamma^N$ vs. inclusion spacing for θ = 0º.

As the inclusion pair aligns with the applied loading direction, i.e., $\theta \rightarrow 45º$, $\Delta\gamma^N$ drops below unity, indicating the shielding influence of the neighboring inclusion. Relative to the orientations resulting in $\Delta\gamma^N$ intensification, the scatter in the $\Delta\gamma^N$ for all the orientations with the shielding effect is much smaller. This indicates that the shielding phenomenon does not appear to be as sensitive to the particle spacing as does intensification.

Figure 8-7 plots $\Delta\gamma^N$ variation near the inclusion of interest versus particle spacing for three neighboring inclusion diameters of 10 μm, 20 μm, and 40 μm at $\theta = 90^o$. As seen in Figure 8-7, the shielding effect depends strongly on the neighboring inclusion diameter. Although a beneficial shielding effect increases with the size of the neighboring inclusion, a neighboring inclusion that is larger than the inclusion of interest most likely lowers initiation life by acting as the dominant initiation site, unless it is suppressed by other means such as improvement in its interfacial bonding. Nevertheless, a neighboring inclusion of equal diameter (i.e., 20 μm) can still have a considerable (~ 30%) shielding effect.

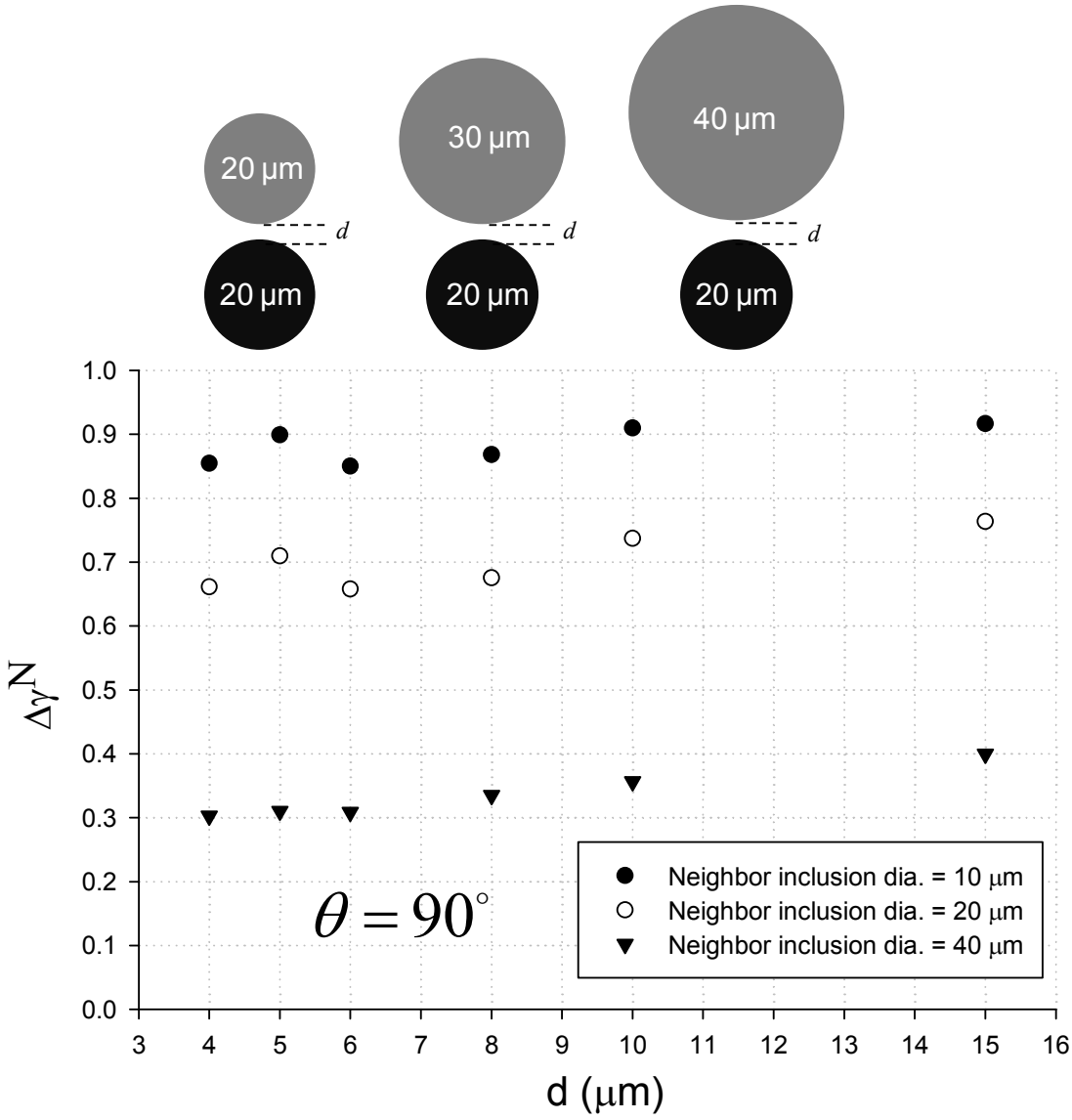

Figure 8-7: (1 - $\Delta\gamma^N$) vs. particle spacing at θ = 90º.

It is instructive to consider the ratio of beneficial shielding gain at θ = 90º to the unfavorable $\Delta\gamma^N$ intensification at θ = 0º, i.e., $(1 - \Delta\gamma^N_{\theta = 90^\circ}) / (\Delta\gamma^N_{\theta = 0^\circ} - 1)$, versus neighboring inclusion diameter, as shown in Figure 8-8 for the three neighboring inclusion diameters of 10 μm, 20 μm, and 40 μm. In general, this ratio may be interpreted

as the relationship of the potential improvement in the longitudinal orientation of loading to the possible weakening in the transverse orientation.

Figure 8-8 may appear to suggest that the beneficial shielding effect of a neighboring inclusion can be exploited by deliberately promoting inclusion clustering during processing to achieve scenarios with higher values of $(1 - \Delta\gamma^{N}_{\theta = 90^{o}}) / (\Delta\gamma^{N}_{\theta = 0^{o}} - 1)$ ratio. However, manufacturing process effects and the state of service loads need to be known prior to material processing in order to take advantage of this shielding effect without introducing additional sources of fatigue life variability. Therefore, in practice, the objective is likely to avoid detrimental intensification due to clustering of inclusions rather than taking advantage of any possible enhancement in fatigue resistance through the shielding effects.

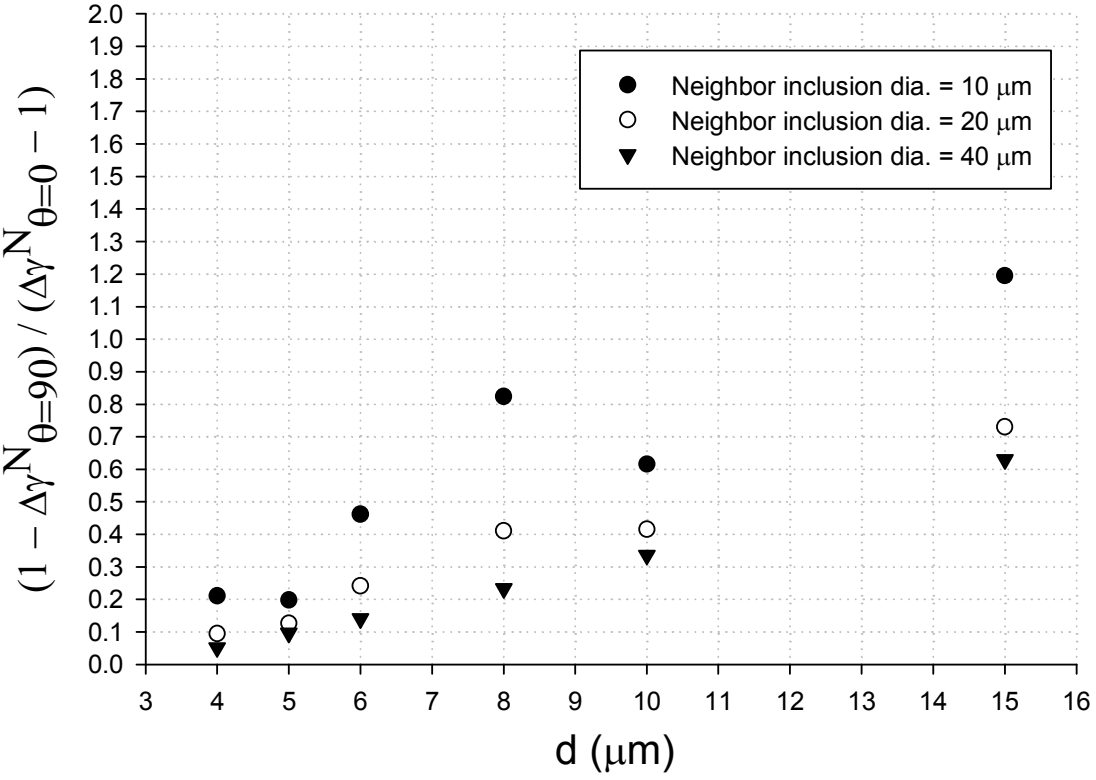

Figure 8-8: Ratio of beneficial shielding gain at θ = 90º to the unfavorable $\Delta\gamma^N$ magnification at θ = 0º vs. particles' spacing.

Next, we study $\Delta\gamma^N$ dependence on the remote applied strain amplitude for three candidate cases with θ = 0º, 45º, and 90º. Inclusions are 20 μm in diameter and d = 10 μm for all cases. As shown in Figure 8-9, intensification and shielding intensities appear to be almost independent of the applied strain level for $R_\varepsilon = \varepsilon_{min}/\varepsilon_{max} = 0$ and $\varepsilon_{max}/\varepsilon_{ys}$= 0.4, 0.5, 0.6, 0.7, and 0.8. Simulations for other inclusion sizes and spacing show the same trend and are not repeated here.

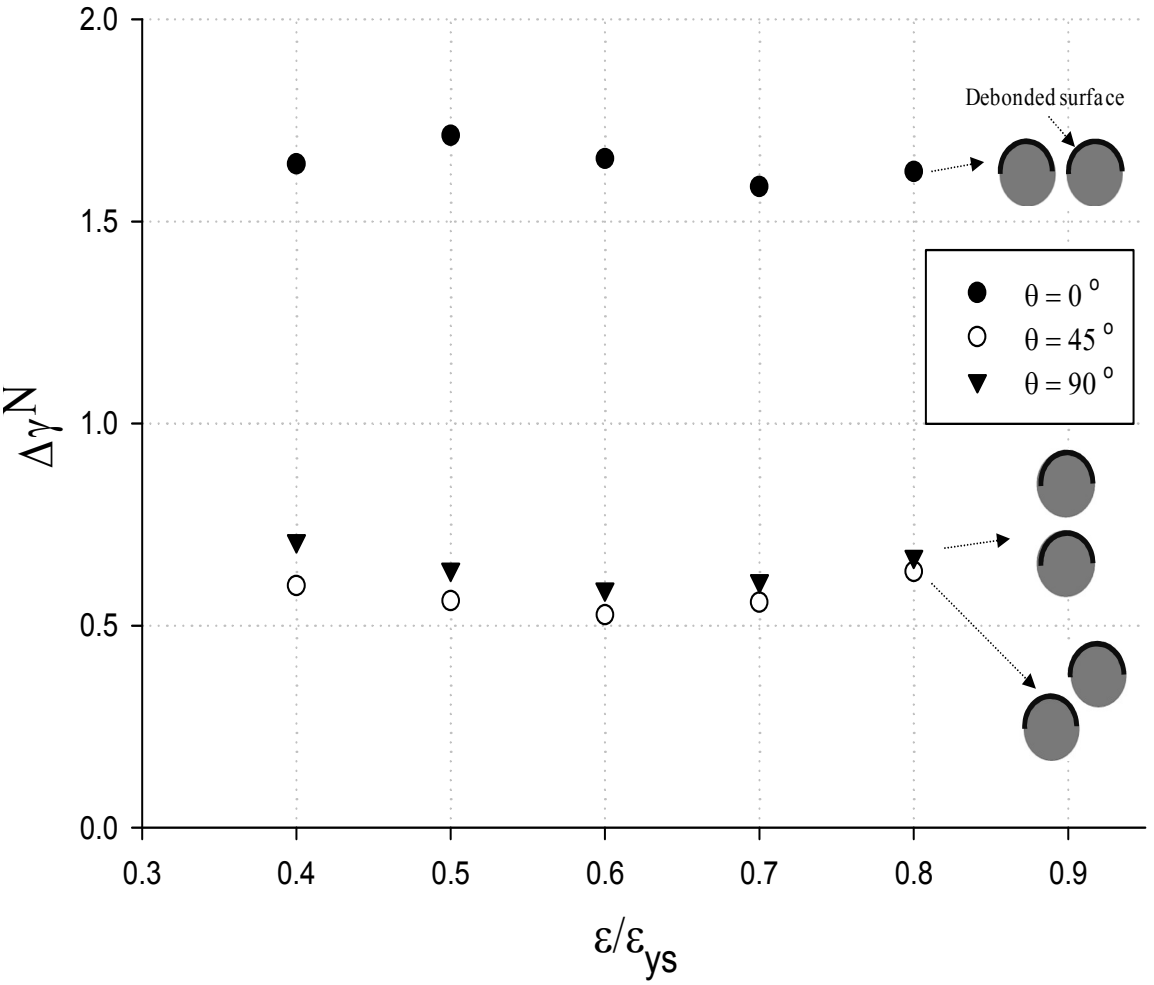

Figure 8-9: $\Delta\gamma^N$ vs. remote applied strain amplitude.

It would be instructive to verify whether the normalized nonlocal $\Delta\Gamma$ parameter, i.e., $\Delta\Gamma^N$, is subject to similar intensification and shielding trends. For brevity, it suffices to present only plots of $\Delta\Gamma^N$ versus θ, for several values of d in Figure 8-10 (counterpart to Figure 8-5 for $\Delta\gamma^N$). The macroscopic applied peak strain and strain ratio for these simulations are $\varepsilon_{max} = 0.8\ \varepsilon_{ys}$ and $R_\varepsilon = \varepsilon_{min}/\varepsilon_{max} = 0$, respectively. The $\Delta\Gamma^N$ values are slightly higher at all θ and d values studied here. This increase is due to the added contribution of the tensile stress and is expected to depend on applied strain ratio, R_ε.

Nevertheless, $\Delta\Gamma^N$ trends are similar to those of $\Delta\gamma^N$ with regard to intensification and shielding effects.

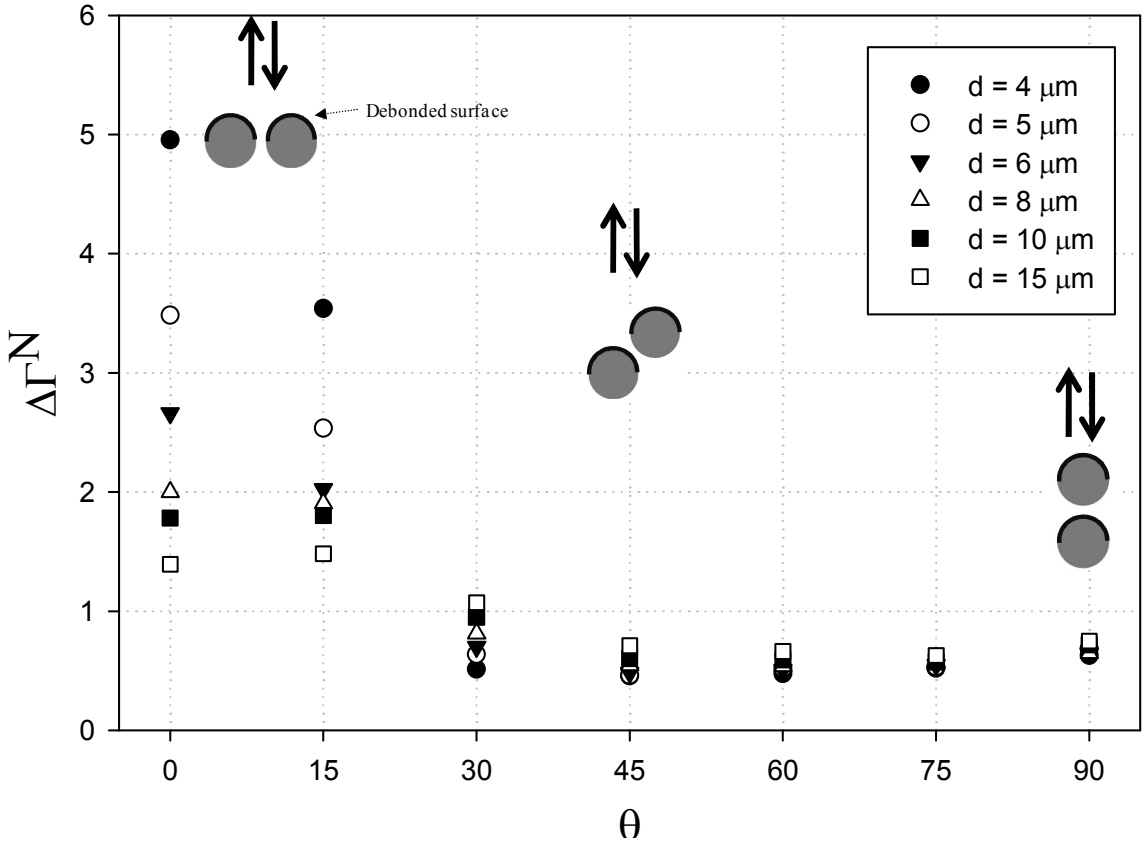

Figure 8-10: $\Delta\Gamma^N$ vs. inclusion pair orientation.

Figure 8-11 illustrates a three-dimensional (3D) representation of an inclusion pair with model dimensions slightly modified to improve computational efficiency. Inclusions are spherical in shape with diameter of 20 μm. Figure 8-12 is the 3D counterpart of Figure 8-5 and shows the prediction of $\Delta\gamma^N$ dependence on θ for d = 4 μm, 5 μm, and 8 μm.

The 3D simulation trends appear less structured and are pointwise different in magnitude from the 2.5D predictions. The lack of smooth trends is mainly due to mesh coarseness in the FIP averaging region due to computational limitations. Nevertheless, the 3D trends generally confirm the aforementioned intensification and shielding effects of the neighboring inclusion as $\theta \to 0^{\circ}$ and $\theta \to 90^{\circ}$, respectively. Little additional insight is gained from much more costly 3D simulation in this case.

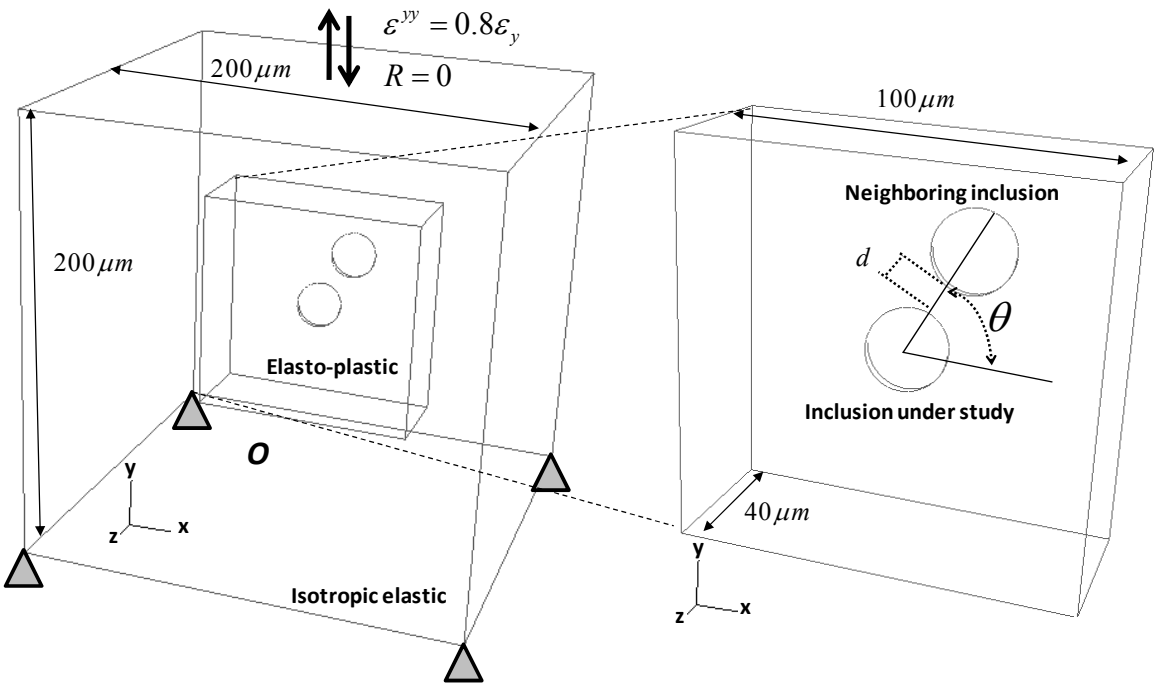

Figure 8-11: Three-dimensional finite element model.

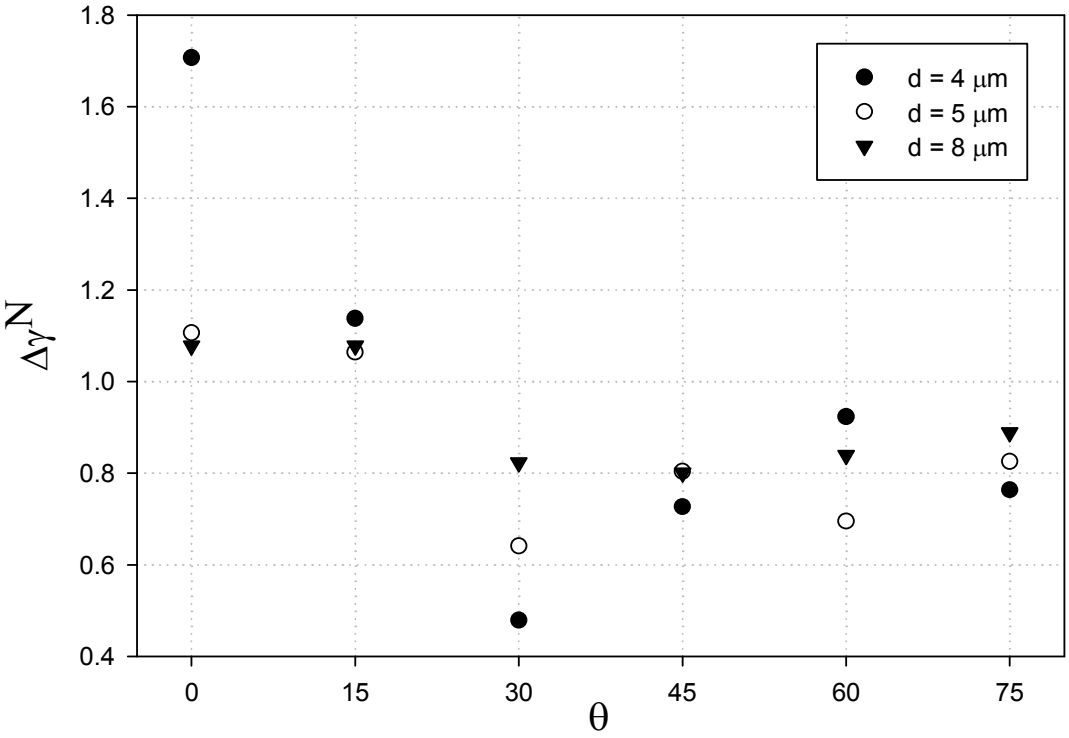

Figure 8-12: 3D FE prediction of $\Delta\gamma^N$ dependence on inclusion pair orientation.

8.4 Inclusion-matrix debonded interface orientation

Throughout this Chapter, we have assumed that the debonded half of the inclusion-matrix interface is normal to the remote applied loading direction for both the center as well as neighbor inclusions, as shown in Figure 8-13 for $\theta = 0^o$ and 45^o.

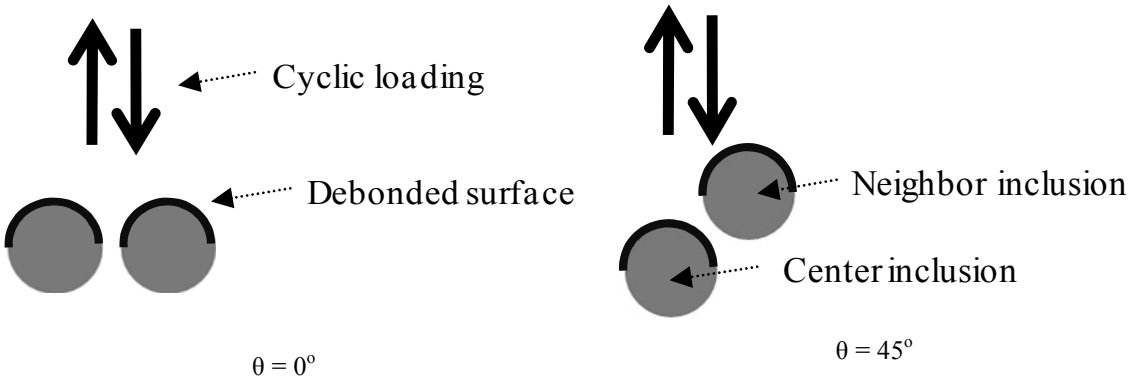

Figure 8-13: Debonded interface orientation.

To justify this assumption for the debonded interface orientation, we simulate the distribution of the magnitude of tensile normal traction (a driving force for inclusion-matrix separation) acting on the inclusion-matrix interface of the center inclusion, for intact, perfectly bonded inclusions. The tensile normal traction is calculated as $\vec{t} = \vec{n}^T \cdot \underset{\sim}{\sigma} \cdot \vec{n}$ at all nodes along the interface, where $\vec{n}$ is the point-wise unit vector normal to the interface. The diameter is 20 μm for both inclusions, and the inclusion spacing is d = 5 μm. In Figure 8-14, the hollow circle and cross symbols mark the locations along the inclusion-matrix interfaces of the center and neighbor inclusions, respectively, where $\vec{t}$ is within 10% of its highest value. Each of the seven concentric circles outlines the

inclusion-matrix interface for a specific inclusion pair orientation with respect to the transverse direction, θ.

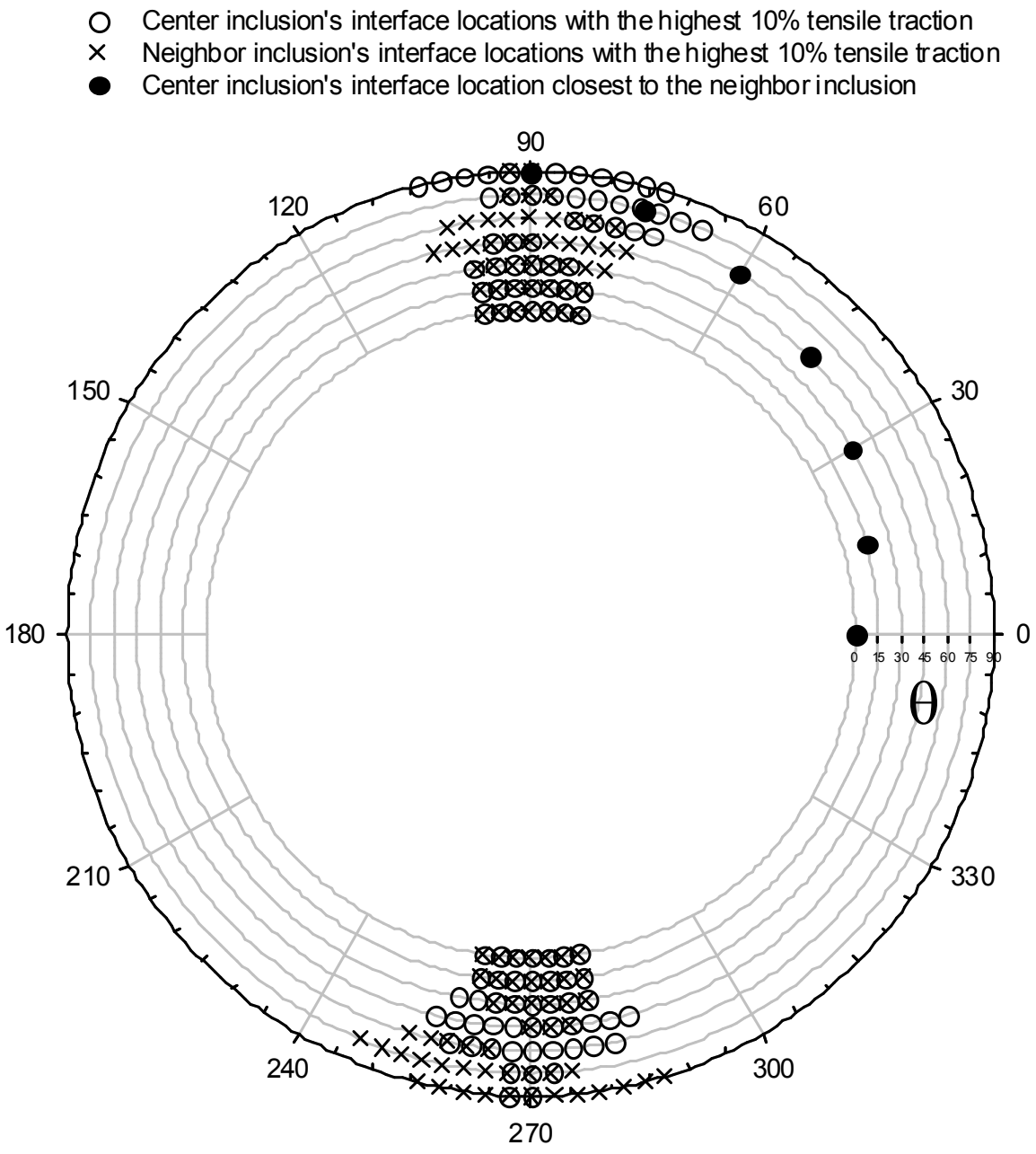

Figure 8-14: Locations along the inclusion-matrix interface with the 10% highest tensile traction for various θ for $\varepsilon_{max} = 0.5\ \varepsilon_{ys}$ ($R_\varepsilon = 0$).

At each θ, the single solid circle symbol marks the location on the center inclusion's interface that is directly facing and closest to the neighbor inclusion. This location is another intuitive debonded interface scenario as shown in Figure 8-15 for θ = 45°.

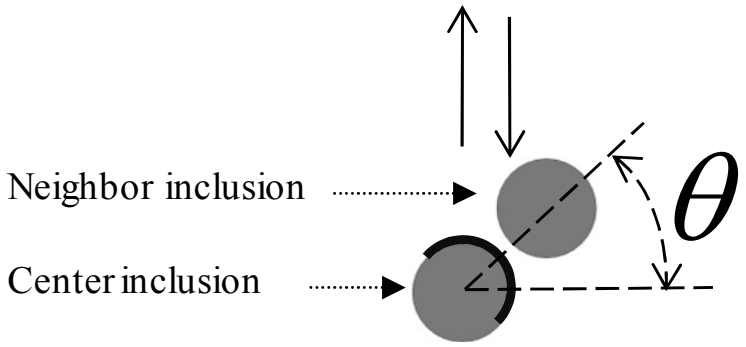

Figure 8-15: Candidate debonded interface scenario for θ = 45°.

The simulations of Figure 8-16 are identical to those of Figure 8-14 except the applied uniaxial peak strain has increased from 0.5 ε_{ys} to 0.8 ε_{ys} ($R_\varepsilon = 0$). Invariably, 10% of all the interface nodes with the highest point-wise magnitude of tensile normal traction, $\|\vec{t}\|$, are located around the inclusions' north and south poles. These points shift slightly when θ or the applied strain amplitude changes, but they are generally confined to these poles. Therefore, the assumption of a debonded interface that is normal to the applied loading direction would be reasonable for both center as well as neighbor inclusions for our qualitative study.

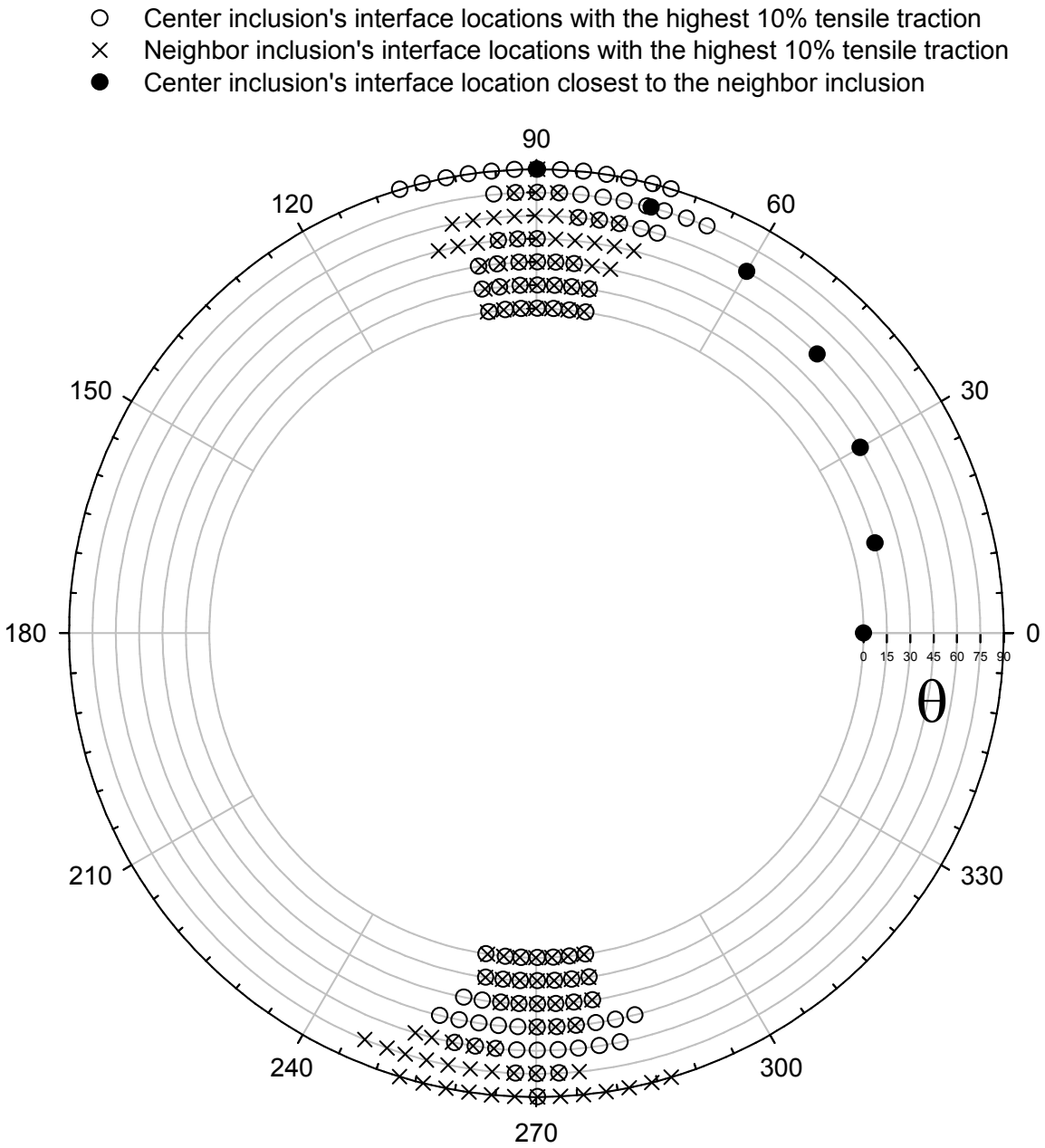

Figure 8-16: Locations along the inclusion-matrix interface with the 10% highest tensile traction for various θ for $\varepsilon_{max} = 0.8\ \varepsilon_{ys}$ ($R_\varepsilon = 0$).

8.5 Integration into the weighted probability approach

In Chapter 6, we introduced a weighted probability approach for modeling surface fatigue crack initiation probability, p_s. An attempt was made to maintain the generality of the framework so as to allow for future refinements such as the integration of inclusion clustering effects. To include the clustering effects, Eq. 7.2 should be revised as

$$P_{inclusion}^{\omega} = \int \left\{ \int \left[\int \left(\int P_R \; \mathrm{f}_{R',d,\theta}^{R} \; C^{R,R',d,\theta,\omega} \; \mathrm{d}R \right) \mathrm{d}R' \right] \mathrm{d}d \right\} \mathrm{d}\theta \tag{8.3}$$

where R is the inclusion size (radius) and P_R refers to the size distribution of inclusions. The variable $\mathrm{f}_{R',d,\theta}^{R}$ is defined as the conditional probability that the nearest neighbor inclusion (to the inclusion with radius R) is of radius R', spacing d, and orientation (with respect to the applied uniaxial stress direction) θ (see Figure 8-3 for the definition of inclusion spacing and orientation). This conditional probability is essentially a nearest-neighbor distribution function [196] that can be based on the experimental data.

The variable $C^{R,R',d,\theta,\omega}$ is defined as the conditional probability that an inclusion with radius R with a nearest neighbor inclusion with radius R', spacing d, and orientation θ is a fatigue hot spot at a given applied strain/stress amplitude, referred to with ω. This conditional probability reflects the shielding/intensification effects of the neighboring inclusion taking into account the spacing and orientation between the inclusions. It can be expressed as the probability that the underlying FIP exceeds a material-specific threshold, FIP*.

$$C^{R,R',d,\theta,\omega} = \Pr(FIP > FIP^*) \tag{8.4}$$

Due to the generality of the weighted probability approach, higher order statistics of microstructure attributes may also be addressed. The study of these effects is beyond the scope of this thesis.

8.6 Summary

Parametric cyclic FE simulations suggest that the HCF crack initiation potency of debonded primary non-metallic inclusions, as reflected through FIPs, is strongly influenced by the existence of a neighboring inclusion. This is the case for the partially debonded inclusions under study, and relative to the case with no neighboring inclusion:

- FIPs are higher (intensification) when the inclusion pair is oriented transverse to the loading direction, weakening exponentially as inclusion spacing increases. The intensification effect of the neighboring inclusion almost completely diminishes for particle spacing on the order of the neighboring inclusion's diameter and beyond.
- FIPs are lower (shielding) as the inclusion pair aligns with the applied loading direction. For this orientation, shielding depends strongly on the neighboring inclusion's size but appears to vary negligibly with particle spacing.
- In practice, the objective may be to avoid detrimental intensification due to clustering of inclusions rather than taking advantage of any possible enhancement in fatigue resistance through the shielding effects.
- Relative to the orientations that result in $\Delta\gamma^N$ intensification, the scatter in the $\Delta\gamma^N$, for all the orientations with the shielding effect, is much smaller. As such, the intensification level is considered more sensitive to the particle spacing than the shielding level.
- Intensification and shielding levels appear to be almost independent of the applied strain levels studied.

Simulation-based strategies offer a convenient platform [85, 197-199] to understand mechanisms of fatigue crack formation and early growth from such second phase particles and through the inclusion cluster. These in turn can be used to:

- Identify means to suppress such phenomena,
- Explain such properties as directional dependence or anisotropy of fatigue response,
- Design alloys with enhanced fatigue properties, and
- Predict the equivalent crack size to be used at the onset of fracture mechanics analysis, as applicable.

We reiterate that such studies of idealized nature are useful for qualitative comparison of different scenarios, discerning trends, and predicting likely effects of neighboring inclusions. A myriad of other microstructural, environmental, and loading attributes influence the fatigue response, and their study is beyond the scope of this work. Further analysis using more realistic crystal plasticity simulations will be pursued to quantify and rank order added effects of microstructure variability at the grain scale, a key factor in the HCF regime. These may shed additional light on particle size and spacing dependencies owing to interplay with microstructure.

9 Contributions and recommendations for future work

9.1 Contributions

This research studies the mechanisms that influence the ratio of surface to bulk fatigue crack initiation probabilities at low stress amplitudes (i.e. HCF and VHCF regimes). The specific contributions of this research are:

1. Studied several simulation-based Fatigue Indicator Parameters (FIPs) that are suitable candidates for assessment of early stages of fatigue crack formation at primary inclusions and pores in the HCF and VHCF regimes.
2. Examined, using crystal plasticity FE simulations, the effects of applied uniaxial strain amplitude on the probability of inclusion-matrix interface separation.
3. Examined, using crystal plasticity FE simulations, the state of compressive residual stresses around inclusions and pores as well as their degree of relaxation due to cyclic loading.
4. Developed a weighted probabilistic construct to characterize the probabilities of fatigue crack formation from surface versus bulk fatigue hot spots. This construct assists in predicting the surface to bulk transition stress/strain amplitude and its dependence on specimen size, inclusion density, inclusion radius distribution, and inclusion-matrix interface strength. The approach is (i) amenable to cost-effective finite element simulations and (ii) accounts for the interplay of microstructure attributes and applied loading.
5. Incorporated FIPs (well-suited for fatigue crack formation and early growth under HCF and VHCF regimes) into the weighted probabilistic construct. This project

provides a fatigue model that is capable of simultaneously handling the effects of multiaxial loading conditions (e.g., tension, torsion, rotating bending and plane bending), stress gradient, and free surface effects on the fatigue response.

6. Devised and performed systematic crystal plasticity FE simulations to exercise the weighted probabilistic construct in a fine-grained subsolvus microstructure of a powder metallurgy processed Ni-base superalloy, IN100, where non-metallic processing inclusions are the main fatigue hot spots in the HCF and VHCF regimes.
7. Examined the effects of neighboring inclusions on the HCF crack formation potency in martensitic gear steel where inclusions appear in clusters [21].

From a broader perspective, the computational approach pursued in this research may offer the following:

8. It assists in predicting variability in early stages of fatigue crack initiation life, including the shape of its distribution; this work thus helps to reduce the number of experiments required in order to predict crack formation. Therefore, it may extend the service life of existing superalloys, as Jha *et al.* [15] suggested can be done, with the confidence level necessary for the relevant applications.
9. It facilitates the implementation of fatigue response properties obtained from experiments on laboratory coupons in the design and life assessment of large components such as turbine disks.

10. It provides information necessary for the development of microstructure–property fatigue models that can be used to make processing and manufacturing recommendations. From the material design perspective, this research will contribute to the current efforts to develop new alloys with enhanced fatigue properties. It will enhance damage tolerant design methodologies and tools such as DARWIN™, Design Assessment of Reliability With INspection, which are used extensively by gas turbine engine manufacturers and the Federal Aviation Administration (FAA) to improve the safety of jet engines [200].

9.2 Recommendations for future work

Extensive computational studies have been performed in this thesis to characterize the fatigue crack formation and early growth in alloys with primary inclusions. The simulated surface initiation probability approach is new and not yet comprehensive in all respects. There are many avenues for future research as listed below:

9.2.1 Experiments

9.2.1.1 Identification of fatigue crack formation mechanisms in other advanced alloys

The methodology proposed in this thesis can be used to simulate surface initiation probability in other advanced alloys such as titanium alloys and clean steels by recognition of similar competing surface and bulk initiation mechanisms involving non-metallic particles, large grains, α cluster-defects, or phases that are particularly susceptible to fatigue crack formation.

In a given material, various crack incubation processes often operate simultaneously. For instance, formation of Zener-Stroh fatigue cracks [cf. 201, 202] due to the impingement of slip bands on the grain boundaries has been reported in polycrystalline Ni [203], as shown by the arrows in Figure 9-1. Understanding the key underlying physical mechanisms is essential in order to define a truly predictive fatigue indicator parameter.

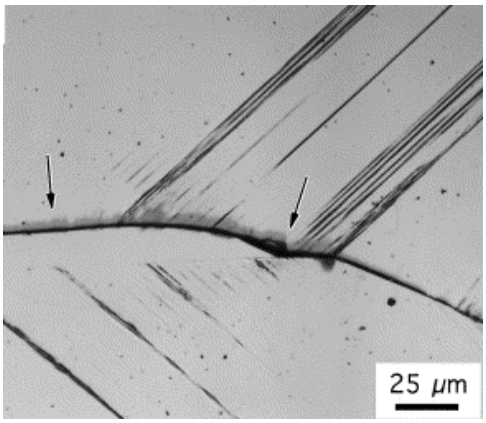

Figure 9-1: Crack formation at grain boundaries of Ni tested at room temperature [203] ($\Delta\varepsilon^p/2 = 2.5\times10^{-4}$).

9.2.1.2 Characterizing the mechanical properties of inclusion-matrix interface and surface oxide scale

We concluded in Chapter 3 that the inclusions-matrix interface characteristics can significantly influence the potency of inclusions to initiate fatigue cracks. The probability of inclusion-matrix debonding at a given applied stress/strain amplitude depends on the bond strength between the two phases. Experimental data are lacking for the bond strength of inclusions and matrix phases under tensile and shear loading. Additionally, this bond strength is expected to depend on the size of the interface, demanding small-scale experiments. With regard to the surface oxide scales, there are relatively few techniques available for measuring their mechanical properties. The mechanical properties of the surface oxides are expected to depend on the scale thickness.

9.2.1.3 Characterizing the cyclic stress-strain response of the treated surface layer

Mechanical surface treatments induce a significant gradient in microstructure attributes from the surface to the core. The altered microstructure in the specimen surface region is likely to respond differently to changes in the loading, thus affecting the surface initiation probability. Detailed experimental study is imperative in order to characterize the cyclic stress-strain response of the case layer. Such studies should provide information regarding the degree of cyclic hardening that occurs during the initial stages of fatigue cycling.

9.2.1.4 Experimental measurement of residual stress state and relaxation behavior

Crystal plasticity simulation findings regarding the degree of residual stress relaxation around inclusions and pores need to be validated with experiments. Interrupted residual stress measurements or non-destructive high energy x-ray diffraction methods can be utilized to gain insight into residual stress profile evolution during cyclic loading. Any additional information regarding the compressive residual stress state and its relaxation behavior can be used to tailor microstructures with improved fatigue resistance.

9.2.2 Computational modeling

9.2.2.1 3D models with irregularly shaped inclusions

We simulated idealized cylindrical inclusions using 2.5D generalized plane strain models. Our philosophy was that such idealized simulations help to delineate the trends and compare scenarios. It may be necessary to construct high resolution 3D FE meshes from realistic microstructures in order to perform a standalone assessment of fatigue initiation potency of various inclusion/pore scenarios. For instance, Gokhale *et al.* [204-206] implemented complex particle morphologies in computer simulated heterogeneous microstructures using digital image processing. Zhang and McDowell [149] also evaluated fatigue potency at primary inclusions by constructing 3D FE meshes from measured (realistic) microstructures containing non-metallic inclusions.

Conducting crystal plasticity simulations of 3D FE domains with complex inclusion/pore morphologies to construct simulated statistical distribution of response parameters can be computationally prohibitive. Therefore, there is a need for multiscale modeling such as the schemes developed by Liu and co-workers [207, 208] to identify the fatigue critical hot spots. Once the fatigue critical hot spots are identified, detailed crystal plasticity simulations can be conducted locally to characterize the variability in HCF.

9.2.2.2 Development of mechanism-specific correlation functions

Przybyla and McDowell [51] have recently proposed a new microstructure-sensitive extreme value statistical framework. It couples the extreme value distributions

of certain response functions (FIPs) to the correlated microstructure attributes that exist at the extreme value locations of these FIPs. By mathematically representing fatigue driving force parameters in the space of basis functions used to represent distribution functions of microstructure attributes, we may be abled to identify hot spot regions that are above a FIP threshold.

9.2.2.3 Development of new adaptive fatigue indicator parameters

For simulating Zener-Stroh fatigue cracks [cf. 201, 202, 203] that could form due to the impingement of slip bands on the grain boundaries, Zhang [84] introduced an impingement parameter that characterizes the effects of directional plastic strain accumulation at the continuum level. Other FIPs could be introduced to reflect MSC growth at the scale of single inclusion and inclusion clusters to estimate the life consumed in crack formation and small crack growth to length of the order of cluster size.

The mechanisms and rate of crack formation and MSC growth processes are known to change over the crack evolution period due to a myriad of short and long range microstructure attributes. As such, there is a need for the FIPs to adapt to and reflect the altered microstructure attributes.

References

[1] I. Papadopoulos, V. Panoskaltsis, Invariant formulation of a gradient dependent multiaxial high-cycle fatigue criterion, Engineering Fracture Mechanics, 55 (1996) 513-528.

[2] F. Morel, T. Palin Luc, A non local theory applied to high cycle multiaxial fatigue, Fatigue & Fracture of Engineering Materials & Structures, 25 (2002) 649-665.

[3] C. Phillips, R. Heywood, The size effect in fatigue of plain and notched steel specimens loaded under reversed direct stress, Proceedings of the Institution of Mechanical Engineers, 165 (1951) 113-124.

[4] Y. Furuya, S. Matsuoka, T. Abe, Inclusion-controlled fatigue properties of 1800 MPA-class spring steels, Metallurgical and Materials Transactions A: Physical Metallurgy and Materials Science, 35 A (2004) 3737-3744.

[5] G. Harkegard, Experimental study of the influence of inclusions on the fatigue properties of steel, Engineering Fracture Mechanics, 6 (1974) 795-805.

[6] Y. Kato, K. Sato, K. Hiraoka, Y. Nuri, Recent Evaluation Procedures of Nonmetallic Inclusions in Bearing Steels. Statistics of extreme value method and development of higher frequency ultrasonic testing method, Sanyo Technical Report, 8 (2001) 59-67.

[7] P.J. Laz, B.M. Hillberry, Fatigue life prediction from inclusion initiated cracks, International Journal of Fatigue, 20 (1998) 263-270.

[8] H. Mughrabi, On the life-controlling microstructural fatigue mechanisms in ductile metals and alloys in the gigacycle regime, Fatigue and Fracture of Engineering Materials and Structures, 22 (1999) 633-641.

[9] H. Mughrabi, Fatigue crack initiation mechanisms and fatigue life in high-cycle and in ultrahigh-cycle fatigue, in, Minerals, Metals and Materials Society, Warrendale, PA 15086, United States, Seattle, WA, United States, 2002, pp. 3-15.

[10] R. Murakami, D. Yonekura, Z. Ni, Fatigue fracture behavior of high-strength steel in super long life range, JSME International Journal, Series A (Solid Mechanics and Material Engineering), 45 (2002) 517-522.

[11] S. Nishijima, K. Kanazawa, Stepwise S-N curve and fish-eye failure in gigacycle fatigue, Fatigue and Fracture of Engineering Materials and Structures, 22 (1999) 601-607.

[12] M.J. Caton, S.K. Jha, A.H. Rosenberger, J.M. Larsen, Divergence of mechanisms and the effect on the fatigue life variability of rene' 88 DT, (2004) 305-312.

[13] S.K. Jha, M.J. Caton, J.M. Larsen, A new paradigm of fatigue variability behavior and implications for life prediction, Materials Science and Engineering: A, 468-470 (2007) 23-32.

[14] S.K. Jha, M.J. Caton, J.M. Larsen, Mean vs. Life-Limiting Fatigue Behavior of A Nickel-Based Superalloy, in: R.C. Reed, K.A. Green, P. Caron, T.P. Gabb, M.G. Fahrmann, E.S. Huron, S.A. Woodard (Eds.) Superalloys 2008, The Minerals, Metals & Materials Society (TMS), Champion, Pennsylvania, 2008.

[15] S.K. Jha, J.M. Larsen, A.H. Rosenberger, Towards a Physics-Based Description of Fatigue Variability Behavior in Probabilistic Life Prediction, Engineering Fracture Mechanics, In Press, Accepted Manuscript (2008).

[16] S. Jha, J. Larsen, A. Rosenberger, G. Hartman, Dual fatigue failure modes in Ti-6Al-2Sn-4Zr-6Mo and consequences on probabilistic life prediction, Scripta Materialia, 48 (2003) 1637-1642.

[17] K. Shiozawa, L. Lu, S. Ishihara, S–N curve characteristics and subsurface crack initiation behaviour in ultra-long life fatigue of a high carbon-chromium bearing steel, Fatigue & Fracture of Engineering Materials & Structures, 24 (2001) 781-790.

[18] K.S. Ravi Chandran, P. Chang, G.T. Cashman, Competing failure modes and complex S-N curves in fatigue of structural materials, International Journal of Fatigue, 32 (2010) 482-491.

[19] G. Cashman, A review of Competing Modes fatigue behavior, International Journal of Fatigue, 32 (2010) 492-496.

[20] K.S. Ravi Chandran, P. Chang, G.T. Cashman, Competing failure modes and complex S-N curves in fatigue of structural materials, International Journal of Fatigue, 32 (2010) 482-491.

[21] B.L. Tiemens, Performance Optimization and Computational Design of Ultra-High Strength Gear Steels, PhD Thesis, Department of Materials Science and Engineering, Northwestern University, Evanston, IL, (2006).

[22] http://www.latrobesteel.com/assets/documents/datasheets/Ferrium_C61.pdf, accessed on October 6, 2010.

[23] J. Davis, Nickel, cobalt, and their alloys, ASM International, 2000.

[24] M. Donachie, S. Donachie, Superalloys: a technical guide, ASM International, 2002.

[25] C. Sims, Superalloys: Genesis and Character, Wiley-Interscience, John Wiley and Sons, Superalloys II--High Temperature Materials for Aerospace and Industrial Power, (1987) 3-26.

[26] H. Miller, W. Chambers, Gas Turbine Design and Superalloys, Wiley-Interscience, John Wiley and Sons, Superalloys II--High Temperature Materials for Aerospace and Industrial Power, (1987) 27-57.

[27] R. Reed, The superalloys: fundamentals and applications, Cambridge University Press, 2006.

[28] The Rolls-Royce Trent Engine, http://www.msm.cam.ac.uk/phase-trans/mphil/Trent1/sld001.htm, accessed on March 3, 2011.

[29] D. Duhl, Directionally solidified superalloys, Wiley-Interscience, John Wiley and Sons, Superalloys II--High Temperature Materials for Aerospace and Industrial Power, (1987) 189-214.

[30] M. Durand-Charre, The microstructure of superalloys, CRC Press, 1997.

[31] Nickel Based Superalloys, http://www.msm.cam.ac.uk/phase-trans/2003/Superalloys/superalloys.html, accessed on March 3, 2011.

[32] C.T. Sims, N.S. Stoloff, W.C. Hagel, Superalloys II: high-temperature materials for aerospace and industrial power, (1987).

[33] K. Li, N.E. Ashbaugh, A.H. Rosenberger, Crystallographic Initiation of Nickel-Base Superalloy IN100 at RT and 538°C Under Low Cycle Fatigue Conditions, in: K.A. Green, T.M. Pollock, H. Harada, T.E. Howson, R.C. Reed, J.J. Schirra, S. Walston (Eds.) Superalloys 2004: proceedings of the tenth international symposium on superalloys The Minerals, Metals & Materials Society (TMS), Champion, Pennsylvania, 2004.

[34] J. Wise, Systems design of advanced gear steels, in: Department of Mechanical Engineering, , Northwestern University, 1998.

[35] G.B. Olson, Materials design: building a better martensite, in: International Conference on Displacive Phase Transformations and their Applications in Materials Engineering. In Honor of Professor C M Wayman on the Occasion of His Retirement, 8-9 May 1996, TMS, Warrendale, PA, USA, 1998, pp. 15-26.

[36] G.B. Olson, Advances in theory: Martensite by design, Materials Science & Engineering A (Structural Materials: Properties, Microstructure and Processing), 438-440 (2006) 48-54.

[37] H. Bomas, P. Mayr, M. Schleicher, Calculation method for the fatigue limit of parts of case hardened steels, in: 11th International Conference on the Strength of Materials, 25-29 Aug. 1997, Elsevier, Switzerland, 1997, pp. 393-396.

[38] Y. Fu, Y. Gu, X. Jing, M. Hu, B. Lou, New method to evaluate fracture toughness of case-hardened steel, International Journal of Fracture, 71 (1995) 71-76.

[39] S. Laue, H. Bomas, F. Hoffmann, Influence of surface condition on the fatigue behaviour of specimens made of a SAE 5115 case-hardened steel, Fatigue and Fracture of Engineering Material and Structures, 29 (2006) 229-241.

[40] S. Seyedi, K.H. Lang, D. Lohe, Fatigue behaviour of case-hardened P/M steels, Key Engineering Materials, (2007) 371-374.

[41] N. Shamsaei, A. Fatemi, Deformation and fatigue behaviors of case-hardened steels in torsion: experiments and predictions, International Journal of Fatigue, 31 (2009) 1386-1396.

[42] J. Wright, J. Sebastian, C. Kern, R. Kooy, Design, Development and Application of New, High–Performance Gear Steels, www.geartechnology.com, accessed on March 3, 2011, (2010).

[43] G. Carinci, M. Hetherington, G. Olson, M2C carbide precipitation in AF1410 steel, Le Journal de Physique Colloques, 49 (1988) 6-6.

[44] QuesTek Innovations LLC, www.questek.com, accessed on March 3, 2011.

[45] J. Pacheco, G. Krauss, Microstructure and high bending fatigue strength in carburized steel, Journal of Heat Treating, 7 (1989) 77-86.

[46] J. Davis, Gear materials, properties, and manufacture, ASM International, 2005.

[47] R. Gorockiewicz, A. Adamek, M. Korecki, Steels for Vacuum Carburizing and Structure of the Carburizing Layer after Low Pressure Carburizing, www.geartechnology.com, accessed on March 3, 2011.

[48] J. Lemaitre, J.L. Chaboche, Mechanics of Solid Materials, Cambridge University Press, 1990.

[49] ABAQUS 6.7, Simulia, Providence, RI, 2006.

[50] M. Shenoy, Y. Tjiptowidjojo, D. McDowell, Microstructure-sensitive modeling of polycrystalline IN 100, International Journal of Plasticity, 24 (2008) 1694-1730.

[51] C. Przybyla, D. McDowell, Microstructure-sensitive extreme value probabilities for high cycle fatigue of Ni-base superalloy IN100, International Journal of Plasticity, 26 (2010) 372-394.

[52] K. Findley, Physically-based model for elevated temperature low cycle fatigue crack initiation and growth in Rene88DT, PhD Thesis, Department of Mechanical Engineering, Georgia Institute of Technology, Atlanta, Georgia, (2005).

[53] K.O. Findley, A. Saxena, Low cycle fatigue in Rene 88DT at 650 degrees C: Crack nucleation mechanisms and modeling, Metallurgical and Materials Transactions A: Physical Metallurgy and Materials Science, 37 (2006) 1469-1475.

[54] E. Lee, Elastic-Plastic Deformations at Finite Strains, ASME Journal of Applied Mechanics, 36 (1969) 1-6.

[55] B. Bilby, R. Bullough, E. Smith, Continuous Distributions of Dislocations: A New Application of the Methods of Non-Riemannian Geometry, Proc. Royal Society, A231 (1955) 263-273.

[56] R. Asaro, Micromechanics of crystals and polycrystals, Advances in Applied Mechanics, 23 (1983) 1-115.

[57] R. Hill, Continuum micro-mechanics of elastoplastic polycrystals, J. Mech. Phys. Solids, 13 (1965) 89-101.

[58] R. Hill, J. Rice, Constitutive analysis of elastic-plastic crystals at arbitrary strain, Journal of the Mechanics and Physics of Solids, 20 (1972) 401-413.

[59] M. Shenoy, A. Gordon, D. McDowell, R. Neu, Thermomechanical Fatigue Behavior of a Directionally Solidified Ni-base Superalloy, Journal of Engineering Materials and Technology, 127 (2005) 325-337.

[60] A. Wang, R. Kumar, M. Shenoy, D. McDowell, Microstructural Constitutive Models for Cyclic Deformation and LCF in Two Phase Ni-base Superalloys, To be submitted, (2005).

[61] W. Osterle, D. Bettge, B. Fedelich, H. Klingelhoffer, Modeling the orientation and direction dependence of the critical resolved shear stress of Nickel base superalloy single crystal, Acta Materialia, 48 (2000) 689-700.

[62] D. Bettge, W. Österle, ``Cube slip``in near-[111] oriented specimens of a single-crystal nickel-base superalloy, Scripta Materialia, 40 (1999).

[63] M. Heilmaier, U. Leetz, B. Reppich, Order strengthening in the cast nickel-based superalloy IN 100 at room temperature, Materials Science and Engineering A, 319 (2001) 375-378.

[64] B. Reppich, P. Schepp, G. Wehner, Some New Aspects Concerning Particle Hardening Mechanisms in Gamma Prime Precipitating Nickel-Base Alloys--Part II: Experiments, (1982).

[65] Y. Estrin, H. Mecking, A unified phenomenological description of work hardening and creep based on one-parameter models, Acta Metallurgica, 32 (1984) 57-70.

[66] H. Mecking, U. Kocks, Kinetics of flow and strain-hardening, Acta Metallurgica, 29 (1981) 1865-1875.

[67] W.W. Milligan, E.L. Orth, J.J. Schirra, M.F. Savage, Effects of microstructure on the high temperature constitutive behavior of IN100, in: K.A. Green, T.M. Pollock, H. Harada, T.E. Howson, R.C. Reed, J.J. Schirra, S. Walston (Eds.) Superalloys 2004: proceedings of the tenth international symposium on superalloys TMS, Warrendale, PA, USA, 2004, pp. 331-339.

[68] W.N. Findley, Combined-stress fatigue strength of 76S-T61 aluminum alloy with superimposed mean stresses and corrections for yielding, in, National Advisory Committee for Aeronautics, Washington, DC, United States, 1953, pp. 90.

[69] W.N. Findley, Fatigue of metals under combinations of stresses, American Society of Mechanical Engineers -- Transactions, 79 (1957) 1337-1347.

[70] F.B. Stulen, H.N. Cummings, W.C. Schulte, Design guide: preventing fatigue failures, Machine Design, 33 (1961).

[71] F.B. Stulen, W.C. Schulte, Fatigue failure analysis and "prevention", Metals Engineering Quarterly, 5 (1965) 30-39.

[72] D.L. McDowell, J.Y. Berard, A ΔJ-based approach to biaxial fatigue, Fatigue & Fracture of Engineering Materials & Structures, 15 (1992) 719-741.

[73] D. Socie, J. Bannantine, Bulk deformation fatigue damage models, Materials Science and Engineering, 103 (1988) 3-13.

[74] D.L. McDowell, Microstructure-sensitive computational fatigue analysis, in: Y. Sidney, M.F. Horstemeyer (Eds.) Handbook of materials modeling, Part A: methods, Springer, The Netherlands, 2005, pp. 1193–1214.

[75] J. Fan, D.L. McDowell, M.F. Horstemeyer, K. Gall, Cyclic plasticity at pores and inclusions in cast Al-Si alloys, Engineering Fracture Mechanics, 70 (2003) 1281-1302.

[76] K. Gall, M. Horstemeyer, D.L. McDowell, J. Fan, Finite element analysis of the stress distributions near damaged Si particle clusters in cast Al-Si alloys, Mechanics of Materials, 32 (2000) 277-301.

[77] R. Prasannavenkatesan, D.L. McDowell, G.B. Olson, H.-J. Jou, Modeling Effects of Compliant Coatings on HCF Resistance of Primary Inclusions in High Strength Steels, Journal of Engineering Materials and Technology, 131 (2009) 121-126.

[78] R. Prasannavenkatesan, J. Zhang, D.L. McDowell, G.B. Olson, H.-J. Jou, 3D modeling of subsurface fatigue crack nucleation potency of primary inclusions in heat treated and shot peened martensitic gear steels, International Journal of Fatigue, 31 (2009) 1176-1189.

[79] A. Fatemi, P. Kurath, Multiaxial fatigue life predictions under the influence of mean-stresses, Journal of Engineering Materials and Technology, Transactions of the ASME, 110 (1988) 380-388.

[80] A. Fatemi, D.F. Socie, Critical Plane Approach to Multiaxial Fatigue Damage Including Out-Of-Phase Loading, Fatigue & Fracture of Engineering Materials & Structures, 11 (1988) 149-165.

[81] D. McDowell, Multiaxial fatigue strength, ASM International, Member/Customer Service Center, Materials Park, OH 44073-0002, USA, 1996., (1996) 263-273.

[82] A. Manonukul, F.P.E. Dunne, High- and Low-Cycle Fatigue Crack Initiation Using Polycrystal Plasticity, Proceedings: Mathematical, Physical and Engineering Sciences, 460 (2004) 1881-1903.

[83] K. Tanaka, T. Mura, A theory of fatigue crack initiation at inclusions, Metallurgical Transactions A (Physical Metallurgy and Materials Science), 13A (1982) 117-123.

[84] M. Zhang, Crystal plasticity modeling of Ti-6Al-4V and its application in cyclic and fretting fatigue analysis, PhD Thesis, Department of Mechanical Engineering, Georgia Institute of Technology, Atlanta, Georgia, (2008).

[85] D.L. McDowell, Simulation-based strategies for microstructure-sensitive fatigue modeling, Materials Science and Engineering A, 468-470 (2007) 4-14.

[86] R. Guo, H.J. Shi, Z.H. Yao, Modeling of interfacial debonding crack in particle reinforced composites using Voronoi cell finite element method, Computational Mechanics, 32 (2003) 52-59.

[87] J. Lankford, Inclusion-matrix debonding and fatigue crack initiation in low alloy steel, International Journal of Fracture, 12 (1976) 155-157.

[88] N. Mandal, G. Bhattacharyya, C. Chakraborty, Extensional detachment at the inclusion-matrix interface in a multiple inclusion system, Journal of Structural Geology, 26 (2004) 1773-1781.

[89] S.K. Samanta, G. Bhattacharyya, Modes of detachment at the inclusion-matrix interface, Journal of Structural Geology, 25 (2003) 1107-1120.

[90] X. Xu, Void nucleation by inclusion debonding in a crystal matrix, Modelling and Simulation in Materials Science and Engineering, 1 (1993) 111.

[91] S. Suresh, Fatigue of materials, Cambridge University Press, 1998.

[92] E. Gumbel, Statistics of extremes, Dover Publications, 2004.

[93] Y. Murakami, Inclusion rating by statistics of extreme values and its application to fatigue strength prediction and quality control of materials, International Journal of Fatigue, 18 (1996) 215-215.

[94] Y. Murakami, M. Endo, Effects of defects, inclusions and inhomogeneities on fatigue strength, International Journal of Fatigue, 16 (1994) 163-182.

[95] Y. Murakami, H. Usuki, Quantitative evaluation of effects of non-metallic inclusions on fatigue strength of high strength steels. II: Fatigue limit evaluation based on statistics for extreme values of inclusion size, International Journal of Fatigue, 11 (1989) 299-307.

[96] Y. Murakami, Analysis of stress intensity factors of modes I, II and III for inclined surface cracks of arbitrary shape, Engineering Fracture Mechanics, 22 (1985) 101-114.

[97] G. Shi, H. Atkinson, C. Sellars, C. Anderson, Comparison of extreme value statistics methods for predicting maximum inclusion size in clean steels, Ironmaking and Steelmaking, 26 (1999) 239-246.

[98] G. Shi, H.V. Atkinson, C.M. Sellars, C.W. Anderson, Application of the Generalized Pareto Distribution to the estimation of the size of the maximum inclusion in clean steels, 47 (1999) 1455-1468.

[99] A. Taliercio, Generalized plane strain finite element model for the analysis of elastoplastic composites, International Journal of Solids and Structures, 42 (2005) 2361-2379.

[100] H. Espinosa, P. Zavattieri, A grain level model for the study of failure initiation and evolution in polycrystalline brittle materials. Part I: Theory and numerical implementation, Mechanics of Materials, 35 (2003) 333-364.

[101] S. Kumar, S. Kurtz, Simulation of material microstructure using a 3D Voronoi tesselation: calculation of effective thermal expansion coefficient of polycrystalline materials, Acta Metallurgica et Materialia, 42 (1994) 3917-3927.

[102] O. Watanabe, H. Zbib, E. Takenouchi, Crystal plasticity: micro-shear banding in polycrystals using Voronoi tessellation, International Journal of Plasticity, 14 (1998) 771-788.

[103] A. Okabe, B. Boots, K. Sugihara, S. Chiu, Spatial tessellations, Wiley Chichester, 2000.

[104] F. Aurenhammer, Voronoi diagrams—a survey of a fundamental geometric data structure, ACM Computing Surveys (CSUR), 23 (1991) 345-405.

[105] D. Gross, M. Li, Constructing microstructures of poly-and nanocrystalline materials for numerical modeling and simulation, Applied Physics Letters, 80 (2009) 746-748.

[106] M. Shenoy, J. Zhang, D. McDowell, Estimating fatigue sensitivity to polycrystalline Ni-base superalloy microstructures using a computational approach, Fatigue & Fracture of Engineering Materials & Structures, 30 (2007) 889-904.

[107] K. Zhang, M. Wu, R. Feng, Simulation of microplasticity-induced deformation in uniaxially strained ceramics by 3-D Voronoi polycrystal modeling, International Journal of Plasticity, 21 (2005) 801-834.

[108] A.M. Wusatowska-Sarnek, P. Bhowal, D. Gynther, R. Montero, Effect of non-metallic inclusions on notched low cycle fatigue in P/M IN100 nickel-base superalloy, in, Trans Tech Publications Ltd, Vancouver, Canada, 2007, pp. 2960-2965.

[109] M.M. Shenoy, R.S. Kumar, D.L. McDowell, Modeling effects of nonmetallic inclusions on LCF in DS nickel-base superalloys, International Journal of Fatigue, 27 (2005) 113-127.

[110] R.M. Hoffman, H.R. Busby, Stress-based convergence analysis for p-adaptive hierarchical finite element analysis, Finite Elements in Analysis and Design, 34 (2000) 25-35.

[111] P. Katragadda, I.R. Grosse, A posteriori error estimation and adaptive mesh refinement for combined thermal-stress finite element analysis, Computers and Structures, 59 (1996) 1149-1163.

[112] C.S. Krishnamoorthy, K. Rajeshirke Umesh, Adaptive mesh refinement for two-dimensional finite element stress analysis, Computers and Structures, 48 (1993) 121-133.

[113] C.K. Lee, R.E. Hobbs, On using different finite elements with an automatic adaptive refinement procedure for the solution of 2-D stress analysis problems, International Journal for Numerical Methods in Engineering, 40 (1997) 4547-4576.

[114] C.K. Lee, S.H. Lo, Automatic adaptive refinement finite element procedure for 3D stress analysis, Finite Elements in Analysis and Design, 25 (1997) 135-166.

[115] Y. Gao, R. Ritchie, M. Kumar, R. Nalla, High-cycle fatigue of nickel-based superalloy ME3 at ambient and elevated temperatures: Role of grain-boundary engineering, Metallurgical and Materials Transactions A, 36 (2005) 3325-3333.

[116] J.M. Hyzak, I.M. Bernstein, The effect of defects on the fatigue crack initiation process in two P/M superalloys. I. Fatigue origins, Metallurgical Transactions A (Physical Metallurgy and Materials Science), 13A (1982) 33-43.

[117] J.M. Hyzak, I.M. Bernstein, The effect of defects on the fatigue crack initiation process in two P/M superalloys. II. Surface-subsurface transition, Metallurgical Transactions A (Physical Metallurgy and Materials Science), 13A (1982) 45-52.

[118] D. Eylon, J.M. Hyzak, An investigation of fatigue origins in superalloy powder compacts, Metallurgical Transactions A (Physical Metallurgy and Materials Science), 9A (1978) 127-129.

[119] J. Gayda, R. Miner, Fatigue crack initiation and propagation in several nickel-base superalloys at 650 C, International Journal of Fatigue, 5 (1983) 135-143.

[120] J. Gayda, T. Gabb, R. Miner, Fatigue crack propagation of nickel-base superalloys at 650 C, (1988) 293.

[121] A. de Bussac, Prediction of the competition between surface and internal fatigue crack initiation in PM alloys, Fatigue and Fracture of Engineering Materials & Structures, 17 (1994) 1319-1325.

[122] J.Y. Guedou, J.C. Lautridou, Y. Honnorat, N18, powder metallurgy superalloy for disks: development and applications, Journal of Materials Engineering and Performance, 2 (1993) 551-556.

[123] E.S. Huron, P.G. Roth, The Influence of Inclusions on Low Cycle Fatigue Life in a P/M Nickel-Base Disk Superalloy, Superalloys 1996, (1996) 359-368.

[124] X. Xie, L. Zhang, M. Zhang, J. Dong, K. Bain, Micro-mechanical behavior study of non-metallic inclusions in P/M disk superalloy Rene'95, in: K.A. Green, T.M. Pollock, H. Harada, T.E. Howson, R.C. Reed, J.J. Schirra, S. Walston (Eds.) Superalloys 2004: proceedings of the tenth international symposium on superalloys, Minerals, Metals and Materials Society, Champion, PA, United states, 2004, pp. 451-458.

[125] G.T. Cashman, A Statistical Methodolgy for the Preparation of a Competing Modes Fatigue Design Curve, Journal of Engineering Materials and Technology, 129 (2007) 159.

[126] G.T. Cashman, A Mathematical Model for Competing Failure Modes in Strain Cycle Fatigue, Journal of Engineering Materials and Technology, 129 (2007) 293.

[127] J. Miao, T.M. Pollock, J.W. Jones, Very High Cycle Fatigue Crack Initiation in Nickel-based Superalloy René 88 DT at 593 C, in: J.E. Allison, J.W. Jones, J.M. Larsen, R.O. Ritchie (Eds.) Fourth International Conference on Very High Cycle Fatigue (VHCF-4), The Minerals, Metals & Materials Society (TMS), Ann Arbor, Michigan, USA, 2007, pp. 445-450.

[128] J. Miao, T.M. Pollock, J.W. Jones, Fatigue Crack Initiation in Nickel-based Superalloy René 88 DT at 593 °C, in: R.C. Reed, K.A. Green, P. Caron, T.P. Gabb, M.G. Fahrmann, E.S. Huron, S.A. Woodard (Eds.) Superalloys 2008, The Minerals, Metals & Materials Society (TMS), Champion, Pennsylvania, 2008, pp. 589-597.

[129] R. Barrie, T. Gabb, J. Telesman, P. Kantzos, A. Prescenzi, T. Biles, P. Bonacuse, Effectiveness of shot peening in suppressing fatigue cracking at non-metallic inclusions in Udimet® 720, Materials Science and Engineering: A, 474 (2008) 71-81.

[130] R. John, J. Larsen, D. Buchanan, N. Ashbaugh, Incorporating residual stresses in life prediction of turbine engine components, in: A.F. Blom (Ed.) Fatigue 2002, Proceedings of the 8th International Fatigue Conference, Stockholm, Sweden, 2002, pp. 1063–1070.

[131] W. Zhuang, G. Halford, Investigation of residual stress relaxation under cyclic load, International Journal of Fatigue, 23 (2001) 31-37.

[132] H. Holzapfel, V. Schulze, O. Vöhringer, E. Macherauch, Residual stress relaxation in an AISI 4140 steel due to quasistatic and cyclic loading at higher temperatures, Materials Science and Engineering A, 248 (1998) 9-18.

[133] R. Landgraf, R. Chernenkoff, Residual stress effects on fatigue of surface processed steels, Analytical and experimental methods for residual stress effects in fatigue, (1986) 1-12.

[134] P. Prevey, D. Hombach, P. Mason, L.R.C. OH, Thermal residual stress relaxation and distortion in surface enhanced gas turbine engine components, (1998).

[135] W. Wallace, J. Frankel, Relief of Residual Stress by a Single Fatigue Cycle, Welding Journal, 28 (1949) 565-568.

[136] T. Gabb, J. Telesman, P. Kantzos, P. Bonacuse, R. Barrie, Initial assessment of the effects of non-metallic inclusions on fatigue life of powder metallurgy processed Udimet Alloy 720, in: G.E. Fuchs, A.W. James, T. Gabb, M. McLean, H. Harada (Eds.) Advanced Materials and Processes for Gas Turbines, TMS, 2003, pp. 237-244.

[137] P. Kantzos, R. Barrie, P. Bonacuse, T. Gabb, J. Telesman, The effects of forging strain on ceramic inclusions in a disk superalloy, in: G.E. Fuchs, A.W. James, T. Gabb, M. McLean, H. Harada (Eds.) Advanced Materials and Processes for Gas Turbines, TMS, 2002, pp. 245-254.

[138] T.P. Gabb, J. Telesman, P.T. Kantzos, J.W. Smith, P.F. Browning, Effects of High Temperature Exposures on Fatigue Life of Disk Superalloys, in: K.A. Green, T.M. Pollock, H. Harada, T.E. Howson, R.C. Reed, J.J. Schirra, S. Walston (Eds.) Superalloys

2004: proceedings of the tenth international symposium on superalloys TMS, Champion, Pennsylvania, 2004, pp. 269-274.

[139] D.J. Buchanan, R. John, N.E. Ashbaugh, Thermal residual stress relaxation in powder metal IN100 superalloy, Journal of ASTM International, 3 (2006) 1-11.

[140] J. Hoffmeister, V. Schulze, A. Wanner, R. Hessert, G. Koenig, Thermal Relaxation of Residual Stresses induced by Shot Peening in IN718, in: K. Tosha (Ed.) Proceedings of the 10th International Conference on Shot Peening, Tokyo, Japan, 2008, pp. 157-162.

[141] R. Mattson, W. Coleman Jr, Effect of Shot-Peening Variables and Residual Stresses on the Fatigue Life of Leaf-Spring Specimens, SAE Transactions, 62 (1954) 546-556.

[142] J. Morrow, G. Sinclair, Cycle-dependent stress relaxation, Sumposium on Basic Mechanisms of Fatigue, ASTM STP 237, American Society for Testing and Materials, (1959) 83-103.

[143] H. Jhansale, T. Topper, Engineering analysis of the inelastic stress response of a structural metal under variable cyclic strains, ASTM special technical publication, (1973) 246–270.

[144] S. Kodama, The behaviour of residual stress during fatigue stress cycles, in: S. Taira (Ed.) International Conference on Mechanical Behaviour of Materials, Kyoto, Japan, 1971, pp. 337.

[145] R. Champoux, J. Underwood, J. Kapp, Analytical and experimental methods for residual stress effects in fatigue, ASTM International, 1988.

[146] R.C. McClung, A literature survey on the stability and significance of residual stresses during fatigue, Fatigue and Fracture of Engineering Materials and Structures, 30 (2007) 173-205.

[147] M. Guagliano, L. Vergani, An approach for prediction of fatigue strength of shot peened components, Engineering Fracture Mechanics, 71 (2004) 501-512.

[148] N. Sidhom, A. Laamouri, R. Fathallah, C. Braham, H.P. Lieurade, Fatigue strength improvement of 5083 H11 Al-alloy T-welded joints by shot peening: Experimental

characterization and predictive approach, International Journal of Fatigue, 27 (2005) 729-745.

[149] J. Zhang, R. Prasannavenkatesan, M.M. Shenoy, D.L. McDowell, Modeling fatigue crack nucleation at primary inclusions in carburized and shot-peened martensitic steel, Engineering Fracture Mechanics, 76 (2009) 315-334.

[150] W. Cao, M. Khadhraoui, B. Brenier, J. Guedou, L. Castex, Therrnornechanieal relaxation of residual stress in shot peened nickel base superalloy, Materials Science and Technology, 10 (1994) 947-954.

[151] R. Dupke, W. Reimers, X-ray diffraction investigations on individual grains in the polycrystalline Ni-base superalloy IN 939 during cyclic loading. II. Residual stresses, Zeitschrift fur Metallkunde, 86 (1995) 665-670.

[152] J.D. Almer, J.B. Cohen, B. Moran, Effects of residual macrostresses and microstresses on fatigue crack initiation, Materials Science and Engineering A: Structural Materials: Properties, Microstructure and Processing, 284 (2000) 268-279.

[153] M.J. Caton, A.H. Rosenberger, Fatigue crack growth variability in waspaloy under representative loading conditions, in: J.M. Larsen (Ed.) Materials Damage Prognosis - Proceedings of a Symposium of the Materials Science and Technology 2004 Conference, Minerals, Metals and Materials Society, Warrendale, PA 15086, United States, New Orleans, LA, United States, 2004, pp. 113-119.

[154] S.K. Jha, J.M. Larsen, Random Heterogeneity Scales and Probabilistic Description of the Long-Lifetime Regime of Fatigue, in: J.E. Allison, J.W. Jones, J.M. Larsen, R.O. Ritchie (Eds.) Fourth International Conference on Very High Cycle Fatigue (VHCF-4), The Minerals, Metals & Materials Society (TMS), Ann Arbor, Michigan, USA, 2007, pp. 385-396.

[155] G.T. Cashman, A model for competing failures modes in elevated temperature strain cycle fatigue, PhD Thesis, Department of Mechanical Engineering, The University of Dayton, Dayton, Ohio, (2000).

[156] W. Porter III, K. Li, M. Caton, S. Jha, B. Bartha, J. Larsen, Microstructural conditions contributing to fatigue variability in p/m nickel-base superalloys, in: R.C. Reed, K.A. Green, P. Caron, T.P. Gabb, M.G. Fahrmann, E.S. Huron, S.A. Woodard (Eds.) Superalloys 2008, 2008.

[157] H. Bernstein, Materials Issues for Users of Gas Turbines, in: Proceedings of the 27th Texas A&M Turbomachinery Symposium, 1998, pp. 197.

[158] N.E. Ashbaugh, D.J. Buchanan, A.L. Hutson, R. John, K. Li, Life Prediction Methodologies for Aerospace Materials, University of Dayton Research Institute Reports, (2000).

[159] P. Bonacuse, P. Kantzos, R. Barrie, J. Telesman, L. Ghosn, T. Gabb, Distribution of Inclusion-Initiated Fatigue Cracking in Powder Metallurgy Udimet 720 Characterized, NASA Technical Report Server, (2004).

[160] S. Everitt, M.J. Starink, H.T. Pang, I.M. Wilcock, M.B. Henderson, P.A.S. Reed, A comparison of high temperature fatigue crack propagation in various subsolvus heat treated turbine disc alloys, Materials Science and Technology, 23 (2007) 1419-1423.

[161] A. Berens, P. Hovey, R. From, Evaluation of NDE Reliability Characterization, University of Dayton Research Institute Reports, (1981).

[162] A. Agresti, Categorical data analysis, (2002).

[163] D. Cox, E. Snell, Analysis of binary data, Chapman & Hall/CRC, 1989.

[164] J. Schaffer, A probabilistic approach to modeling microstructural variability and fatigue behavior in ASTM F562 medical grade wire, in: J. Gilbert (Ed.) Medical device materials IV: proceedings of the Materials & Processes for Medical Devices Conference, ASM International, Palm Desert, California, USA, 2007.

[165] G.T. Cashman, A review of Competing Modes fatigue behavior, International Journal of Fatigue, 32 (2010) 492-496.

[166] D. Freedman, R. Pisani, R. Purves, Statistics, (1997).

[167] I. Kueppenbender, M. Schuetze, Deformation behavior of NiO scales on Ni in argon and air at temperatures from 20 to 800°C with respect to the relief of growth stresses, Oxidation of Metals, 42 (1994) 109-144.

[168] A. Ul-Hamid, A.I. Mohammed, S.S. Al-Jaroudi, H.M. Tawancy, N.M. Abbas, Evolution of oxide scale on a Ni-Mo-Cr alloy at 900 °C, Materials Characterization, 58 (2007) 13-23.

[169] J.B. Johnson, J.R. Nicholls, R.C. Hurst, P. Hancock, The mechanical properties of surface oxides on nickel-base superalloys. I. Oxidation, Corrosion Science, 18 (1978) 527-541.

[170] C. Bruns, M. Schutze, Investigation of the Mechanical Properties of Oxide Scales on Nickel and TiAl, Oxidation of Metals, 55 (2001) 35-68.

[171] H. Mughrabi, Specific features and mechanisms of fatigue in the ultrahigh-cycle regime, International Journal of Fatigue, 28 (2006) 1501-1508.

[172] Q.Y. Wang, C. Bathias, N. Kawagoishi, Q. Chen, Effect of inclusion on subsurface crack initiation and gigacycle fatigue strength, International Journal of Fatigue, 24 (2002) 1269-1274.

[173] T. Kunio, M. Shimizu, K. Yamada, K. Sakura, T. Yamamoto, The early stage of fatigue crack growth in martensitic steel, International Journal of Fracture, 17 (1981) 111-119.

[174] A. Melander, A finite element study of short cracks with different inclusion types under rolling contact fatigue load, International Journal of Fatigue, 19 (1997) 13-24.

[175] J. Lankford, Inclusion-matrix debonding and fatigue crack initiation in low alloy steel, International Journal of Fracture, 12 (1976) 155-156.

[176] J. Lankford, Initiation and early growth of fatigue cracks in high strength steel, Engineering Fracture Mechanics, 9 (1977) 617-624.

[177] J. Lankford, F.N. Kusenberger, Initiation of fatigue cracks in 4340 steel, Metallurgical Transactions A (Physical Metallurgy and Materials Science), 4 (1973) 553-559.

[178] K. Shiozawa, Y. Morii, S. Nishino, L. Lu, Subsurface crack initiation and propagation mechanism in high-strength steel in a very high cycle fatigue regime, International Journal of Fatigue, 28 (2006) 1521-1532.

[179] K. Kanazawa, S. Nishijima, Fatigue fracture of low alloy steel at ultra-high-cycle region under elevated temperature condition, Zairyo/Journal of the Society of Materials Science, Japan, 46 (1997) 1396-1401.

[180] J. Lankford, F. Kusenberger, Initiation of fatigue cracks in 4340 steel, Metallurgical and Materials Transactions B, 4 (1973) 553-559.

[181] Y. Murakami, S. Kodama, S. Konuma, Quantitative evaluation of effects of non-metallic inclusions on fatigue strength of high strength steels. I: Basic fatigue mechanism and evaluation of correlation between the fatigue fracture stress and the size and location of non-metallic inclusions, International Journal of Fatigue, 11 (1989) 291-298.

[182] R. Prasannavenkatesan, Microstructure-sensitive fatigue modeling of heat treated and shot peened martensitic gear steels, PhD Thesis, Department of Mechanical Engineering, Georgia Institute of Technology, Atlanta, Georgia, (2009).

[183] D. Kuhlmann-Wilsdorf, P.F. Thomason, The role of vacant lattice sites in the low-amplitude fatigue failure at inclusions in steel, Acta Metallurgica, 30 (1982) 1243-1245.

[184] H. Mughrabi, On 'multi-stage' fatigue life diagrams and the relevant life-controlling mechanisms in ultrahigh-cycle fatigue, Fatigue and Fracture of Engineering Materials and Structures, 25 (2002) 755-764.

[185] W. Cao, K.Y. Lam, Effect of multi-flat inclusions on stress intensity factor of a semi-infinite crack, Engineering Fracture Mechanics, 47 (1994) 157-168.

[186] B.A. Cheeseman, M.H. Santare, The interaction of a curved crack with a circular elastic inclusion, International Journal of Fracture, 103 (2000) 259-277.

[187] K.Y. Lam, C. Wen, Enhancement/shielding effects of inclusion on arbitrarily located cracks, Engineering Fracture Mechanics, 46 (1993) 443-454.

[188] C. Wen, K.Y. Lam, Effect of a flat inclusion on stress intensity factor of a semi-infinite crack, Theoretical and Applied Fracture Mechanics, 19 (1993) 183-193.

[189] E. Castillo, Extreme value theory in engineering, Academic Press, Inc., New York, 1988.

[190] C.W. Anderson, J. De Mare, H. Rootzen, Methods for estimating the sizes of large inclusions in clean steels, Acta Materialia, 53 (2005) 2295-2304.

[191] M. Tiryakioglu, Statistical distributions for the size of fatigue-initiating defects in Al-7%Si-0.3%Mg alloy castings: A comparative study, Materials Science and Engineering A, 497 (2008) 119-125.

[192] C. Bathias, Piezoelectric fatigue testing machines and devices, International Journal of Fatigue, 28 (2006) 1438-1445.

[193] A. Shyam, C.J. Torbet, S.K. Jha, J.M. Larsen, M.J. Caton, C.J. Szczepanski, T.M. Pollock, J.W. Jones, Development of Ultrasonic Fatigue for Rapid, High Temperature Fatigue Studies in Turbine Engine Materials, in: K.A. Green, T.M. Pollock, H. Harada, T.E. Howson, R.C. Reed, J.J. Schirra, S. Walston (Eds.) Superalloys 2004: proceedings of the tenth international symposium on superalloys Minerals, Metals and Materials Society, Champion, Pennsylvania, 2004, pp. 259-268.

[194] L.F. Coffin, Jr., Fatigue at high temperature em dash prediction and interpretation, Proceedings of the Institution of Mechanical Engineers, 188 (1974) 109-127.

[195] L.F. Coffin, Jr., Multi-stage nature of fatigue: a review, Metal Science, 11 (1977) 68-72.

[196] S. Torquato, Author, H.W. Haslach, Jr, Reviewer, Random Heterogeneous Materials: Microstructure and Macroscopic Properties, Applied Mechanics Reviews, 55 (2002) B62-B63.

[197] D.L. McDowell, Microstructure-Sensitive Computational Fatigue Analysis, in: Y. Sidney, M.F. Horstemeyer (Eds.) Handbook of Materials Modeling, Springer Netherlands, 2005, pp. 1193-1214.

[198] D.L. McDowell, K. Gall, M.F. Horstemeyer, J. Fan, Microstructure-based fatigue modeling of cast A356-T6 alloy, Engineering Fracture Mechanics, 70 (2003) 49-80.

[199] D.L. McDowell, G.B. Olson, Concurrent design of hierarchical materials and structures, Scientific Modeling and Simulation, 15 (2008) 207-240.

[200] Design Assessment of Reliability with Inspection, www.darwin.swri.org, accessed on March 3, 2011.

[201] J.H. Hollomon, C. Zener, Problems in fracture of metals, Journal of Applied Physics, 17 (1946) 82-90.

[202] A.N. Stroh, A theory of the fracture of metals, Advances in Physics, 6 (1957) 418-465.

[203] D.J. Morrison, J.C. Moosbrugger, Effects of grain size on cyclic plasticity and fatigue crack initiation in nickel, International Journal of Fatigue, 19 (1997) 51-59.

[204] H. Singh, Y. Mao, A. Sreeranganathan, A.M. Gokhale, Application of digital image processing for implementation of complex realistic particle shapes/morphologies in computer simulated heterogeneous microstructures, Modelling and Simulation in Materials Science and Engineering, 14 (2006) 351-363.

[205] A.M. Gokhale, S.I. Lieberman, S. Tamirisakandala, Reconstruction of three-dimensional microstructures of TiB phase in a powder metallurgy titanium alloy using montage serial sectioning, Scripta Materialia, 55 (2006) 63-68.

[206] A.M. Gokhale, S.G. Lee, A. Sreeranganathan, Reconstruction and visualization of complex 3D pore morphologies in a high-pressure die-cast magnesium alloy, Materials Science and Engineering A, 427 (2006) 92-98.

[207] C. McVeigh, W.K. Liu, Linking microstructure and properties through a predictive multiresolution continuum, Computer Methods in Applied Mechanics and Engineering, 197 (2008) 3268-3290.

[208] F. Vernerey, W.K. Liu, B. Moran, Multi-scale micro morphic theory for hierarchical materials, Journal of the Mechanics and Physics of Solids, 55 (2007) 2603-2651.